Optical and Quasi-Optical Design and Analysis of Astronomical Instrumentation including a Prototype SAFARI Pixel

Presented by

Stephen Doherty, B.Sc., M.Eng.

A thesis submitted for the degree of

Doctor of Philosophy

NUI MAYNOOTH

Ollscoil na hÉireann Má Nuad

Terahertz Optics Group

Department of Experimental Physics

NUI Maynooth, Maynooth

Co.Kildare, Ireland

18th October 2012

Head of Department

Prof. J. A. Murphy, M.Sc., M.S, Ph.D.

Research Supervisor

Dr. Neil Trappe, B.Sc., Ph.D.

Contents

Abstract

The work of this thesis focuses primarily on the quasi-optical analysis of optical systems in the Terahertz region of the spectrum. This included the development of novel simulation techniques based on the principles of mode matching and gaussian beam mode analysis, which are uniquely suited to the simulation of electrically large optical systems at millimeter wavelengths. Additionally, several commercial software packages were used and experimental measurements conducted for the purpose of both validating the newly developed simulation techniques, as well as simulating / measuring specific elements beyond the scope of the in-house software.

The main drivers behind this work were a Technology Research Programme of the European Space Agency, the optical payload design of the future proposed Space Infrared-Telescope for Cosmology and Astrophysics mission and work on the Atacama Large Millimeter Array. Once the simulation tools were developed and proven an analysis of these optical systems was conducted. In the case of the Atacama Large Millimeter Array this involved the analysis of the proposed system, whilst for the other projects of the European Space Agency, although an initial optical system was proposed, much work was also required in maturing the design as well as conducting a standard analysis. This was carried out in conjunction with the other groups of the Technology Research Programme, which included the Terahertz optics group of NUI-Maynooth, the Space Research Organisation of the Netherlands, Rutherford Appleton Laboratory Space, and work groups of the universities of Cambridge and Cardiff.

The work of this thesis also considered the technical feasibility and design of a future space mission for the purpose of characterising Earth-type exoplanets up to 30 pc distant. This involved the establishment of the science goals and the associated technical requirements, as well as a detailed optical design of the proposed spectropolarimetric payload.

Acknowledgements

I would firstly like to thank my supervisor, Dr. Neil Trappe, for all his assistance over the years of this work. I could not have asked for a more dedicated and helpful supervisor and very much appreciate the time he devoted to me. I would also like to thank the other members of the group, Professor Anthony Murphy, Dr. Créidhe O'Sullivan, Dr. Marcin Gradziel and Mr. Tully Peacock all of whom always had an open door and offered much advice and assistance throughout. Also many thanks to the other members of the department including especially the department secretary Ms. Gráinne Roche for always ensuring everything ran smoothly, and chief technical officer Mr. John Kelly for sorting out the multiple computer, software and printer related issues. My thanks also go out to all the other postgraduates of the group and particularly to those with whom I've shared an office; Mark, Enda, Ronan, Darragh and Paul for the many useful discussions and also for the non-work related distractions. Also an extra thanks to Darragh and Paul for proof reading various chapters!

I also wish to acknowledge my family for their ever present support throughout my studies. Thanks to my parents, brother and sister for their encouragement and support. And to Alve, who always helped me forget any of the stresses of work or life. Muchas gracias por toda la alegría que traes a mi vida!

Finally, I would like to thank all my work colleagues from institutions outside of the THz-group and indeed also those from outside of NUI-Maynooth, as well as the many friends with whom I've shared my time over past number of years.

1. Motivation

1.1. Introduction

Since the success of the Infrared Space Observatories (ISO); Spitzer and AKARI of the United States and Japan, Europe and Korea, respectively, it has become evident that observations of mid-infrared (MIR) and far-infrared (FIR) dust and gas emissions are necessary should we wish to develop a more complete understanding of the Universe and its evolution. More recently, ESA launched its millimeter wavelength Herschel space telescope on the 14/05/2009, which is providing valuable new insights to the evolution of stars and galaxies and their interaction with the interstellar medium. As such, future missions are being considered to build and expand on what is being achieved by Herschel. Addressing this need is the Japanese led JAXA-ESA mission proposal for the **SP**ace **I**nfrared-Telescope for **C**osmology and **A**strophysics, otherwise referred to as SPICA. The primary goal of SPICA will be to improve our understanding of how galaxies, stars and planets form and evolve, as well as the interaction between the astrophysical processes that have led to the formation of our own Solar System. Such a mission would build on what Herschel has achieved and allow us, for example, to move from studying the formation of stars to being able to study the formation of planets. To achieve this SPICA would require much higher sensitivities and colder temperatures than is the case with Herschel. The European contribution to this mission would draw on the heritage and expertise in Europe from ESA's Herschel Space Observatory and Planck satellite and focus on the payload contribution of the Far-Infrared Instrument (SAFARI). To this end ESA has also

run a Technology Research Programme for the purpose of developing new technological capabilities required for the realisation of the SAFARI instrument.

The **A**tacama **L**arge **M**illimeter **A**rray, or ALMA, of the European Southern Observatory (ESO), also represents a major step forward in the area of millimeter wave astronomy. It is a project comparable to some of the world's major facilities at other wavelengths, including the Hubble Space Telescope and the VLT (Very Large Telescope) in terms of sensitivity and angular resolution. This chapter provides a brief overview of the science case behind these astronomical projects as well as elaborating on some of the novel technological challenges associated with their realisation.

1.2. SPICA

1.2.1. Scientific Objectives

The MIR / FIR Wavebands

The SPICA mission is designed to investigate the origin and composition of the Universe, determine the conditions necessary for stellar and planetary formation, and examine the Universe's chemical evolution. More specifically SPICA will focus on the following two areas: Planetary System Formation and Galactic Evolution.

The MIR and FIR wavebands include the richest windows for astrophysical objects during the evolution of galaxies (5 - 210 μm). Apart from being unaffected by dust extinction, MIR and FIR radiation contain many Polycyclic Aromatic Hydrocarbon (PAH) and silicate emission features. PAHs are a class of very stable organic molecules made up of only carbon and hydrogen. They are very common in space, allowing them to be used to probe conditions in distant regions. Light emitted from excited PAHs has been detected both from the hot regions of space where stars are being born and around dying stars. Additionally, these molecules have been detected in comets and asteroidal dust and are also

common in meteorites. Thus, investigation of these molecules is significant for both our understanding of star and planet formation and AGN activity.

Furthermore, MIR and FIR observations allow us to probe further back in time, by examining UV and optical spectral lines of a galaxies rest frame, which have been shifted to the MIR / FIR due to extreme cosmological red shift.

Planetary System Formation

The spectral range of SPICA will allow for the gas chemistry and gas/grain processes within obscured stellar nurseries to be observed. This also includes lines from O, OH and H_2O (gas and ice) from proto-planetary gas disks. Such gas disks establish the boundary conditions for planet formation. SPICA will be sensitive in the gas regions including the H_2 ground state, ortho and para rotation lines of 5 - 15 μm, 17 and 28 μm.

Analysis of the dust in circumstellar disks may reveal processes responsible for the formation of terrestrial planets. FIR spectroscopy will determine the mineral makeup of dusty disks in young star systems. SPICA's instruments will be a factor of 100 times more sensitive to those of the ISO and as such, should be capable of conducting detailed mineralogy of the dust, determining the variation in grain size, distribution and temperature. In nearby star systems it will also be possible to map the mineral content and grain size distribution as a function of radius [1].

The MIR and FIR wavebands contain information regarding the chemical composition of the dust and ice and FIR Spectral Energy Distributions (SED's) enable one to constrain the dust size distribution. As such, SPICA will record data pertaining to the dust life-cycle. This data will include information on the role of stellar winds in the evolution of massive stars, the formation of dust around evolved stars, the evolution of dust in the interstellar medium, the destruction of dust in supernova generated shock waves and the formation of proto-planetary disks.

SPICA's coronagraph operating from 3 - 27 μm will allow it to perform direct imaging and MIR spectroscopy of young gas giants within 1 Gyr of formation. The binary mask type coronagraph should improve the contrast ratio by a factor of 10^6. This would be sufficient to achieve a working angle capable of detecting a planet 9 AU from its host star 10 pc distant at 5 μm [1], there are 30 target stars within a range of 10 pc. Extending the wavelength range to 3.5 μm significantly increases the instruments sensitivity to planets close to their host star and will also include the expected 5 μm emission feature [2].

Galaxy Evolution

Although ultra-luminous and luminous infrared galaxies in the rest frame are rare in our Universe, the integrated luminosity of high red-shift galaxies in the infrared is believed to account for a significant fraction of the cosmic infrared background [3]. The existence of these galaxies challenges the expectations of cold dark matter cosmological models, indicating the necessity of serious revisions being made to these models [4].

The wide range of MIR and FIR instruments aboard SPICA will make it possible to detect and quantify the star formation and the black hole accretion components at increasing red-shift, thus essentially peering further back in time to examine galaxy evolution. More specifically the physical conditions in active galactic nuclei, central starbursts, circumnuclear rings, disks, winds and halos in the local universe will be studied [1].

Observational evidence to date suggests that the properties of faint MIR / FIR population differ significantly from those of similarly luminous, local infrared galaxies [5]. Amongst other details, the connection between AGN and starbursts will be probed by SPICA, which will use spectroscopy to constrain many of the physical properties of the gas, such as the temperature, density and metallicity, as well as characterising the radiation fields from AGN (Active Galactic Nuclei) and starbursts [1].

Science Requirements

To achieve the ambitious scientific programme necessitates key functional and performance requirements. These include all sky access during the course of the mission, which would require a 3-axis stabilised spacecraft with high pointing accuracy and stability in a thermally benign orbit.

The high photometric sensitivity observations in the MIR/FIR would require a telescope aperture as large as 3.5 m (which remains compatible with available launcher fairings) and diffraction limited image quality at 5 μm at the operational temperature. This would require a surface roughness of less than 20 nm. A two mirror on-axis Ritchey Chrétien design is being considered due to its compact nature and wide field of view. Furthermore, active cooling to below 5 K would be required to effectively eliminate non-astronomical photon noise. To achieve this a new form of mechanical cooler achieving temperatures of less than 5 K without the need of consumables will be implemented.

The focal plane instruments must also cover the full wavelength range from 5 to 210 μm. These will include a MIR coronagraph (3.5 to 27 μm) with photometric and spectral capabilities, a MIR wide-field camera and high resolution spectrometer, and the European contribution, which the work of this Thesis will focus on, a FIR imaging spectrometer (SAFARI).

1.2.2. SAFARI

SAFARI is an imaging fourier transform spectrometer covering 30 - 210 μm that is to allow for broad-band photometry imaging as well as variable resolution imaging spectrometry. The wavelength range is to be divided into 2 or 3 sub-bands, with the short wavelength limit being defined by the overlap with the MIR instrument and the long wavelength limit defined by the [NII] 206 μm fine structure line. The spectral resolution is to range from $R \approx 100$ in the low resolution mode to $R \approx 2{,}000$ and $R \approx 10{,}000$ at 100 μm in the medium

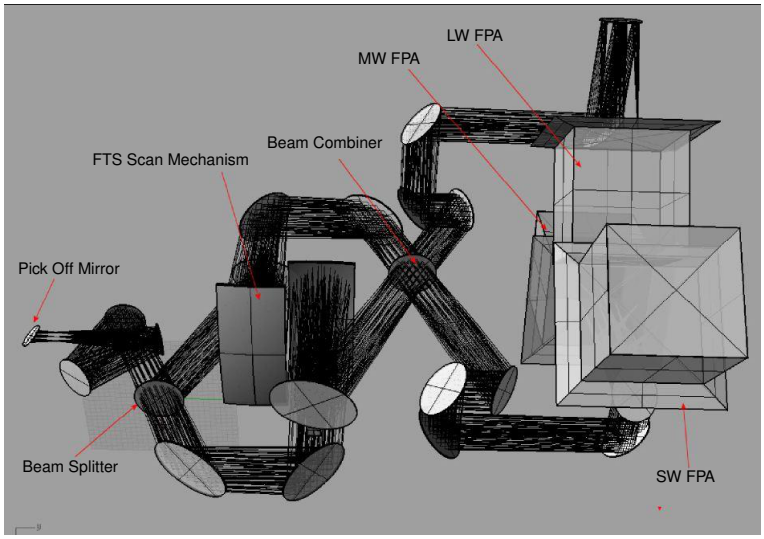

Figure 1.1.: Front End SAFARI Optics [6]. The acronyms are as follows: FTS - Fourier Transform Spectrometer, FPA - Focal Plane Array, LW - Long Wavelength, MW - Mid Wavelength, and SW - Short Wavelength.

and high resolution modes, respectively. It should therefore be noted, that throughout this work the terms L- and S-band refer to the short and long wavelength bands of SAFARI, that is 35 - 70 µm and 110 - 210 µm, respectively.

The main optical elements of a proposed design are shown in figure 1.1. The input optics re-image the telescope pupil for stray light control and expands and partially collimates the beam entering the spectrometer. The dimensions are to be such that the spectral resolution requirement of R = 2000 at 100 µm will be met. The final element is the beam combiner, which produces interference beams in the two output arms. The camera optics then focus the image onto the Focal Plane Arrays. These Arrays consist of an array of horns feeding into detector cavities. A graphical representation of this can be seen in figure 1.2(a). The pixel spacing between these horns is to be set at $F\lambda_0/2$ to achieve critical image sampling.

The scientific performance of SAFARI is critically dependant on the sensitivity of the detector system. Two different such systems are under consideration for SAFARI: Transition Edge Sensor (TES) bolometers and photoconductors. Although the use of TES bolometers would be complicated by their requirement of a base temperature of approximately

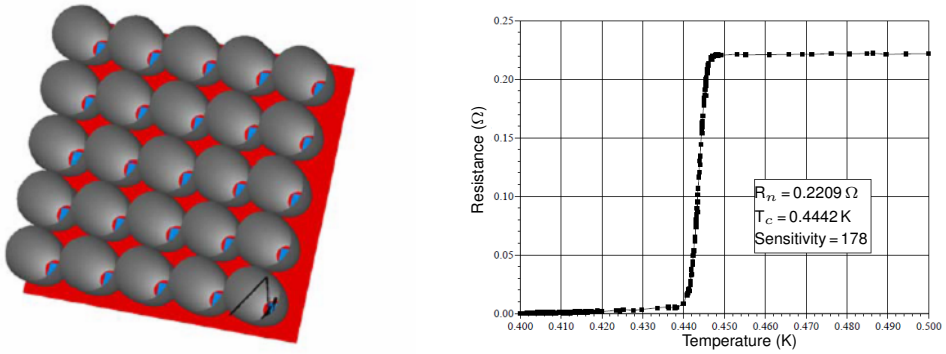

(a) Graphical representation of the horn array (b) Superconducting transition at 444 mK for a Mo/Au bilayer, [7]

Figure 1.2.: Horn array and TES principle

50 - 70 mK (in order to achieve the required noise-equivalent power (NEP)), their spectral response provides good access to the wavelength band around 40 µm, where photoconductors perform poorly. Furthermore, the relatively low absorber cross-section compared to the high cross-sectional area of photoconductors results in a low hit rate and thus should result in the TES bolometers being less susceptible to the effects of cosmic rays. As such, TES detectors are adopted as the reference case and will be considered as the absorber for the purpose of this work. TES technology exploits the transition between the superconducting and normal state of a system to obtain large variations in resistance for small temperature fluctuations. Such a transition is displayed in figure 1.2(b) [7]. The transition itself occurs over an extremely narrow temperature range of approximately 1 mK. The bilayer can be optimised for a variety of optical loads by varying the relative thicknesses of the normal metal (Au) and superconducting metal (Mo), so as to shift the transition temperature.

SAFARI detector sensitivity requirements imply that coupling to the detector system must be stringently controlled. The susceptibility of bolometric detectors to currents coupling into the detector system and dissipating power within the bolometers is a particular susceptibility of the class of detector technology considered [6]. As such, the coupling to the detector system is of utmost importance.

At present the use of both pyramidal and cylindrical horn configurations is being explored. When one considers the array configuration, depicted in figure 1.2(a), the packing advantages of the pyramidal horns becomes obvious. Each antenna horn is to feed into a detector cavity containing an absorber and TES detector. The function of the cavity is analogous to that of an integrating sphere in optics, i.e. a hollow sphere providing diffuse reflection on the inside. Thus, power not absorbed at first by the absorber and detector is ideally trapped in the cavity until such a point as it is absorbed. However, unlike the integrating sphere of IR and visible optics the modal nature of the incoming field require that cavity designs based both on classical optics and also those following the microwave approach be considered.

The design of the feed horn antennas have to attempt to maximise the entrance aperture as close as possible to that of the pixel and the exit aperture to the size of the detector absorber ($D_{exit} = D_{abs}/2$). Furthermore, considering the extremely faint nature of the signals to be measured, and the fact that the detectors are not polarisation dependent, a highly multi-moded horn is preferable, so as to maximise the throughput and consequently the levels of absorbed power. Thus, while matching the horns exit aperture to the size of the detector care must also be taken not to reduce the number of modes at the long wavelength end of the band.

At this early stage in the SAFARI instrument design the front-end optics have yet to be finalised. As such, the present design of the of the horn-cavity system is driven by the goals of maximising coupling to an on-axis plane wave, maximising the through-put of the horn antenna and the resulting total absorbed power, while minimising the cross-talk between pixels.

1.3. TES - Technology Research Programme (TRP)

1.3.1. Overview

One of the primary drivers of this work was the ESA Technology Research Programme to develop a Transition Edge Sensor (TES) array technology for future mm-wave to Far-Infrared (FIR) space applications. The Terahertz optics group of NUI Maynooth worked with a consortium of 4 other research institutions, the Space Research Organisation of the Netherlands (SRON), Rutherford Appleton Laboratory Space (RAL Space), and work groups of the universities of Cambridge and Cardiff on this 2 year programme. The SPICA mission outlined in the previous section is one of three future missions under consideration which would require such technology. For the purpose of this work the SAFARI system is therefore taken as the base example and as such, whilst the analyses conducted are not tailored to the intricate specifics of the system, the pixel designs considered are relevant to SAFARI.

The ESA statement of work, as mentioned, considered three mission concepts requiring this TRP. As well as SPICA this also included B-Pol and the Far Infrared Interferometer (FIRI), which both propose a focal plane array similar to that in SAFARI and would therefore also require such technology. B-Pol is the next generation Cosmic Microwave Background (CMB) satellite dedicated to a full sky survey at mm-wavelengths for the purpose of characterising the polarisation of the CMB and search for primordial gravitational waves in the B-mode polarisation power spectrum [8]. And the FIRI proposal considers the feasibility of an interferometer to achieve an angular resolution of less than 1 arcsecond at wavelengths between 25 and 300 μm. The selected baseline concept is a single spacecraft Michelson interferometer with cryogenically cooled SPICA-sized telescopes on deployable booms with a central hub [9].

The work packages of NUI Maynooth focused primarily on the modelling of the optical coupling of the horn antenna and integrating cavity, as well as full pixel bandwidth mod-

elling. This work included first the development of the modelling tools required and consequently the analysis and potential improvement of the proposed feedhorn antenna and cavity designs. It should be noted that the modelling of such multimoded horn-cavity combinations at THz frequencies can present significant difficulties for standard simulation packages. Much of the difficulties encountered in this work were the result of technological limitations in the manufacturing process, due primarily to both the array format and micron scale dimensions. Accounting for these restrictions results in unconventional designs and also compromises in the optical performance. To better appreciate these trade offs, and understand the design types considered throughout the work of this thesis, some of the results of the work groups of RAL Space and Cardiff University are outlined here.

1.3.2. Array Manufacturing Process

The standard proven approach of producing coupling optics for a single detector involves electroforming a feedhorn on a mandrel. Typically, Stainless Steel or Aluminium are used to form the mandrel, which can then be mechanically extracted or chemically etched from the electroformed feedhorn, respectively. Unfortunately, this single pixel approach does not translate well to the situation of large arrays, due to the difficulty in integrating the individual feedhorns into an array format. A novel approach for the production of electroformed pyramidal feedhorns in an array format was developed at RAL Space and involved wire cutting an array of mandrels around which copper could be electroformed.

Due to the narrow dimensions of the proposed horn exit apertures ($\approx 50\,\mu$m S-band) there results a poor ability to transfer heat away from the tip of the mandrels during the wire cutting process. This leads to burning and distortion of the tips of the mandrels, as can be seen in figure 1.3(a). One proposed solution involved the introduction of a stepped tip allowing for better thermal conduction (see figure 1.3(b)) and has been successfully employed in the manufacture of mandrel arrays, such as those in figure 1.3(c).

(a) Distortion resulting in the tips of the mandrels due to poor thermal conductivity at the narrow tip ends.

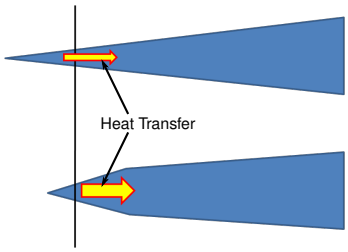

(b) Proposed stepped tip design allowing for a greater transfer of heat away from the tips.

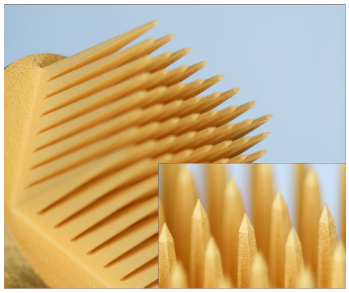

(c) Resulting mandrel array using the stepped tip design.

Figure 1.3.: Wire cutting technique for the manufacture of pyramidal horn mandrel arrays and the difficulties imposed by poor thermal conductivities (provided by RAL Space).

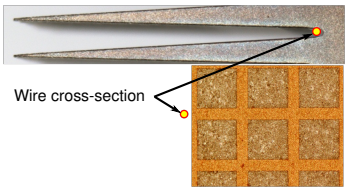

(a) Cutting wire cross-section determines the minimum spacing available between the horn entrance apertures of an array.

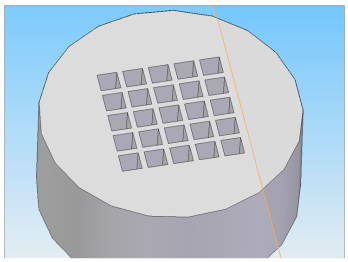

(b) Resulting dead space between entrance apertures.

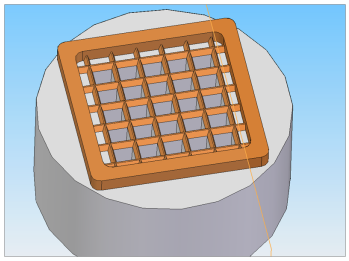

(c) Triangular profiled grid proposed to improve the filling factor.

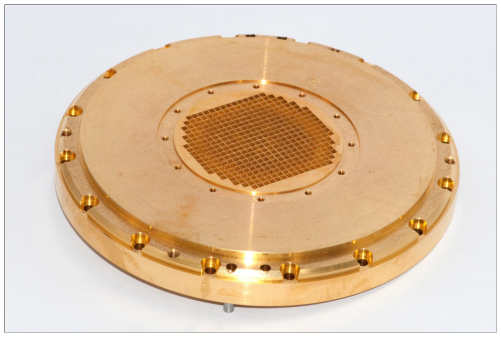

(d) Final horn array prototype - front

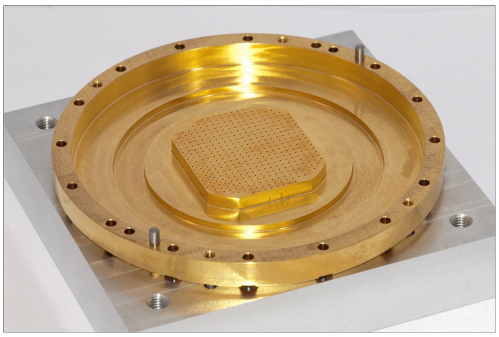

(e) Final horn array prototype - back

Figure 1.4.: Restrictions imposed by the cutting wire's dimensions and completed prototype arrays (provided by RAL Space)

A further limiting feature of the approach is introduced by the diameter of the wire (190 µm), which establishes the minimum spacing between the horn entrance apertures

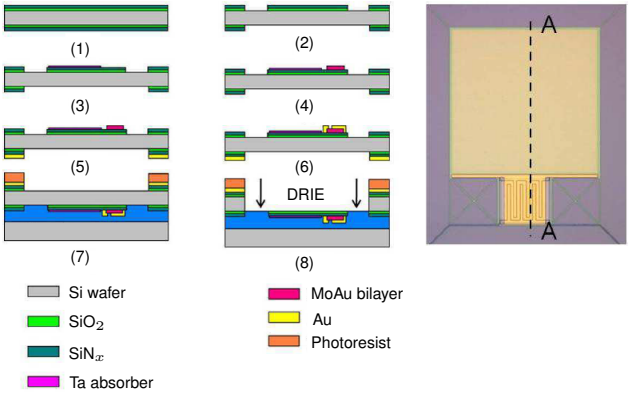

(a) Schematic diagram of the wafer production process showing the process flow for a single array. The cross-section is along the line marked.

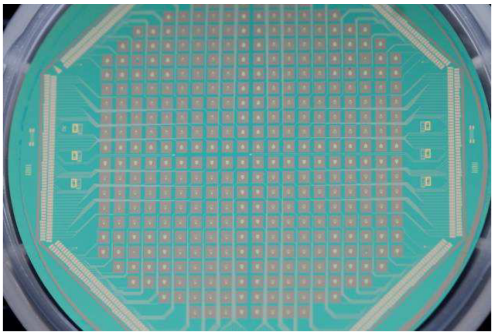

(b) Completed wafer before the DRIE process.

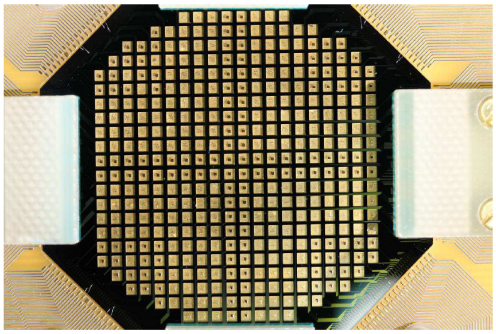

(c) Completed wafer after DRIE and mounted.

Figure 1.5.: Wafer production process and sample images of a wafer towards and at the end of the production process (provided by Cardiff University)

of an array (see figure 1.4(a)). Attempts to overcome this restriction include the use of a triangular profiled grid to improve the filling factor, this is depicted in figure 1.4(c). Prototype arrays made using this technique are displayed in figures 1.4(d) and 1.4(e).

The array of absorbers is produced on a single wafer. Once completed and the electronics attached the array may then be placed to sit behind the feed horn array. One significant optical complication arising from this methodology is the resultant open space between the absorbers, which may allow for cross-talk. The processing of a wafer to an array of absorbers and TES detectors is outlined in figure 1.5. The steps are as follows:

1. Si wafer with 200 nm SiN_x
2. Etch SiN_x from front and back of the wafer

3. Deposit MoAu bi-layer (40/195 nm)
4. Etch TES
5. Deposit Au on the back surface
6. Deposit Au on front as banks and thermalising bars
7. Deposit Nb connection and contact pads
8. Deep Reactive Ion Etching (DRIE)

Three design features emerging from these manufacturing techniques and restrictions include, firstly, the adoption of pyramidal over cylindrical feedhorn geometries. Secondly, a non-standard two step pyramidal feedhorn design. And thirdly, a physical opening between the detector regions of each pixel. Each of these points require careful optical analysis in order to both ascertain the direct impact on the optical efficiency of the system and also to optimise the proposed optical design with consideration given to these manufacturing constraints.

1.4. ALMA

1.4.1. Scientific Objectives

The ALMA system will achieve an angular resolution of 5 milliarcseconds [10], representing an improvement of two orders of magnitude in comparison to present systems. It is designed as an all purpose telescope with targets ranging from our own solar system to the most distant galaxies.

The main science objectives of ALMA include:

- Origins of galaxies, stars and planets
- The detection of dust enshrouded star forming galaxies and galaxies whose light is obscured by dust extinction and/or redshifted out of the optical/UV.

- To explore in detail the physical and chemical processes of star and planet formation in nearby dusty molecular clouds and protoplanetary disks.

To comprehensively cover the entire science case of ALMA exceeds the outline of this work. As such, the following will briefly describe some of the goals of ALMA in regard to Galaxies and Cosmology, and Star and Planet Formation. Further areas of interest for ALMA, including Stars and their Evolution and the study of the Solar System are not outlined below. For information on these areas and for a more detailed overview of the areas covered below [11] should be consulted, upon which the following sections are based.

Galaxies and Cosmology

ALMA has the potential to probe into many areas regarding Galaxies and Cosmology. This section will only very briefly outline some of these cases. The high redshift Universe leaves the early Universe very accessible to observations at millimeter and sub-millimeter wavelengths, as photons are redshifted out of the optical and UV. Apart from opening up the high population of dusty star forming galaxies at high redshift, ALMA will also provide a means for direct measurement of the redshift, made possible by the many available spectral lines. Furthermore, ALMA will be capable of measuring the pronounced 100 µm feature of luminous star forming galaxies. This is thought to be the result of UV and optical absorption by dust, which then re-emits photons at longer wavelengths.

An understanding of the physical and chemical properties of distant galaxies is necessary to understand star formation and other phenomena at high redshift. One possible means of studying these distant galaxies is to observe rare and diagnostically important lines, such as Quasar absorption lines. The depth of absorption lines is independent of distance, allowing them to serve very well as diagnostic lines. This also provides information on chemical evolution as a function of redshift and a means of measuring the temperature of the Cosmic Microwave Backround radiation as a function of temperature.

Gas in Galactic Nuclei presents yet another target of interest for ALMA. The centers of galaxies are often obscured at optical wavelengths due to large amounts of dust. ALMA will be capable of mapping the structure of the nuclei and tracing the kinematics of molecular gas. This should allow a determination of the masses and kinematics of optically obscured galactic nuclei with a resolution of a few parsecs.

Apart from probing into distant galaxies this will also present the possibility to examine our own galactic center at a very high spatial resolution. This should provide data on a number of physical processes of interest, such as, the nature of molecular cloud populations and the physical phenomena occurring in the vicinity of massive black holes.

ALMA also intends on exploiting gravitational lensing, which will not only make it possible to study background galaxies that would be otherwise too faint to detect but will also allow constraints to be imposed on the gravitational potential of the foreground lens.

Star and Planet Formation

Considering that diffuse interstellar gas often becomes part of denser clouds from which stars are ultimately born, one may appreciate how understanding the physical and chemical properties of this gas is important in understanding the initial conditions of star formation.

Studies of diffuse interstellar clouds to date suggest the presence of PAH's (Polycyclic Aromatic Hydrocarbons), fullerences and long carbon chains. It is as yet unknown how these molecules can survive the intense UV radiation. Further study of these clouds at the mm wavelength may help to further explain this. Also in comparison to optical and UV absorption studies, mm absorption observations will allow comparison of diffuse cloud properties in different regions of the galaxy, also beyond the solar neighbourhood.

Dense pre-stellar cores are also of interest in understanding star formation. The fragmentation of the cloud may determine the initial mass function (IMF) of young stars. The

IMF is a crucial parameter in the study of galactic evolution. Mass distribution follows a law of $\frac{\Delta N}{\Delta M} \propto 10^{-1.5}$ below $0.5\,M_\odot$ and $\propto 10^{-2.5}$ above $0.5\,M_\odot$. This is similar to the stellar IMF, which follows a law $\propto 10^{-1.2}$ for 0.1 - $1\,M_\odot$ and $\propto 10^{-2.5}$ for 1 - $10\,M_\odot$. This suggests that the IMF may be established at the prestellar stage of star formation, thus motivating the study of such pre-stellar cores.

The structure of protostellar envelopes and disks also warrants investigation. ALMA will allow tracing of the structure of the thick envelope around young and embedded protostars. Compact structures, such as newly forming disks, may be identified through analysis of the spatial distribution of the dust and gas. Motions due to infall, outflow and rotation all play significant roles in the envelopes of class 0 protostars and result in very complicated kinematical behaviour. ALMA also presents the possibility of studying such phenomena as out- and in-falling envelopes by looking for redshifted absorption against the disk / star continuum.

Several further areas relating to star formation will also be considered by ALMA, such as; High-mass star formation (eg. Orion), the chemistry of star-forming regions will be explored, as will be cold collapse envelopes, embedded phase and outflows and photon dominated regions.

One of the key areas of exploration for ALMA in regard to planet formation will be the study of protoplanetary disks. These have typical temperatures of 30 - $300\,K$ and thus are very suited to sub-millimeter observations. Key questions to be addressed in their study include:

- How do disks evolve from the massive gas-rich disks seen around pre-main sequence T Tauri stars to the tenuous dust debris disks seen around mature stars such as Vega?
- When is the gas and dust dissipated?
- How many disks have formed planets that are revealed by tidal gaps in the disks?

- What is the associated time-scale for planet formation?
- What is the chemical composition of the gas in disks, providing the building blocks from which future planetary systems are made?

Massive protoplanetary disks around main sequence stars as well as the dispersal of dust and gas in disks, debris disks and zodiacal dust systems and of coarse the chemistry of protoplanetary disks will all also be examined by ALMA with a motivation to further understanding planet formation.

1.4.2. The ALMA Telescope

ALMA will be a single telescope composed initially of 66 high-precision antennas, and operating at wavelengths of 0.3 to 3.6 mm. The main 12 m array will have fifty antennas, 12 m in diameter, acting together as a single telescope. An additional compact array of four 12 m and twelve 7 m antennas will complement this. The array works as an interferometer with a variable baseline with the maximum distance between antennas ranging from 150 m - 18 km (this is achieved by having each antenna designed so as to be mobile as outlined in figure 1.6). The resulting sensitivity and resolution should achieve images up to ten times sharper than the Hubble Space Telescope, and complementing images made with the VLT Interferometer.

The Front End refers to the beginning of a chain comprising detection, amplification, conversion and digitisation of a signal. From the antenna sub-reflector the signal passes through a series of mirrors and waveguides to the cold (≈ 4 K) detector region. At this point the signal (between 30 and 950 GHz) is mixed with a reference frequency to an intermediate frequency of less than 15 GHz.

One of the main challenges presented for the design of the ALMA optics was the need to couple 10 separate dual polarisation frequency bands to the sky. To accomplish this each frequency band was built in a removable cartridge, thus allowing for all 10 bands to fit

(a) ALMA Telescope transport truck

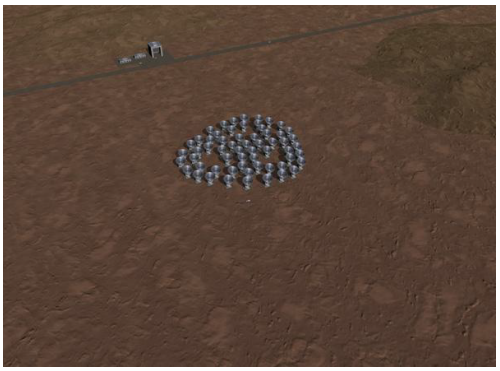

(b) ALMA array in a compact configuration

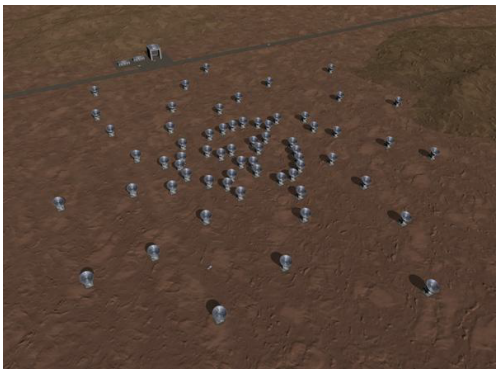

(c) ALMA array in a seperate spread out configuration

Figure 1.6.: The ALMA array can be moved to provide baselines ranging from 150 m to 18 km.

into a single cryostat. Further technical requirements included each of the ten receiver bands being capable of receiving two orthogonal linear polarisations. One should note that the cross-polar energy level refers to energy orthogonal to the desired polarisation and the co-polar to radiation in the desired polarisation. The cross-polar energy level were to be at least 24 dB below the co-polar total energy level. Each of the ten bands had to be optimised to provide good coupling with the ALMA telescope beam as well as provide low side lobe levels at the sky. During operations the secondary mirror could then be adjusted to refocus the telescope from one band to another. The coupling to the telescope was therefore to be frequency independent. Furthermore, no manual adjustments were to be required after installation of the front-end at the telescope. Corrugated horn antennas were adopted as the feed system. These requirements are summarised under the following points:

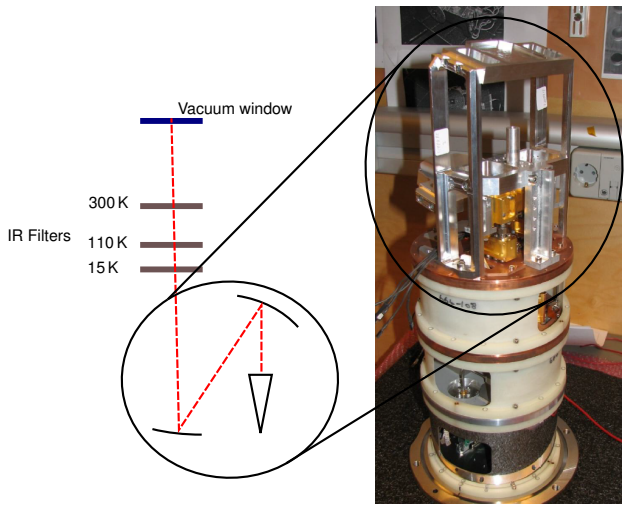

Figure 1.7.: An image of the ALMA Band 5 cartridge along with a non-scale schematic of the front end optics

- ALMA receiver frequency coverage of 30 - 950 GHz is to be split into ten bands following the atmospheric transmission windows.
- Each of the ten receiver bands should receive two orthogonal linear polarisations. The cross-polar energy level should be at least 24 dB below the co-polar total energy level.
- All low noise mixers should be contained within one front-end cryostat.
- The optics design should allow for simultaneous operation of ALMA band 3 at times (for phase calibration).
- Each of the ten bands should be optimised to provide good coupling with the ALMA telescope beam (aperture efficiency) as well as low side lobe levels at the sky. The coupling to the telescope should be frequency independent.
- No manual adjustments should be required after installation of the front-end at the telescope.
- Beams for the two polarisations on the sky should coincide.

The work considered in this thesis examined the ALMA Band 5 system developed at Chalmers Technical University, Sweden. This band covers a spectral range of 163 - 211 GHz. The initial proposed corrugated horn consisted of 190 segments each 0.26 mm in length. The total horn length was 54.87 mm and the corrugation depths approximately $\frac{\lambda}{4}$ for a center frequency of 187 GHz ($\lambda = 1.6$ mm). Due to the expense involved in the manufacture of such corrugated horns; simulations of the proposed horn design were conducted as part of this work using proven mode matching software. Additionally, a cheaper prototype horn was machined at the GARD institute of Chalmers Technical University and measured for comparison with the simulated results. This analysis may be seen in section 3.4.

2. Simulation and Measurement Techniques

2.1. Introduction

This chapter provides an overview of the various commercial simulation packages used and focuses very much on the aspects of the software applied throughout the work of the thesis. Furthermore, some of the more fundamental principles drawn upon throughout the thesis are elaborated on for future reference. As well as considering the various simulation techniques and packages, an overview of the basic operation of a Vector Network Analyser for measurements in the Terahertz region is presented.

The direct contribution of the author to the work of this section is to be found in the testing and adaption of the commercial packages for specific use relevant to work conducted throughout the thesis.

2.2. CST Microwave Studio

The CST Studio Suit is a commercially available software package, which makes use of finite integration techniques (FIT) to carry out electromagnetic simulations. Unlike most numerical methods, FIT discretises the integral form of Maxwell's equations rather than the differential ones. To solve these numerically one must define a finite calculation domain. To that end, a mesh system is implemented to divide the domain into many grid cells. The primary mesh can be visualised in CST using "Mesh View", however, internally

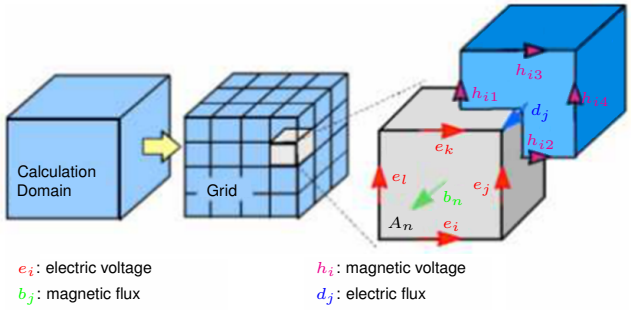

Figure 2.1.: An image of the CST mesh system - source: CST Documentation Center

a second or dual mesh is set up orthogonal to the first one, see figure 2.1. The spatial discretisation of Maxwell's equations is performed on these two orthogonal grid systems. Maxwell's equations are formulated for each of the cell facets separately. To illustrate the FIT technique consider the following of Maxwell's equations (equation 2.1).

$$\int \vec{E} \cdot \vec{dS} = -\frac{\partial}{\partial t} \int \int \vec{B} \cdot \vec{dA} \tag{2.1}$$

When considering a mesh cell Faraday's law permits the closed integral $\int \vec{E} \cdot \vec{dS}$ to be rewritten as the sum of four grid voltages $(e_i + e_j - e_k - e_l)$. Also the magnetic flux on the enclosed cell facet (b_n) is equivalent to $\int \int \vec{B} \cdot \vec{dA}$. Thus resulting in equation 2.2.

$$e_i + e_j - e_k - e_l = -\frac{\partial}{\partial t} b_n \tag{2.2}$$

Repeating this for all the cell facets results in the following matrix formulation of expression 2.3, which can also be expressed using operator notation (see equation 2.4).

Applying a similar scheme to Ampère's law on the dual grid, which requires the definition of the dual discrete curl operator $\widetilde{C}$, and discretising the remaining divergence equations results in the complete discretised set of Maxwell's equations. The material relations may then be approximated over the grid edges and cell areas, respectively. A noteworthy point of the FIT technique is that the properties of the continuous gradient, curl and divergence operators are maintained in grid space. In addition to orthogonal hexahedral

grids, FIT can also be applied to more general mesh types such as topologically irregular and tetrahedral grids.

$$\begin{pmatrix} & . & . & . & & \\ 1 & . & 1 & . & -1 & . & -1 \\ & . & . & . & & \end{pmatrix} \begin{pmatrix} e_i \\ . \\ e_j \\ . \\ e_k \\ . \\ e_l \end{pmatrix} = -\frac{\partial}{\partial t} \begin{pmatrix} . \\ b_n \\ . \end{pmatrix} \tag{2.3}$$

$$\mathbf{Ce} = -\frac{\partial}{\partial t}\mathbf{b} \tag{2.4}$$

Solver Types

CST Microwave Studio has three basic solvers from which to choose; the Transient, Frequency Domain and Eigenmode solvers. The correct choice of solver appropriate to the problem type can be of critical importance in accurate and efficient simulations, as such, a brief overview of the more relevant solvers is considered here. The work of this thesis made frequent use of the transient and frequency domain solvers. The transient solver allows for the simulation of a structure's behaviour over a wide frequency band in a single computation. It is available using only a hexagonal mesh type and is based on the discretised set of Maxwell's Grid equations where central differences are substituted for the time derivatives (see equation 2.5).

$$\begin{aligned} \mathbf{e}^{n+1/2} &= \mathbf{e}^{n-1/2} + \Delta t \mathbf{M}_{\epsilon}^{-1} \left(\widetilde{\mathbf{C}} \mathbf{M}_{\mu}^{-1} \mathbf{b}^{n} + \mathbf{j}_{s}^{n} \right) \\ \mathbf{b}^{n+1} &= \mathbf{b}^{n} - \Delta t \mathbf{C} \mathrm{e}^{n+1/2} \end{aligned} \tag{2.5}$$

The calculation is then conducted through consideration of electric voltages and magnetic fluxes. Both sets of unknowns are located alternately in time, and the approach is implemented as in the leap-frog scheme outlined in figure 2.2.

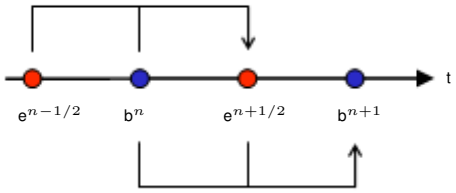

Figure 2.2.: The leapfrog scheme implemented in CST Microwave Studio's transient solver.

Alternatively, the frequency domain solver can be used together with the hexahedral or tetrahedral grids and is also equipped with specialised modules for quick S-parameter calculations in highly resonant, loss free structures. It is ideally suited to the simulation of narrow band problems. The solver is again based on Maxwell's Grid equations, however in this instance for the time harmonic case, that is for $\partial/\partial t = i\omega$. This condition leads to the relation outlined in equation 2.6.

$$\begin{aligned} &\left(\nabla \times \mu^{-1} \nabla \times \left(-\omega^2 \epsilon\right)\right) \mathbf{E} = -i\omega \mathbf{J} \\ \Rightarrow &\left(\widetilde{\mathbf{C}} \mathbf{M}_{\mu^{-1}} \mathbf{C} - \omega^2 \mathbf{M}_{\epsilon}\right) \mathbf{e} = -i\omega \mathbf{j} \end{aligned} \tag{2.6}$$

This solver does not compute fields but is extremely fast compared to other simulation methods. As a further alternative, an extension of this solver is available which is able to calculate the fields as well. However, the additional field computation significantly increases the required simulation times.

To contrast these two solver types, one may consider the transient solver ideally suited to the analysis of time varying problems and broadband signals. This enables the S-parameters for an entire desired frequency range and, optionally, the electromagnetic field patterns at various desired frequencies to be calculated in a single run. Alternatively, the frequency domain technique is best considered for narrow band problems, as each frequency sample requires a new simulation run. However, it should be noted that a broadband S-parameter simulation with adaptively chosen frequency samples can be performed to minimise the number of solver runs. In comparison to the transient solver, the frequency

domain solver may be useful for strongly resonant structures because these are marked by long settling times of the time domain signals.

In summary, time domain approaches are:

- Suitable for non-linear and time varying problems.
- Suitable for broadband problems.
- Not suitable for resonant problems.

While frequency domain techniques are

- Suitable for resonant and periodic problems.
- Suitable for structures with dimensions less than that of the wavelength being considered.
- Not suitable for non-linear and time varying problems.

Materials and Resistive Sheets

CST provides two basic materials, perfect electric conductors (PEC) and vacuums as well as containing an extensive library of material properties for various metals, dielectrics and others. More complex material types can be defined as isotropic (i.e. normal) or made to consider anisotropic behaviour. Some of the more complex material types available include conducting materials, lossy metals, dispersive materials, surface impedance models, coated materials as well as thermally dependent materials. The work of this thesis made extensive use of PECs, vacuums and resistive sheet models. As such, a brief overview of the resistive sheet model of CST is provided here.

In defining a resistive sheet element in CST one may choose between an "Ohmic Sheet" or a "Tabulated Surface Impedance" model. Two dimensional ohmic sheets will have the same electric field on both sides and thus be transparent. The user specifies the resistance

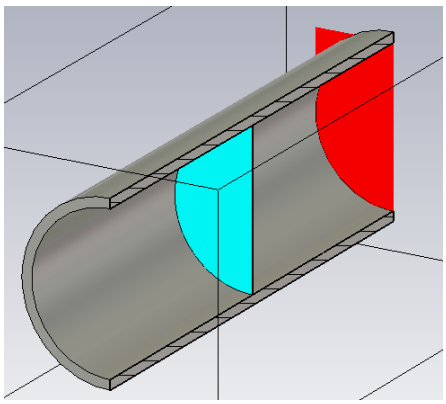

(a) CAD model of the CST waveguide containing a resistive sheet

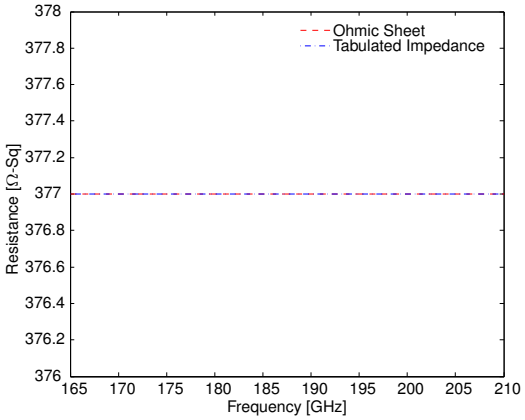

(b) The resultant fit of the resistance value as a function of frequency for a reactance of 0.

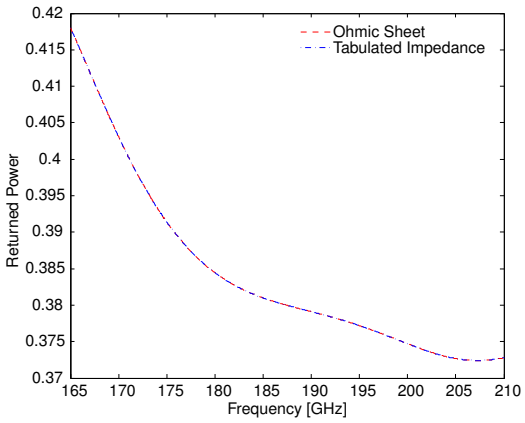

(c) Resulting S_{11} for both the ohmic sheet and tabulated impedance models

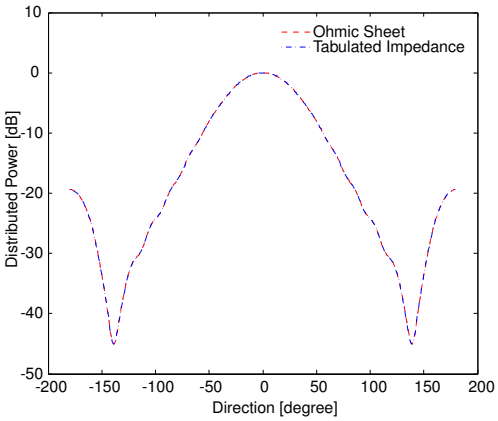

(d) Resulting farfields for both the ohmic sheet and tabulated impedance models

Figure 2.3.: An overview of the equivalence of the tabulated impedance and ohmic sheet model for a constant resistive value independent of frequency.

and reactance at a reference frequency, the frequency domain solvers then compute a frequency independent model, that is the resistance and reactance remain constant across the band. This model can lead to non-causal or otherwise non-physical behaviour and may therefore not always be directly simulated by the transient solver. For simulations in the time domain a first order model of the frequency dependence of the complex impedance is adopted to exactly reproduce the given resistance and reactance values at the reference frequency. Alternatively, the tabulated surface impedance model may be used to provide a more accurate fit of a table of reference resistance and reactance values for a series of frequencies. One may also approximate a frequency independent model for reactance values of zero, as the fitting model considers only the frequency dependence of the complex

impedance. An example of the equivalence of the two different models with frequency independent resistance values is shown in figure 2.3. One should however remain aware of the frequency dependance for non-zero values of reactance. In such instances, should a predefined impedance level be of interest, the tabulated model may prove advantageous.

2.2.1. Setting up a simulation

Creating a model

The first step involved in running a simulation in CST involves generating a CAD model of the object to be simulated. The work reported on in this thesis frequently involved corrugated horn antenna, as such this section will consider such an antenna in the description of the CST system. It is possible in CST to import a previously generated CAD model or construct the model in the CST CAD environment. Lacking a CAD model generating a corrugated horn antenna would prove an unnecessarily lengthly task, as such antenna may consist of hundreds of individual corrugations. A macro was thus written to read in a .txt geometry file specifying the number of segments, and the length and radius of each segment.

The macro is entitled "Horn.mcs" and is available on the physicsmain server of the Terahertz group at NUI Maynooth. A number of minor modifications are necessary for using the macro on specific horn geometries, these are outlined below:

1. The macro can be seen in appendix A.1 and must be copied into the Macros folder in the CST directory (e.g. C:\Program Files\CST STUDIO SUITE 2009\Library\Macros).

2. Create two .txt files, one containing a column of the length of individual segments and the other a column of the radii of the segments.

3. Since the macro counts from zero the n on line 60 of the code must be set to "the total number of segments - 1". So for a horn with 182 segments n was set to: n = 181.

4. The correct file name and path must be entered into the macro on lines 62 and 70. These lines are as follows:
   Open "C:\...\Geometry_lengths.txt" For Input As #1
   Open "C:\...\Geometry_radii.txt" For Input As #2

The macro can either be edited in CST or opened using wordpad or any other text editor. Once this is done the macro can be selected from the Macros tab in CST and will generate the horn. A modified version of this macro is also available for generating pyramidal horns in the same manner.

Establishing Parameters

Before initiating a simulation a number of parameters have to be defined. The first of these is the port. This is defined as being at the waveguide aperture of the horn and it is from here that the horn is excited, by a specified waveguide mode or modes. It is worth noting that, although not required for the work of this thesis, additional methods of exciting a simulation are also available in CST. Next the frequency range must be set to cover the region of interest. To further reduce the computational power required, and the time needed for the simulation, electrical symmetries may be exploited. An example of this can be seen graphically in figure 2.4, where the yz plane is set as magnetically symmetric and the xz plane as electrically symmetric. However, care must be taken when making use of symmetries that both the field distribution as well as the geometrical arrangement are symmetric about the relevant axis, this is often not the case for higher order modes. Field monitors may then be optionally set up should one wish to record, among other things, the farfield patterns, surface currents, or the electric or magnetic fields.

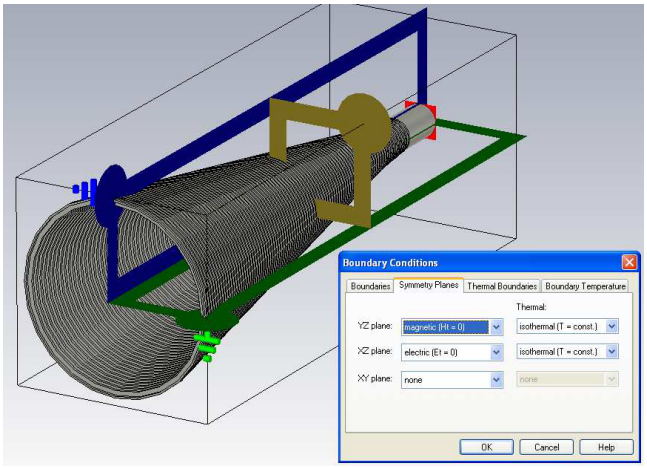

Figure 2.4.: Planes of symmetry in the ALMA band 9 horn

The mesh density is a parameter of critical importance, as an insufficient number of mesh cells may result in inaccurate results, while higher mesh densities require increased computational power. One may develop a rule of thumb for the simulation of specific structures, for example, the horn antennas considered throughout this thesis were generally sufficiently sampled with ≈ 13 mesh cells per wavelength. However, such "rules of thumb" may vary greatly for different systems. As such, for simulating any new system type it is highly recommended to first run an adaptive mesh refinement. Thus, to have confidence in the accuracy of a simulation an adaptive mesh refinement should ideally have at some point been performed and the steady state criteria of the specific simulation met. It should although be noted that, especially for high frequency simulations of electrically large structures, the adaptive mesh refinement can prove an incredibly time consuming operation.

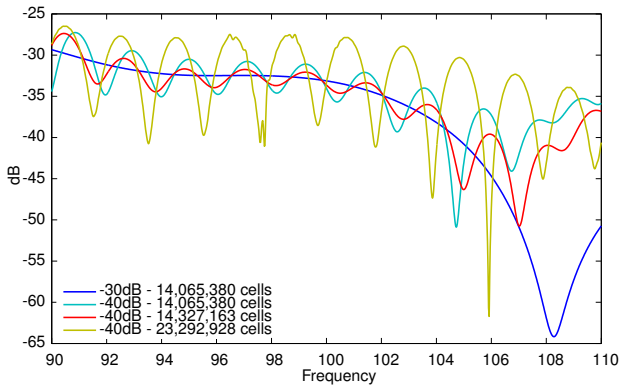

Figure 2.5.: CST simulated S11 results at varied accuracy settings for the 100 GHz Maynooth horn

The default accuracy setting in CST is -30 dB. This setting determines the required level of convergence for the steady state criterion and as such essentially influences the duration of the simulation. When the simulation stops the calculated results are truncated at this point. If these values are non-zero the fourier transform may produce an error as only part of the signal is considered. Increasing the accuracy level of the simulation also increases the required number of mesh cells and computational power. Thus, as can be seen in figure 2.5 increasing the accuracy level of the simulation can result in inaccurate solutions if the mesh density isn't accordingly increased. Considering the accuracy settings are logarithmic, a shift from -30 dB to -40 dB significantly increases the number of mesh cells needed. For all -40 dB simulations carried out CST reported the steady state criterion not to have been met, thus indicating that the mesh of even the last simulation using over 23 million mesh cells, and at the limits of the available computational capacity, was not sufficient.

When considering electrically large systems in CST one may opt to break the system into a number of individual components. For example, a system consisting of a horn antenna feeding a receiver array could be simulated by considering the horn antenna in isolation and propagating the resultant horn antenna fields through the receiver system in a second individual run. There will however exist systems which cannot be subdivided, such as for example, a single electrically large horn antenna. In such an instance one may attempt to

use the distributed computing feature of CST. This allows the calculation domain to be split up over multiple computer cores, however, this option may be severely limited by the license agreement. The license agreement used for the work of this thesis only allowed for the Frequency Domain solver to fully exploit this functionality, by running two separate frequencies of a single simulation simultaneously on two separate machines.

2.3. Ray Tracing

When considering the propagation of light in the presence of objects, with dimensions far exceeding the wavelengths considered, the wave nature of light can be neglected and its behaviour accurately approximated as the propagation of rays subject to specific geometrical laws. These laws can be derived from the following postulates of ray optics [12].

- Light propagates in the form of rays emitted from light sources and which may be detected once incident on an optical detector.

- An optical medium is characterised by a value $n \geqslant 1$ referred to as the "refractive index". This index is defined as $n = \frac{c_0}{c}$, where c_0 represents the speed of light in a vacuum and c the speed of light in the considered medium. As such, the time required for light to travel a distance d is given by $\frac{d}{c} = \frac{nd}{c_0}$, proportional to the product nd known as the optical length.

- In an inhomogeneous medium the refractive index is a function of position $n = n(r)$. The optical distance for a given path between points A and B is therefore:

$$\text{optical distance} = \int_A^B n(r)ds \tag{2.7}$$

  Where ds represents the length element along the path. The time required by the light to travel the path from A to B is proportional to this optical distance.

- **Fermats Principle:** The path followed by a light ray between two points A and B is that for which the time taken represents an extrema. Mathematically this can be described as:

$$\frac{\partial}{\partial t}\int_A^B n(r)ds = 0 \tag{2.8}$$

  This generally equates to a minimum and not maximum, so that one may consider the path chosen to represent that of least time.

From these postulates one may derive that in any homogeneous medium light rays propagate as straight lines. Furthermore, it can be shown that the angle of incidence of light incident on a reflective surface (e.g. a mirror) is equivalent to the angle of reflection and a law for the reflection and refraction of light at the boundary between two mediums of differing refractive indices can be derived, otherwise known as Snell's law [12] [13].

Optica, an optional add on package to Wolfram Mathematica, is one of many commercially available software packages applying this technique and which was applied in the work of this thesis. Another similar ray tracing package is ZEMAX of the ZEMAX Development Corporation. Such ray tracing software packages apply the laws of geometrical optics, based on the postulates outlined, to predict the propagation of light through a system.

As sample of the setup of a basic system in Optica is outlined here. To initialise a simulation in Optica one must define a source, the components of interest and an optional screen at which to record the ray intersections. Optica contains a wide variety of sources including, amongst others, single rays, a cone of rays, a wedge of rays and a grid of rays as well as an extensive optical database of over 6800 elements. Furthermore, elements and structures can be imported to Optica as .stl files, which can be generated from a CAD model. Figure 2.6 depicts the initialisation of a simple lens simulation using Optica, including the command lines used to generate the simulation, as well as a slightly more involved example of including an imported .stl file.

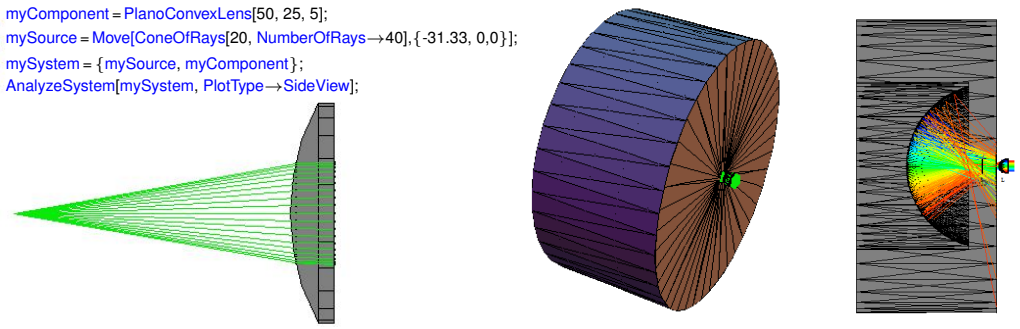

(a) Basic Optica example using library elements and including command lines

(b) Optica example using a CAD generated .stl component model

Figure 2.6.: Optica examples

2.4. Gaussian Beam Modes

The technique of Gaussian Beam Mode Analysis is a computationally efficient alternative to the standard Fresnel integral approach to solving problems involving diffraction dominated propagation. The basis of this technique lies in the assumption that an electric field can be described as the sum of a series of Gaussian modes. Whereby each mode is multiplied by a weighting factor or mode amplitude A_i.

$$E = \sum_i A_i \psi_i \tag{2.9}$$

The weighting factors remain constant throughout an optical system, provided power is conserved (i.e. no truncation). As such, they need only be determined once, after which the evolution of the diffracting beam can be easily found by computationally evaluating the modal sum for any value of z (the distance along the axis of propagation from a reference plane). The overlap integral between E and ψ_i on some transverse plane where E is known yields the mode amplitudes. For example, in cylindrical polar coordinates such an integral has the form of equation 2.10.

$$A_n = \int E(r)\psi_n(r, z_0, W(z), R(z))^* \, 2\pi \, r \, dr \tag{2.10}$$

The variable r represents the radial distance outward from the axis of propagation. W(z) represents the beam radius and R(z) the phase radius of curvature of the mode. The beam radius and phase radius of curvature are described by equations 2.11 and 2.12. Where W_0 represents the waist radius of the beam, a point at which $R = \infty$.

$$W = \sqrt{W_0^2 \left[1 + \left(\frac{\lambda z}{\pi W_0^2}\right)^2\right]} \tag{2.11}$$

$$R = z \left[1 + \left(\frac{\pi W^2}{\lambda z}\right)^2\right] \tag{2.12}$$

As one would also expect, the individual modes experience a phase slippage with respect to a plane wave propagating in the z direction, while evolving through the optical system. The degree of slippage varies for each mode (see equation 2.13), since each mode has a different phase velocity. Considering the modal and z dependence of the phase slippage, one may appreciate how the amplitude distribution of a composite field alters shape with z.

$$\phi_n = (2n + 1) \times \tan^{-1}\left(\frac{\pi W^2}{\lambda R}\right) \tag{2.13}$$

A complete set of orthonormal Laguerre-Gaussian modes can be seen in equation 2.14. Here one may note that the last term in the modal equation is the phase slippage.

$$\begin{aligned} \psi_n = & \sqrt{\frac{2}{\pi W^2}} L_n \left[2\left(\frac{r}{W}\right)^2\right] \times exp\left[-\left(\frac{r}{W}\right)^2\right] \\ & \times exp\left[-jk\left(z + \frac{r^2}{2R}\right)\right] \\ & \times exp\left[j\,(2n + 1) \times \tan^{-1}\left(\frac{\pi W^2}{\lambda R}\right)\right] \end{aligned} \tag{2.14}$$

$$E_x = \frac{D_{nl}}{2} J_{n-1}\left(q_{nl}\frac{r}{a}\right)\begin{pmatrix}\cos\left((n-1)\,\phi\right)\\ -\sin\left((n-1)\,\phi\right)\end{pmatrix} + \frac{D_{nl}}{2} J_{n+1}\left(q_{nl}\frac{r}{a}\right)\begin{pmatrix}\cos\left((n+1)\,\phi\right)\\ -\sin\left((n+1)\,\phi\right)\end{pmatrix} \tag{2.15}$$

It has been shown that the beam radius and the phase radius of curvature of a Gaussian beam are functions of the distance z. Often when working with Gaussian beams it is more practical to consider the complex beam parameter q (see equation 2.16). This has both W(z) and R(z) encoded in it and describes the evolution of a Gaussian beam. Furthermore, lenses and other optical elements can be modelled as transformations of the q-parameter through the use of ABCD matrices.

$$q(z) = \left(\frac{1}{R} + \frac{-j\,\lambda}{\pi\,W^2}\right)^{-1} \tag{2.16}$$

To use an ABCD matrix the initial beam width and radius of curvature are entered into the initial complex beam parameter q_{in}. The transformed q or q_{out} is then given by equation 2.17, where A,B,C and D represent the elements of the matrix in terms of q_{in}.

$$q_{out} = \frac{A\,q_{in} + B}{C\,q_{in} + D} \tag{2.17}$$

The resulting R and W components can then be calculated from the q_{out} parameter as:

$$R = \left(Re\left(\frac{1}{q_{out}}\right)\right)^{-1} \tag{2.18}$$

$$W = \sqrt{\frac{-\lambda}{\pi\,Im\left(\frac{1}{q_{out}}\right)}} \tag{2.19}$$

A further advantage of the use of ABCD matrices is that the individual matrices describing each component of the system can be combined. This is realised by multiplying each

matrix of the quasioptical system in reverse order. Thus, a single matrix can be generated, which describes the entire quasioptical system for a given input. The use of ABCD matrices throughout this work involved the combination of only three different element types. As such, the three relevant matrix forms are outlined below in expression 2.20, where d represents the distance of propagation, and n_1 and n_2 the refractive indices of the respective media. A more detailed outline of the use of ABCD matrices with Gaussian beams can be found in [14].

$$\begin{aligned} \text{Free space propagation: } & \begin{pmatrix} A & B \\ C & D \end{pmatrix} = \begin{pmatrix} 1 & d \\ 0 & 1 \end{pmatrix} \\ \text{Refraction at dielectric interface: } & \begin{pmatrix} A & B \\ C & D \end{pmatrix} = \begin{pmatrix} 1 & 0 \\ 0 & \frac{n_1}{n_2} \end{pmatrix} \\ \text{Reflection from flat mirror: } & \begin{pmatrix} A & B \\ C & D \end{pmatrix} = \begin{pmatrix} -1 & 0 \\ 0 & 1 \end{pmatrix} \end{aligned} \tag{2.20}$$

2.5. Vector Network Analyser

Vector network analysis is a method of accurately characterising a device under test (DUT) by measuring its affect on the amplitude and phase of swept-frequency and power test signals. Most commonly the reflection and transmission of the applied test signal is measured. Consider for example a two port system, where a sinusoidal test wave is incident on the DUT from port 1 and the response measured at port 2. This situation is depicted in figure 2.7 with a representing the incident wave from port 1 and d the response at port 2. In this example one may observe how the magnitude of the transmitted power $|S_{21}|$ and the phase of the transmitted signal $\arg(S_{21})$ are determined. To completely characterise the reflected and transmitted signals all scattering parameters of the DUT are required. This

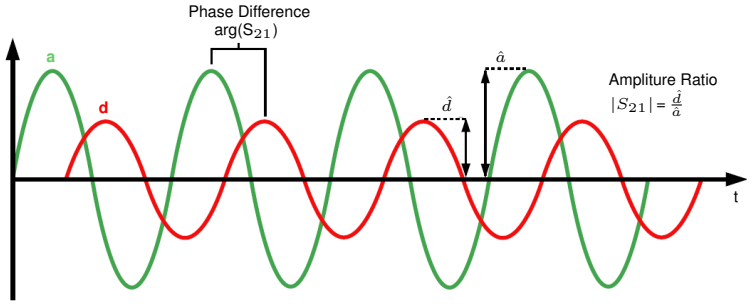

Figure 2.7.: Example of a sinusoidal test signal from port 1, a, and the response signal at port 2, d [15]

relationship is characterised by expression 2.21.

$$\begin{pmatrix} b \\ d \end{pmatrix} = \begin{pmatrix} S_{11} & S_{12} \\ S_{21} & S_{22} \end{pmatrix} \begin{pmatrix} a \\ c \end{pmatrix} \tag{2.21}$$

To achieve this measurement of both phase and magnitude components in practise can be accomplished using a heterodyne system, such as that depicted in figure 2.8. A radio frequency (RF) generator provides a stimulus to an attenuator for the purpose of controlling the total output power. This signal then passes through a splitter and results in two identical waves, one of which is transmitted to the DUT and the other to the reference channel. The test port also receives the reflected signal from the DUT, which is transmitted to the measurement channel. Consequently, the test port has now both the incident and reflected signals isolated in separate channels.

As seen in figure 2.8 a radio frequency generator is used as the stimulus to the system. In the Rohde and Schwarz ZVA-24 system used at NUI Maynooth this corresponds to a frequency range of 10 MHz-24 GHz. In order to change the bandwidth to the Terahertz region, of interest to the work of this thesis, frequency extension heads are required. The in-house system incorporates two ZVA-Z110 W-band (75 GHz-110 GHz) converter heads. The stimulus is thus applied to, and split into two identical signals in, the converter head itself. These signals are then transmitted to the DUT and the reference channel, as

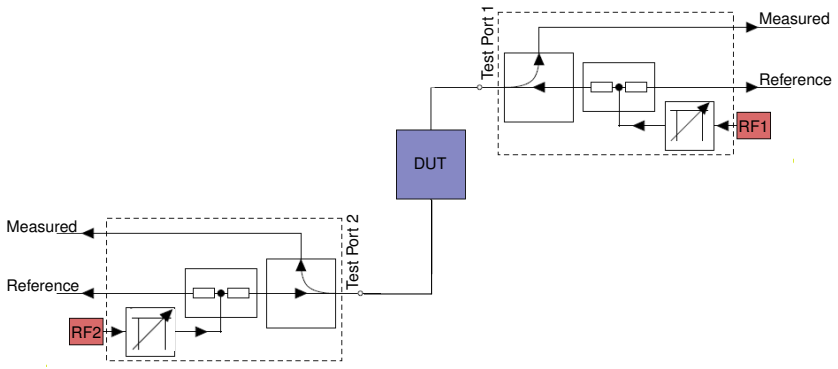

Figure 2.8.: Example of the internal workings of a 2-port heterodyne VNA [15]

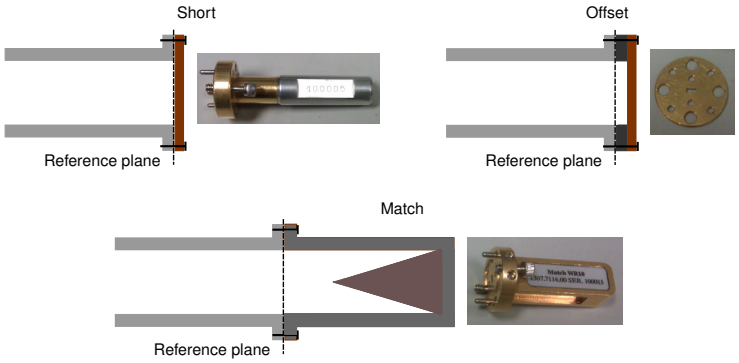

Figure 2.9.: Calibration kit of the NUI Maynooth VNA system

before. Before any measurements can be conducted the system has to be calibrated. This is accomplished using special previously characterised DUTs, that is devices with known S-parameters. The characterisation of these devices is carried out in accordance with accepted principles set down by, for example, the Physikalisch-Technische Bundesanstalt in Germany and the National Physical Laboratory in the UK. This characterisation process is typically carried out by a commercial company, from which a calibration kit, including the characteristic data, can be purchased.

Standard calibration devices, also used with the in-house system, include a Short, Offset and Match (see figure 2.9). A short refers to a conductive plate mounted flat against the waveguide flange with a zero offset and is generally characterised by a 100% return. An offset is realised by extending the distance between a short and the waveguide flange. A match is generally made of a cone-shaped absorbing material, which attenuates the signal.

One additional calibration step possible is termed a “Through” and achieved through a direct connection between the test ports.

Using a combination of these fully characterised DUTs an OSM (**O**pen/**S**hort/**M**atch) approach to a one port calibration, or a TOSM (**T**hrough/**O**pen/**S**hort/**M**atch) approach to a two port calibration can be conducted. A more complete description of the VNA and the calibration process my be found in [16].

3. Mode Matching for Horn Antenna

3.1. Introduction

The work of this chapter was primarily motivated by an ESA TRP (Technology Research Programme). Objectives of this project, relevant to this chapter, included the development of modelling capabilities of over-moded waveguide and horn structures and the expansion of existing modelling approaches to include rectangular structures. This chapter will outline the mode matching software Scatter with particular emphasis on its application to the analysis of horn antennas. The cylindrical Scatter code, developed by the NUI Maynooth Terahertz group, has a strong heritage in horn analysis and has been successfully used in the optical design and analysis of several systems, including ESA missions such as Planck, HIFI and Quest. A complete overview of the code can be found in the PhD Thesis of Emily Gleeson [17].

The work carried out directly by the author include making use of the cylindrical Scatter code as well as continuing the development, debugging and verifying of the pyramidal Scatter. Initially work began on the pyramidal Scatter with Karen Foley (a previous PhD student of the Terahertz group). The contribution of the author to this work included debugging this code, specifically isolating and consequently avoiding the occurrence of underdetermined matrices in the system. This initially involved the complete re-scripting of the code in Python as well as continuing work on the Mathematica script. Furthermore, the author of this thesis completely reevaluated the power coupling integrals upon which the code is based for a separate, but equivalent normalisation condition, as well as

making comparison to the independently evaluated integrals of Research Fellow Mr. Tully Peacocke. The code was also further supplemented with the inclusion of a fast Fourier transform to the farfield. Upon completion the author validated the pyramidal Scatter against the theoretically expected results of simple systems and CST Microwave Studio simulations of more complex systems.

The use of singular value decomposition was also explored by the author with particular emphasis on its potential for establishing aperture efficiencies of horn antenna. This approach was then implemented in both the cylindrical and pyramidal Scatter codes. In the context of the TRP, which emphasised the development of tools capable of considering the SAFARI-type horns, a detailed analysis was carried out by the author of the original proposed horn designs. Furthermore, the author considered modified horn designs for the purpose of optimisation.

The Scatter code was finally also applied to the analysis of the ALMA band 5 horn. As well as considering this system computationally, the author also took part in a measurement campaign at the GARD institute of Chalmers Technical University in Sweden. The direct contribution of the author to the measurement campaign focused primarily on the alignment and testing of the system.

3.2. Scatter

3.2.1. Technique Overview

Before considering the application of the mode matching technique, one must first have a general appreciation for the definition of waveguide modes and the physical rules by which they are governed. A waveguide refers to a metallic tube of uniform cross section in the plane perpendicular to the guide axis. For the work of this chapter the simplifying assumption is made that the metallic walls are perfectly conducting and the field confined to the interior of the guide. In such a guide there exists a finite number of TE and/or TM modes,

that is discrete field distributions for which the electric and/or magnetic field components are orthogonal to the direction of propagation, respectively. Each mode is supported only above its cut-off frequency and has an associated intrinsic guide wavelength. The field of a propagating mode can be regarded as a superposition of elementary plane waves arising from successive reflections at the various inner guide surfaces. Examining the difference in the group and phase velocities of such incident plane waves will yield that at the cut-off frequency the group velocity becomes zero and the phase velocity infinite, thus representing plane waves at normal incidence to the guide walls and hence no propagation of energy.

Alternatively, to understand this behaviour an electromagnetic approach can be taken. To find possible fields supported by such a waveguide one must seek solutions to Maxwell's equations, which provide the standard wave equation of expression 3.1. The simplest geometry to solve is that of the rectangular waveguide and is considered here for descriptive purposes. In this case solutions are sought for the form $\psi(x, y, z, t) = \psi_0 e^{j(\omega t - k_z z - k_x x - k_y y)}$, where k_z represents the longitudinal wavenumber and k_x and k_y the transverse wavenumbers resulting from the boundary conditions of the rectangular geometry cross-section.

$$\left(\nabla^2 - \frac{1}{c^2}\frac{\partial^2}{\partial t^2}\right)\psi(r, t) = 0 \tag{3.1}$$

Solving this equation results in the dispersion relation of the rectangular waveguide (expression 3.2), where m and n are positive integers representing specific eigenmodes, c is the group velocity of propagation in the waveguide and a and b represent the widths of the rectangular guide. In order for the field to propagate the longitudinal wavenumber k_z must be greater than zero. As such, equation 3.2 can be solved for a value of $\omega = \omega_c$, which corresponds to the case of $k_z = 0$. In this instance ω_c is defined as the critical angular frequency between propagation and attenuation and given by expression 3.3. This is referred to as the cut-off frequency of the supported TE and TM modes and is also directly related to the intrinsic guide wavelength of that mode by k_z. A more complete and mathematically detailed description of this behaviour is provided for both cylindrical and

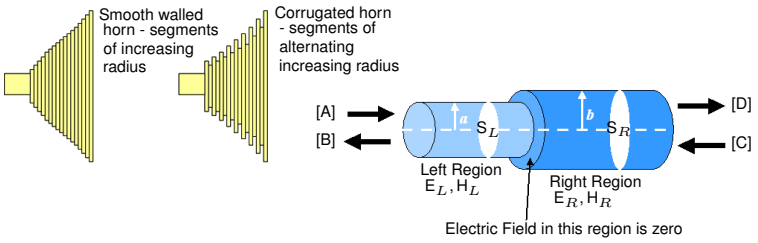

Figure 3.1.: Scatter overview [19]

rectangular waveguides in [18]. The specific mode forms, guide wavelengths and cut-off frequencies will be shown throughout the chapter as required.

$$\frac{\omega^2}{c^2} = \left(\frac{n\pi}{a}\right)^2 + \left(\frac{m\pi}{b}\right)^2 + k_z^2 \tag{3.2}$$

$$\omega_c = c\sqrt{\left(\frac{n\pi}{a}\right)^2 + \left(\frac{m\pi}{b}\right)^2} \tag{3.3}$$

The basis of the mode matching technique lies in the assumption that the field power distribution of a waveguide can be described as the sum in quadrature of the waveguide TE and TM modes. Consequently, one may propagate a field through a uniform segment of constant dimension by considering the propagation of the supported component modes individually, before recombining the modes to provide the resulting field. A waveguide structure can then be represented as a finite series of continuous sections (typically 10 - 20 sections per wavelength). At each junction, i.e. geometrical discontinuity, an overlap integral is performed between each modal component of the incident field and each possible modal component of the transmitted field, this provides the level of coupling between the modes. Essentially mode matching can be summarised as a technique which propagates a waveguide modal basis set, appropriate to the geometry, through successive junctions while conserving power. The modes are then propagated through the length of any uniform waveguide section in the standard manner to the next scattering junction.

Figure 3.1 depicts both how a horn antenna may be constructed using successive waveguide segments and examines an individual junction between two such segments. At any single

junction power may be either transmitted from left to right, reflected from right to right, transmitted from right to left or reflected from left to left. These four alternatives are represented by the matrices [A], [B], [C] and [D], respectively, and are determined by the scattering matrices (see equation 3.4). The Scatter code implementation considers the previously mentioned overlap integrals along with propagation phase shifts to establish these scattering matrices for each successive junction. A complete mathematical description of this process and the mode matching theory for the pyramidal and cylindrical Scatter codes is outlined in the following sections.

$$\begin{pmatrix}[B]\\[D]\end{pmatrix} = \left([S^a]\right)\begin{pmatrix}[A]\\[C]\end{pmatrix} = \begin{pmatrix}[S^a_{11}] & [S^a_{12}]\\[S^a_{21}] & [S^a_{22}]\end{pmatrix}\begin{pmatrix}[A]\\[C]\end{pmatrix} \tag{3.4}$$

3.2.2. Pyramidal Scatter Theory

To initiate a mode matching simulation, as with all such EM simulation techniques, the input aperture of the structure has to be excited. To accomplish this in the Scatter code an initial S_{21} (and S_{12}) matrix is defined, with the modal components scaled by their attenuation through the length of the first section. To that end it is assumed that each mode propagates in the z direction as $e^{-j\beta z}$, where the attenuation factor β is dependent on the guide dimensions, mode numbers and free space wavenumber. The total number of supported modes for any waveguide is dependent on the cut-off frequency and guide dimensions. In the case of a rectangular geometry of width a and height b the TE and TM modes share the same cut-off frequencies given by equation 3.5.

$$(\nu_c)_{mn} = \frac{1}{2\pi\sqrt{\mu\epsilon}}\sqrt{\left(\frac{m\pi}{a}\right)^2 + \left(\frac{n\pi}{b}\right)^2} \tag{3.5}$$

Letting k denote the wavenumber in free space and m and n the mode numbers in the x and y directions, the modal wavenumbers and the attenuation in the guide can then be

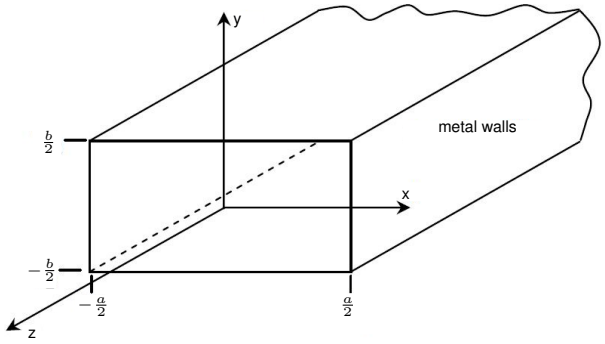

Figure 3.2.: Rectangular geometry as described by pyramidal Scatter geometry files

expressed as:

$$\begin{aligned} k_x &= \frac{\pi m}{a} & k_y &= \frac{\pi n}{b} \\ k_{mn} &= \sqrt{\left(\frac{\pi m}{a}\right)^2 + \left(\frac{\pi n}{b}\right)^2} & \beta^* &= \sqrt{k^2 - k_{mn}^2} \end{aligned} \tag{3.6}$$

In this case the scalar mode functions are defined by cosine and sine terms and can be seen in expressions 3.7 and 3.8. These are the scalar distributions which feed into the equations defining the vector fields, and are derived from first principles in chapter 6 of [18]. The resulting electric and magnetic transverse electric field vectors are outlined in equations 3.9 to 3.12, where A_{mn} and B_{mn} are the normalisation constants and the notation $\mathrm{TE}_{mn}(E)$ refers to the electric field component of the TE_{mn} mode, and $\mathrm{TE}_{mn}(H)$ to the magnetic field component.

$$\text{TM mode: } \phi(x,y) = \sin\frac{m\pi x}{a}\sin\frac{n\pi y}{b} \tag{3.7}$$

$$\text{TE mode: } \psi(x,y) = \cos\frac{m\pi x}{a}\cos\frac{n\pi y}{b} \tag{3.8}$$

$$\mathrm{TE}_{mn}(E) = \frac{j\omega\mu A_{mn}}{k_{mn}^2}\begin{pmatrix} k_y cos\left(k_x\left(x+\frac{a}{2}\right)\right) sin\left(k_y\left(y+\frac{b}{2}\right)\right) \\ -k_x sin\left(k_x\left(x+\frac{a}{2}\right)\right) cos\left(k_y\left(y+\frac{b}{2}\right)\right) \end{pmatrix} \tag{3.9}$$

$$\mathrm{TE}_{mn}(H) = \frac{j\beta_{mn} A_{mn}}{k_{mn}^2}\begin{pmatrix} k_x sin\left(k_x\left(x+\frac{a}{2}\right)\right) cos\left(k_y\left(y+\frac{b}{2}\right)\right) \\ k_y cos\left(k_x\left(x+\frac{a}{2}\right)\right) sin\left(k_y\left(y+\frac{b}{2}\right)\right) \end{pmatrix} \tag{3.10}$$

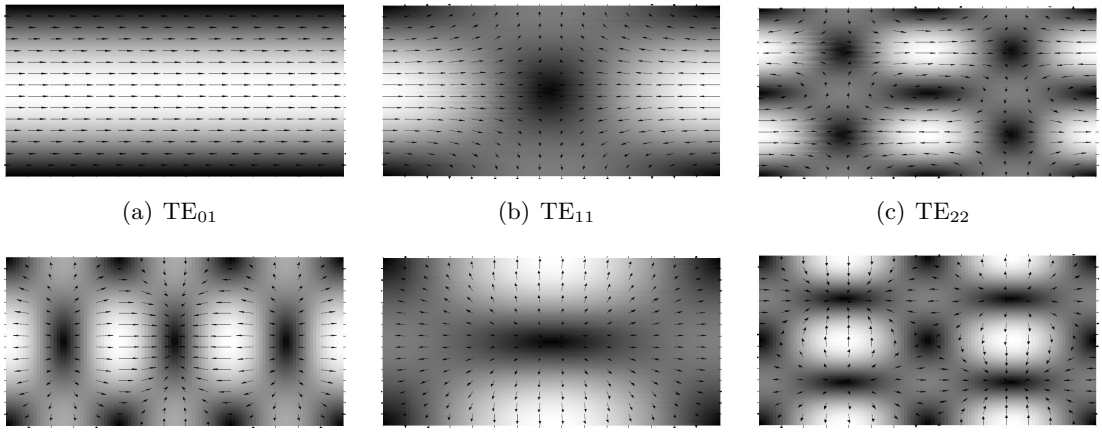

(a) TE_{01} (b) TE_{11} (c) TE_{22}

(d) TM_{31} (e) TM_{11} (f) TM_{22}

Figure 3.3.: Sample of transverse electric and magnetic field forms for a rectangular guide.

$$\mathrm{TM}_{mn}(E) = \frac{-j\beta_{mn}B_{mn}}{k_{mn}^2}\begin{pmatrix} k_x cos\left(k_x\left(x+\frac{a}{2}\right)\right) sin\left(k_y\left(y+\frac{b}{2}\right)\right) \\ k_y sin\left(k_x\left(x+\frac{a}{2}\right)\right) cos\left(k_y\left(y+\frac{b}{2}\right)\right) \end{pmatrix} \tag{3.11}$$

$$\mathrm{TM}_{mn}(H) = \frac{-j\omega\epsilon B_{mn}}{k_{mn}^2}\begin{pmatrix} k_y sin\left(k_x\left(x+\frac{a}{2}\right)\right) cos\left(k_y\left(y+\frac{b}{2}\right)\right) \\ -k_x cos\left(k_x\left(x+\frac{a}{2}\right)\right) sin\left(k_y\left(y+\frac{b}{2}\right)\right) \end{pmatrix} \tag{3.12}$$

The normalisation coefficients A_{mn} and B_{mn} are derived by solving the separable integrals seen in equation 3.13, or equation 3.14. Either normalisation approach is equivalent, provided it is consistently applied, however the derivations outlined in this chapter are based on equation 3.13. The resulting expressions of equation 3.13 are displayed in equation 3.15, where it is worth noting that no results are outlined for the cases of the TE_{00}, TM_{01}, TM_{10} or TM_{00} modes, which themselves are not defined. This may be appreciated through consideration of the scalar mode functions of equations 3.7 and 3.8, where one observes in the case of the TM modes that neither of the integers m or n can be zero, or the function vanishes. In the case of the TE modes, although no mode corresponding to $m = n = 0$ exists (constant scalar function generates no electromagnetic field), one of the integers may be zero.

Table 3.1.: Example of a Scattering matrix for the Pyramidal Scatter for a maximum mode order of 2. The matrix is divided into four quadrants representing coupling from TE to TE and TM modes and from TM to TE and TM modes. For example the blue cell represents power coupled from the TE_{12} mode to the TE_{20} mode and the red cell power coupled from the TM_{21} to the TM_{12} mode.

				Input Mode Number i											
Output Mode Number j				1	2	3	4	5	6	7	8	9	10	11	12
				TE_{mn}								**TM_{mn}**			
				10	20	01	11	21	02	12	22	11	21	12	22
	1	**TE_{mn}**	10												
	2		20												
	3		01												
	4		11												
	5		21												
	6		02												
	7		12												
	8		22												
	9	**TM_{mn}**	11												
	10		21												
	11		12												
	12		22												

$$\int_{-\frac{a}{2}}^{\frac{a}{2}} \int_{-\frac{b}{2}}^{\frac{b}{2}} \left(E_x^2 + E_y^2\right) dxdy = 1 \tag{3.13}$$

$$\int_{-\frac{a}{2}}^{\frac{a}{2}} \int_{-\frac{b}{2}}^{\frac{b}{2}} (\mathbf{E} \times \mathbf{H}^*) \, dxdy = 1 \tag{3.14}$$

$$\begin{aligned} A_{m0} &= \sqrt{\frac{2}{ab}} \frac{k_x}{\omega\mu} \qquad A_{0n} = \sqrt{\frac{2}{ab}} \frac{k_y}{\omega\mu} \\ A_{mn} &= \frac{2k_{mn}}{\omega\mu\sqrt{ab}} \qquad B_{mn} = \omega\mu \frac{A_{mn}}{\mid \beta_{mn} \mid} \end{aligned} \tag{3.15}$$

At the interface between the first and second section the total transverse field in the two guides must be matched, so that the total complex power is conserved and Maxwell's equations are satisfied with the usual boundary conditions applying to the fields at the conducting walls. The power in the constituent modes of the field may be either reflected or transmitted. Additionally, there is also the prospect for self reactance or self coupling between modes on the same side of a junction, thus giving rise to the four scattering matrices of equation 3.4.

Obtaining an expression for the power coupled between modes across a junction requires that one consider the field distribution of the mode to be coupled into, and is accomplished through the integration of the Poynting vector over the surface area of the junction. The power reflected either from the left to the left, or from the right to the right, is determined in a similar manner, however as it experiences no variation in geometry one may suspect it only to be dependent on the modal impedance. The integrals are outlined in equations 3.17 to 3.19, where P refers to the power coupled between modes across a junction, or left to right, Q the power transmitted from right to right and R the power reflected from left to left, where the subscripts l and r refer to the left and right side of the junction.

$$Z_{\mathrm{TE}} = \frac{\omega\mu}{\beta} \quad Z_{\mathrm{TM}} = \frac{\beta}{\omega\epsilon} \tag{3.16}$$

$$P = \int e_l \times h_r^* dS = \int_{-\frac{a}{2}}^{\frac{a}{2}} \int_{-\frac{b}{2}}^{\frac{b}{2}} \left(E_{x,l} \frac{E_{x,r}^*}{Z_{TE/M,r}^*} + E_{y,l} \frac{E_{y,r}^*}{Z_{TE/M,r}^*} \right) dxdy \tag{3.17}$$

$$Q = \int e_r \times h_r^* dS = \int_{-\frac{a}{2}}^{\frac{a}{2}} \int_{-\frac{b}{2}}^{\frac{b}{2}} \left(E_{x,r} \frac{E_{x,r}^*}{Z_{TE/M,r}^*} + E_{y,r} \frac{E_{y,r}^*}{Z_{TE/M,r}^*} \right) dxdy \tag{3.18}$$

$$R = \int e_l \times h_l^* dS = \int_{-\frac{a}{2}}^{\frac{a}{2}} \int_{-\frac{b}{2}}^{\frac{b}{2}} \left(E_{x,l} \frac{E_{x,l}^*}{Z_{TE/M,l}^*} + E_{y,l} \frac{E_{y,l}^*}{Z_{TE/M,l}^*} \right) dxdy \tag{3.19}$$

From this point onwards the convention is adopted that modes to the right of the junction are labelled with M and N and the waveguide dimensions by c and d and those to the left of the junction with m, n, a and b, respectively. The solutions to the P integral (equation 3.17) are outlined in equations 3.20 to 3.29, in the compact form simplified by research fellow Mr. Tully Peacocke, and to the Q and R integrals (see equations 3.18 and 3.19) in equations 3.30 to 3.33 for all possible mode combinations.

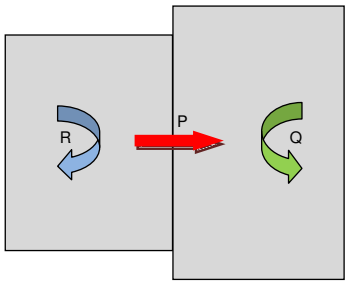

Figure 3.4.: Graphical representation of the direction of flow of power between modes for the three power coupling integrals P, Q and R.

$$P^{\text{TE-TE}}_{m,n,M,N} = \frac{4k_{(c,M)}k_{(d,N)}K_{(a,b,m,n)}}{Z^*_{\text{TE},r}K_{(c,d,M,N)}\left(k^2_{(a,m)} - k^2_{(c,M)}\right)\left(k^2_{(b,n)} - k^2_{(d,N)}\right)\sqrt{abcd}} \times\alpha(a,c,m,M)\alpha(b,d,n,N) \tag{3.20}$$

$$P^{\text{TE-TE}}_{0,n,M,N} = \frac{-2\sqrt{2}k_{(b,n)}k_{(d,N)}}{Z^*_{\text{TE},r}k_{(c,M)}K_{(c,d,M,N)}\left(k^2_{(b,n)} - k^2_{(d,N)}\right)\sqrt{abcd}} \times\alpha(a,c,0,M)\alpha(b,d,n,N) \tag{3.21}$$

$$P^{\text{TE-TE}}_{m,0,M,N} = \frac{-2\sqrt{2}k_{(a,m)}k_{(c,M)}}{Z^*_{\text{TE},r}k_{(d,N)}K_{(c,d,M,N)}\left(k^2_{(a,m)} - k^2_{(d,M)}\right)\sqrt{abcd}} \times\alpha(a,c,m,M)\alpha(b,d,0,N) \tag{3.22}$$

$$P^{\text{TE-TE}}_{0,n,0,N} = \frac{2ak_{(b,n)}}{Z^*_{\text{TE},r}\left(k^2_{(b,n)} - k^2_{(d,N)}\right)\sqrt{abcd}} \times \alpha(b,d,n,N) \tag{3.23}$$

$$P^{\text{TE-TE}}_{m,0,n,0} = \frac{2bk_{(a,m)}}{Z^*_{\text{TE},r}\left(k^2_{(a,m)} - k^2_{(c,M)}\right)\sqrt{abcd}} \times \alpha(a,c,m,M) \tag{3.24}$$

$$P^{\text{TM-TM}}_{m,n,M,N} = \frac{4k_{(a,m)}k_{(b,n)}K_{(c,d,M,N)}}{Z^*_{\text{TM},r}K_{(a,b,m,n)}\left(k^2_{(a,m)} - k^2_{(c,M)}\right)\left(k^2_{(b,n)} - k^2_{(d,N)}\right)\sqrt{abcd}} \times\alpha(a,c,m,M)\alpha(b,d,n,N) \tag{3.25}$$

$$P^{\text{TE-TM}}_{m,n,M,N} = \frac{-4\beta\left(k^2_{(a,m)}k^2_{(d,N)} - k^2_{(b,n)}k^2_{(c,M)}\right)}{Z^*_{\text{TM},r}K_{(a,b,m,n)}K_{(c,d,M,N)}\left(k^2_{(a,m)} - k^2_{(c,M)}\right)\left(k^2_{(b,n)} - k^2_{(d,N)}\right)\sqrt{abcd}} \times\alpha(a,c,m,M)\alpha(b,d,n,N) \tag{3.26}$$

$$P^{\text{TE-TM}}_{0,n,M,N} = \frac{-2\sqrt{2}\beta k_{(b,n)}}{Z^*_{\text{TM},r}K_{(c,d,M,N)}\left(k^2_{(b,n)} - k^2_{(d,N)}\right)\sqrt{abcd}} \times \alpha(a,c,0,M)\alpha(b,d,n,N) \tag{3.27}$$

$$P^{\text{TE-TM}}_{m,0,M,N} = \frac{-2\sqrt{2}\beta k_{(a,m)}}{Z^*_{\text{TM},r} K_{(c,d,M,N)} \left(k^2_{(a,m)} - k^2_{(c,M)}\right) \sqrt{abcd}} \times \alpha(a,c,m,M)\alpha(b,d,0,N) \tag{3.28}$$

$$P^{\text{TM-TE}}_{m,n,M,N} = 0 \qquad \forall\, m,\, n,\, M,\, N \tag{3.29}$$

As was previously suggested, less variation in the power coupling equations exists for the Q and R matrices, which are dependent only on the mode impedances. These are displayed in equations 3.30 to 3.33. Other functions referred to in these expressions are outlined in equations 3.34 to 3.35. It may be noted that should one normalise by equation 3.14 then the Q and R matrices turn by definition into the identity matrices.

$$Q^{\text{TE-TE}}_{m,n} = Q^{\text{TE-TE}}_{0,n} = Q^{\text{TE-TE}}_{m,0} = \frac{1}{Z^*_{\text{TE},r}} \tag{3.30}$$

$$Q^{\text{TM-TM}}_{m,n} = \frac{1}{Z^*_{\text{TM},r}} \tag{3.31}$$

$$R^{\text{TE-TE}}_{m,n} = R^{\text{TE-TE}}_{0,n} = R^{\text{TE-TE}}_{m,0} = \frac{1}{Z^*_{\text{TE},l}} \tag{3.32}$$

$$R^{\text{TM-TM}}_{m,n} = \frac{1}{Z^*_{\text{TM},l}} \tag{3.33}$$

$$\alpha(a,c,m,M) = sin\left(\frac{(a-c)\,M\pi}{2a}\right) - (-1)^m sin\left(\frac{(c+a)\,M\pi}{2a}\right) \tag{3.34}$$

$$K_{(a,b,m,n)} = \sqrt{\left(\frac{\pi m}{a}\right)^2 + \left(\frac{\pi n}{b}\right)^2}, \qquad k_{(a,m)} = \frac{m\pi}{a} \tag{3.35}$$

The resulting [P], [Q] and [R] matrices may then be combined, as outlined in [19], to form the scattering matrices for a step discontinuity as described by equations 3.36 to 3.39. It is worth noting that the derivation thus far has implicitly assumed the discontinuity to be of a smaller waveguide feeding one of larger dimensions. However, the situation of a field propagating from a larger to a smaller waveguide may be considered by reversing the direction of propagation of the modes. Essentially this is achieved by setting $[S'_{11}] = [S_{22}]$, $[S'_{12}] = [S_{21}]$, $[S'_{21}] = [S_{12}]$ and $[S'_{22}] = [S_{11}]$, where the primes represent the propagation

from the wider to narrower waveguide.

$$[S_{11}] = [[R^*] + [P]^\dagger[Q]^{-1}[P]]^{-1} - [P]^\dagger[Q]^{-1}[P]] \tag{3.36}$$

$$[S_{12}] = 2\,[[R^*] + [P]^\dagger[Q]^{-1}[P]]^{-1}[P]^\dagger \tag{3.37}$$

$$[S_{21}] = 2\,[[Q] + [P][R^*]^{-1}[P]^\dagger]^{-1}[P] \tag{3.38}$$

$$[S_{22}] = -\,[[Q] + [P][R^*]^{-1}[P]^\dagger]^{-1}[[Q] - [P][R^*]^{-1}[P]^\dagger] \tag{3.39}$$

The scattering matrices of successive sections are then finally cascaded together to form the overall scattering matrix of the structure. Thus, the initial scattering matrices used to excite the waveguide are labelled $[S^a]$ and the matrices determined by equations 3.36 to 3.39 at the first junction $[S^b]$. These are then cascaded together to give $[S^c]$ as shown in equations 3.40 to 3.43, where $[I]$ refers to the identity matrix. In this manner an iterative process can be employed in which the $[S^c]$ matrices become the $[S^a]$ matrices for the following junction and an overall scattering matrix for the entire structure can be built up. The form of such a scattering matrix is depicted in table 3.1.

$$[S^c_{11}] = [S^a_{12}][[I] - [S^b_{11}][S^a_{22}]]^{-1}[S^b_{11}][S^a_{21}] + [S^a_{11}] \tag{3.40}$$

$$[S^c_{12}] = [S^a_{12}][[I] - [S^b_{11}][S^a_{22}]]^{-1}[S^b_{12}] \tag{3.41}$$

$$[S^c_{21}] = [S^b_{21}][[I] - [S^a_{22}][S^b_{11}]]^{-1}[S^a_{21}] \tag{3.42}$$

$$[S^c_{22}] = [S^b_{21}][[I] - [S^a_{22}][S^b_{11}]]^{-1}[S^a_{22}][S^b_{12}] + [S^b_{22}] \tag{3.43}$$

Once the overall scattering matrix of a structure is known the aperture field can be established by correctly summing the modes, weighted by their scattering coefficients. For multi-moded structures particular care must be taken as to whether the modes are to be summed coherently or in quadrature. It should be noted that multi-moded horn antennas are frequently partially coherent in nature.

Partial coherence is the property of two waves whose relative phase undergoes random fluctuations, which are not, however, sufficient to make the waves completely incoherent. This property has been studied mathematically and a more detailed consideration can be found in [20] and [21]. Finite element and other such approaches would require the entire system to be solved separately for each individual mode and the modes then to be combined at the post-processing stages. Furthermore, combining these modes in a partially coherent manner would require the use of a phase-coherence factor, which would first have to be determined [22].

The modal approach of Scatter makes the inclusion of partial coherence more straightforward. Expression 3.45 outlines the form of S matrices referred to in equation 3.4, where, for example, the upmost left cell represents the power transferred from the TE_{10} to the TE_{10} mode. Given that the columns of this matrix refer to power originating from the same mode, modes in each column are summed coherently and then each column is added incoherently to all other columns (taking the square of the absolute value of each coefficient) to correctly add the contribution of each mode.

The aperture field, NF, in units of watts, of such a partially coherent structure is determined as outlined in equation 3.44.

$$\begin{aligned} NF = \sum_{columns} & Abs\left(\sum_{mn}(S21_{mn}\mathrm{TEx}_{mn} + \sum_{mn} S21_{mn}\mathrm{TMx}_{mn})\right)^2 \\ & + Abs\left(\sum_{mn}(S21_{mn}\mathrm{TEy}_{mn} + \sum_{mn} S21_{mn}\mathrm{TMy}_{mn})\right)^2 \end{aligned} \tag{3.44}$$

$$\begin{array}{c} \\ TE_{10} \\ TE_{20} \\ TE_{01} \\ TE_{11} \\ TE_{21} \\ \vdots \end{array} \begin{array}{c} \begin{array}{cccc} TE_{10} & TE_{20} & TE_{01} & \dots \end{array} \\ \begin{pmatrix} TE_{10} \leftarrow TE_{10} & TE_{10} \leftarrow TE_{20} & TE_{10} \leftarrow TE_{01} & \dots \\ TE_{20} \leftarrow TE_{10} & TE_{20} \leftarrow TE_{20} & TE_{20} \leftarrow TE_{01} & \dots \\ TE_{01} \leftarrow TE_{10} & TE_{01} \leftarrow TE_{20} & TE_{01} \leftarrow TE_{01} & \dots \\ TE_{11} \leftarrow TE_{10} & TE_{11} \leftarrow TE_{20} & TE_{11} \leftarrow TE_{01} & \dots \\ TE_{21} \leftarrow TE_{10} & TE_{21} \leftarrow TE_{20} & TE_{21} \leftarrow TE_{01} & \dots \\ \vdots & \vdots & \vdots & \ddots \end{pmatrix} \end{array} \tag{3.45}$$

Moving to the farfield is accomplished by use of Fourier transforms. To ensure an accurate transform to the farfield the sampling theorem of fourier optics must be considered, [23]. This tells us that the sampling of the farfield is determined by the range of the aperture field and that the range of the farfield is determined by the sampling of the aperture field. This is depicted in equation 3.46, where δu and δx represent the sampling of the far- and near-fields, respectively, and m and x the range of the respective fields.

$$\delta u = \frac{1}{m}, \quad u_{max} = \frac{1}{2\delta x} \tag{3.46}$$

In implementing this it was found that a near field sampling of $\delta x = \frac{a}{500}$ and a range extended by a factor of 20 generally results in a reasonable description of the farfield.

As was the case in determining the aperture field one must also consider the coherence of the modes in moving to the farfield. Again the case considered here is for a partially coherent system, with the power in each column of the scattering matrix being coherently summed and each column incoherently summed with the others. Considering this, and the fact that the phase information must be maintained before moving to the farfield, the co and cross polar components of each column must be summed separately and coherently in the near field, and transformed to the farfield before being combined. Each column is then Fourier transformed in this manner and combined in the farfield, as outlined in

equation 3.47, where FF represents the farfield.

$$\begin{aligned} FF = \sum_{columns} & Abs\left(FFT\left[\sum_{mn}(S21_{mn}\mathrm{TEx}_{mn} + \sum_{mn} S21_{mn}\mathrm{TMx}_{mn})\right]\right)^2 \\ & + Abs\left(FFT\left[\sum_{mn}(S21_{mn}\mathrm{TEy}_{mn} + \sum_{mn} S21_{mn}\mathrm{TMy}_{mn})\right]\right)^2 \end{aligned} \tag{3.47}$$

The mathematical theory outlined in this section was scripted using both Mathematica and Python. The format chosen for the geometry file was such that the first row contains the labels “Frequency”, “Max mode order” and “Step No.”, tab separated, and the second row the tab separated values corresponding to these terms. Each following successive row provides the step number, step size, and rectangular dimensions a and b, after an initial row labels the columns. This format is depicted in table 3.2. The term “Max mode order” specifies the highest mode index. For example a maximum mode order of 8 would consider all modes from TE_{10} to TE_{88} and TM_{11} to TM_{88}. This may be better appreciated by considering the form of the scattering matrix outlined in table 3.1.

Table 3.2.: Geometry file format for the pyramidal Scatter code

Frequency	Max mode order	Step No.	
□	□	□	
Step No.	Step Size	Dimension a	Dimension b
1	□	□	□
2	□	□	□
□	□	□	□

Verification of the code

To test the code a single moded pyramidal horn was considered at 60 GHz; the dimensions of this horn are displayed in figure 3.5. Theoretically, for the case of only the fundamental TE_{10} mode being supported, the near- and far-field of such a horn can be predicted by equations 3.48 and 3.49 [24], where Lx_h and Ly_h represent the slant length of the horn,

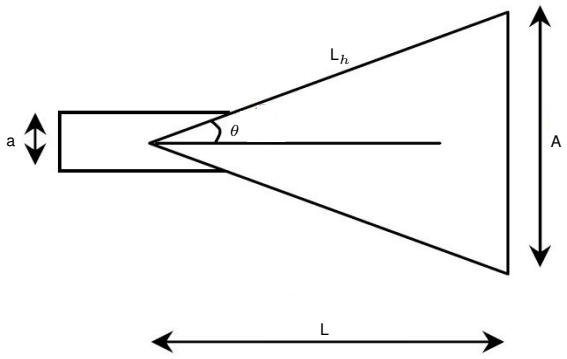

Figure 3.5.: The single moded pyramidal horn used in verifying the Scatter code. Parameters $a_x = 2.54\,\text{mm}$, $a_y = 1.26\,\text{mm}$, $A_x = 13.65\,\text{mm}$, $A_y = 10.15\,\text{mm}$, $Lx_h = 33.4\,\text{mm}$, $Ly_h = 37\,\text{mm}$.

θ the angle of the farfield axis, and ϕ the cut of the field. This analytical analysis of the horn is possible due to the lack of higher order modes, which results in very minor levels of scattering. The phase of the near field plot can be read directly as the argument of equation 3.48. It should however be noted that these ideal theoretical predications allow for no contribution from higher order modes and as such represent a much more limited analysis of the horn than for example the Scatter analysis. These ideal predications for the near field, phase and magnitude, with the Scatter results are depicted in figure 3.6.

$$\text{NF} = cos\left(\frac{\pi x}{A}\right) e^{-i\frac{k}{2}\left(\frac{x^2}{Lx_h}+\frac{y^2}{Ly_h}\right)} \tag{3.48}$$

$$\text{FF} = \frac{k}{4\pi r}\left(1 + cos(\theta)\right) \int\int \text{NF(x,y)} e^{ik(xsin(\theta)cos(\phi)+ysin(\theta)sin(\phi))} dxdy \tag{3.49}$$

Further tests were conducted in conjunction with CST Microwave Studio. The macro discussed in chapter 2.2 was used to read in the same geometry file. A farfield monitor was then activated at the frequency of interest, 60 GHz, and the results compared to those of both the theoretical plot and of Scatter. These can be seen in figure 3.6 with minor discrepancies only occurring below -10 dB in the sidelobes.

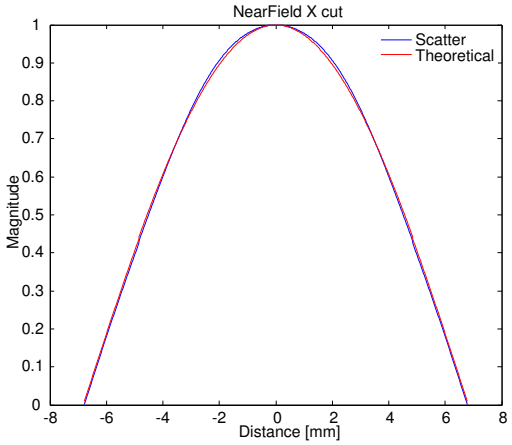

(a) Comparison of the aperture field of the test horn as predicted by Scatter and theoretically.

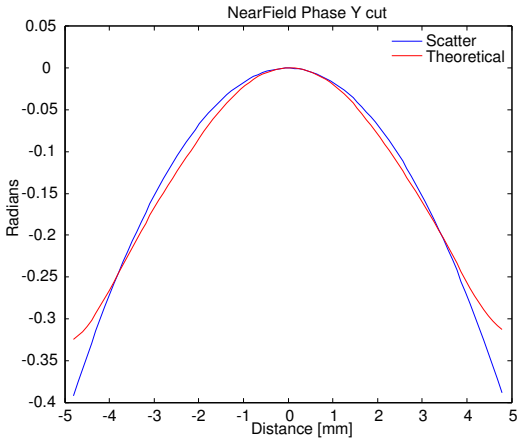

(b) Comparison of the phase of the aperture field of the test horn as predicted by Scatter and theoretically.

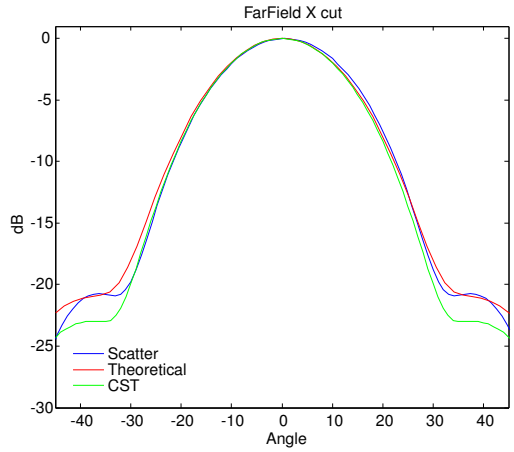

(c) Farfield comparisons X-cut

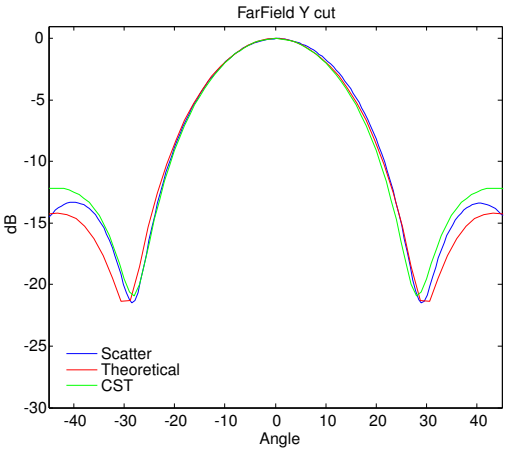

(d) Farfield comparisons Y-cut

Figure 3.6.: Results of a single moded horn analysis: Theoretical plots of equation 3.48 compared to Scatter predictions and the farfield as predicted theoretically by equation 3.49 and simulated by CST Microwave Studio and Scatter

When setting up a new simulation and creating the geometry file several variables must be considered, such as the number of segments per wavelength with which the structure is to be modelled and the maximum mode order. Each mode considered throughout the simulation is initially excited with unity power, however, depending on the input guide dimensions, these could also include evanescent modes (i.e. modes for which the frequency of the simulation is above their respective cut-off frequencies). Such evanescent modes are attenuated and do not propagate through the system, nonetheless, as they are equally excited with unity power, should the initial guide segment be sufficiently thin compared

to the wavelength it is possible for power to couple from these evanescent modes to other modes at the first junction. This can lead to inaccurate results, as such evanescent modes would not truly contain such levels of power. To avoid this scenario, one should consider extending the length of the initial segment in the geometry file, so as all evanescent modes are completely attenuated before the power coupling integrals are evaluated. In the single moded example considered the horn was fed by an initial waveguide section, however to examine the influence of these evanescent modes this section was removed. The results of this analysis can be seen in figure 3.7(a). Considering first the CST results, one observes no significant levels of fluctuation in the results when the neck is removed. Furthermore, these results oscillate about the Scatter profiles for the case of a waveguide neck. Removing the waveguide feed from the Scatter simulations however results in significant deviations dependent on the maximum mode order considered. The dependence on the number of modes considered is as expected as each successive higher order evanescent mode is fully excited and couples power into the system. To better demonstrate this effect the single moded horn antenna of figure 3.5 was considered both with and without a waveguide attenuator and the $|S_{21}|^2$ matrix representing the power coupled between modes recorded for a maximum mode order of 1. The resulting matrices are outlined in tables 3.3 and 3.4 and demonstrate how significant amounts of power are coupled into the system through the excitation of evanescent modes in the absence of a waveguide attenuator segment.

Table 3.3.: $|S_{21}|^2$ values generated using the Scatter software for a maximum of 1 mode order for the pyramidal test horn without a waveguide attenuator

0.999	0	0	0
0	0.149	0	0
0	0	0.016	0
0	0	0	0.018

Table 3.4.: $|S_{21}|^2$ values generated using the Scatter software for a maximum of 1 mode order for the pyramidal test horn with a waveguide attenuator

0.999	0	0	0
0	0	0	0
0	0	0	0
0	0	0	0

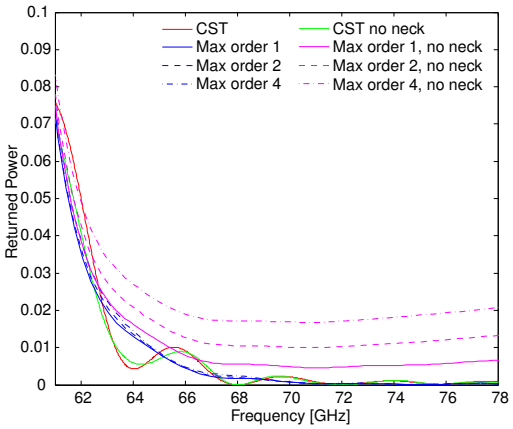

(a) S_{11} of the single moded horn antenna with and without a waveguide feed. Simulations were conducted using CST Microwave Studio and pyramidal Scatter for a varying max number of mode orders

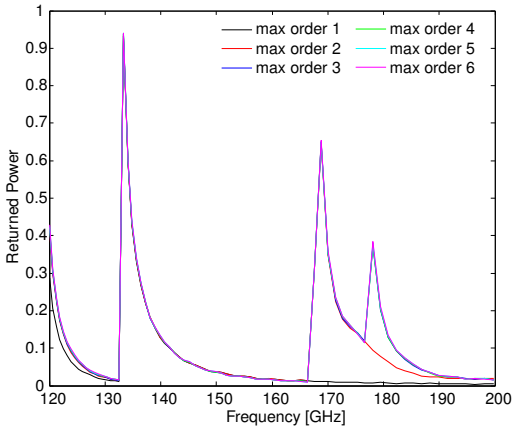

(b) Variation in the S_{11} of a multimoded horn for a varying number of maximum mode orders.

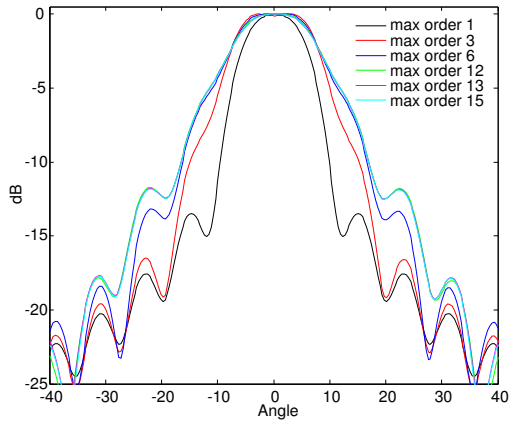

(c) Variation in the farfield of a multimoded horn for a varying number of maximum mode orders.

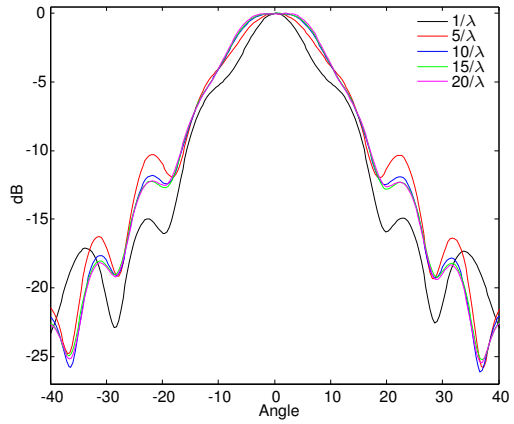

(d) Variation in the farfield of a multimoded horn for a varying number of segments per wavelength.

Figure 3.7.: The effect of varying geometry file variables on the pyramidal Scatter simulation results. The horn of figure 3.5 is considered between 60 GHz to 78 GHz for single moded simulations and between 120 GHz to 200 GHz to investigate the multimoded performance. It should be noted that the sub-figures (a) - (d) represent a natural progression, where, for example, the waveguide segment is adopted in sub-figures (b), (c), and (d) having been demonstrated to be necessary in sub-figure (a).

To examine the influence of the input parameters on the multimoded performance, the same horn geometry was considered between 120 GHz and 200 GHz. Figure 3.7(b) outlines the variation in the S_{11} of the multimoded case for different values of the maximum mode order considered. One observes that a mode order of 3 accurately describes the entire

band. Considering the highest mode supported by the system at 200 GHz is the TE_{30} (determined by the cut-off frequencies of equation 3.5) this result is as expected. The farfield results are also considered at 160 GHz and can be seen in figure 3.7(c). Here one may note that the results continue to evolve for maximum mode orders beyond a value of 3, which satisfied convergence when considering the S_{11}. This too is as expected as the highest order modes supported at the exit aperture of the horn are the $TE_{13\,2}$ and the $TM_{13\,2}$. As such, although only 3 mode orders are supported at the entrance aperture, higher order modes are subsequently supported throughout the horn into which power from the initial 3 mode orders may couple. To accurately model the farfield one may therefore infer that a minimum of 13 mode orders is required. This is confirmed by figure 3.7(c). Determining the maximum number of mode orders to include in a simulation is therefore dependent both on the structure and the sought after data. However, in general it is advisable to consider a minimum number of modes greater than the total number supported by the system.

One further variable to be decided upon when creating a geometry file is the number of segments per wavelength with which to simulate the structure. This is particularly relevant when approximating a slanted surface through successive segments of increasing or decreasing dimensions, such as is the case with a smooth walled horn antenna. For such structures it is advised that between 10 - 20 segments per wavelength be considered. This is confirmed in figure 3.7(d), which depicts the farfield results of the same horn antenna of figure 3.5 at 160 GHz. Here one may note only minor variations below -12 dB for 10 segments per wavelength and almost no deviation for more than 15 segments per wavelength.

3.2.3. Cylindrical Scatter

A complete derivation of cylindrical Scatter can be seen in [17]. This section will highlight only significant differences to the pyramidal case, as the underlying physics is similar. Whilst sine and cosine functions represent the basis set for rectangular modes, in the

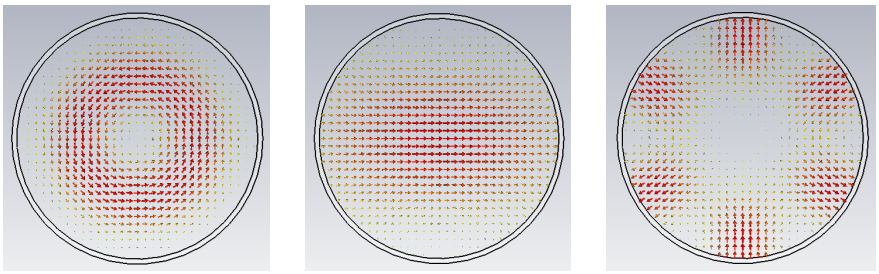

(a) TE_{01} (b) TE_{11} (c) TE_{31}

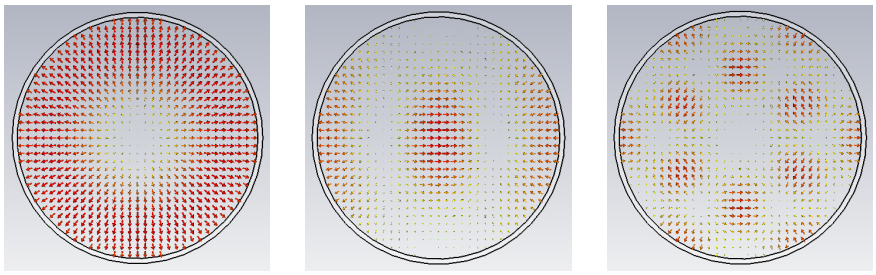

(d) TM_{01} (e) TM_{11} (f) TM_{31}

Figure 3.8.: Sample of transverse electric and magnetic field forms for a circular guide.

cylindrical case Bessel functions describe the mode set. To illustrate the general form of the expressions the x-component of the TE electric field is given in equation 3.50 below for the conical geometry [17].

$$\begin{aligned} E_x &= \frac{D_{nl}}{2} J_{n-1}\left(q_{nl}\frac{r}{a}\right)\begin{pmatrix}\cos\left((n-1)\,\phi\right)\\ -\sin\left((n-1)\,\phi\right)\end{pmatrix} \\ &\quad + \frac{D_{nl}}{2} J_{n+1}\left(q_{nl}\frac{r}{a}\right)\begin{pmatrix}\cos\left((n+1)\,\phi\right)\\ -\sin\left((n+1)\,\phi\right)\end{pmatrix} \end{aligned} \tag{3.50}$$

In equation 3.50, J_n represents the Bessel functions and q_n the roots of n^{th} function, n and l the mode numbers, a the radial dimensions of the guide and D_{nl} is determined through normalisation. The propagating modes are normalised the same way as in the rectangular case, by setting the power to unity over any transverse plane.

$$\int \left(|E_x|^2 + |E_y|^2\right) dS = 1 \tag{3.51}$$

In the cylindrical case not all modes can couple into one another, as was the case for the pyramidal Scatter. Here scattering only occurs between modes of the same azimuthal order as only they share the same z-component dependence on $\cos(n\phi)\sin(n\phi)$ (see equation 3.50). As such, to avoid unnecessary computations, separate matrices are established for each azimuthal order and the coupling integrals only solved and evaluated for modes of the same order. This results in a series of scattering matrices for each individual azimuthal order, as outlined in table 3.5.

Table 3.5.: Example of a Cylindrical Scattering matrix for azimuthal order n = 1. The matrix is divided into four quadrants representing coupling from TE to TE and TM modes and from TM to TE and TM modes. For example the blue cell represents power coupled from the TE_{12} mode to the TE_{12} mode and the red cell power coupled from the TM_{12} to the TM_{14} mode.

n = 1	**Input Mode Number i**										
Output Mode Number j				1	2	3	4	5	6	7	8
				TE_{ni}				**TM_{ni}**			
				11	12	13	14	11	12	13	14
	1	**TE_{nj}**	11								
	2		12								
	3		13								
	4		14								
	5	**TM_{nj}**	11								
	6		12								
	7		13								
	8		14								

As modes of different azimuthal order do not couple they are considered incoherent to one another and summed as such in the formation of the near- and far-fields. Furthermore, since the Fourier transform of the bessel modes are themselves Bessel functions, the Fourier transforms need not be performed as analytical farfield mode expressions can be used to form the farfield in the same manner as is done with the aperture field.

The format chosen for the geometry file for cylindrical Scatter is organised into a single column with the first three elements refereing to the “frequency”, “number of azimuthal orders” and the “number of steps”, respectively. This is then followed by the values for the lengths of each segment before the radii are listed. For the purpose of distinguishing

between the two an entry is made in the second column beside the radii values (for example "50"), as outlined in table 3.6.

Table 3.6.: Geometry file format for the cylindrical Scatter code

Frequency	
Mode No.(azi)	
Step No.	
ΔL_i	
ΔL_{i+1}	
ΔL_{i+2}	
r_i	50
r_{i+1}	50
r_{i+2}	50

Verification of the code

The cylindrical Scatter code has been robustly tested in the past, examples of which may be seen in [17]. As such, the results here focus primarily on demonstrating the effectiveness of the technique in modelling smooth walled horns as profiled horns made up of multiple sub-wavelength thick segments of increasing radius. To that end a smooth walled, single moded, conical horn with an entrance aperture of $r_{entrance} = 0.1975\,\text{mm}$, an exit aperture of $r_{exit} = 0.4108\,\text{mm}$ and a length of $l = 5.795\,\text{mm}$ fed by a waveguide of radius $r_{guide} = r_{entrance}$ and length 0.85 mm was considered in both CST Microwave Studio and Scatter. The macro outlined in section 2.2 was used to read in the same geometry file as was used in creating the Scatter horn to ensure the exact same structure was considered in both cases. Subsequently the minimum number of segments per wavelength required for an accurate description of the farfield was examined on a multimoded, smooth walled, horn with parameters $r_{entrance} = 1.25\,\text{mm}$, $r_{exit} = 6.82\,\text{mm}$ and $l = 30.2\,\text{mm}$ and excited at 160 GHz.

The results of figure 3.9(a) demonstrate firstly perfect agreement between the Scatter and CST farfields for the same profiled horn design. Furthermore, the approach of using

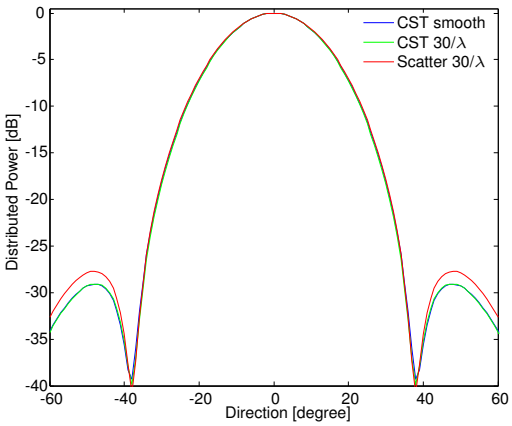

(a) Farfield results of a true smooth walled horn from CST Microwave Studio and the profiled equivilent from both CST and Scatter

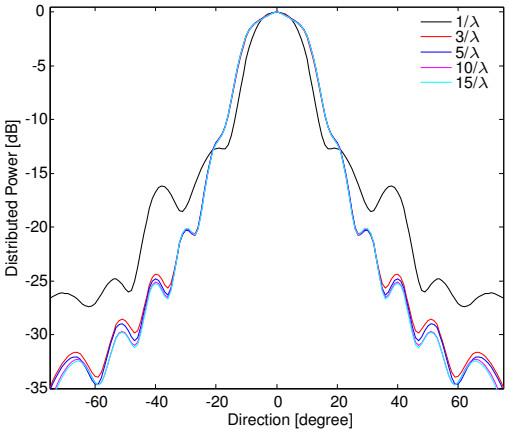

(b) Affect of increasing the number of segments per wavelength on the Scatter farfield results of a multimoded horn.

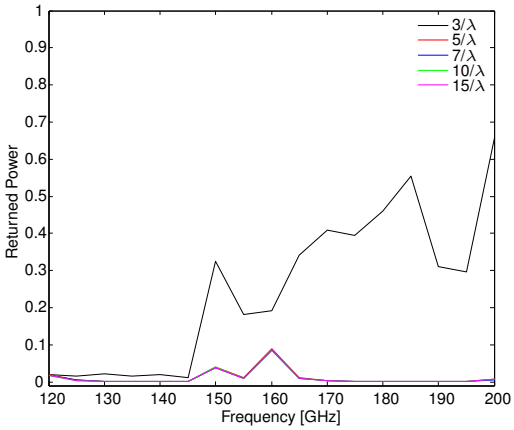

(c) Variation of the S_{11} for varying number of segments per wavelength of the multimoded horn.

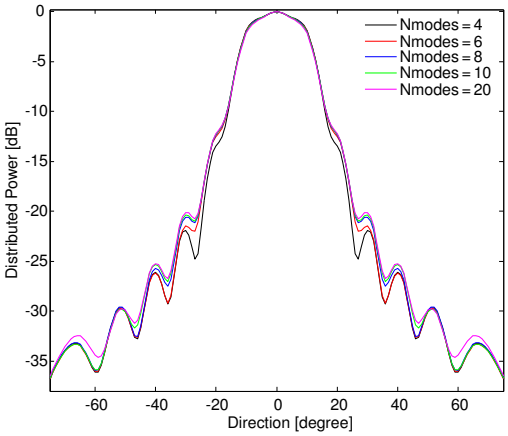

(d) Influence of the number of modes considered on the farfields of the multimoded horn.

Figure 3.9.: Farfield and S_{11} results of smooth walled horn antennas of dimensions, single moded: $r_{entrance} = 0.1975\,\text{mm}$, $r_{exit} = 0.4108\,\text{mm}$ and $l = 5.795\,\text{mm}$, and multimoded: $r_{entrance} = 1.25\,\text{mm}$, $r_{exit} = 6.82\,\text{mm}$ and $l = 30.2\,\text{mm}$

a profiled horn as an approximation to a smooth walled structure can be seen to yield almost identical results, with minor variations only occurring in the sidelobes and below -27 dB. These variations are attributed to surface currents not accounted for in the mode matching approach. Figure 3.9(b) displays the farfield results of Scatter for a multimoded horn design. One observes almost perfect agreement in the farfield results down to -25 dB for 5 segments per wavelength and down to -35 dB for 10 segments. The variation in the S_{11} appears less dependent on the number of segments per wavelength (see in figure 3.9(c)), this is most likely due to the initial segments dominating the behaviour of the S_{11}.

It is thus suggested that 10 segments per wavelength be considered the default value for geometry file constructions.

Two variables regarding the number of modes have to be defined in the cylindrical Scatter code; the maximum azimuthal and the radial order. Considering the nature of the azimuthal modes, between which no power can couple, one need only consider a total number of azimuthal orders equivalent to the number supported by the initial segment. It is suggested that the maximum number of radial orders considered correspond to the highest number supported throughout the system. For the multimoded horn considered here the horn exit aperture supports a total of 6 azimuthal orders and the entrance aperture a maximum radial order of 7. The results of figure 3.9(d) also confirm this assumption with no significant variation below -30 dB occurring for maximum radial mode orders exceeding a value of 8.

3.2.4. Aperture Efficiencies

A parameter often of interest in the design of horn antenna is the aperture efficiency. This is defined by considering a point source in the farfield producing a plane wave over the aperture of the antenna. The aperture efficiency is then defined as the ratio of the effective area (A_e) to the physical area (A_p) of the antenna, where the effective area is defined as the power per unit frequency collected from a plane wave for an incident flux density.

$$\epsilon_a = \frac{A_e}{A_p} \tag{3.52}$$

In practice this can be realised by considering the coupling of the aperture field to a truncated plane wave over the physical area of the antenna. This is outlined in equation 3.53, where E_{in} represents the incident plane wave and E_a the aperture field [14], where $E_{in} = E_{in}(x, y)$ and $E_a = E_a(x, y)$.

$$\epsilon_a = \left| \frac{\int E_{in} E_a^* dA}{\sqrt{\int E_a E_a^* dA \int E_{in} E_{in}^* dA}} \right|^2 \tag{3.53}$$

Furthermore, in the case of the Scatter code it is possible to consider the coupling of the plane wave to the independent modes (or eigenmodes) comprising the aperture field to gain a more complete understanding of the behaviour of the antenna. In this case the integrals of equation 3.53 can be replaced by finite sums over the coefficients of the total number of eigenmodes of the system, as the orthogonal basis components remain constant.

$$\epsilon_a(i) = \left| \frac{\sum_{(x,y)} E_{in}\psi_i^*}{\sqrt{\sum_{(x,y)} \psi_i\psi_i^* \sum_{(x,y)} E_{in}E_{in}^*}} \right|^2 \tag{3.54}$$

For this work the field is represented as the sum of its eigenmodes, that is the set of modes representing an orthonormal basis set, or the independent channels of power that do not mix, in the horn antenna. The term ψ_i ($\psi_i = \psi_i(x,y)$) of equation 3.54 represents the coefficients of these modes comprising the aperture field. In the more general case these can be determined using singular value decomposition, which allows one to decompose the scattering matrix $\mathbf{S}$ into a product of two unitary matrices $\mathbf{U}$ and $\mathbf{V}$, and a diagonal matrix of the singular values Σ. Thus $\mathbf{S} = \mathbf{U}.\Sigma.\mathbf{V}^\dagger$, where the columns of $\mathbf{U}$ and $\mathbf{V}$ are the left and right singular vectors of $\mathbf{S}$, respectively. The right singular vectors of $\mathbf{S}$ are also equivalent to the right eigenvectors (referred to generally as the eigenvectors) of $\mathbf{S}^\dagger.\mathbf{S}$, and the singular values Σ to the square roots of the eigenvalues of $\mathbf{S}^\dagger.\mathbf{S}$ or $\mathbf{S}.\mathbf{S}^\dagger$. Considering the case of the S_{21} matrix the columns of $\mathbf{V}$ can be used as a basis set $\mathbf{v}_i$ for expanding the field on the input (equation 3.55), where $\mathbf{S}\mathbf{v}_i = \sigma_i\mathbf{u}_i$ and σ_i is the ith singular value. The power in the input beam may be shown to be the sum of the square of the coefficients of the modes (equation 3.56).

$$\mathbf{E_{in}} = \sum_i A_i\mathbf{v_i} = \mathbf{V}.\mathbf{A} \tag{3.55}$$

$$\Rightarrow \mathbf{E_{in}^\dagger}.\mathbf{E_{in}} = \mathbf{A}^\dagger.\mathbf{V}^\dagger.\mathbf{V}.\mathbf{A} = \sum_i |A_i|^2 \tag{3.56}$$

Similarly, the field at the output may be expanded in terms of the basis set $\mathbf{u}_i$. This can in turn be expressed in terms of the input basis set $\mathbf{v}_i$ and consequently the output mode coefficients in terms of the input coefficients, as is outlined in expressions 3.57 to 3.58. Thus, the power in the output beam can be shown to be related to that of the input beam

by the singular values σ_i (see equation 3.59).

$$\begin{aligned} \mathbf{E_{out}} &= \sum_i A_i \mathbf{S v_i} = \mathbf{S.V.A} \qquad (3.57) \\ &= \mathbf{U.\Sigma.V^\dagger.V.A} = \mathbf{U.\Sigma.A} = \mathbf{U.B} \\ \Rightarrow \mathbf{B} &= \Sigma.\mathbf{A} \Leftrightarrow B_i = \sigma_i A_i \qquad (3.58) \\ \Rightarrow \mathbf{E^\dagger_{out}.E_{out}} &= \mathbf{A^\dagger.\Sigma^\dagger.U^\dagger.U.\Sigma.A} = \sum_i |\sigma_i|^2 |A_i|^2 \qquad (3.59) \end{aligned}$$

Essentially, this confirms the statement that these "eigenmodes" represent an orthonormal basis set of the system, as the scattering process is described by the diagonal matrix Σ of singular values and no scattering occurs between these modes.

As the Scatter code described in this chapter is formulated so as the matrices are always square, the eigenvectors and values of $\mathbf{S^\dagger.S}$ are used in finding the eigenmodes ψ_i of the system. Therefore, in this case the scattering matrix is decomposed as $\Psi\lambda\Psi^{-1}$, where Ψ represents the square matrices of eigenvectors (composed of columns of $\psi_\mathbf{i}$) and λ the diagonal matrix of eigenvalues. The eigenfields of the horn are found by considering these eigenvectors and the sum of their product with the waveguide modes as depicted in equation 3.60, where ψ_{mn} refers to the element of the eigenvector ψ_i corresponding to the waveguide mode $\mathrm{TE}_{mn}/\mathrm{TM}_{mn}$. The eigenvalues then provide the relative power of each eigenmode.

$$\mathrm{Eigenfield}_i = \sum_{mn} \psi_{mn} \mathrm{TE}_{mn} + \sum_{mn} \psi_{mn} \mathrm{TM}_{mn} \qquad (3.60)$$

The coupling of each eigenmode of the system to an incident plane wave can be determined using equation 3.54, where ψ_i are the coefficients of the eigenfields of the horn antenna provided by equation 3.60.

Establishing the efficiency of a pyramidal horn can be accomplished as outlined above and performing eigendecomposition of the $S_{21}^\dagger.S_{21}$ matrix. However, as previously outlined the cylindrical Scatter code only considers scattering between modes of the same azimuthal order (see table 3.5). As such, in order to be able to directly use the eigenvalues for establishing the relative power contributions of each mode, it is necessary to first combine

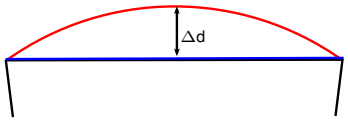

Figure 3.10.: The aperture phase of a horn antenna depicted in red and that of the flat incident phase front in blue, with the maximum phase displacement between the two as Δd

the separate S_{21} scattering matrices before performing eigendecomposition of the resultant matrix. As no coupling occurs between azimuthal orders this results in a block diagonal matrix, such as that depicted in table 3.7. Care must be taken with this arrangement when combining the resulting eigenvectors with the waveguide modes that correct indexing is used for the TE and TM components.

An ideal single moded pyramidal horn antenna, supporting the TE_{10} mode, has a maximum aperture efficiency of 81% [14] resulting from the field distribution. The efficiency may however also be less than this maximum value should the phase fronts not be matched. Considering for example figure 3.10, one may appreciate that should a phase mismatch between the aperture field and the incident field of π exist, that is $\Delta d = \pi$, then destructive interference will occur and thus reduce the overall efficiency. Ideally when possible a horn antenna should therefore be designed so as to match the incident phase front.

To test the implementation of the aperture efficiency code outlined in this section the single moded pyramidal test horn of figure 3.5 was again considered using the pyramidal Scatter code. This predicted an aperture efficiency of $\epsilon_a = 0.802$, which compares favourably with the ideal maximum of 0.81. This value represents the coupling efficiency of the TE_{10} mode existing at a rectangular aperture upon which a plane wave is incident, however it does not account for the propagation of power coupled into that mode through the horn.

For the work of this thesis the effective value of interest was not the power coupled into the aperture field, but rather the proportion of the flux incident on the horn entrance aperture that emerged through the horn's exit aperture. This value can be retrieved by considering the horn throughput of each eigenmode, which is provided by the respective eigenvalues.

Table 3.7.: An example of the combined S_{21} matrix of cylindrical Scatter for the purpose of eigendecomposition. The matrix corresponds to 3 azimuthal orders being supported and a mode number of 4. The green, blue and red quadrants correspond to the original S matrices of azimuthal orders 0, 1 and 2, respectively, with zeros elsewhere as no coupling between azimuthal orders occurs.

				Input Mode Number i											
Output Mode Number j				1	2	3	4	5	6	7	8	9	10	11	12
				TE		**TM**		**TE**		**TM**		**TE**		**TM**	
				01	02	01	02	11	12	11	12	21	22	21	22
1	**TE**	01						0	0	0	0	0	0	0	0
2		02						0	0	0	0	0	0	0	0
3	**TM**	01						0	0	0	0	0	0	0	0
4		02						0	0	0	0	0	0	0	0
5	**TE**	11	0	0	0	0						0	0	0	0
6		12	0	0	0	0						0	0	0	0
7	**TM**	11	0	0	0	0						0	0	0	0
8		12	0	0	0	0						0	0	0	0
9	**TE**	21	0	0	0	0	0	0	0	0					
10		22	0	0	0	0	0	0	0	0					
11	**TM**	21	0	0	0	0	0	0	0	0					
12		22	0	0	0	0	0	0	0	0					

As such, the corresponding eigenvalue of the decomposition is applied as a scaling factor to the efficiency of each individual eigenmode and in the case of a multimoded horn summed over all supported eigenmodes (as seen in equation 3.61). Applying equation 3.61 to the single moded horn under consideration here results in an effective aperture efficiency of $\epsilon_a = 0.7$.

$$\epsilon_{\text{total}} = \sum_i \left(|\lambda_i|^2 \left| \frac{\sum_{(x,y)} E_{in}\psi_i^*}{\sqrt{\sum_{(x,y)} \psi_i\psi_i^* \sum_{(x,y)} E_{in}E_{in}^*}} \right|^2 \right) \tag{3.61}$$

3.3. SAFARI-type Horn Analysis

The feedhorns proposed for the SAFARI instrument, and under consideration in the ESA TRP project, are of significant electrical size and also multi-moded. Both of these factors prove significantly challenging to more generic commercial software packages. The electrical size of the horns would require massive computational resources and times with more generic methods, such as those employed by CST Microwave Studio. Furthermore,

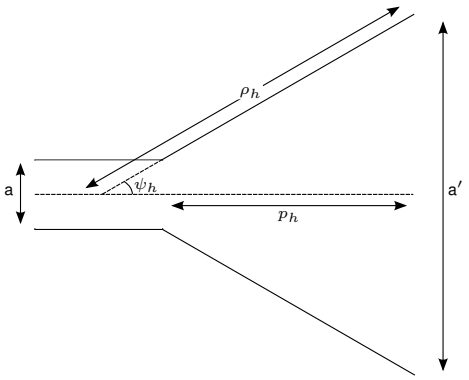

Figure 3.11.: Cross section of a pyramidal horn for the purpose of variable definition. Note: In the orthogonal plane $a \rightarrow b$, $a' \rightarrow b'$, $\rho_h \rightarrow \rho_e$, $p_h \rightarrow p_e$ and $\psi_h \rightarrow \psi_e$

the partial coherence of the modes is a property not well accommodated for in generic software.

The Long wavelength or L-band region of the SAFARI instrument covers 110 µm - 210 µm and is considered first in detail before applying the same analysis to the S-band (35 µm - 70 µm). A traditional single moded design was first considered as a starting point. This was designed as a standard gain antenna following equation 3.62, also known as the horn design equation [24], in conjunction with the expressions outlined in equation 3.63, where the variables are as outlined in figure 3.11. That is a and b represent the horn exit width and height, respectively, a' and b' the entrance dimensions, ψ_e, ψ_h, ρ_e and ρ_h the horn opening angles and slant lengths in the E and H plane, respectively, and $p_h = p_e$ the on axis horn length.

$$\left(\sqrt{2\chi} - \frac{b}{\lambda}\right)^2 (2\chi - 1) = \left(\frac{G_0}{2\pi}\sqrt{\frac{3}{2\pi}}\frac{1}{\sqrt{\chi}} - \frac{a}{\lambda}\right)^2 \left(\frac{G_0^2}{6\pi^3}\frac{1}{\chi} - 1\right) \tag{3.62}$$

$$\chi = \frac{\rho_e}{\lambda}, \quad \frac{\rho_h}{\lambda} = \frac{G_0^2}{8\pi^3}\left(\frac{1}{\chi}\right) \tag{3.63}$$

Initial dimensions of the feed waveguide along with a target gain G_0 are used as a starting point in the design of the horn. Considering the SAFARI horn will be one of many in an array (see section 1.2.2), the pixel spacing sets a maximum entrance aperture of 1.4 mm and a square as opposed to a rectangular aperture is considered to maximise the packing

density. Using equation 3.64 and considering the highest wavelength (210 µm) yields two modes (TE_{01} and TE_{10}) with identical cutoff frequencies, due to the square geometry, for an exit aperture dimension of a = b = 0.12 mm. An initial and ambitious target gain of $G_0 = 30\,dB$ was considered (standard commercially available pyramidal horn antenna generally have a gain of 10 - 20 dB [25]), however remained subject to the exit aperture not exceeding a width of 1.4 mm. In order to meet this physical limit the target gain was finally reduced to $G_0 = 25\,dB$.

$$\nu_{cut-off} = \frac{c}{2\pi}\sqrt{\left(\frac{m\pi}{a}\right)^2 + \left(\frac{n\pi}{b}\right)^2} \tag{3.64}$$

An iterative technique was then employed to find a value of χ, which satisfies equation 3.62 for the target gain value, using an initial value of $\chi = \frac{G_0}{2\pi\sqrt{2\pi}}$. Once a value of χ was found ρ_e and ρ_h were determined via the expressions of equation 3.63 and the horn entrance aperture dimensions a' and b' by the expressions of 3.65. Due again to the unique design requirements of the SAFARI instrument the horn was then extended out (with the same slant radius) to achieve an entrance aperture dimension of $a' = b' = 1.4$ mm.

$$a' = \sqrt{3\lambda\rho_h}, \quad b' = \sqrt{2\lambda\rho_e} \tag{3.65}$$

Table 3.8.: Geometric parameters of a fewer moded SAFARI pyramidal horn design for the LW band

Parameter	**Design 0**
$\mathbf{a = b}$	120 µm
$\mathbf{a' = b'}$	1.4 mm
$\theta = \psi_\mathbf{h} = \psi_\mathbf{e}$	11.195°
$\mathbf{L = p_e = p_h}$	3.234 mm

The results of this design are outlined in table 3.8 and is from this point on referred to as “design 0”. A multimoded analysis of this design was conducted using Scatter and the results are displayed in figure 3.12. As can be seen from figure 3.12(a) the farfield

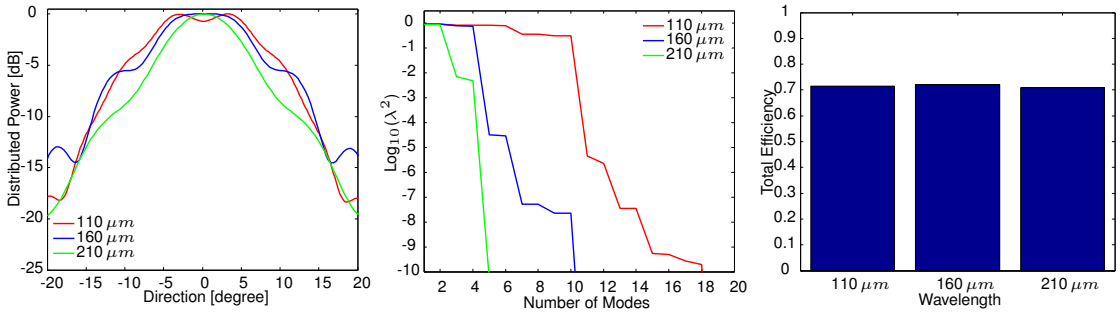

(a) Farfield plots of the LW design 0 horn across the band

(b) Number of eigenmodes supported by the horn, where λ represents the eigenvalues. Note: Only integer numbers of modes exist.

(c) Efficiencies of the LW design 0 horn at the lower, mid and upper regions of the band

Figure 3.12.: Results of the Scatter analysis of the LW design 0 horn design.

pattern at 210 µm out performs the shorter wavelengths with more on axis power and lower side lobes. This can be explained as the horn was designed for the few moded long wavelength range. Considering the eigendecomposition of $S_{21}^{\dagger}.S_{21}$ allows for the number of eigenmodes with significant power to be determined. The mid and short regions of the band support 4 and 10 modes with significant power, respectively (see figure 3.12(b)). Although one generally expects a more divergent beam pattern for larger wavelengths (as the entrance aperture is smaller in terms of wavelength), the shorter wavelengths in this case also support a significantly higher number of modes, which generally results in a larger beam width. This explains the less linear trend of farfield patterns observed for this horn antenna. The aperture efficiency of the antenna was calculated by considering the coupling to a farfield on-axis point source producing a plane wave at the aperture (as previously described in equation 3.54) and predicts approximately 70% efficiency across the band (figure 3.12(c)).

Given the goal of SAFARI to detect extremely faint sources an efficiency of more than 70% of the horns would be preferable. To that end it was considered that a higher number of modes, each free to couple to the incident flux, would further contribute to the coupling achieved by the dominant mode and thus increase the overall efficiency. With this in mind a horn with an exit aperture of 160 µm was proposed. Mechanical constraints in the wire cutting technology employed in the horn construction due to heat build up at

the shorter aperture dimension required the introduction of a kink at the narrower end of the horn (see section 1.3). Both the proposed design with and without the kink were analysed and are referred to as "design 1" and "design 2", respectively (see table 3.9). A further variation was also considered by opening the exit aperture out to 300 µm. This was investigated both as an extreme in regard to creating a highly over-moded horn but also to accommodate the analysis performed at Cambridge University under the TRP project. Given constraints of the pixel spacing, the entrance aperture was fixed at 1.4 mm and the slant radius of the horn was then designed so as to maximise coupling to a plane wave. This was accomplished by consideration of the maximum phase displacement, Δd, between a plane wave and the phase radius of curvature of the horn as outlined in figure 3.10. Minimum coupling to a plane wave occurs for a phase difference of $\pi/2$. Thus, to avoid this scenario the aperture phase (ϕ_{ap} in equation 3.66) must be less than 90°. This results in the condition of expression 3.67, where R_h is the slant radius and a half the aperture width. Given the entrance aperture is fixed at 1.4 mm due to design constraints this results in a conditional slant radius of $R_h > 2.227$ mm. Designs 3 and 4 both observe this condition, where Design 3 includes a kink to account for manufacturing difficulties and Design 4 only a single opening angle.

$$\phi_{ap} = \frac{\pi a^2}{\lambda R_h} \tag{3.66}$$

$$\frac{\pi a^2}{\lambda R_h} < \frac{\pi}{2} \Leftrightarrow R_h > \frac{a^2}{2\lambda} \tag{3.67}$$

Considering figure 3.13(a) one observes an improvement of the order of ≈5% in the

Table 3.9.: Geometric parameters of designs 1 and 2 for the LW band

Parameter	**Design 1**	**Design 2**	**Design 3**	**Design 4**
$\mathbf{a = b}$	160 µm	160 µm	300 µm	300 µm
$\mathbf{a' = b'}$	1.4 mm	1.4 mm	1.4 mm	1.4 mm
$\boldsymbol{\theta_1}$	30°	3.97°	30°	3.94°
$\boldsymbol{\theta_2}$	6°		6°	
$\mathbf{L_1}$	500 µm	9 mm	500 µm	7.98 mm
$\mathbf{L_2}$	9.4 mm		8.03 mm	

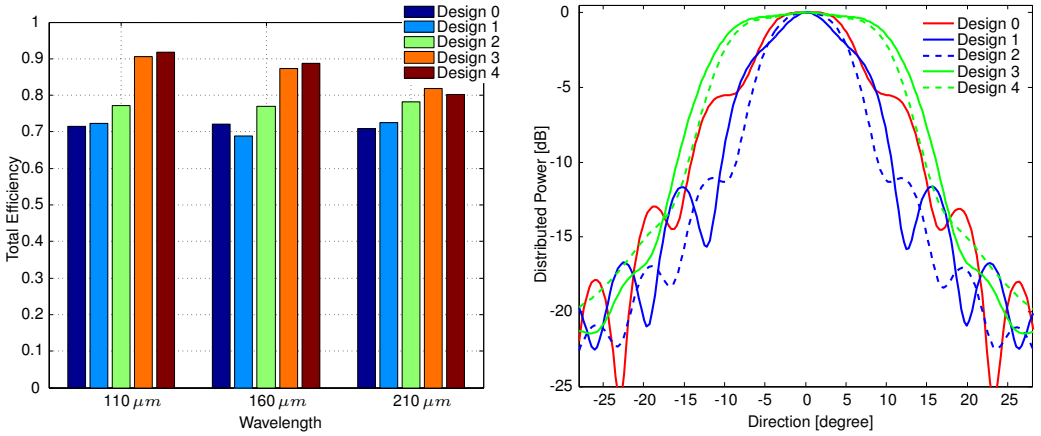

(a) Total efficiencies of the 5 proposed horn designs

(b) Farfield plots of the 5 LW designs at 160 µm

Figure 3.13.: Analysis of the 5 LW horn designs

coupling efficiencies of design 2 over that of design 1. The drop in efficiency of design 1 is attributed to the transition from the 30° to the 6° opening angles compared to the single tapered geometry of design 2. Examining the resultant eigenmodes of the horn's aperture fields reveals that the kink in design 1 excites an eigenmode with less on-axis power as its dominant mode (see figure 3.14(a)), as opposed to the standard TE_{10} or TE_{01} waveguide modes. This results in an overall drop in the coupling to a farfield point source. It should be noted from these results that although an increase in the number of higher order modes contributes to the total horn efficiency, it is nonetheless the fundamental waveguide modes (or other modes with on-axis power) that best couple to a plane wave at normal incidence and can individually attribute for up to an efficiency of ≈70%, that is after having accounted for horn throughput. As such, a deviation of the dominant mode to an off-axis eigenmode in a multimoded horn may perform worse than its fewer moded counterpart.

The performance of the higher moded horns (designs 3 and 4) both significantly out perform the fewer moded horns (designs 0-2), by over 10% at the shorter wavelength range where they support the most modes (see figure 3.13(a) and table 3.10). Comparatively, the drop in efficiency caused by the kink in design 1 relative to design 2 is not observed between designs 3 and 4, also similar apart for the kink in design 3 (see table 3.9). Examination

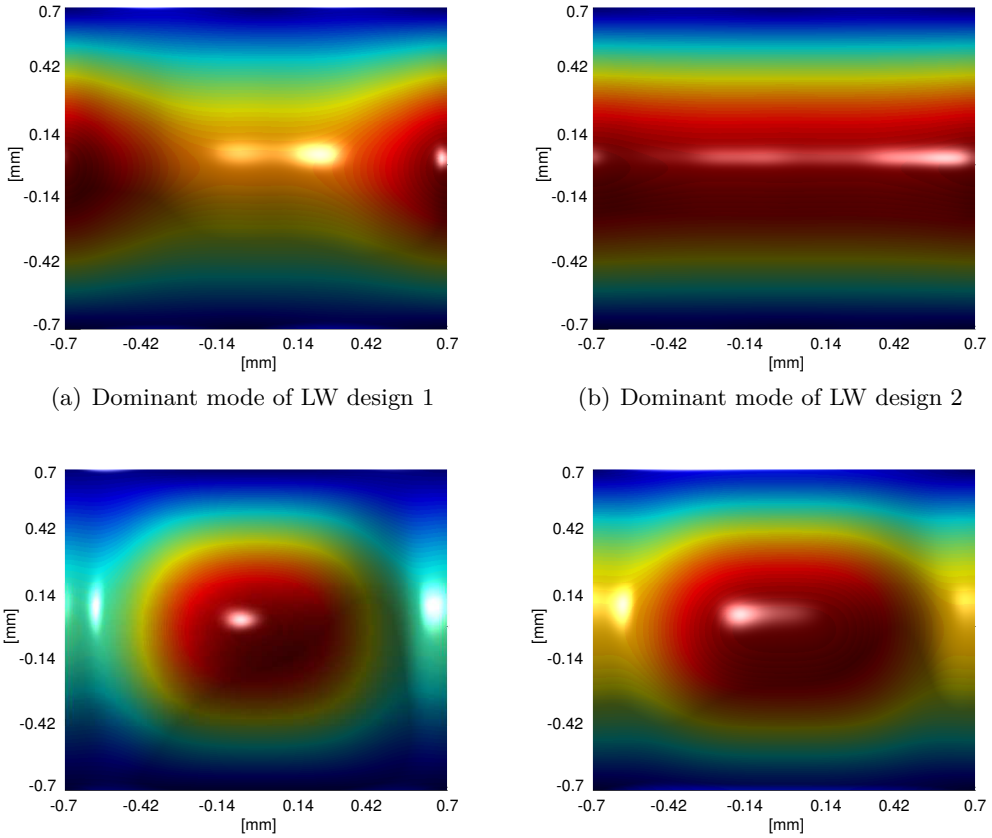

(a) Dominant mode of LW design 1

(b) Dominant mode of LW design 2

(c) Dominant mode of LW design 3

(d) Dominant mode of LW design 4

Figure 3.14.: The dominant eigenmodes of the various LW designs plotted over the entrance aperture dimensions of the horn

of the dominant modes present in both these designs can be seen in figures 3.14(c) and 3.14(d) and although they are both eigenmodes they contain significant on-axis power and thus couple well to a plane wave.

Table 3.10.: The number of modes (n) and total efficiency (ϵ) calculated for each of the LW horn designs at the short, mid and far regions of the band.

	110 µm		160 µm		210 µm	
	n	ϵ	n	ϵ	n	ϵ
Design 1	18	0.723	8	0.689	6	0.725
Design 2	18	0.773	8	0.769	4	0.782
Design 3	60	0.906	34	0.874	18	0.819
Design 4	50	0.918	23	0.887	16	0.802

Table 3.11.: Circular variations of the LW horn designs. The total number of modes (n), the total number of azimuthal order 1 modes (n_{azi1}) and the total efficiency (ϵ) calculated for each of the cylindrical LW horn designs at the short, mid and far regions of the band.

	110 µm			160 µm			210 µm		
	n	n_{azi1}	ϵ	n	n_{azi1}	ϵ	n	n_{azi1}	ϵ
Circ Design 1	32	6	0.718	16	4	0.666	10	3	0.634
Circ Design 2	28	6	0.716	14	4	0.66	9	3	0.640
Circ Design 3	100	12	0.734	50	8	0.726	32	6	0.722
Circ Design 4	90	11	0.756	43	7	0.740	26	5	0.715

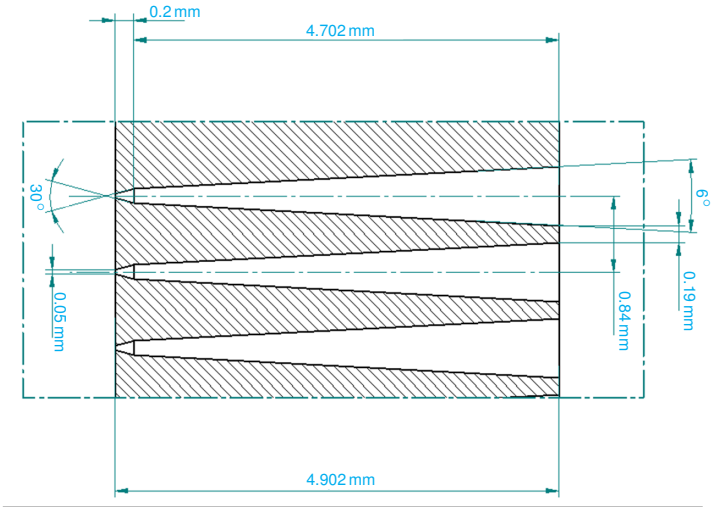

Figure 3.15.: Schematic of the S-band design 1 horn

An additional consequence of increasing the number of supported modes of the horn can be seen in the farfield plots of figure 3.13(b), where the higher number of modes result in wider beam widths. It is also worth noting that this trend is conserved when comparing the influence of introducing the kink into the horn, which increases the number of supported modes. As such, one may improve the efficiency of the beam by increasing the dimensions of the exit aperture to support more modes, however, this consequently broadens the beam and thus could potentially lead to cross-talk between the pixels.

Although creating an array of cylindrical horns presents significant manufacturing difficulties, a series of such horn designs were also considered here for comparative purposes.

In order to produce comparable results with the pyramidal designs considered, the same geometric parameters outlined in table 3.9 for the pyramidal feed horns were used for the cylindrical designs, with the width parameters a and a' representing the radii of the conical horns. This results in four cylindrical configurations; "Circ Design 1", "Circ Design 2", "Circ Design 3" and "Circ Design 4", each with a diameter double the width of the corresponding pyramidal horn design. This increase in the total surface area of the cylindrical designs was necessary to produce horns supporting approximately the same number of modes as in the rectangular case. The results of the cylindrical horn analysis are outlined in table 3.11. One observes again the increase in overall efficiency with increasing mode numbers as seen in the pyramidal case, however, the increases are much more moderate and result in efficiencies lower than those of the pyramidal horns.

This is a result of the special case considered of coupling to a plane wave at normal incidence. In such a scenario it is only on-axis power that significantly contributes to the coupling and in the case of cylindrical waveguide modes only those of azimuthal order 1 contain on-axis power (see section 3.2.3). As such, for this special case one may consider pyramidal designs more advantageous.

The above analysis was repeated for the S-band. In this instance the single proposed horn design is referred to as design 1, a schematic of which can be seen in figure 3.15. Additionally, the effect of removing the kink from this design was considered (design 2) and a horn supporting a higher number of modes was designed by opening the exit aperture dimensions to $150\,\mu\text{m} \times 150\,\mu\text{m}$, maintaining an entrance aperture of width $650\,\mu\text{m}$ (due to pixel spacing design constraints) and ensuring a slant radius of $R_h > 1.509\,\text{mm}$ as calculated using the condition of expression 3.67, this resulted in design 3. These designs are outlined in table 3.12. An overview of the efficiency results can be seen in figure 3.16(a). Considering first the results of design 1 the counterintuitive scenario is observed of the efficiency dropping off by $\approx$10% at the shortest range of the band. Since the number of supported modes is highest at shorter wavelengths one would have expected the efficiency to be maximised in this region. Upon examination the dominant eigenmode of the design 1 horn at

Table 3.12.: Geometric parameters of the S-band horn designs

Parameter	**Design 1**	**Design 2**	**Design 3**
$\mathbf{a = b}$	50 µm	50 µm	150 µm
$\mathbf{a' = b'}$	650 µm	650 µm	650 µm
$\theta_\mathbf{1}$	30°	7°	19.074°
$\theta_\mathbf{2}$	6°		
$\mathbf{L_1}$	200 µm	4.9 mm	1.488 mm
$\mathbf{L_2}$	4.7 mm		

35 µm is found to be identical to that of the L-band design 1 horn (see figure 3.14(a)), whereas at 52 µm the mode form is much closer to that of the fundamental waveguide modes and can be seen in figure 3.17(a). Therefore, the reduced efficiency may again be attributed to dominant off-axis eigenmodes being excited at the shorter wavelength range. From figure 3.17(a) one observes that the dominant mode at higher wavelengths is also an eigenmode, however it is much more akin to the fundamental waveguide modes and contains significant on-axis power. Presumably at these longer wavelengths one of the modes forming the basis set of the off-axis eigenmode is not supported, thus resulting in a more favourable dominant mode. Removing the kink from the horn (design 2) results in a significant improvement in efficiencies (as was also the case in the L-band), which can again be attributed to the form of the dominant eigenmode (see figure 3.17(b)). Opening the exit aperture to form a more multimoded horn, as in design 3, significantly increases the efficiency (figure 3.16(a)) but also broadens the beam (figure 3.16(b)). The analysis was then repeated for cylindrical designs following those of the pyramidal horns in table 3.12 again with the widths a and a' representing the radii of the cylindrical designs. The results of this analysis are displayed in table 3.14 and mirror the results observed in the L-band analysis.

Apart from the manufacturing difficulties encountered in the construction of an array of such cylindrical feed horns, one may appreciate that pyramidal horns offer several advantages from a packaging point of view. The rectangular apertures of pyramidal feed horns could achieve a packing density factor of nearly 1 (reduced only by the width of the aperture flanges, see section 1.3). An array of conical horns arranged in a square packing

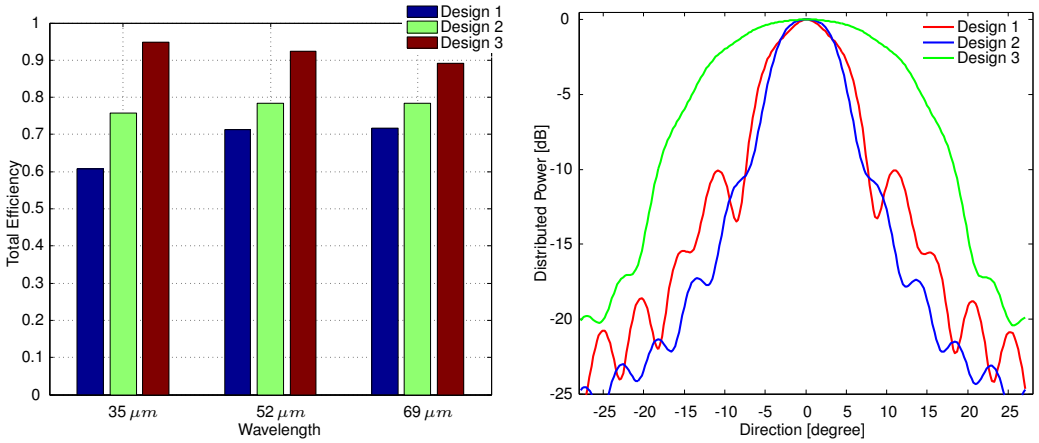

(a) The total efficiencies calculated for the various SW horn designs

(b) Farfield plots of the SW horn designs at 52 µm

Figure 3.16.: Comparison of the optical performance of the SW horn designs

Table 3.13.: The number of modes (n) and total efficiency (ϵ) calculated for each of the SW horn designs at the short, mid and far regions of the band.

	35 µm		52 µm		69 µm	
	n	ϵ	n	ϵ	n	ϵ
Design 1	18	0.608	10	0.712	4	0.716
Design 2	14	0.757	6	0.783	4	0.784
Design 3	120	0.947	60	0.924	40	0.892

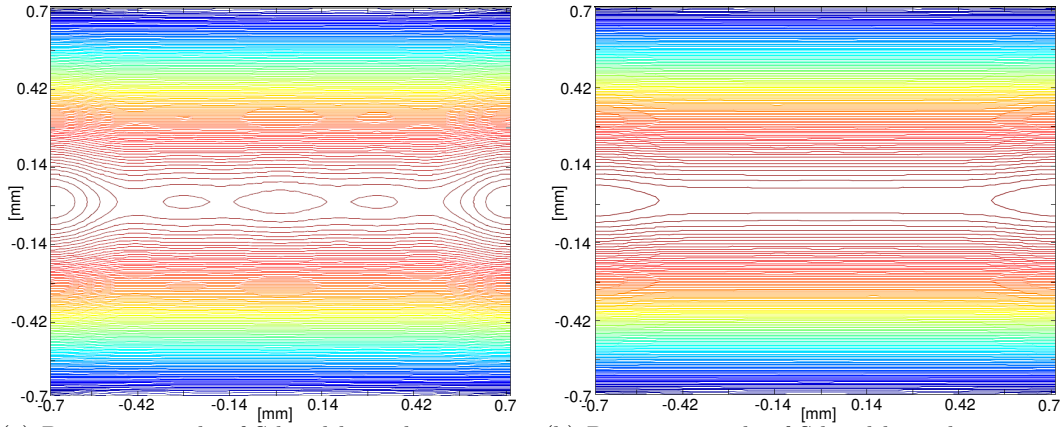

(a) Dominant mode of S-band horn design 1 at 52 µm

(b) Dominant mode of S-band horn design 2 at 52 µm

Figure 3.17.: Contour plots of the dominant eigenmodes of the S-band horn designs 1 and 2 at 52 µm

Table 3.14.: Circular variations of the SW horn designs. The total number of modes (n), the total number of azimuthal order 1 modes (n_{azi1}) and the total efficiency (ϵ) calculated for each of the cylindrical SW horn designs at the short, mid and far regions of the band.

	35 µm			52 µm			69 µm		
	n	n_{azi1}	ϵ	n	n_{azi1}	ϵ	n	n_{azi1}	ϵ
Circ Design 1	30	6	0.718	15	4	0.656	9	3	0.627
Circ Design 2	26	5	0.716	12	3	0.66	7	2	0.637
Circ Design 3	190	18	0.740	105	12	0.754	63	9	0.722

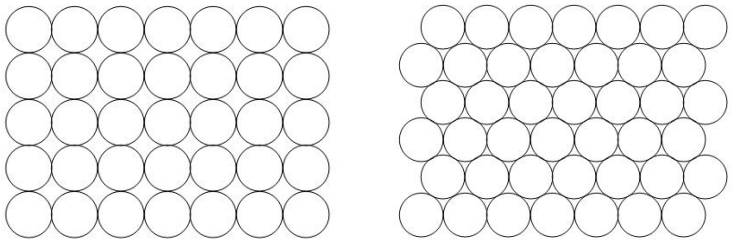

(a) Square Packing (b) Hexagonal Packing

Figure 3.18.: Different packing arrangements possible for the use of conical horn antenna.

formation (see figure 3.18(a)) would achieve a best packing density, η, determined by the ratio of the surface areas of the conical aperture and that of a square of equivalent width; $\eta = \pi r^2/4r^2 = \pi/4 = 0.785$. The densest packing of circles in a rectangular plane is that of the hexagonal lattice of a bee's honeycomb [26] (see figure 3.18(b)) and has a packing density of $\eta = \frac{1}{6}\pi\sqrt{3} = 0.907$. Thus, should the manufacturing obstacles for the cylindrical horns be overcome, their optical performance would have to exceed that of the pyramidal horns by a factor of 0.093 to justify their selection. For the case of coupling to an on-axis plane wave, as was considered in this analysis, this is clearly not the case.

In conclusion, this analysis has focused primarily on the pyramidal variations of potential SAFARI horn antenna and found that increasing the total number of supported modes results in significant improvements in the optical efficiency. Additionally, the higher number of modes significantly broaden the beam pattern. As such, a trade off analysis considering beam width, horn efficiency and pixel cross-talk should be considered before a final design is selected. Furthermore, the analysis outlined in this chapter calculated the aperture ef-

ficiencies for coupling to a farfield point source. This may not represent the final SAFARI arrangement when finalised, in which case the analysis should be repeated by considering the appropriate field distribution (E_{in}) when performing the overlap integral of equation 3.53. This section also examined the behaviour of similarly high moded cylindrical horn designs. In order to achieve a similar number of supported modes it proved necessary to double the cylindrical horn diameter compared to the width of the original rectangular designs. This fundamentally limits the effectiveness of cylindrical feedhorn antennas for a system of this type where physical restrictions also apply to the dimensions due to the array format.

One further point to be considered in the general case when comparing conical to pyramidal horn antenna is the polarisation. In the case of the SAFARI system however the system is not sensitive to polarisation, which was also one of the crucial factors in the choice of non-polarised horns of a square rather than a rectangular cross-section.

3.4. ALMA Band 5 System

3.4.1. Horn Design Simulations

The ALMA system is outlined in section 1.4. The horn design proposed was a cylindrical corrugated horn antenna with an exit aperture diameter of 9.2 mm, an input waveguide diameter of 1.52 mm and a central wavelength of 1.6 mm. This design was considered using a variety of simulation packages, Scatter, CST Microwave Studio and MODAL. MODAL is a hard coded version of cylindrical Scatter, which builds upon the mode matching software and includes physical optics, reactive near fields, Gaussian Beam Mode Analysis and additional elements, such as lenses etc. The results of one such MODAL simulation at $\lambda = 1.6\,mm$ can be seen in figure 3.19(c). For final validation of the horn design a prototype was constructed and measured, the following sections outline the setup of the measurement system and the results of those measurements.

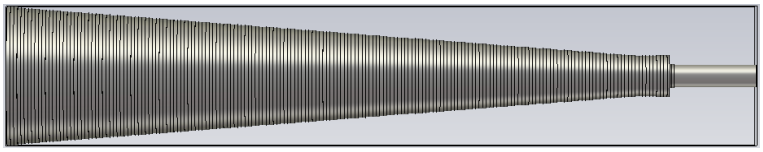

(a) CAD Model of the ALMA Band 5 horn

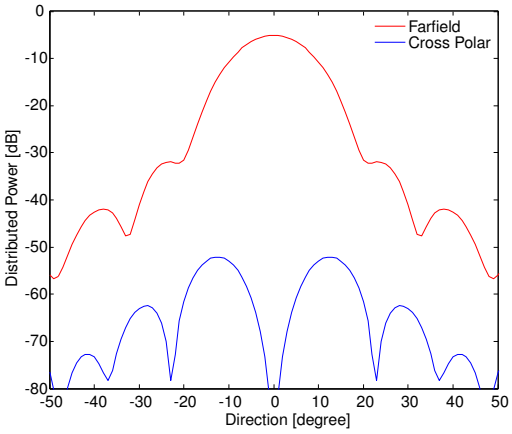

(b) Scatter simulation results of the farfield and cross-polar farfield results

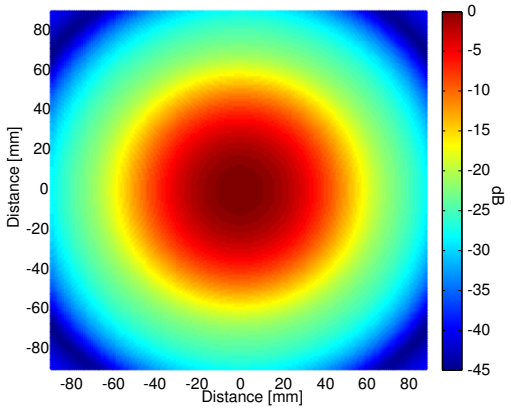

(c) A simulation of the ALMA Band 5 horn at the measurement plane of the VNA scanner

Figure 3.19.: Simulations of the ALMA Band 5 Horn

3.4.2. Warm Optics Measurement System Setup

An overview of the measurement system can be seen in figure 3.20(a). The scanner assembly consists of three linear positioning stages arranged so that each stage represents one of three axes in the measurement coordinate system, x, y and z. This allows for the horn under test to be positioned in a 3D space defined by the travelling range ($\approx$ 300 mm) of the stages. The receiver is mounted on the scanner assembly and the transmitter on the turn and tilt table (see figure 3.20). A reference plate is used in both instances for the purpose of mounting. Additionally, the reference plates in conjunction with the turn and tilt table are used for alignment of the system with both plates being perfectly parallel after successful alignment.

In this setup the transmitter remains stationary on the tilt and turn table, which is also in a fixed position throughout the measurement process. The horn under test, attached to the receiver assembly, is moved through a predefined set of measurement points.

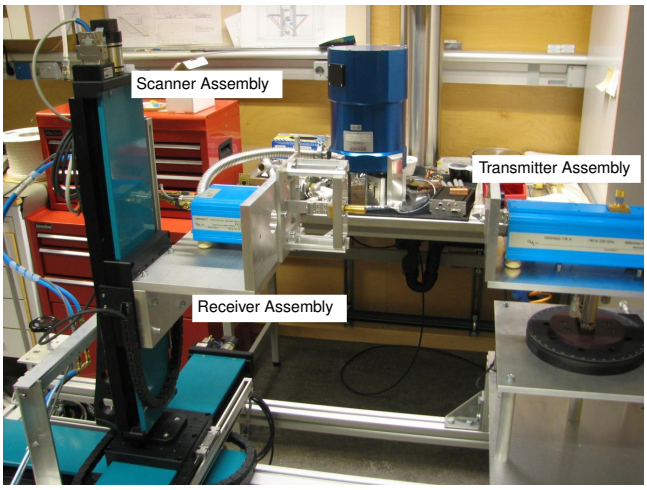

(a) ALMA Band 5 Horn measurement setup. Receiver seen to the left mounted on the scanner assembly and the transmitter on the right mounted to the tilt and turn table.

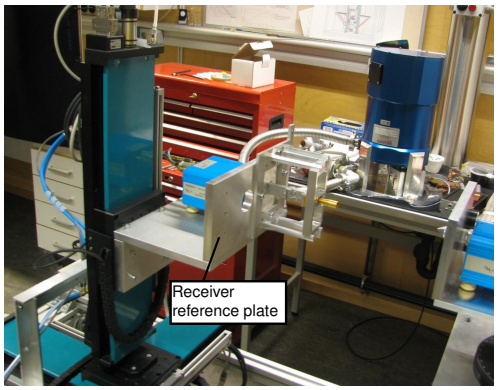

(b) The receiver assembly

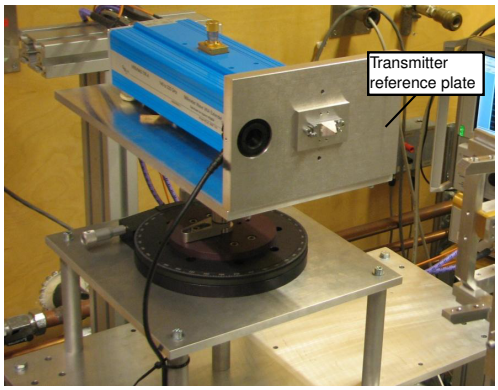

(c) The transmitter assembly

Figure 3.20.: ALMA Band 5 measurement system and close ups of the receiver and transmitter assemblies.

The alignment of the receiver and the transmitter reference plates is critical to the measurement accuracy. As one of the measured parameters is the tilt of the beam, the parallelism of the reference planes is crucial to ensure that any discrepancies between the design and measured values are not due to misalignment of the scanner setup. The alignment procedure is outlined below.

First a micrometer probe was mounted on the reference plate of the scanner, in place of the horn, and moved into position (in the z-axis), so as the probe end was only several microns away from the surface of the transmitter platform (see figure 3.21(a)). The scanner

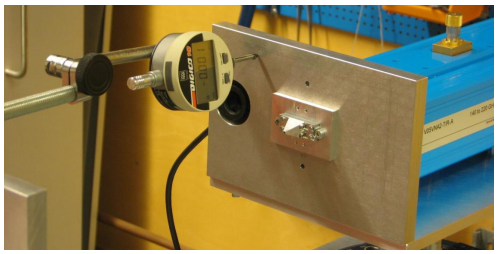

(a) The Waveguide-Micrometer used to align the two planes parallel to one another.

(b) CCD sensor used for laser alignment to center the setup

Figure 3.21.: ALMA Band 5 Measurement System - alignment procedure

was then moved either vertically or horizontally in the xy plane, keeping the orthogonal distance constant. In the event of the micrometer reading a varying orthogonal distance to the transmitter platform during the procedure the transmitter platforms tilt was adjusted with the micrometer screws and the procedure repeated until both surfaces were recorded as being perfectly parallel to each other, in both the horizontal and vertical directions. This technique successfully allowed an accuracy of 10 µm over a distance of 150 mm to be achieved.

The second phase in the alignment procedure involved removing the waveguide micrometer and placing a laser in place of the horn. The detector mounted on the reference plate of the tilt table, seen in figure 3.21(b), is a known distance from the transmitter. As such, by centering the laser on the CCD detector it was possible to infer the position of the center of the horn in relation to the transmitter and hence establish the scanner's coordinate system as a reference coordinate system for that of the measured beam.

Initial measurement results indicated that the center points obtained through the laser alignment were inaccurate. This was due to a misalignment of the laser itself and was consequently avoided by aligning the laser setup. To achieve this the laser was moved along the optical axis in the z direction, thus any misalignment resulted in an off-axis drift of the detected signal and could be corrected for.

A further point of concern arises from the mounting of the conical Band 5 horn to the rectangular waveguide. The aperture area of the two are relatively well matched, with the

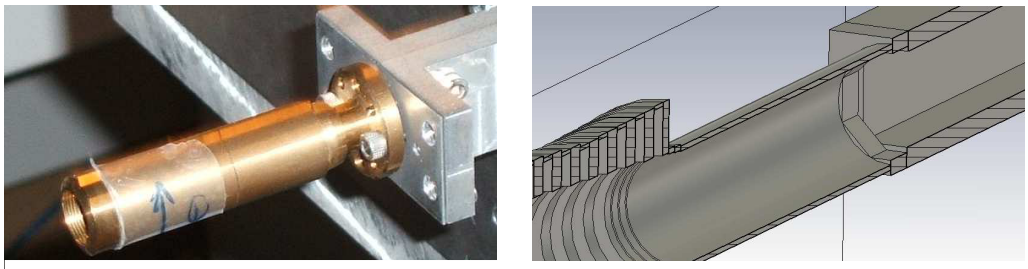

(a) The prototype ALMA Band 5 horn mounted to the VNA head

(b) A CAD model of the hexagonal tranistion step used in the ALMA Band 5 system

Figure 3.22.: A photograph of the mounted prototype Band 5 horn and a CAD model of the transition step.

radius of the horn aperture 0.76 mm and half the width of the rectangular guide 0.63 mm, furthermore only the fundamental mode is supported and thus most of the power centered and not directly incident on the mismatched region. Nonetheless, the discontinuity does result in unnecessary reflections. Two alternative approaches were considered in minimising the return loss; a tapered segment slowly transitioning from the circular to the rectangular cross-section over a length equivalent to the central guide wavelength of the band ($\lambda_{guide} = 2.077\,\text{mm}$), and a hexagonal transition step designed at the National Astronomical Observatory of Japan (NAOJ) [27]. A return loss of less than -25 dB across the entire ALMA Band 5 band was specified as the desired performance [28]. Figure 3.22 displays a photograph of the mounted horn and a CAD image of the hexagonal transition. Simulations of the proposed alternatives were carried out in CST Microwave Studio, firstly for a junction between two waveguides and then also for the transition to the Band 5 horn itself. The results of these simulations can be seen in figure 3.23. The results of figure 3.23(c) show a return loss across the band already within acceptable levels (-26.2 dB) for the case of a single step (without a guided transition). This was however expected due to the single moded nature of the guides and the similar cross-sections. Implementing a transition step improves this to a level of -27.5 dB and -27 dB for the tapered and hexagonal steps, respectively. Coupling to the band 5 horn is considered in figure 3.23(d) and merely improves slightly on the performance of each of the cases seen between the waveguides with return losses of -26.8 dB, -28.6 dB and -28.2 dB for the single step, tapered and hexagonal transitions, respectively. The further reduction in return loss here may be

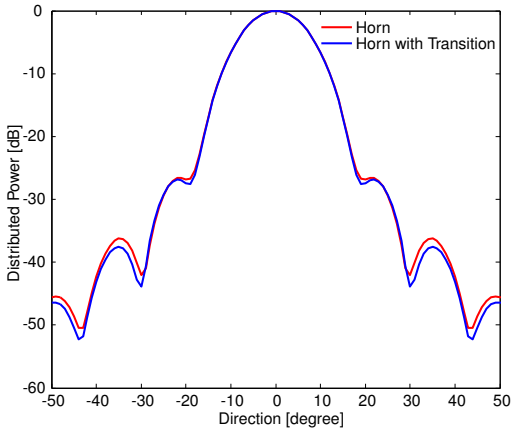

(a) Simulated farfield results of the ALMA Band 5 Horn design with and without the square to circular transition using CST microwave studio.

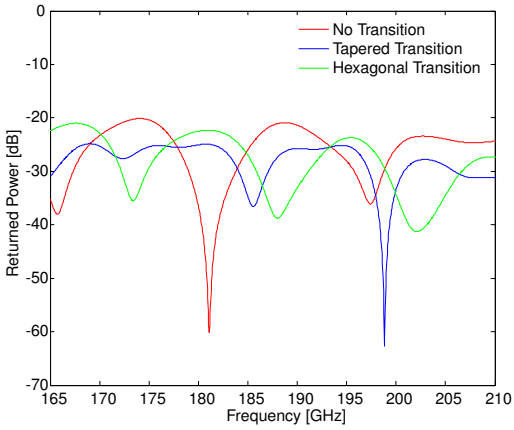

(b) S_{11} returned power of the ALMA Band 5 horn accross the band for the cases of no transition, a tapered and a hexagonal transition

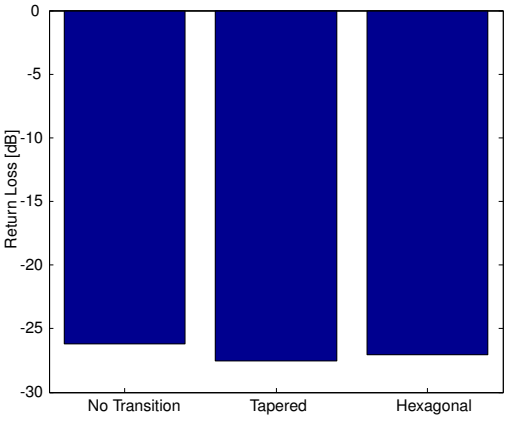

(c) The return loss averaged over the entire Band 5 band for the rectangular to circular transition of a 1.26×1.26 mm rectangular waveguide to a circular guide of radius 0.76 mm.

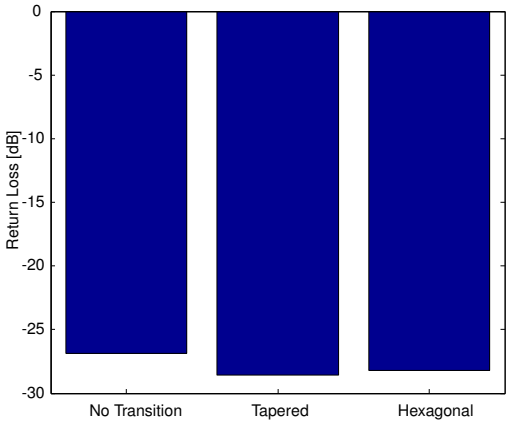

(d) The return loss averaged over the entire Band 5 band for the ALMA Horn with various transition setups

Figure 3.23.: Analysis of the influence of the transition stage on the Band 5 horn

attributed to the improvement in coupling to free-space provided for by the horn. The marginal improvement of 0.4 dB between the tapered and hexagonal transitions is not sufficient to warrant the expense in manufacturing such a tapered step and as such the hexagonal configuration was used.

To reduce the measurement time a raster scan or *On the Fly* approach was implemented. This meant, instead of conducting a standard point for point scan, the horn was moved at a constant velocity from the beginning to the end position and measurements taken while in motion. This raster approach had to be calibrated to yield identical results to the step

by step scan. This involved adjusting the velocity, acceleration, number of measurement points and the dwell time between measurements. The dwell time could be determined from the number of measurement points and the total distance covered, the acceleration and velocity values were determined through trial and error to match the step by step approach. The final velocity chosen was 10 mm/s with an acceleration of 20 mm/s^2.

Originally the system was setup to run raster scans from (x_0, y_0) to (x_1, y_0) and then from (x_1, y_1) to (x_0, y_1). However, this resulted in a "rippled" effect manifesting itself in the contour plots, where every second cut appeared as slightly displaced. As a result, the system was altered so as always to return to (x_0, y_i) before recording any data. This unfortunate necessity increased the overall measurement time by approximately a factor of 2. The cause of the observed ripple is unknown, one possible source may be an offset in the first measurement point starting from x_{end} as opposed to x_0.

3.4.3. Warm Optics Measurements - Prototype Horn

Before the final horn was ordered a prototype horn of the proposed design was milled in house at the GARD institute of Chalmers Technical University, Sweden. This horn was constructed in three segments and pressed together. Although it was assumed that none of the horn's structure, specifically the corrugations, would be affected during this process, it remained a distinct possibility. Furthermore, as the corrugations had dimensions on the micron scale the milling machine was operating at the limits of its operational precision. This horn was measured for comparison with the simulated performance of the design.

An x and y cut of the horn measurements can be seen in figure 3.24(a). Each plot was the result of 10 averaged scans. Furthermore, the horn was dismounted and reattached for a second set of 10 scans to ensure repeatability with identical results. The results of the measurements can be seen in figure 3.24(a). The measurement system proved capable of producing perfectly reproducible results, however the plots did not conform to those expected for a well designed corrugated horn antenna. A corrugated horn is designed so as

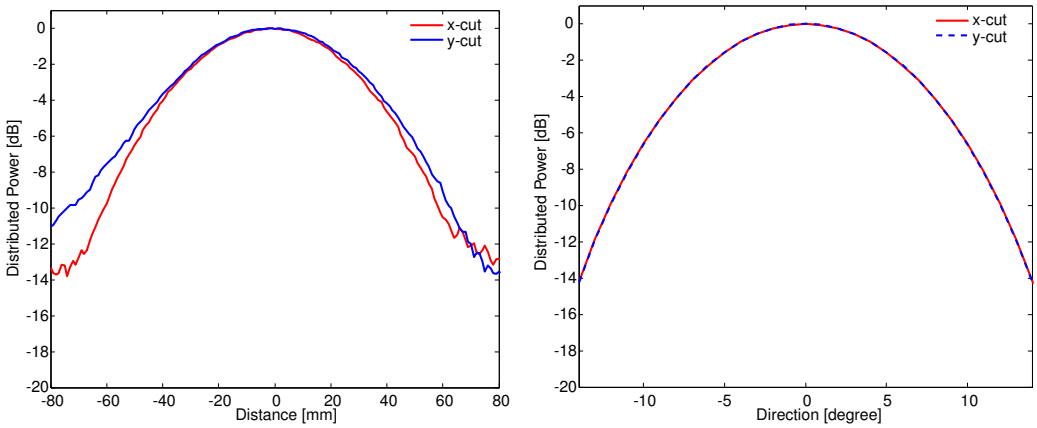

(a) Y and X cuts of the measured farfield of the ALMA Band 5 prototype horn averaged over 10 scans

(b) Simulated farfield results of the ALMA Band 5 Horn design using CST microwave studio.

Figure 3.24.: ALMA Band 5 horn measured and simulated farfields

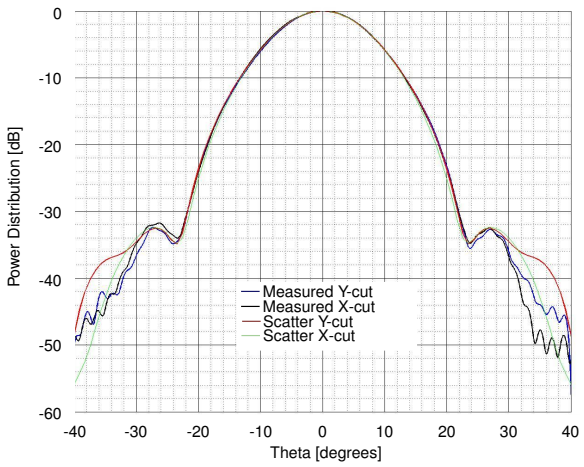

Figure 3.25.: x- and y-cuts of the farfield of the ALMA Band 5 horn in comparison to the Scatter results

to avoid any surface currents and thus should result in a symmetrical beam. As is evident from the measurement results this was not the case with this prototype horn.

Two possible sources for the asymmetry were considered, 1) flaws in the horns construction and 2) the circular to square transition that occurs in moving from the detector heads rectangular waveguide to the circular structure of the horn antenna.

Simulations of the hexagonal transition phase were conducted to assess its impact on the farfield. These results can be seen in figure 3.24(b) and indicate perfect performance of the hexagonal transition with no asymmetric consequences in the farfield. As such, it was concluded that the prototype suffered either imperfect corrugation milling or was otherwise damaged while the three separate pieces were pressed together. This was later confirmed on dissection of the horn.

A more diligent effort to machine a second prototype horn at the workshop in GARD revealed it to exceed the limitations of the tools available. As such, considering the agreement of all simulations, the final horn was ordered in from a British company using electroforming techniques. The results of the measurements of this horn and the scatter simulations are shown in figure 3.25 and can be seen to be in perfect agreement.

3.4.4. Front-End Standing Waves

As outlined in chapter 1 the ALMA band 5 feed horn is part of the front-end optics, which also includes two mirrors and IR filters after the signal passes from the secondary mirror of the telescope. When a beam is partially reflected along its path of propagation standing waves can occur as the reflected wave interferes with the forward travelling wave. This situation is depicted in figure 3.26 and may be considered mathematically by assuming the incident sinusoidal wave to suffer a phase jump at the reflecting surface, and for a first order approximation one may assume no loss of energy in the medium. Expressions 3.68 and 3.69 describe such incident and reflected waves and the resulting total E-field, where $re^{i\phi}$ represents the complex reflection coefficient. The amplitude of the field at any point is found by taking the absolute value, which as can be seen in equation 3.70 results in a cosine variation along the axis of propagation.

$$\begin{aligned} E_i &= E_0 e^{i(\omega t - kx)} \\ E_r &= r e^{i\phi} E_0 e^{i(\omega t + kx)} \end{aligned} \tag{3.68}$$

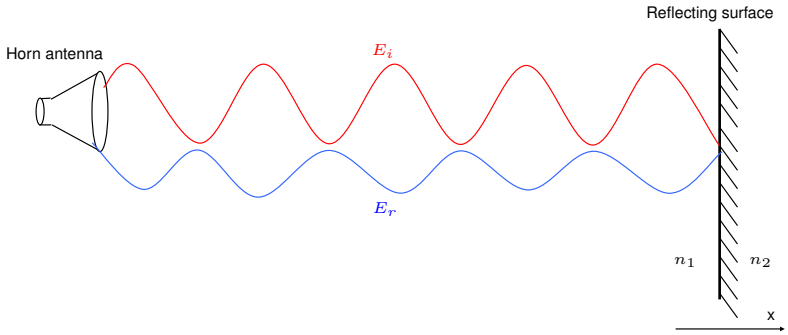

Figure 3.26.: Typical standing wave scenario [29]

$$E_{\text{total}} = E_0 \left(e^{-ikx} + re^{i\phi} e^{+ikx} \right) e^{i\omega t} \tag{3.69}$$

$$|E_{\text{total}}| = E_0 \sqrt{(1+r^2) + 2r(\cos(2kx+\phi))} e^{i\omega t} \tag{3.70}$$

A combination of Scatter and Gaussian Beam Mode techniques were used to analyse this scenario in the ALMA band 5 system for the worst case, that is where the beam is incident normally on the reflecting surface. In practise a tilted surface may be used to reduce multiple reflections. To accomplish this the waveguide modes of the Scatter output must first be transformed to free space modes, which then allow for the field to be propagated through a multi-element optical system using the free space scattering technique of Gaussian Beam Modes (see chapter 2). For free space coupling to a scalar corrugated conical horn the Associated Laguerre Gaussian mode set prove most appropriate, due to their cylindrical symmetry.

$$\begin{aligned}
\begin{pmatrix} \Psi_n^{\alpha,\cos}(r,\phi) \\ \Psi_n^{\alpha,\sin}(r,\phi) \end{pmatrix} &= \Psi(r,\phi)_n^{\alpha} \exp\left(-ikz + i(2n+\alpha+1)\arctan\left(\frac{\pi W^2}{\lambda R}\right)\right) \begin{pmatrix} \cos(\alpha\phi) \\ \sin(\alpha\phi) \end{pmatrix} \\
&= \sqrt{\frac{2(2-\delta_{0n})n!}{\pi W^2 (n+\alpha)!}} \left(2\frac{r^2}{W^2}\right)^{\alpha/2} L_n^{\alpha}\left(2\frac{r^2}{W^2}\right) \exp\left(\frac{-r^2}{W^2}\right) \\
&\quad \exp\left(-ikz + i(2n+\alpha+1)\arctan\left(\frac{\pi W^2}{\lambda R}\right)\right) \\
&\quad \exp\left(-ik\left[\frac{r^2}{2R}\right]\right) \begin{pmatrix} \cos(\alpha\phi) \\ \sin(\alpha\phi) \end{pmatrix}
\end{aligned} \tag{3.71}$$

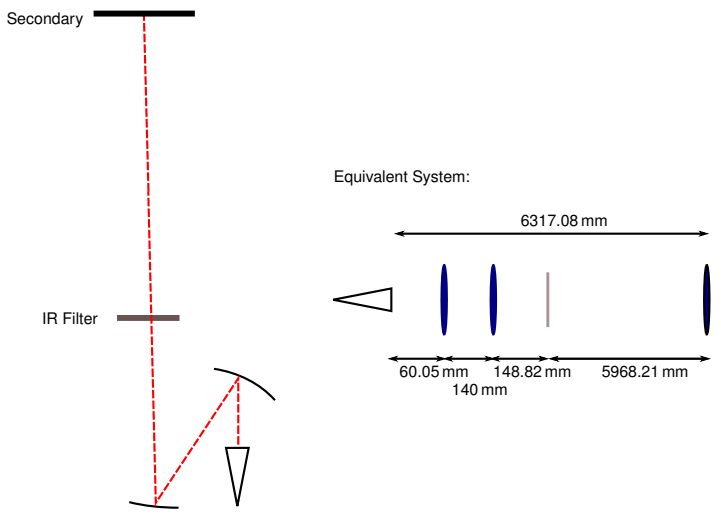

Figure 3.27.: A not to scale diagram of the front end optics of the ALMA Band 5 system and (right) the equivalent system constructed for the purpose of a standing wave analysis

The general form of these modes for waves travelling in the positive z direction have the form outlined in equation 3.71, where α is an integer representing the degree of the Laguerre polynomial, W and R the waist and radius of curvature of the beam and the term $\arctan\left(\pi W^2/\lambda R\right)$ is the phase slippage for the fundamental mode between the waist and plane of interest.

The waveguide modes of a single moded conical horn couple only to free space Associated Laguerre Gaussian modes of degree 0 and 2. This is due to cylindrically symmetric components and their dependence on $\cos(2\phi)$ and $\sin(2\phi)$. As such, in moving to free space an overlap integral must only be performed between the waveguide modes of the Scatter aperture field and the free space modes of order 0 and 2. For the work of this thesis this resulted in a free space scattering matrix of the form depicted in equation 3.72. A complete mathematical description of this free space transformation may be seen in the Ph.D. Thesis of Dr. Neil Trappe [29].

$$\mathbf{S} = \begin{pmatrix} \mathrm{T}^0_{\mathrm{TE}} & \mathrm{T}^0_{\mathrm{TM}} \\ \mathrm{T}^2_{\mathrm{TE}} & \mathrm{T}^2_{\mathrm{TM}} \end{pmatrix} \tag{3.72}$$

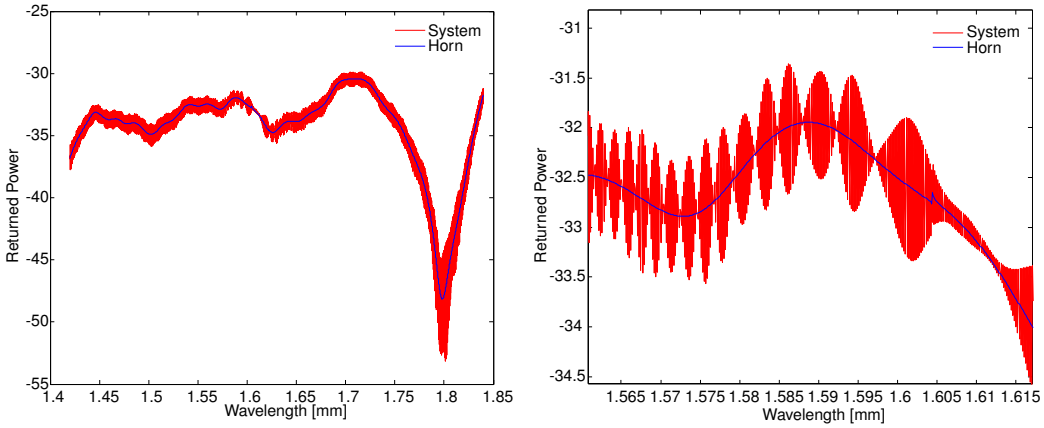

(a) Entire band (b) Narrow band

Figure 3.28.: Standing wave analysis of the ALMA Band 5 front end optics mirrors

To examine the ALMA band 5 setup an equivalent system is constructed in which the mirrors are represented by lenses of identical focal lengths (32.759 mm and 67.192 mm), as depicted in figure 3.27. The system was then first considered in the absence of any IR filter. To accomplish this the ALMA band 5 feed horn was simulated using Scatter and the resulting aperture field, described in terms waveguide modes, transformed to a free space basis set, as previously described. Standard ABCD matrices were used to propagate from the horn, through the first two mirrors and out to the secondary (see section 2.4). The results of this analysis can be seen in figure 3.28 and show very high frequency standing waves oscillating about the S_{11} of the horn itself. Considering the distance of over 6 m between the horn aperture and the secondary mirror such high frequency oscillation are as expected and of no significant practical importance to the system.

For the analysis of the ALMA Band 5 IR filters we assume a refractive index of 1.52 and thickness of 0.64 mm. When considering the propagation of beams within such a medium of different refractive index the reduced complex beam parameter, $\hat{q}$, is considered, which is analogous to the reduced radius of curvature $\hat{R}$ used in geometrical optics. This is outlined in expression 3.73, where $R(z)$ represents the free space radius of curvature, $W(z)$ the real beam radius and λ_0 the free space wavelength, which becomes λ_0/n in the dielectric. Furthermore, the Fresnel reflection and transmission coefficients have also to be considered. These are outlined in expression 3.74.

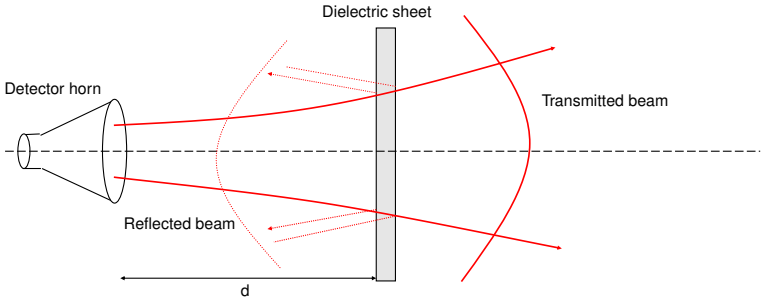

Figure 3.29.: Depiction of a gaussian beam incident on a dielectric sheet from a horn antenna [29].

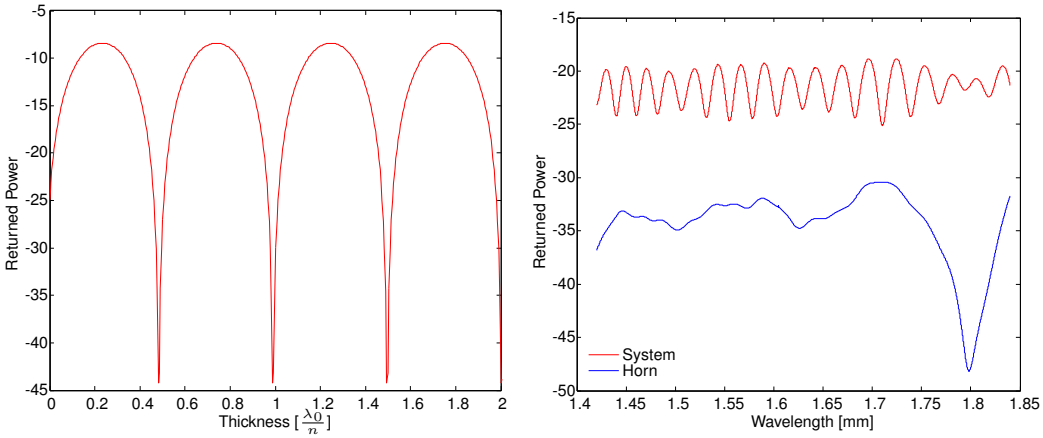

(a) Variation in the levels of returned power for a sheet of dielectric of varying thickness

(b) Standing waves occuring in the ALMA band 5 system including an IR filter

Figure 3.30.: Effect of introducing an IR filter to the ALMA standing wave analysis

$$\begin{aligned} \hat{R} &= \frac{R}{n} \\ \frac{1}{\hat{q}} &= \frac{n}{q} = \frac{1}{\hat{R}} - j\frac{\lambda_0}{\pi W(z)^2} \end{aligned} \tag{3.73}$$

$$\begin{aligned} r &= \frac{n_1 - n_2}{n_2 + n_1} \\ t &= \frac{2n_1}{n_2 + n_1} \end{aligned} \tag{3.74}$$

To first test the accuracy of the code the mirrors were removed from the system and the dielectric element placed at the aperture of the horn. The thickness of the dielectric material was then varied from 0λ to 2λ, where $\lambda_0 = 1.5\,mm$ and $n = 1.52$. As can be seen from figure 3.30(a) this behaved exactly as expected, with periodic behaviour

representing points of absolute minimum return for multiples of half wavelengths. This dielectric element was then inserted to the ALMA band 5 analysis with a fixed thickness of 0.64 mm. As can be seen in figure 3.30, this results in a significant increase in the level of reflected power and a regular standing wave pattern. Considering however the resulting reflection coefficient (amplitude) alone of $\approx 20\%$ for a refractive index of 1.52 the increased level of reflected power is again as expected. It is the suggestion of this work that the introduction of a tilt in the IR filter setup may help reduce these standing wave effects.

4. Cavities

4.1. Introduction

The following chapter examines the behaviour of detector cavities. These are, ideally, sealed hollow regions into which a bolometer type (absorbing) detector can be placed. They essentially seek to trap all incident energy, not absorbed on the first pass, in the region of the detector and thus maximise absorption. The work outlined examines the behaviour of such cavity structures in the high frequency regime and investigates the divergence in behaviour from that expected for traditional low frequency optical systems, such as predicted by ray tracing techniques. The results of the general analysis are then used in considering the optimum design of the SAFARI detector cavities, which will utilise TES detectors with sheet absorbers.

The contribution of the author included developing, modifying and verifying both the cylindrical and pyramidal Scatter codes to be capable of modelling a sealed hollow cavity, as well as establishing how the same structure can be considered using CST Microwave Studio. Furthermore, a sealed Al cavity was designed by the author and constructed in the departmental workshop. This allowed for the simulation results to be verified against measurements as well as identifying specific physical effects inside the cavity. The author also verified the implementation of an ohmic sheet absorber model in cylindrical Scatter and further developed, implemented and verified such a model in pyramidal Scatter. A second adaptable cavity kit was designed and manufactured for experimental verification.

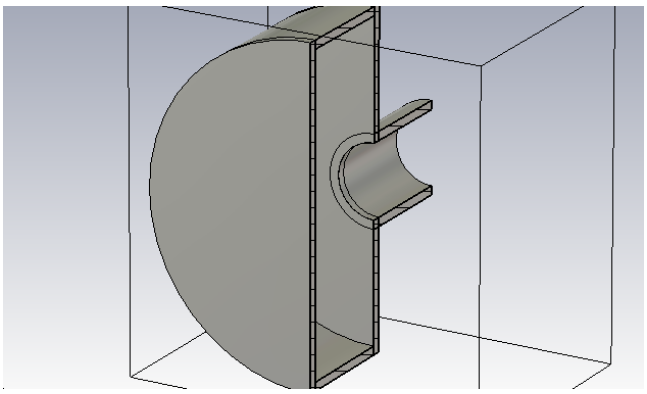

Figure 4.1.: CAD model of a simple empty sealed cavity

The author also explored various methods of including a gap in the wall of a cavity in both Scatter and CST Microwave studio.

Finally using the simulation techniques and tools developed, an in depth analysis of various cavity geometrical designs was conducted. This work was performed independently by the author and expanded to the specific case of the SAFARI system.

4.2. Simple Empty Cavities

The first type cavity to be considered here is a simple sealed cylindrical waveguide composed of a PEC material and fed by a cylindrical waveguide of sufficiently smaller radius so as only the TE_{11} is supported, as depicted in figure 4.1. Such a structure can be easily modeled using Finite Element methods, although these will be limited by the electrical size of the cavity in question, or through the use of mode matching amongst many other approaches.

The Scatter code, described in section 3.2.3, can be used to model a cavity by including a final segment with an opening of essentially zero compared to the wavelength. Alternatively, appropriate S matrices can be constructed and cascaded with the open ended waveguide by creating transmission matrices (S_{21} and S_{22}) of zeros and the reflection matrices of unity power.

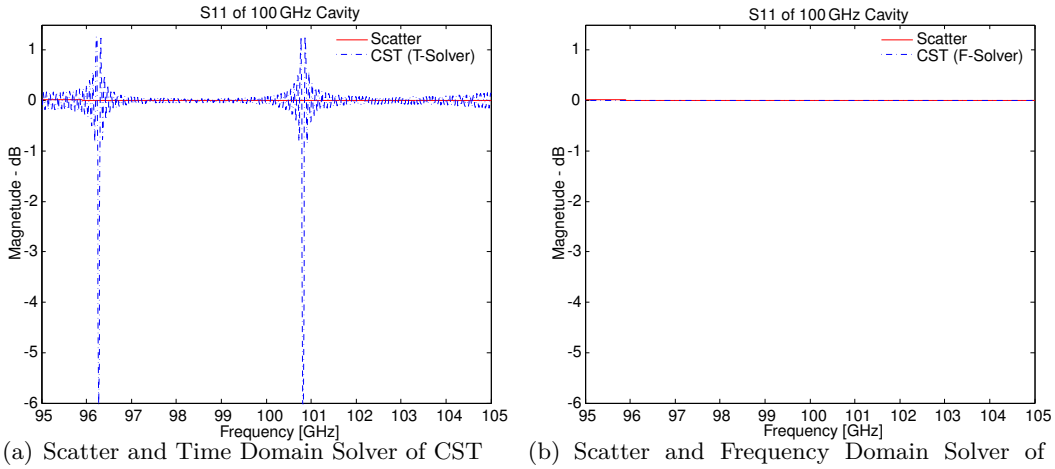

(a) Scatter and Time Domain Solver of CST

(b) Scatter and Frequency Domain Solver of CST

Figure 4.2.: S_{11} of a sealed PEC cavity using different simulation techniques

As can be seen from figure 4.2(a) the results from the CST Transient Solver are not in perfect agreement with those of Scatter. The CST results oscillate about a return of 0 dB and suggest that power is somehow coupled between frequencies, whereas the Scatter results predict a constant return of 0 dB. Considering the cavity in question is composed of a PEC and void of optically active or dielectric material it is expected that all the power entered into the cavity would be eventually reflected back out of the cavity, as predicted by Scatter. The CST Transient Solver results are to be understood by considering the time domain aspect of the approach. The oscillatory nature of the S_{11} is the result of the system not having reached a truly steady state with power at some frequencies still being trapped in the cavity. Both the scatter results and this explanation of the Transient Solver results are confirmed by the Frequency Domain Solver of CST, the results of which agree with Scatter (see figure 4.2(b)). See section 2.2 for an overview of the Transient and Frequency domain solvers of CST.

It is thus worth noting that for such resonant structures frequency domain techniques are preferable when possible. However, due to some limitations in the functionality of the Frequency Domain Solver of CST Microwave Studio the Transient Solver will be used at many points throughout the rest of this chapter when considering cavity structures. This may be justified when considering the various systems, which mostly include some lossy

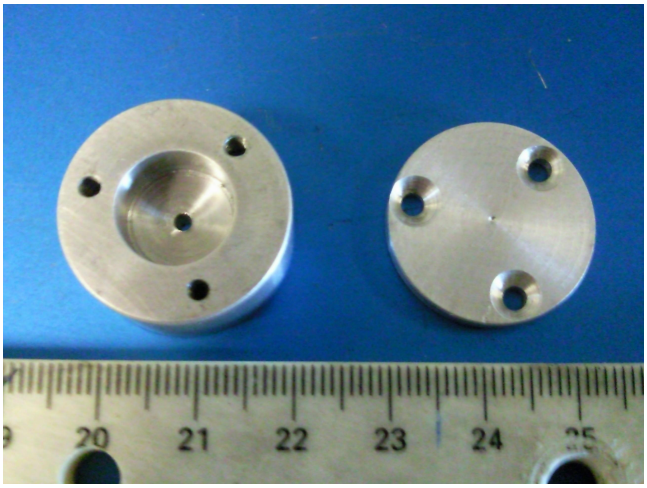

Figure 4.3.: Aluminium Cavity constructed in the departmental workshop. It has an internal radius of 6 mm and an internal depth of 6 mm and is feed by a circular waveguide of internal radius 1 mm and length 5 mm

metallic or absorbing material or a leakage mechanism and are thus not as susceptible to non-steady state resonant artifacts in the time domain.

The previously outlined PEC cavity behaved as expected, that is considering no other exit apertures were present nor any absorbing material a 100% return through the input port was observed. Realistically however, detector cavities will be composed of some lossy material. To investigate the properties of such a structure an Aluminium cavity was constructed in the departmental workshop. Measurements were conducted using the department's VNA (Vector Network Analyser) and compared to simulations carried out in CST Microwave Studio. The results of this analysis may be seen in figure 4.4. The interface to the VNA is achieved via a WR10 waveguide, this is of rectangular geometry with internal dimensions of 2.54 mm×1.27 mm. As such, apart from the transition to rectangular waveguide modes the WR10 guide additionally obstructs the surface area of the circular guide above radial values of 0.635 mm in one plane.

Figure 4.4(a) compares the CST simulations to VNA measurements taken. Before inspecting these results one should appreciate that the fabricated cavity also includes manufacturing errors in terms or smoothness, flatness and exact internal dimensions, as such, minor shifts in resonant features were to be expected. Furthermore, the physical aluminium cav-

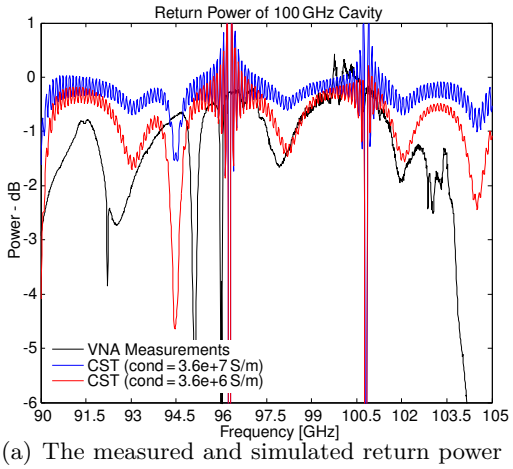

(a) The measured and simulated return power of the Aluminium Cavity. The black plot represents the measurements while the blue and red plots are CST results for different conductivity values.

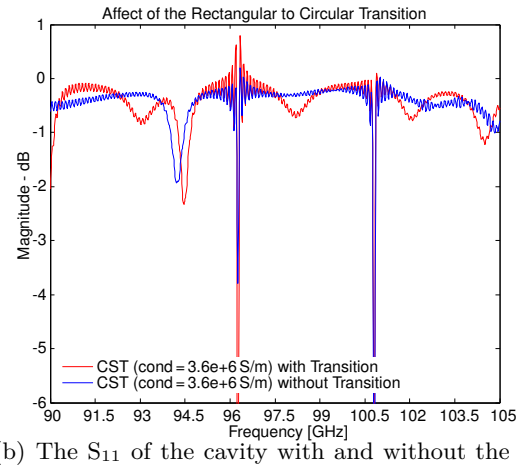

(b) The S_{11} of the cavity with and without the rectangular to circular transition present in the measurements at the junction between the cavity waveguide and the WR10 waveguide interface to the VNA head.

Figure 4.4.: S_{11} as measured and simulated (using CST) of the Al Cavity. Note: Values of the S_{11} exceed 0 dB. This non-physical behaviour is the result of the resonant structure being considered in the time domain, limitations in the frequency domain solver of CST Microwave Studio prevented it from being used.

ity may have been subject to oxidation and other effects not considered in the simulations. Considering that for the PEC case (see figure 4.2(b)) 100% of the power is returned any observed return loss for the Aluminium cavity may be attributed to ohmic losses. To further classify the absorptions present the conductivity of the material was kept as a free variable in the simulations. This allowed for ohmic losses to be better identified. The skin depth of Aluminium was also considered in setting up the simulation, to ensure sufficient wall thicknesses were used. Considering a first approximation for the skin depth (equation 4.19) and taking a value of $\rho = 3.33 \times 10^{-8}\,\Omega m$ for the resistivity of Aluminium and a magnetic permeability of $\mu_{Al} = 1.256 \times 10^{-6}\,Hm^{-1}$, then for 100 GHz the skin depth is found to be $\delta = 0.29\,\mu$m. Considering the high frequencies being employed such small values of skin depth are as expected for conductors. Therefore a wall thickness of 0.5 mm was considered more than sufficient.

$$\delta = \sqrt{\frac{2\rho}{\omega\mu}} \left(= \sqrt{\frac{2\rho}{2\pi\nu\mu_0\mu_R}} \right) \tag{4.1}$$

The black plot of figure 4.4(a) depicts the measurement results obtained using the VNA. The initial simulated results (blue plot) were conducted for the properties of pure Aluminium, loaded from the CST Microwave Studio material library, and demonstrated peak features roughly corresponding to those of the measured data but significantly less pronounced. Decreasing the conductivity by a factor of 10 to $3.6\times10^6\,Sm^{-1}$ (the red plot) dramatically improved the agreement between measured and simulated data. From this one may first conclude that the material used in the construction of the cavity contained impurities and may also have been subject to oxidation, which would have further increased the resistivity. Examining the difference resulting from the reduced conductivity of the simulations the five broader dips can be conclusively attributed to ohmic losses.

At approximately 96 GHz a very sharp resonant dip is observed in the measured data, which corresponds to a very slightly shifted simulated dip. This is also the exact same resonant feature observed by the Transient analysis of the PEC cavity in figure 4.2(a). In the PEC case these features may be attributed to not having yet reached a steady state, however, they do still represent eigenfrequencies of the geometrical structure. As such, it is to be expected that any lossy material, such as Aluminium, present in the cavity would absorb at these frequencies. The absence of the second dip at approximately 100.5 GHz in the measured data is attributed to imperfections in the constructed cavity.

Figure 4.4(b) examines the influence of the rectangular to circular waveguide transition present in the measurements when mounting the cavity to the VNA head via a WR10 waveguide. The absence of two absorption dips at ≈ 93 and 98 GHz in the case without the transition strongly suggests that these two specific losses are the result of this transition. Further supporting this conclusion figure 4.5(a) displays a significant amount of power in the vertical plane of the waveguide at 98 GHz, which is also the plane in which the WR10 waveguide would truncate the circular guide beyond $r = 0.635$ mm. Moving to a frequency at which no transition related absorptions are suggested by figure 4.4(b), 100 GHz, one observes in figure 4.5(b) that the field is more homogenously distributed over the guide area.

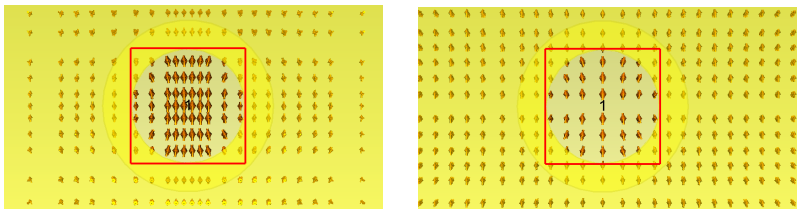

(a) E-field distribution at 98 GHz (b) E-field distribution at 100 GHz

Figure 4.5.: E-field distribution inside the Aluminium cavity at 98 GHz and 100 GHz

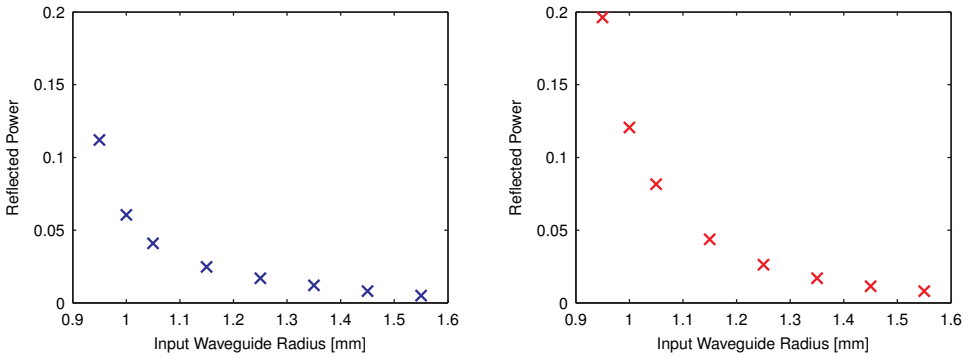

(a) The returned power of the TE_{11} mode integrated across the band of a waveguide of radius r feeding into an open ended waveguide of radius 5.25 mm

(b) Reflected power calculated using the reflection coefficient for the TE_{11} mode determined by the impedance mismatch occuring in entering a waveguide of radius 5.25 mm from various input waveguide radii

Figure 4.6.: The affects of varying the radius of the input waveguide to a cavity on the TE_{11} mode for a frequency range of 95 - 105 GHz.

Another point of interest lies in the relationship between the waveguide feeding the cavity and the dimensions of the cavity itself. A series of simulations were conducted to explore this by taking waveguides of varying radii feeding into a waveguide of significantly larger radius (as is often the case when a cavity is used). The large variation in geometries can lead to reflections caused by the impedance mismatch on entering the larger section. In the scenario outlined most of the power successfully coupled into the second waveguide should be lost to free space and thus the S_{11} of such a setup would directly correspond to power reflected at the junction between waveguides. Figure 4.6(a) shows the reflected power integrated across the band of a waveguide of radius r feeding into an open ended waveguide of radius 5.25 mm, where r ranges from 0.95 mm to 1.55 mm. Theoretically these results follow the expected trend with the returned power of the TE_{11} mode decreasing

for increasing input waveguide radius. To appreciate this one should consider that the waveguide impedance of a specific TE mode is given by equation 4.2, where Z_0 represents the impedance of free space, f_c the cut-off frequency of the mode and f the free space frequency. At the junction of two waveguides of different radius an impedance mismatch may result in an effective reflection coefficient, this is given by equation 4.3. The resulting reflected power predicted by this theoretical reflection coefficient is plotted in figure 4.6(b) and depicts a trend agreeing with the simulated data of figure 4.6(a), albeit not exactly agreeing in the level of reflected power. This discrepancy between the ideal theoretical case and the simulated results is not unexpected as the simulations consider also currents and higher order modes not accommodated for in the calculation of the reflection coefficients.

$$Z = \frac{Z_0}{\sqrt{1 - \left(\frac{f_c}{f}\right)}} \tag{4.2}$$

$$\Gamma_{12} = \frac{Z_2 - Z_1}{Z2 + Z_1} \tag{4.3}$$

4.3. Including an Absorber

4.3.1. Theory

Cavities are often used to house detectors and as such it is important to be capable of including some form of absorber in the cavity models. One common approach to this is to model an absorber as an infinitely thin resistive sheet. This approach is available in the Transient and Frequency domain Solver of CST Microwave Studio (see section 2.2) and was also developed for use in Scatter.

The mode matching approach of Scatter outlined in the previous chapter assumes a two port perfectly electric conducting waveguide with the total power distributed over both ports being conserved. It is interesting to consider the situation of an absorbing material being placed inside such a waveguide. To accurately model a block of such a material,

only partially filling the guide, it would be necessary to define a new basis set of modes inside of the absorbing material and a set of coaxial modes in the surrounding waveguide section. Solving the boundary conditions at the interface between coaxial and absorber modes would be an involved process and would have to account also for differing phase velocities of the supported modes. As such, a simplification is employed in which a thin two dimensional resistive sheet is instead considered. The boundary conditions at such a junction require that the electric field remains continuous across the sheet while the magnetic field jumps by the current density and as the outer coaxial modes now exist over a null space the assumption is made that they need not be considered.

$$\mathbf{E}_L = \mathbf{E}_R \tag{4.4}$$

$$\mathbf{H}_L = \mathbf{H}_R - \mathbf{K} \times \widehat{k} \tag{4.5}$$

$$\mathbf{K} = \frac{\mathbf{E}_L}{R_s} = \frac{\mathbf{E}_R}{R_s} \tag{4.6}$$

In the above expressions, subscripts L and R represent the left and right side of the junction, respectively, E the electric field, H the magnetic field and R_s the impedance of the resistive sheet in ohms per square. Note: Ohms per square is the unit of the surface resistivity across any given square area of a material; it is the measurement of the opposition to the movement of electrons across an area of a material's surface normalised to a unit square. R_s must also be made a function of r, $R_s(r)$, so as $R_s(r) = \infty$ outside the absorber and $R_s(r) = R_s$ inside the absorber.

The electric and magnetic fields on the left and right sides of the junction are given by equations 4.7 to 4.10, where A_n and B_n are the forward and reflected amplitude coefficients of mode n on the left side of the junction and C_n and D_n the amplitude coefficients on

the right side.

$$E_L = \sum \left[A_n \exp\left(-\gamma_n z\right) + B_n \exp\left(-\gamma_n z\right)\right] e_n \tag{4.7}$$

$$H_L = \sum \left[A_n \exp\left(-\gamma_n z\right) - B_n \exp\left(-\gamma_n z\right)\right] h_n \tag{4.8}$$

$$E_R = \sum \left[D_n \exp\left(-\gamma_n z\right) + C_n \exp\left(-\gamma_n z\right)\right] e_n \tag{4.9}$$

$$H_R = \sum \left[D_n \exp\left(-\gamma_n z\right) - C_n \exp\left(-\gamma_n z\right)\right] h_n \tag{4.10}$$

Applying the boundary conditions to the electric and magnetic fields and taking appropriate cross products yields the equations displayed in 4.11. Taking the same number of modes on either side of the junction, i.e. letting $N' = N$, and considering that matrix Q is a diagonal matrix with elements $Q_{ii} = \int \left(e_i \times h_i^*\right) \cdot \widehat{k}\, dS$ then integrating over the area of the guide results in a set of simultaneous equations for the mode coefficients as depicted, in matrix form, in expression 4.12.

$$\begin{aligned} \sum_{n=1}^{N} \left(A_n + B_n\right) e_n \times h_m^* &= \sum_{n=1}^{N'} \left(D_n + C_n\right) e_n \times h_m^* \\ \sum_{n=1}^{N} \left(A_n - B_n\right) e_m^* \times h_n &= \sum_{n=1}^{N'} \left(D_n - C_n\right) e_m^* \times h_n - \frac{1}{R_s(r)} \\ \times \sum_{n=1}^{N} \left(A_n + B_n\right) e_m^* \times \left(e_n \times \hat{k}\right) & \end{aligned} \tag{4.11}$$

$$\begin{aligned} \mathbf{Q} \cdot [\mathbf{A} + \mathbf{B}] &= \mathbf{Q} \cdot [\mathbf{D} + \mathbf{C}] \\ \mathbf{Q}^* \cdot [\mathbf{A} - \mathbf{B}] &= \mathbf{Q}^* \cdot [\mathbf{D} - \mathbf{C}] - R^{-1} \Gamma [\mathbf{A} + \mathbf{B}] \end{aligned} \tag{4.12}$$

Where;

$$\Gamma_{mn} = Z_m P_{mn} \tag{4.13}$$

Z represents the mode impedance and P_{mn} the fractional scattering of power between modes. As the sheet is implemented as being infinitely thin, and as $\left(R_s(r)\right)^{-1} = 0$ $\forall r > r_{absorber}$ and thus vanishes outside of the sheet, the P integral of equation 3.17 is

solved across the area of the resistive sheet only.

$$P_{absorb} = \int_{S_{absorb}} (e_m \cdot e_n)\, dS \tag{4.14}$$

Solving the equations of 4.12 for $\mathbf{B}$ in terms of $\mathbf{A}$ and $\mathbf{C}$ provides expressions for S_{11} and S_{12}. These can be seen in 4.15, with the intermediary steps as follows.

$$\begin{aligned}
&\Rightarrow \mathbf{Q} \cdot \mathbf{D} = \mathbf{Q} \cdot [\mathbf{A} + \mathbf{B} - \mathbf{C}] \\
&\Rightarrow \mathbf{Q}^* \cdot [\mathbf{A} - \mathbf{B}] = \mathbf{Q}^* \cdot [\mathbf{A} + \mathbf{B} - 2\mathbf{C}] - \frac{\Gamma\,[\mathbf{A} + \mathbf{B}]}{R_s} \\
&\Rightarrow \left[-2\mathbf{Q}^* - \frac{\Gamma}{R_s}\right] \cdot \mathbf{B} = \mathbf{Q}^* \cdot [-2\mathbf{C}] - \frac{\Gamma\,[\mathbf{A}]}{R_s} \\
&\Rightarrow \mathbf{B} = \left[2\mathbf{Q}^* - \frac{\Gamma}{R_s}\right]^{-1} \cdot R_s\Gamma \cdot \mathbf{A} + 2\left[2\mathbf{Q}^* - \frac{\Gamma}{R_s}\right]^{-1} \mathbf{Q}^* \cdot \mathbf{C}
\end{aligned}$$

Thus,

$$\begin{aligned}
S_{11} = S_{22} &= \left[\mathbf{Q}^* + \frac{\mathbf{Z} \cdot \mathbf{P}}{2R_s}\right]^{-1} \cdot \frac{\mathbf{Z} \cdot \mathbf{P}}{2R_s} \\
S_{12} = S_{21} &= \left[\mathbf{Q}^* + \frac{\mathbf{Z} \cdot \mathbf{P}}{2R_s}\right]^{-1} \mathbf{Q}^*
\end{aligned} \tag{4.15}$$

To avoid undefined expressions and improve computational performance this integral was solved several times under varying assumptions so as to cover all mutually exclusive cases. In all instances the waveguide dimensions at either side of the absorber are set equal, so $a = c$ and $b = d$. To avoid the derivation of any undefined expressions in the pyramidal case separate integrals are evaluated for the cases of $m = M$, $n = N$, and where the mode forms allow m, n, M and/or $N = 0$. In the cylindrical case the overlap integral is only considered for modes of the same azimuthal order, as only these modes can couple to one another (see section 3.2.3).

Considering the return response of a hollow PEC cavity of unity power, a value for the total amount of absorbed power in the system can then be established, once the previously outlined integrals have been included, as $P_{\text{absorbed}} = |S_{21\text{a}0}|^2 - |S_{11}|^2$, where $S_{21\text{a}0}$ refers

to the initial excitation matrix introducing power to the system. That is the absorbed power is directly equated to the power not returned from the otherwise sealed cavity.

These integrals where both solved and coded for use in the pyramidal Scatter code and the cylindrical Scatter code. Future work may explore including a circular absorber in a rectangular guide and a rectangular absorber in a circular guide. The most simplistic approach to this would involve working with the modes of the guide geometry. Taking as an example a circular absorber being implemented in Pyramidal Scatter would have to re-express the rectangular modes in polar co-ordinates (equation 4.16). This would then allow for the rectangular modes to be integrated over the area of the circular absorber when calculating the power coupled between modes, as in equation 4.17.

$$x = r\cos\theta \quad y = r\sin\theta \tag{4.16}$$

$$P_{absorb} = \int_{r=0}^{r=R}\int_{\theta=0}^{\theta=360^\circ} e_m(r,\theta)\cdot e_n(r,\theta)\, dr d\theta \tag{4.17}$$

4.3.2. Application to a sealed waveguide

Single Moded Waveguides

To initially validate the technique both a simple single moded sealed rectangular and cylindrical waveguide was considered. An ohmic sheet was placed at one quarter of the calculated guide wavelength from the sealed end of the guide and given an impedance value of 377 Ω/Sq. The rectangular waveguide had cross-sectional dimensions of 2.54 mm×1.26 mm and was 10 mm in length and the circular waveguide a radius of 1.26 mm and length of also 10 mm. Both of these waveguides are single moded between 75 GHz and 86 GHz with central guide wavelengths of $\lambda_{rec} = 7.329$ mm and $\lambda_{circ} = 10.487$ mm, calculated using equation 4.18, where λ_c refers to the cut-off wavelength of the mode in question. These situations were considered in both CST Microwave Studio using the ohmic sheet model

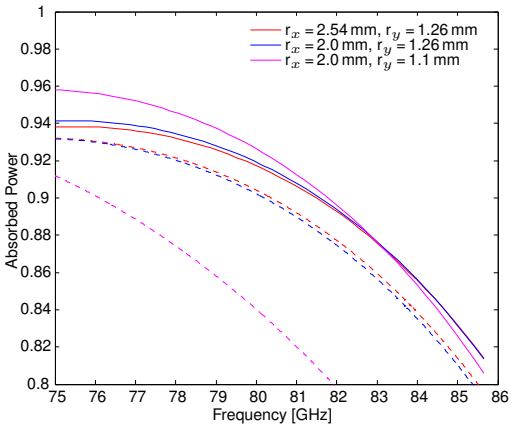

(a) Rectangular Waveguide results.

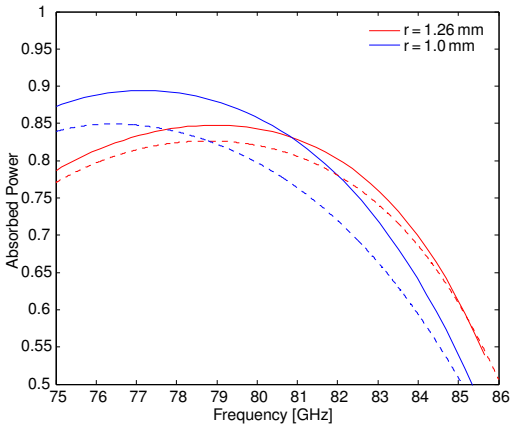

(b) Circular Waveguide results.

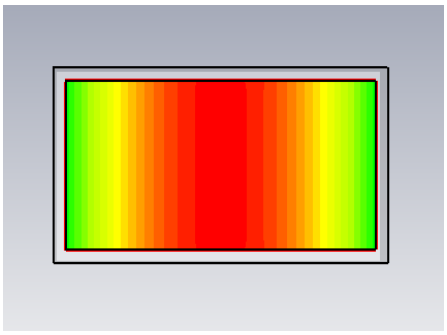

(c) Rectangular mode form

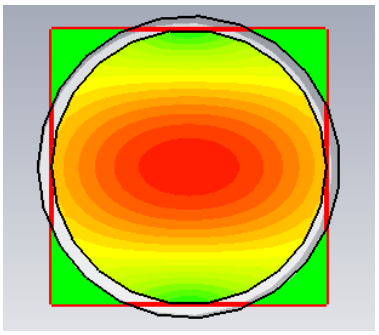

(d) Circular mode form

Figure 4.7.: Results of single moded sealed waveguides containing ohmic sheets as predicted by Scatter and CST Microwave Studio. The solid plots represent the Scatter results and the dashed plots those from CST. Also displayed is the power distribution of the fundamental (and only) mode supported in the rectangular and circular waveguides used for the absorber analysis (recorded for the instance of the absorber fully filling the guides).

(see section 2.2) and the outlined Scatter Absorber code.

$$\lambda_{guide} = \frac{\lambda_{freespace}}{\sqrt{1 - \left(\frac{\lambda_{freespace}}{\lambda_c}\right)}} \tag{4.18}$$

The results of figure 4.7 demonstrate reasonable agreement between CST Microwave Studio and the Scatter Absorber technique for the case of an ohmic sheet fully filling a single moded waveguide. Here one observes a maximum deviation of less than 2% in both the rectangular and circular case. However, when the absorber dimensions are reduced the

Scatter and CST results are observed to diverge in the circular case. Similarly reducing the absorber dimensions in the y-plane of the rectangular case results in significant divergence, however the difference between the CST and Scatter predictions remains constant for a reduction of the absorber dimensions in the x plane. Considering the standard mode forms dominate in a single moded rectangular and circular guide explains this behaviour (see figures 4.7(c) and 4.7(d)). In a circular waveguide the fundamental mode's power distribution falls off radially, however in the rectangular case power is uniformly distributed in the y plane and falls off only in the x plane. This result suggests that the higher levels of absorbed power observed in the Scatter simulations are the result of the field distribution being confined to the area of the resistive sheet. As such, one may conclude it not valid to neglect the propagation of power between modes outside of the area of the resistive sheet and across the junction, as was assumed, for the instance of significant power existing in the surrounding region. It should however at this point be noted that the systems for which this work was developed are centrally excited. See for example section 1.2, where the SAFARI cavity entrance aperture has smaller dimensions to those of the absorber.

The variation in the level of absorbed power across the band seen in figure 4.7 is attributed to the variation in distance between the resistive sheet and the sealed waveguide end in terms of wavelength. Considering interference effects one may expect maximum absorption to occur for a distance between the absorber and the sealed waveguide end of $\Delta d = \frac{1}{4}\lambda_g$, however in a broadband system this can only be accomplished for a single specific wavelength. To further probe this relationship the single moded waveguides were again considered at a single frequency of 80 GHz. The sealed end of the waveguide was then extended from a minimum distance of 0.1 mm from the absorber to a maximum of 5 mm and the same parameter sweep examined in both Scatter and CST. The results of this analysis (figure 4.8) show excellent agreement between the Scatter and CST results. The placement of the absorber with respect to the sealed guide end is observed to be of critical importance with variations in the levels of absorbed power ranging from below 10% to values in excess of 90%. One may also note that the peak values do not correspond to one quarter of the intrinsic guide wavelength, as was initially assumed would be the case,

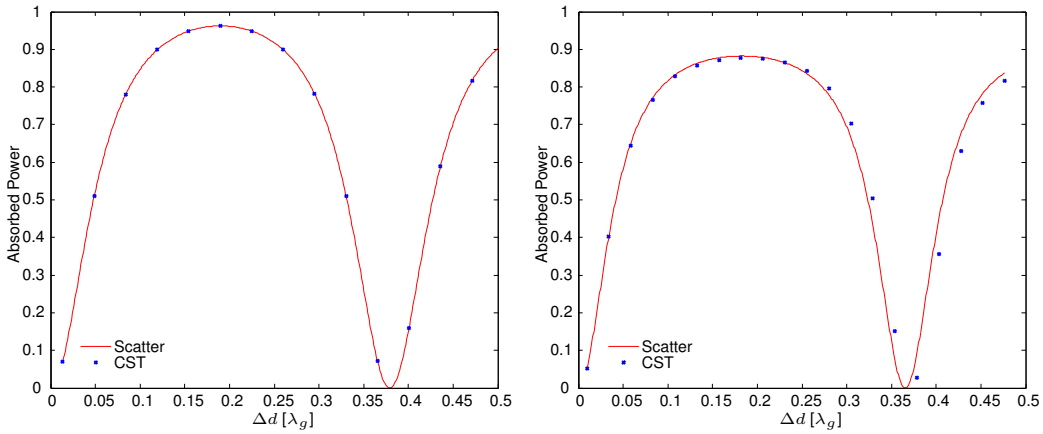

(a) Rectangular Waveguide (b) Circular Waveguide

Figure 4.8.: Absorbed power at 80 GHz for varying values of Δd in the single moded rectangular and circular waveguides with resistive sheets fully filling the guide. Simulations were conducted using Scatter and CST Microwave Studio.

but rather occur at displacement values of $0.191\,\lambda_g$ and $0.184\,\lambda_g$ for the rectangular and circular case, respectively.

Examination of the Scatter S_{11} matrix revealed that in the absence of the absorber the single moded guides behave as expected, with all significant power contained in the fundamental mode. Once however the absorber is introduced significant power is coupled along the main diagonal to higher order modes. As such, it is concluded that the presence of the absorber itself induces the excitation of a different basis set of modes and thus alters the effective guide wavelength of interest.

One further variable considered is the impedance value of the resistive sheet element. This was again considered for the single moded waveguides previously outlined at a frequency of 80 GHz and for Δd values corresponding to the points of maximum absorption observed in figure 4.8, that is $\Delta d_{rec} = 1.38\,\text{mm}$ and $\Delta d_{circ} = 1.95\,\text{mm}$. The results of both the CST Microwave Studio and Scatter simulations of this analysis are displayed in figure 4.9 and can be seen to show excellent agreement between both techniques for the case of the absorber fully filling the guide. Reducing the absorber dimensions, radially in the cylindrical waveguide and in the x plane in the rectangular guide, results in a minor divergence of the CST and Scatter results compared to the full sized absorber case. Reducing

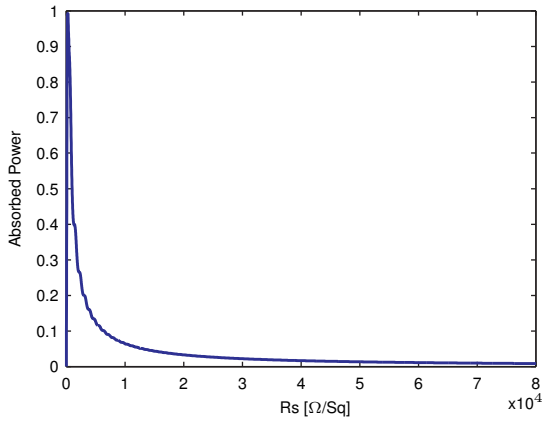

(a) The absorbed power predicted by the cylindrical Scatter absorber code for a 10 mm long sealed cylindrical waveguide of radius 1.26 mm containing an absorber placed 1.95 mm from the backend of the guide and excited at a frequency of 80 GHz for very large impedance values

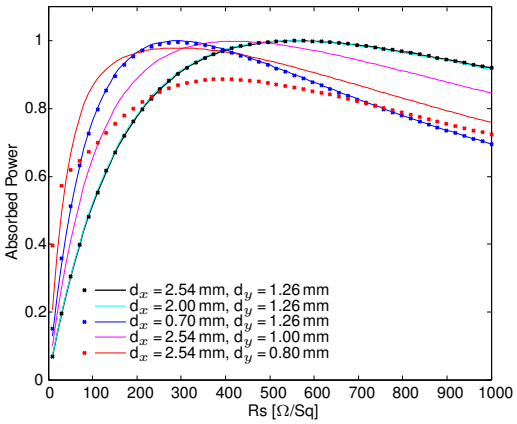

(b) The absorbed power predicted by the pyramidal Scatter absorber code and CST Microwave Studio for the 10 mm long 2.54 mm × 1.26 mm sealed single moded waveguide containing an absorber placed 1.38 mm from the backend of the guide (point of maximum absorption of figure 4.8(a)) and excited at a frequency of 80 GHz

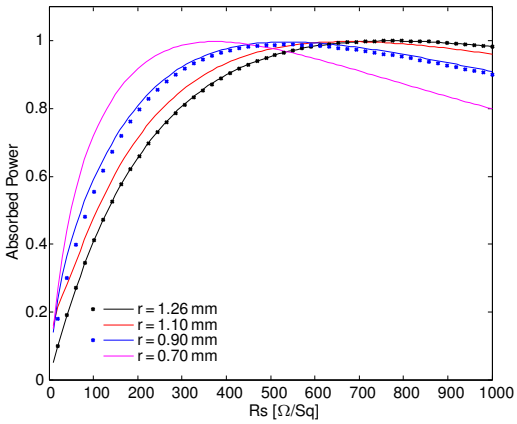

(c) The absorbed power predicted by the cylindrical Scatter absorber code and CST Microwave Studio for a 10 mm long sealed cylindrical waveguide of radius 1.26 mm containing an absorber placed 1.95 mm from the backend of the guide (point of maximum absorption of figure 4.8(b)) and excited at a frequency of 80 GHz

Figure 4.9.: Results of the Scatter absorber code (solid line plots) and CST Microwave Studio (datapoints depicted by ×) examining the affect of the absorber impedance value; Rs, and the absorber dimensions on the total level of absorbed power.

the absorber dimensions however in the y plane of the rectangular case results in significant divergences between the Scatter and CST results (see the red plots of figure 4.9(b)), which is consistent with the results of figure 4.7 and again demonstrates the Scatter ab-

sorber approximations to break down for the case of significant power existing outside the perimeter of the absorber. Figure 4.9(a) outlines asymptotic behaviour of the absorber for extreme impedance values, which is as expected considering the inverse dependence on the impedance R_s, see equation 4.15.

Considering the results of figure 4.9 the dependance on the impedance is as expected, with the absorbed power rapidly rising from null to some maximum value for an initial impedance of $0\,\Omega/Sq$, which corresponds to infinite conductivity and total reflection, after which point the absorbed power begins to decline. However, a curious feature of the results is seen in the implication that at certain low impedance values an absorber of smaller dimensions outperforms its larger counterpart. To better understand this behaviour the CST model was used to examine the behaviour of the electric field for various absorber impedance values and filling factors.

Figure 4.10 displays the E-field inside the waveguide. For the case of a very low impedance value ($\mathrm{Z} = 50\,\Omega/\mathrm{Sq}$), and when the absorber fully fills the guide, one observes in figure 4.10(a) that the ohmic sheet behaves as a conductor, with little power being transmitted through the sheet and significant reflections taking place. Decreasing the physical dimensions of the absorber to 0.7 times the guide dimensions but keeping the impedance constant (as in figures 4.10(b) and 4.10(c)) now allows power to propagate around the edges of the sheet, where a cavity like state then exists between the sheet and the sealed waveguide end, thus augmenting the absorbed power in general. It is worth noting in this case that again the form of the fundamental rectangular mode (figure 4.7(c)) particularly exploits this arrangement. Should the absorber again be set to fully fill the guide, but the impedance increased to a value of $500\,\Omega/\mathrm{Sq}$ (as in figure 4.10(d)), one observes that the field now permeates the ohmic sheet and thus optimal absorption is achieved for the maximum sheet dimensions.

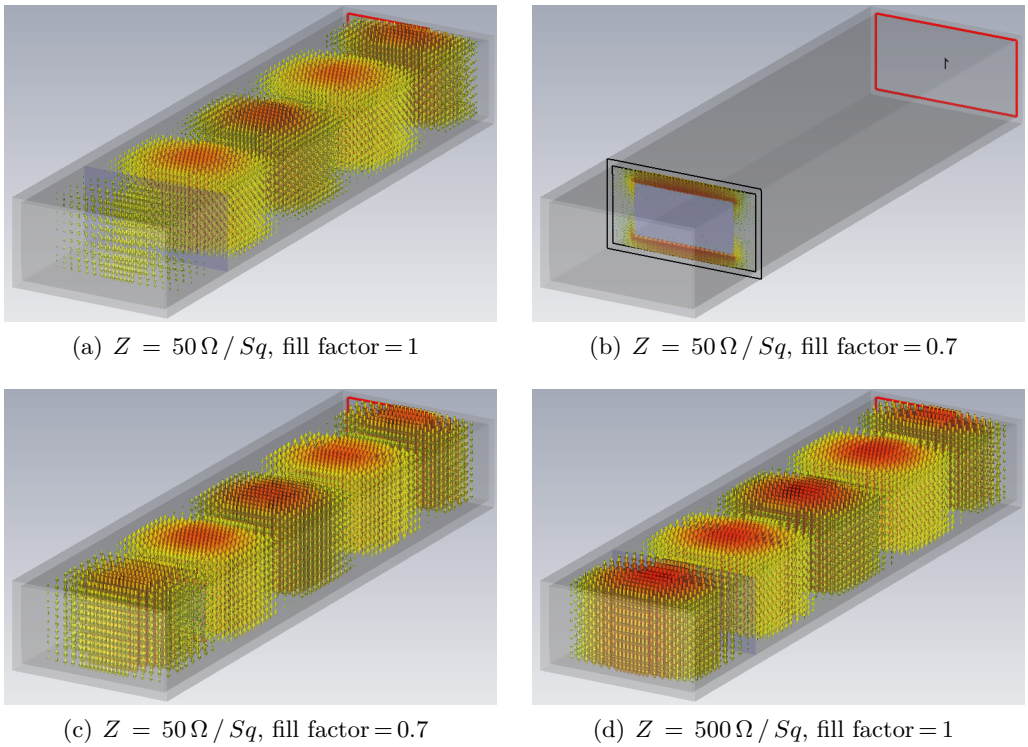

(a) $Z = 50\,\Omega\,/\,Sq$, fill factor = 1

(b) $Z = 50\,\Omega\,/\,Sq$, fill factor = 0.7

(c) $Z = 50\,\Omega\,/\,Sq$, fill factor = 0.7

(d) $Z = 500\,\Omega\,/\,Sq$, fill factor = 1

Figure 4.10.: The electric field inside the single moded rectangular waveguide containing an ohmic sheet. The impedance of the sheet is considered at 50 and 500 Ω/Sq and for a fill factor of 1 and 0.7. Sub-figures (a), (c) and (d) display the field along the entire length of the waveguide. Sub-figure (b) is of the exact same scenario as that of (c), however, here aa 2 dimensional cut of the field at the plane of the absorber is displayed.

Multimoded Moded Waveguides

Having validated the Scatter approach against CST Microwave Studio for the single moded case in the previous section, this section conducts a similar Scatter analysis for a multimoded rectangular waveguide. A 300 µm×300 µm waveguide 2.4 mm in length was considered at a free space wavelength of 210 µm (≈ 1.4 THz). At the considered frequency this guide completely supports the propagation of a total of 10 separate modes, these modes along with their respective quarter guide wavelengths are listed in table 4.1. The placement of an absorber in such a sealed waveguide is of critical importance and the initial assumption of maximum absorption occurring for an absorber distance to the sealed

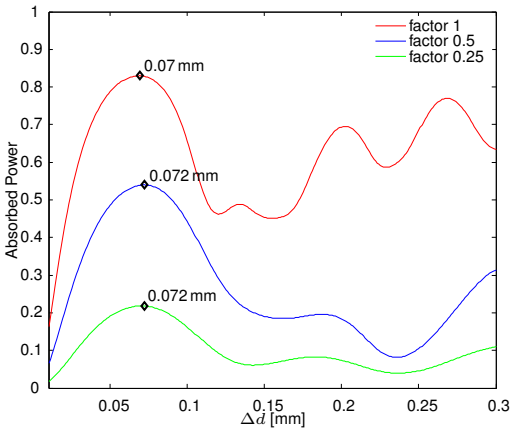

(a) The total absorbed power calculated for an absorber (scaled to the guides dimension by the parameter "factor") a distance Δd from the sealed end of the multi-moded waveguide

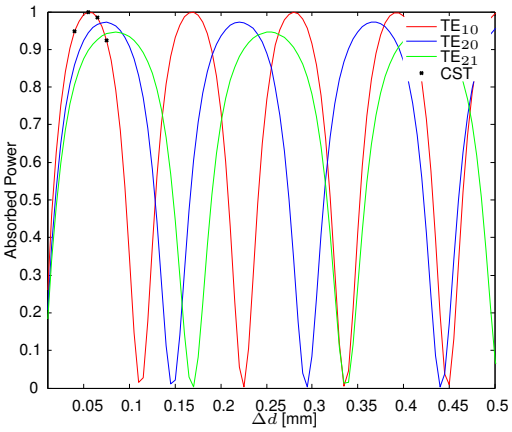

(b) The total absorbed power as a function of Δd of the individual waveguide modes for an absorber totally filling the guide. Note: Maximum absorption is recorded at $\Delta d(\mathrm{TE}_{10}) = 0.056\,\mathrm{mm}$, $\Delta d(\mathrm{TE}_{20}) = 0.074\,\mathrm{mm}$ and $\Delta d(\mathrm{TE}_{21}) = 0.084\,\mathrm{mm}$

Figure 4.11.: Absorbed power of an absorber with an impedance value of $377\,\Omega/\mathrm{Sq}$ placed inside a waveguide of dimensions $300\,\mu\mathrm{m}\times300\,\mu\mathrm{m}$ and excited at a wavelength of $210\,\mu\mathrm{m}$.

waveguide end of $\frac{1}{4}\lambda_g$ was found not to hold in the single moded case (as seen in figure 4.8). This behaviour is further examined for a multimoded guide.

A series of simulations were carried out in which the absorber distance to the sealed waveguide end (Δd) was varied in steps of 0.001 mm and the total absorbed power recorded. The results of these simulations for three different absorber sizes can be seen in figure 4.11(a) and indicate that maximum absorption occurs for a value of $\Delta d \approx 0.07\,\mathrm{mm}$, or $0.3\lambda_f$.

An initial assumption may consider the distance of maximum absorption of a multimoded guide to correspond to one quarter of the averaged guide wavelength of the modes. However, as this assumption did not hold for the single moded case it was also not expected to prove valid in a multimoded system. The results of this analysis indeed confirm this conclusion, as may be seen in comparing the data of table 4.1 with the simulated results, where one quarter of the averaged guide wavelengths is calculated as $\frac{1}{4}\overline{\lambda_\mathbf{g}} = 0.092\,\mathrm{mm}$, however maximum absorption occurs for a value of $\approx 0.071\,\mathrm{mm}$ or $0.195\,\overline{\lambda_\mathbf{g}}$.

Table 4.1.: The modes supported in the multimoded waveguide considered as well as the guide wavelength of each mode, calculated using equation 4.18 for a free space wavelength of 210 µm. Furthermore, the power contained in each mode, as calculated by Scatter, is provided as well as the average of the guide wavelengths $\overline{\lambda_g}$ and the average of the weighted guide wavelengths $\overline{\Lambda_g}$. The weighting is established as the ratio of power in the mode compared to the total power of the matrix. The standard deviations of the means are also provided.

Mode	$\lambda_\mathbf{g}/4$**[mm]**	**peak [mm]**	**peak** $[\lambda_\mathbf{g}]$	$\mathbf{S}_{11}$ **power [W]**
TE_{10}	0.0651	0.056	0.215	0.7869
TE_{20}	0.0959	0.074	0.193	0.2717
TE_{01}	0.0651	0.056	0.215	0.1137
TE_{11}	0.0739	0.06	0.203	0.0202
TE_{21}	0.1126	0.084	0.187	0.1088
TE_{02}	0.0959	0.074	0.193	0.0393
TE_{12}	0.1126	0.084	0.187	0.1088
TM_{11}	0.0739	0.06	0.203	0.0255
TM_{21}	0.1126	0.084	0.187	0.1280
TM_{12}	0.1126	0.084	0.187	0.1280
	$\frac{1}{4}\overline{\lambda_\mathbf{g}} = 0.092\,\text{mm}$	$\overline{\text{peak}} = 0.0716\,\text{mm}$		$\frac{1}{4}\overline{\mathbf{\Lambda_g}} = 0.0717\,\text{mm}$
	$\sigma_{\lambda_g} = 0.0206\,\text{mm}$	$\overline{\text{peak}} = 0.195\,\overline{\lambda_\mathbf{g}}$		

To further examine these results the Scatter code was modified so as to suppress the excitation of all but a single mode, thus allowing for the absorption of individual higher order modes of a multimoded guide to be examined. This was accomplished by creating a 1×N matrix, **uu**, consisting of only a single non zero element of magnitude 1, where N represents the total number of waveguide modes considered. This vector was then used to scale the initial excitation matrix, **VV**, that establishes the power contained in the individual modes in the initial S matrices, so as to isolate the single mode of interest. The results of this modification were then successfully compared against CST Microwave Studio simulations of individual modes.

The modified Scatter code was used to examine the variation in absorbed power of each of the individual modes in the multimoded waveguide, the results of three of these simulations are displayed in figure 4.11(b) and the value of Δd for which maximum absorption occurred is recorded in table 4.1 for each of the modes, under the variable "peak". One may note that again the maximum value for absorbed power does not correspond to a placing of

$\Delta d = \frac{1}{4}\lambda_g$ for the individual modes. CST frequency domain simulations were conducted at discrete points to confirm the Scatter results and show maximum absorption of the TE_{10} mode to occur for $\Delta d = 0.056\,\text{mm}$ or $0.215\,\lambda_g$ and not $0.25\,\lambda_g$. Furthermore, the averaged displacement of the peak absorption values of the individual modes $\overline{\text{peak}}$ evaluates to $0.0716\,\text{mm}$ or $0.195\,\overline{\lambda_\mathbf{g}}$, which agrees with the point of maximum absorption of the fully excited multimoded guide, the results of which are shown in figure 4.11(a).

In the fully excited case the total power is not equally distributed amongst the modes. As such, a second averaged quarter guide wavelength of the modes was calculated in which the overall contribution of power in each mode was considered in weighting the average. The power contained in each mode was taken from the S_{11} matrix of Scatter and is listed in table 4.1. Weighting the guide wavelength values by the ratio of the modal power to the total power results in a value of $\frac{1}{4}\Lambda_g = 0.0717\,\text{mm}$. This can be seen to be in agreement both with the observed maximum of the fully excited guide ($0.07\,\text{mm}$) and also with the average of the peak absorptions of the individual modes ($0.0716\,\text{mm}$).

This accuracy of this result may be considered to confirm the hypothesis reached in examining the single moded waveguides, that is, that the resistive sheet impacts on the mode forms present resulting in a different effective guide wavelength. As such a weighting of the averaged wavelength would correctly distribute the power to the modes making up the basis set of the induced field. Furthermore, the confirmation of the results by CST microwave studio also supports that this is a physical anomaly to be associated with such an ohmic sheet type material and not an artifact of the Scatter mode matching approach.

Considering again the results of the individual modes of the multimoded waveguide of figure 4.11(b) one further curious feature is observed. That is the progressive drop in the maximum, or peak, absorbed power for higher order modes. One possible explanation for this may lie in the fundamental concept of the mode. That is that the field of a propagating mode can be regarded as a superposition of elementary plane waves resulting from successive reflections off the inner guide surfaces. The guide wavelength is then the distance between equiphase planes of this superposition along the direction of propagation, i.e. the

waveguide axis. As such, it is hypothesised that for higher order modes progressively less power of the coherent plane waves will lie completely in phase at any single plane thus resulting in a very minor drop in the total power observed over the plane. This would explain the minor drop off in the peak absorption observed for the higher order modes.

4.3.3. Measurements

Building on experience of the in house cavity manufacturing process and the measurements conducted on this cavity (see section 4.2), a cavity kit was designed to permit the assembly of multiple cavities of varying internal dimensions and also potentially include a thin metallic or dielectric sheet for the purpose of emulating the absorber of the Scatter and CST simulations. The manufacturing of this kit was then arranged with Farran Technologies, a company based in Cork, Ireland, using brass Ms58 with a natural finish. Preference was given to maximising the fitting of the annular ring components to the holding cylinder at the expense of a gold coating. Considering the results obtained using the Aluminium cavity this was assumed to represent an acceptable trade off. The WR10 interface pieces were made in a single part with the waveguide produced using EDM machining.

The design is outlined in figure 4.12 and consisted of a holding cylinder, two WR10 waveguide interface pieces, a stop, and several annular rings of varying radius and thickness, which fit perfectly inside the holding cylinder. This was designed so as to be versatile allowing for the assembly of cavities of varying length and internal diameter and also to allow for the addition of corrugations. Furthermore, the construction of a cavity through the successive use of annular rings allows for a sheet material to be placed in the cavity. Removing the stop would also allow for a corrugated waveguide to be assembled. Assuming a frequency of 100 GHz the radii of the annular rings were chosen to allow for $\frac{\lambda}{4}$ corrugations.

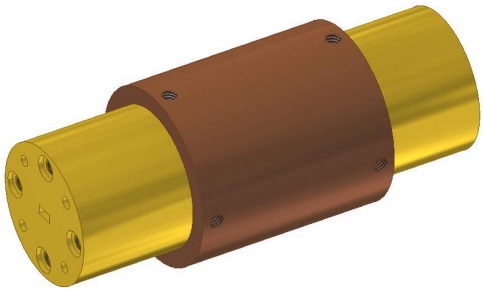

(a) CAD image of the assembled cavity kit design

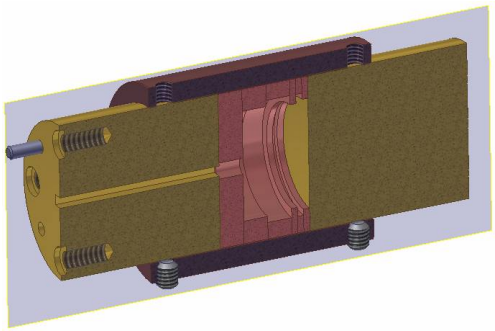

(b) CAD cross-section of proposed cavity kit design

(c) Various components of the Cavity Kit

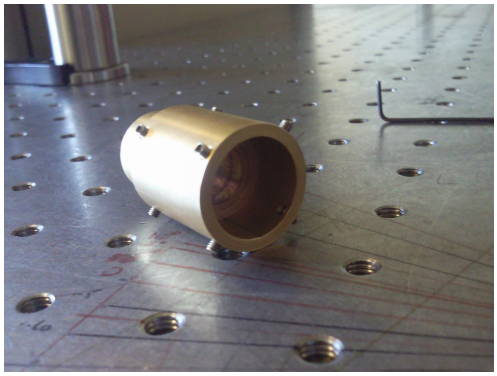

(d) A semi-assembled cavity including a thin film used to emulate an absorber. The WR10 interface piece would still be inserted to seal the cavity and allow for attachment to the VNA scanner.

Figure 4.12.: The Cavity Kit consisting of multiple individual components and an assembled variation.

A series of measurements were conducted using the VNA system of the department. The system was first calibrated in the standard manner (see section 2.5). To ensure repeatability all measurements were performed a minimum of two times and involved the cavity being dismantled and completely reassembled. Figure 4.13(a) displays the results of one such measurement. Two variations of a cavity 6 mm in depth and with a radius of 6.375 mm were assembled. One, referred to as "var 1", consisted of a total of 5 annular rings arranged 2×0.75 mm, 1×3 mm and 2×0.75 mm, where the dimensions represent the thickness of the elements, and all of radius 6.375 mm. The second variation, "var 2", consisted of 2×3 mm segments also 6.375 mm in radius. The results demonstrate almost perfect repeatability for any single variation, however the specific annular ring makeup is seen to significantly

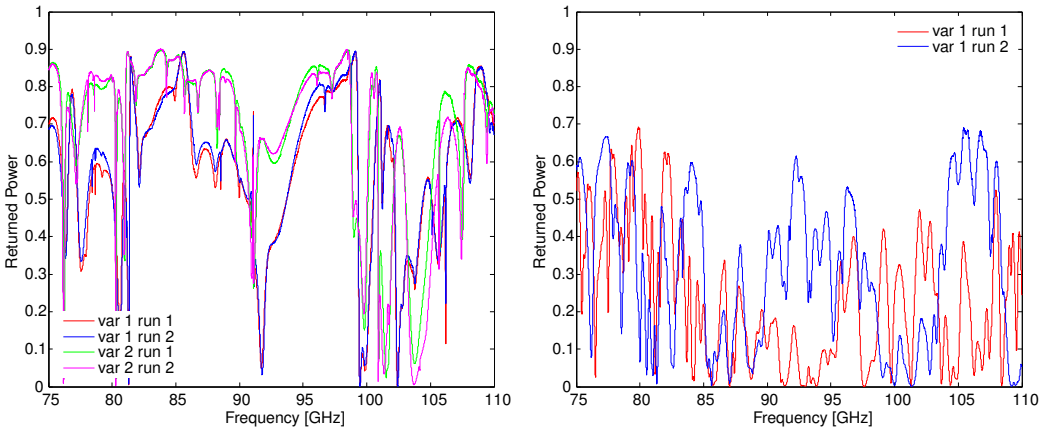

(a) The returned power of the hollow cavity assembled in variation 1 and 2.

(b) The returned power of a cavity assembled in variation 1 with a 0.75 µm thick aluminium sheet between the final two ring segments.

Figure 4.13.: VNA measurement results of a cavity 6 mm in depth and with a radius of 6.375 mm assembled using two different combinations of annular rings. Var 1 used 2 0.75 mm thick rings, followed by 1 3 mm thick ring, and another 2 0.75 mm thick rings. In the case of the resistive element, a 0.75 µm thick aluminium sheet was placed between the final two rings. Var 2 used 2 3 mm thick rings.

impact on the results. In the design phase the spacing between the annular ring segments (on the order of microns) was assumed to be of negligible consequence considering it would only represent a tiny fraction of a wavelength ($\lambda \approx 3\,\text{mm}$). Unfortunately, these measurement results indicates this not to be the case and demonstrate significant variation for different ring makeups of a single cavity design. This may be the result of the resonant structure of the cavity itself being altered more than initially expect and thus amplifying the effect of these otherwise insignificant features.

Even though the ring make up of the cavity appears to prevent specific features to be characterised, as was done in the case of the aluminium cavity, efforts were continued to include a resistive sheet element for comparison with the Scatter absorber model. In selecting an appropriate material the skin depth of the metal had to be considered. This is defined as the distance a wave can travel into a conductor before its amplitude is reduced by a factor of e ($\approx$0.37) as outlined in expression 4.20, and is given by equation 4.19, where ρ represents the material bulk resistivity, ν the frequency, and μ_R the relative permeability. For aluminium, with a bulk resistivity of $\rho = 2.65\,\mu\Omega cm$ and at a frequency of 100 GHz

this equates to a skin depth of 0.26 µm.

$$\delta_s = \sqrt{\frac{2\rho}{2\pi\nu\mu_0\mu_R}} \tag{4.19}$$

$$E(z,t) = e^{-\frac{z}{\delta_s}} \mathrm{Re}\left(E_0 e^{j(kz-\omega t)}\right) \tag{4.20}$$

Ideally a sheet of aluminium of thickness less than the skin depth would be used to best emulate the resistive sheet element of the Scatter code, however, the thinnest sheet available was 0.75 µm in thickness. Equation 4.20 can be used to determine that only 6% of the incident field will permeate such an aluminium sheet at 100 GHz and 7.5% at 80 GHz. Nonetheless, the element is marginally transparent and should also allow for current losses. This aluminium sheet was clamped between the final two ring segments of the arrangement "var 1", with care taken to ensure it remained as flat as possible. Considering the delicate nature of the 0.75 µm thick foil ensuring a perfectly flat and smooth stretch proved not to be achievable to the levels desired. A sample of the results of these measurements can be seen in figure 4.13(b). Compared to the return power of the hollow cavity of variation "var 1" (see figure 4.13(a)) a greater return loss is observed once the aluminium foil is inserted. The measurements including metallic foils however do not prove to be reproducible. It is assumed that creases are introduced to the foil during the assembly of a specific cavity which cannot be exactly replicated and thus add a significant and unknown variable to the results.

Although this measurement exercise failed to provide further confirmation of the simulation techniques, the significant levels of agreement of the Scatter and CST Microwave studio simulations are considered sufficient for the purpose of the Scatter code validation. Particularly when considering the excellent levels of agreement obtained between the CST and aluminium cavity measurements of section 4.2. The measurements of the cavity kit also provide an insight into the behaviour of cavity structures in general and emphasise their enhanced sensitivity to sub-wavelength variations. Future work might include producing a gold plated replica of this cavity kit for the purpose of determining how sensitive

a highly conductive cavity structure is to sub-wavelength variations. This could have practical implications for the manufacturing tolerances of back to back horn antenna and other analogous systems.

4.4. Including a Gap

4.4.1. Return Loss Approach

For mechanical reasons outlined in section 1.2 some of the cavities motivating the work of this chapter include an opening, or gap, in the cavity wall (see figure 4.14). Such an opening has significant consequences for the optical performance of a detector cavity, such as possible power leakage, which for an array of cavities as in the proposed SAFARI system would correlate to cross-talk between pixels. For a simple empty PEC cavity it has been shown that the S_{11} returns unity power (figure 4.2(b)), as such, the power leaked out of a cavity such as that in figure 4.14 may be determined in a similar manner as used in calculating the total absorbed power, that is as $1 - |S_{11}|^2$. For the case of a cavity either composed of a non-PEC material or containing other lossy or absorbing materials, it is considered that the leaked power could be established through comparison with the sealed case, i.e. $|S_{11(\text{Sealed})}|^2 - |S_{11(\text{Open})}|^2$. The work of this section is conducted for a cylindrical cavity and the technique expanded to rectangular geometries in later applications.

Cavity Scaling

As the mode matching method employed by Scatter is essentially a two port system with no immediate facility for the implementation of such a gap CST Microwave Studio was first considered. As previously outlined electrically large structures can require excessive computational resources and lengthly simulation times using this method. As such, an initial analysis was conducted in an effort to identify any trends present in the amount of leaked power for cavities of increasing dimensions.

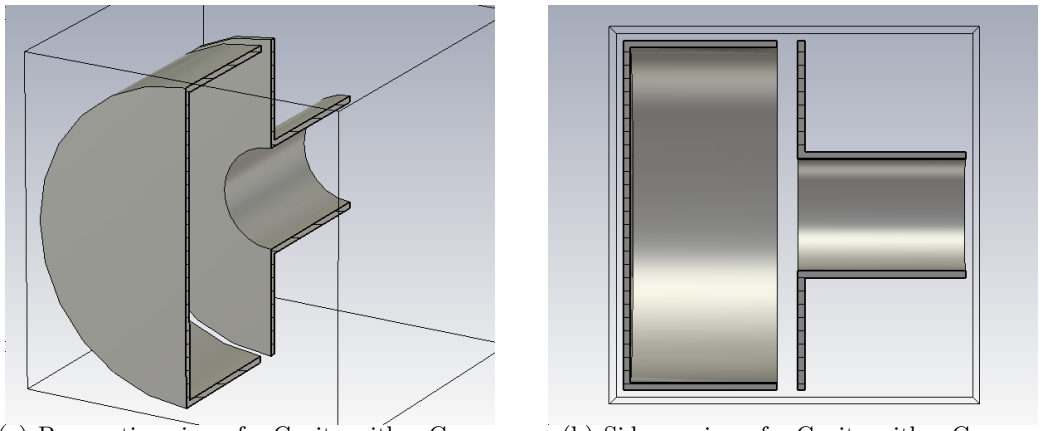

(a) Perspective view of a Cavity with a Gap (b) Side on view of a Cavity with a Gap

Figure 4.14.: Open Cavity fed by a single moded waveguide of radius 1.2 mm

A small PEC cavity was considered and excited at a central frequency of 100 GHz. The length of the cavity was varied from one to four times the central wavelength and this repeated for four different radius values. The initial single moded analysis was conducted for a sealed waveguide, that is the cavity radius across from the gap equaled the waveguide radius of 1.2 mm. Following this the same waveguide was kept constant however the cavity radius varied to values of 1 λ_0, 1.2 λ_0 and 1.5 λ_0 and the simulations performed over a range of cavity depths in each case. The gap width was kept constant in all simulations at 0.5 λ_0.

The results displayed in figure 4.15(a) are those of the single moded cavity of radius 1.2 mm. This case depicts significant losses in power, although this is as expected considering the significant ratio of the surface area of the free space opening to that of the overall structure. Furthermore, the small cross section resulting from the radius of 1.2 mm represents a significant impedance mismatch between the free space leaky section and re-entry into the guide. The variation in the amount of power leaked with the depth of the guide was found to follow a sinusoidal pattern and was successfully fitted using equation 4.21. The fit parameters are; A = 0.974, B = 0.0235, T = 0.736 and c = 2.344 and result in a fit residual of R = 0.986, where the A and B terms establish the maximum variation in leaked power as ranging from ≈0.95 to 1. These results indicate that for a single moded waveguide with a side wall opening it may indeed be possible to predict the behaviour of the leaked power

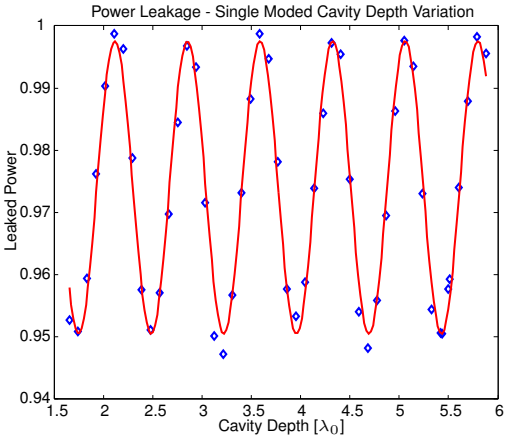

(a) Power leaked as a function of cavity length for a single moded cvaity, 1.2 mm in radius. The blue points represent inidividual data points and the red curve a fit. The equation fitted to the data is: $u(x) = A + B \times \sin\left(\frac{2\pi x}{T} + c\right)$, with the parameters; $A = 0.974$, $B = 0.0235$, $T = 0.736$ and $c = 2.344$ resulting in a fit of residual R = 0.986.

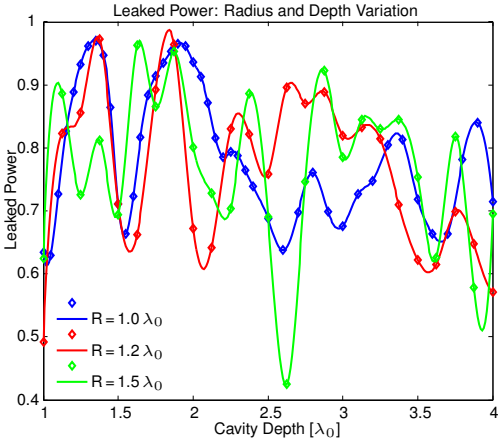

(b) Power leaked as a function of cavity length for a multi-moded cvaities of radius 1.0 λ_0, 1.2 λ_0 and 1.5 λ_0. The data points are fit using a cubic spline interpolant.

Figure 4.15.: Leaked Power for various cavity geometries

for longer structures by extrapolating from the fitted curve.

$$u(x) = A + B \times \sin\left(\frac{2\pi x}{T} + c\right) \tag{4.21}$$

The results of the extension of this analysis to cavities of varying width can be seen in figure 4.15(b). Here one observes firstly a breakdown in the sinusoidal dependance on the cavity depth observed in the previous case and secondly no immediately discernable pattern between the cavities of different width. One possible explanation of the apparent lack of a relationship between the scaled structures may lie in the presence of higher order modes supported by the larger radius. Although the simulation only excites the fundamental waveguide mode feeding the cavity, power couples into higher order cavity modes supported by the wider region. In such an instance effects similar to those observed with the absorber placement may manifest. This could lead to to a shift in the effective guide wavelength and of perhaps greater significance a higher degree of leakage, as higher order modes often contain power isolated in the outer edges and are thus more likely to

couple out of a gap in the cavity wall. Further supporting this argument peak leakage results are observed for shorter cavity depths. This is consistent with the results of figure 4.11(b), where the various supported modes are seen to be most in phase for shorter values of Δd. Although in the situation considered here the gap in the cavity wall is not infinitely thin, but rather of significant width, and as such, a simple quarter wavelength approximation is no longer of benefit.

To investigate the presence of such higher order modes the waveguide port was set to support a total of 20 modes but only excite the fundamental. Additionally, the entrance waveguide was removed and replaced by a simple circular opening into the cavity. This facilitated the observation of power coupled into higher order modes, as with the waveguide structure in place any such modes would have been prevented from reaching the waveguide port through the single moded guide. The results of this simulation confirmed coupling of power between modes, with an S_{11} return of $0.48\sqrt{W}$, $0.22\sqrt{W}$ and $0.06\sqrt{W}$, where the returns of $0.22\sqrt{W}$ and $0.06\sqrt{W}$ represent power returned in the 7^{th} and 15^{th} supported port modes.

One may conclude from these results that the existence of ever higher order modes for increasing cavity radius significantly impacts on the response of the system to an annular opening in the cavity wall. As such, no correlation is observed in the amount of leaked power between cavities of different widths. Furthermore, the sinusoidal dependance on the cavity depth, observed for the single moded sealed waveguide with an annular wall opening, is no longer present for wider multimoded cavities of constant radius. Therefore, no reliable pattern between scaled cavity dimensions can be discerned thus removing the possibility of simulating electrically smaller structures and inferring results for larger designs.

Discerning between Absorbed and Leaked Power

Although monitoring the return power via the S_{11} provides a means for determining the amount of power leaked the same technique is also applied in establishing the total amount

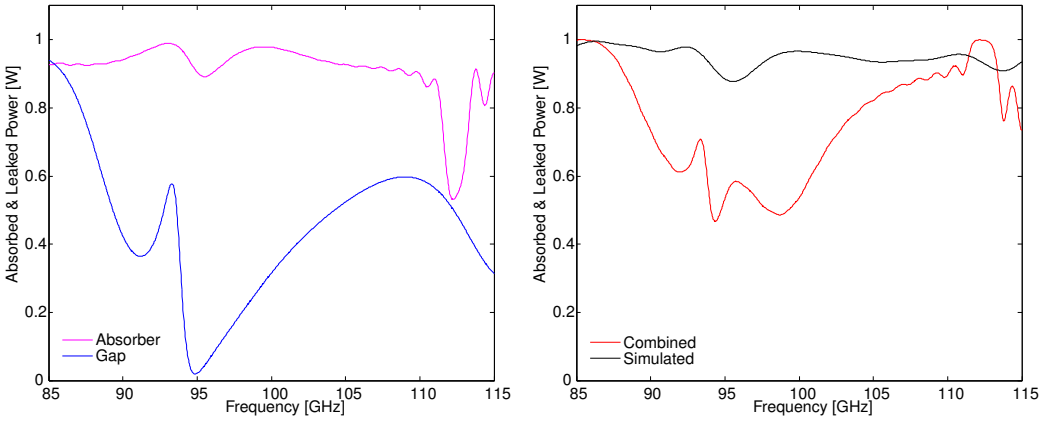

(a) Separate simulations for the sealed cavity containing an absorber 0.75 mm from the backend and an open cavity without the absorber

(b) Total leaked and absorbed power as inferred from the combination of the separate cases and as directly simulated

Figure 4.16.: CST Microwave Studio simulation results of a cavity 3.6 mm in depth, 3 mm in radius and being fed by a single moded waveguide 1.2 mm in radius and 1.5 mm in length. Separate simulations were conducted for the case of the sealed cavity containing an absorber fully filling the guide at a distance of 0.75 mm from the backend, an empty cavity with a 0.75 mm opening, and the open cavity containing the absorber.

of power absorbed. As such, care must be taken that one can distinguish between the two. An initial attempt at establishing the total power leaked and absorbed for an open cavity housing an absorber was made by considering the two scenarios separately. The results of these simulations are outlined in figure 4.16. A cavity 3.6 mm in depth, 3 mm in radius and being fed by a single moded waveguide 1.2 mm in radius and 1.5 mm in length was considered in three separate simulations across a band spanning from 2.6 mm to 3.53 mm.

Figure 4.16(a) displays the total non-returned power for an absorber fully filling the cavity and 0.75 mm from the backend at an impedance of $377\,\Omega/Sq$ and those of a hollow cavity with a gap of 0.75 mm in length. These results were combined in an effort to establish the total non-returned power of an open cavity housing the absorber and this case also directly simulated. The results of this analysis are depicted in figure 4.16(b). The directly simulated case (black curve) is seen not to agree with the combined data inferred from the individual cases (red curve). This is attributed to both the gap and absorber significantly

altering the electromagnetics of the system. For example, the drop in absorbed power inferred from the separate simulations at ≈95 GHz corresponds to a drop in the leaked power of the figure 4.16(a). At this frequency the gap in the cavity wall essentially results in a step to free space, which corresponds to a large impedance mismatch with the modes of the single moded guide. As such, significant power is reflected without ever entering the cavity. Furthermore, it has already been shown that the presence of the ohmic sheet in the guide alters the modes propagating, again not accounted for in the empty opened cavity. Therefore, one may conclude that a sealed cavity sustains a fundamentally different mode set to that of an open cavity.

Given that the absorbed and leaked power cannot be discerned from one another when monitoring only the return loss an alternative means of establishing the leaked power is required. CST Microwave Studio provides the possibility of using a broadband farfield monitor to calculate the power radiated out of a structure and incident on the bounding region. This approach was verified against simulations that were carried out for the SPIRE instrument of Herschel [30]. The goal of the SPIRE simulations was to determine the amount of cross-talk between pixels, where each pixel refers to a cavity housing an absorber and fed by a horn, as is also the situation with the SAFARI instrument.

The SPIRE simulations reported in the paper that cross-talk between the pixels was less than 0.5 %. This was established by exciting the central pixel (see figure 4.17(a)) with the dominant TE_{11} mode and recording the amount of power absorbed by the neighbouring pixels absorber [30]. This analysis was reproduced using CST and considering only a single pixel, where the radiated power of the broadband field monitor provided the total leaked power. Accounting for this leakage then allowed for the total absorbed power to be calculated from the return loss of the system, that is $P_{\text{absorbed}} = (1 - P_{\text{radiated}}) - |S_{11}|^2$. For comparison with the SPIRE results, which outline the power absorbed by a single neighbouring pixel's absorber (i.e. the cross-talk), the total leaked power was divided by six and scaled by the efficiency calculated for the absorber of 0.8975. As can be seen below this results in a cross-talk value of 0.4723 %, which agrees with the reported value

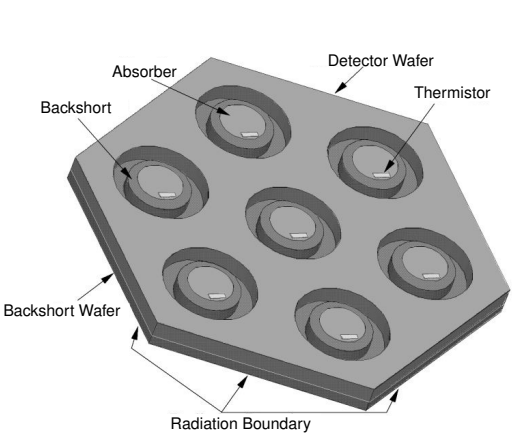

(a) Schematic of seven-pixel simulation model for the P/SW cavity with the top metal cover (frontshort) removed. This model was used to determine the cross-coupling performance of the cavity. [30]

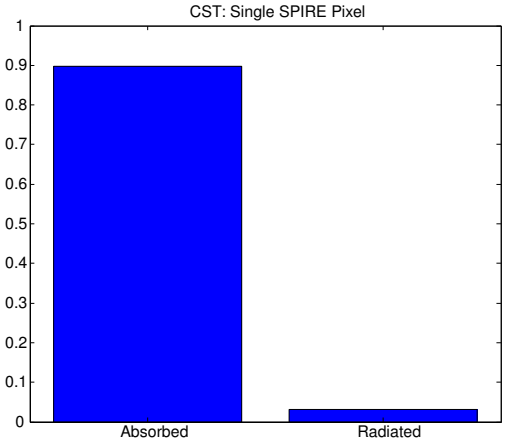

(b) Results obtained from the simulation of a single pixel of the SPIRE system using CST Microwave Studio with broadband farfield monitors active. The absorbed power is calculated at 89.75 % and the radiated, or leaked, power at 3.16 %.

Figure 4.17.: SPIRE simulation model and the CST equivalent results.

of $< 0.5\%$.

$$\text{Cross-talk} = \frac{0.0316}{6} \times 0.8975 = 0.004723 \tag{4.22}$$

It should be noted when using the CST farfield monitors that the radiated power is provided in units of Watts (rms) and must be scaled by a factor of 2 to yield units of Watts (peak). Unfortunately, simulating the exact setup so as to include a neighbouring pixel and absorber proved too computationally intensive.

4.4.2. Annular Trap Approach

Another approach explored involved incorporating a mechanism into the mode matching Scatter code to establish an upper limit on the amount of leaked power. This approach considers the individual supported cavity modes and integrates the total amount of power contained in each mode between the boundaries of R_{cav} and R_{trap} (see figure 4.18(b)). The scattering matrices are then used to establish how much power is coupled into each respective mode on the transition from the waveguide to the trap region. It should be

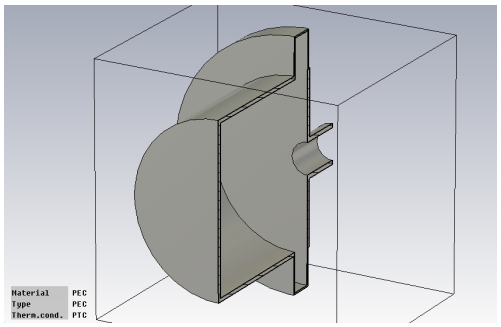

(a) A CAD model of the mode count approach used in establishing an upper limit on the amount of power leaked.

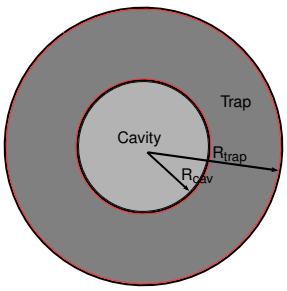

(b) Cross-section of the Annular Trap model outlining the Trap region between the red boundaries

Figure 4.18.: Annular Trap model

noted that this approach therefore essentially breaks open the cavity and at best could be expected to provide an estimate for the amount of leaked power.

In executing the technique the "Trap" region is set equal in length (in the plane of propagation) to the opening which is to emulated. The width of the region (R_{cav}) remains at first a free variable, the effects of which will be examined. Minor modifications must then be made to Scatter to, firstly, record the S_{21} and S_{22} matrices at the junction between the waveguide and the trap region, these specific matrices are from this point on are referred to as S'_{21} and S'_{22}. The S'_{21} contains power coupled from the waveguide to modes in the following section, i.e. the annular trap, and the S'_{22} the self reactance between modes in the trap. It was then necessary to establish which modes were supported only in the extended trap region of the section but not within the boundaries of the cavity, that is which modes contained power in the domain $R_{trap} > r > R_{cav}$. This was accomplished by considering the cut-off frequencies as outlined in equation 4.23. The fraction of the mode's power located solely in the trap, so beyond the boundaries of the cavity, is thus considered an upper bound to the amount of power of that mode lost to free space were it a true opening (see equations 4.24 and 4.25).

$$\lambda_{c(\text{cavity})} < \lambda < \lambda_{c(\text{trap})} \tag{4.23}$$

$$\text{Ratio}_{\text{TE}} = 1 - \frac{\int_0^{R_{Cavity}} \int_0^{\phi} \text{TE}_{mn}\, d\phi\, dr}{\int_0^{R_{Trap}} \int_0^{\phi} \text{TE}_{mn}\, d\phi\, dr} \tag{4.24}$$

$$\text{Ratio}_{\text{TM}} = 1 - \frac{\int_0^{R_{Cavity}} \int_0^{\phi} \text{TM}_{mn}\, d\phi\, dr}{\int_0^{R_{Trap}} \int_0^{\phi} \text{TM}_{mn}\, d\phi\, dr} \tag{4.25}$$

To implement the above the rows of the recorded S'_{21} and S'_{22} matrices corresponding to the power coupled into the modes supported in the trap were extracted, scaled by the Ratio factor of equation 4.24 or 4.25 to ensure only power in the trap region was considered and combined to form two new matrices, the $S_{21(\text{trap})}$ and $S_{22(\text{trap})}$. The power in these new matrices was then summed partially coherently, that is by summing the columns coherently and the rows incoherently, as each column still corresponded to power originating from a single mode. This represented the total amount of power coupled into the annular trap. As such, it was considered an upper bound to the amount of leaked power and was normalised by the total power coupled across the junction to all modes in both the cavity and trap regions of the section, as outlined in equation 4.26.

$$\text{LeakedPower} = \frac{|S_{21(\text{trap})}|^2 + |S_{22(\text{trap})}|^2}{|S'_{21}|^2 + |S'_{22}|^2} \tag{4.26}$$

The above approach was tested on a cavity 3 mm in radius and 12 mm in length, which was fed by a single moded waveguide 1.1 mm in radius and excited at a frequency of 100 GHz. The gap length was first kept constant at $1\,\lambda_0$ (≈ 3 mm) and the depth of the trap region varied. The results of this analysis proved to be critically dependent on the depth of the annular trap, as can be seen in figure 4.19(c). Essentially a deeper trap supports a higher number of modes over which the power is distributed and thus a higher percentage of the power is localised in the trap region. The spread in results does however begin to converge and approaches an asymptote for ever increasing trap depths, as can be seen in figure 4.19(c).

The variation of the gap length is also of interest. One may expect a larger degree of power leakage for increasing gap dimensions, however the results of the mode trap analysis indicate rather erratic behaviour with the power leaked increasing and then decreasing for

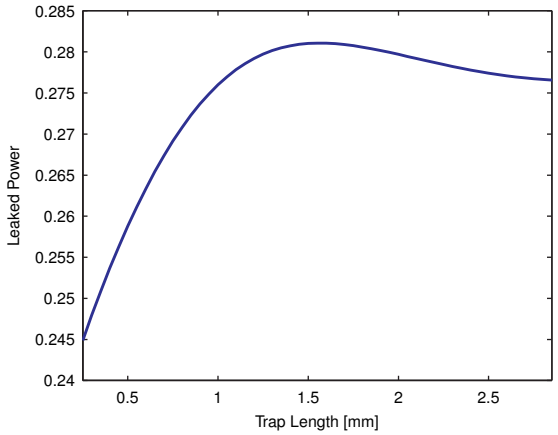

(a) Variation of the Leakage values with varying length of the Trap section for a Trap depth of 20 mm

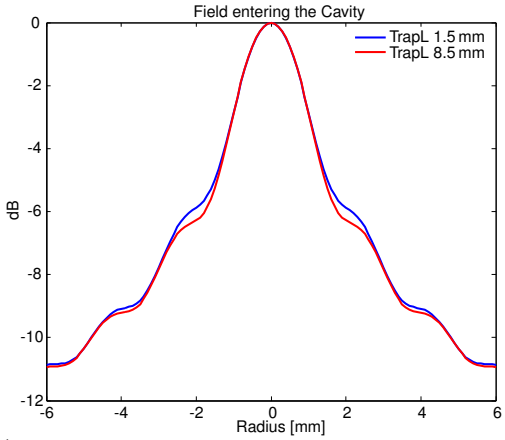

(b) Fields propagating into the cavity at the boundary between the trap and cavity region for different gap lengths (GapL)

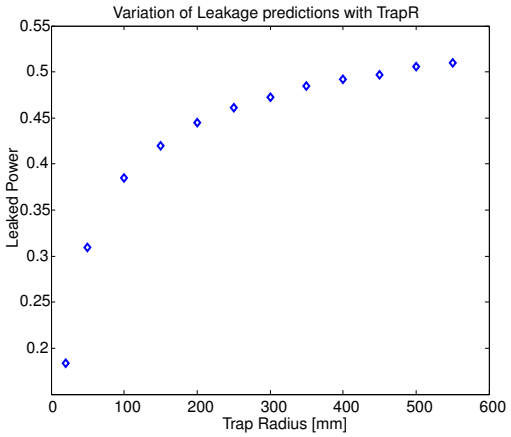

(c) Variation of the Leakage values with varying Trap radius

Figure 4.19.: Analysis of the mode count approach to determining the power leaked.

increasing gap lengths (see figure 4.19(a)). Plotting the field inside the cavity (see figure 4.19(b)) shows that exiting the waveguide is essentially a beam similar in form to the fundamental mode. Furthermore, as one may recognise in comparing the two plots the beam slightly converges with propagation distance as opposed to diffracting and diverging as may have been expected. This behaviour of the total leaked power with respect to gap dimension is considered a side effect of the fact that the technique does not remove power from the system.

At this point it is important to consider the limitations of this model, which considers only the power coupling into the cavity from the waveguide and does not completely consider reflected power or power successfully coupled out of the trap and back into the cavity. Although the asymptotic behaviour observed in figure 4.19(c) suggests that this approach may be capable of successfully establishing an upper bound on the leaked power, the extensive trap width required before the results tend to this asymptote, and the high number of associated modes required to accurately modal such a wide region, result in extremely lengthly simulation times. Furthermore, the convergent nature of the field being considered prevents accurate evaluations for the influence of the gap length, which would be of significant interest in design optimisations. As such, attempts to apply this technique were abandoned in its present form. Future work may consider applying this technique with a set of free space modes, which would remove the free variable of the trap radius.

4.5. Optimised Cavity Geometries

As previously outlined, cavities often serve the purpose of enhancing the absorption of detector bolometers by trapping power, not absorbed in the first pass, in the region of the detector. Furthermore, in multi-pixel devices, such as those found in the proposed SAFARI design, it can prove mechanically necessary to leave a small ($\approx 50\,\mu m$) opening between the pixels in order to couple the detectors to a feedhorn array. Any such cavity should therefore maximise absorption while minimising reflected and leaked power. Focusing specifically on SAFARI type cavity structures, this section considers various geometrical configurations to this end.

4.5.1. Rectangular vs. Cylindrical

Before considering the more specific aspects of the structure, whether either a rectangular or cylindrical basis proves advantageous with regard to the optical efficiency is considered. This was accomplished using CST Microwave Studio with broadband farfield monitors

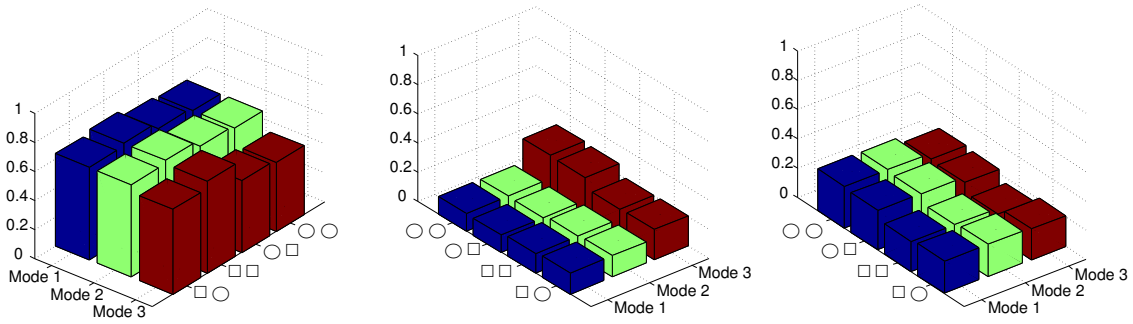

(a) Absorbed power (b) Radiated power (c) Returned power

Figure 4.20.: These three plots represent the results of simulations run between 4.25 and 4.55 THz for rectangular and circular cavities. The symbols ◯, □ represent whether the structure was rectangular or circular in dimension with the first symbol defining the cavity and the second the absorber. For example □◯ indicates a rectangular cavity housing a circular absorber.

to analyse a PEC hollow cavity containing an absorber in both circular and rectangular configurations. It should however be noted, that this analysis considered single and few moded cases, which may differ to highly multi-moded structures.

Table 4.2.: This table provides the internal dimensions used in the rectangular and cylindrical cavities. The central wavelength $\lambda_0 = 47.5\,\mu m$, and the variables l and dist representing the length and the distance back from the waveguide respectively. The variables r, d_x and d_y represent the radius in the cylindrical case and the x and y widths in the rectangular cavity.

Cylindrical		**Rectangular**	
Parameter	**Value**	**Parameter**	**Value**
waveguide: r	35 µm	waveguide: d_x	70 µm
		waveguide: d_y	70 µm
waveguide: l	$\frac{\lambda_0}{2}$	waveguide: l	$\frac{\lambda_0}{2}$
cavity: r	$2\,\lambda_0$	cavity: d_x	$4\,\lambda_0$
		cavity: d_y	$4\,\lambda_0$
cavity: l	$4\,\lambda_0$	cavity: l	$4\,\lambda_0$
gap: l	$\frac{\lambda_0}{2}$	gap: l	$\frac{\lambda_0}{2}$
absorber: dist	$\frac{\lambda_0}{2}$	absorber: dist	$\frac{\lambda_0}{2}$
absorber: r	35.5 µm	absorber: d_x	71 µm
		absorber: d_y	71 µm

The results of the rectangular and circular cavity simulations for the first 3 supported modes can be seen in figure 4.20. Considering the first 3 modes beyond cut-off these results show the rectangular cavity housing a rectangular absorber to perform best in terms of

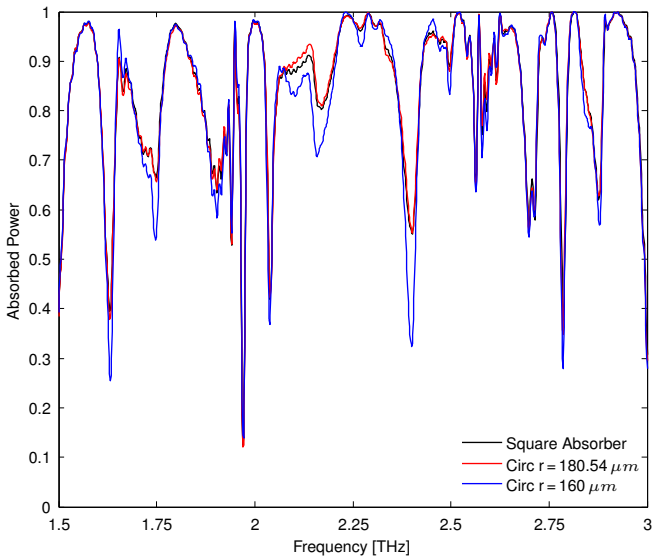

Figure 4.21.: The absorbed power $(1 - S_{11}^2)$ of a sealed cavity, dimensions; $l_{cavity} = 500\,\mu m$, $r_{cavity} = 250\,\mu m$ fed by a single moded waveguide, dimensions; $l_{guide} = 150\,\mu m$, $r_{guide} = 60\,\mu m$ for three different absorbers located $50\,\mu m$ from the waveguide opening into the cavity. A square absorber $320\,\mu m \times 320\,\mu m$, a circular absorber with $r = 180.54\,\mu m$ and a circular absorber with $r = 160\,\mu m$.

maximising absorption and minimising both radiated and returned power. Using a circular absorber in the rectangular cavity negatively impacts on the results, however, continues to out perform the alternative circular cavities. It is first assumed that the decrease in effectiveness of the circular absorber can be attributed to the decreased surface area. To further test this assumption a smaller cavity $500\,\mu m$ in diameter and depth and fed by a single moded waveguide $120\,\mu m$ in diameter was considered. Three different absorbers were then placed $50\,\mu m$ inside the cavity; a square absorber $320\,\mu m \times 320\,\mu m$, a circular absorber with $r = 180.54\,\mu m$ designed to perfectly match the surface area of the square absorber and a circular absorber with $r = 160\,\mu m$ designed to fit perfectly inside the area of the square absorber.

The results of the simulations can be seen in figure 4.21 and indicate almost identical performance between the circular and square absorbers. A drop in performance occurs at certain frequencies for the smaller circular absorber, which further supports the hypothesis that the surface area and not the geometry of the absorber is of importance. This

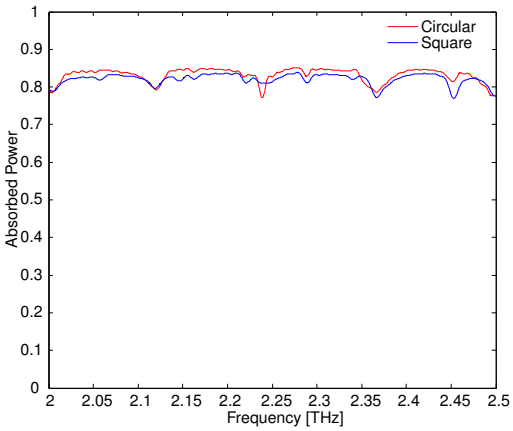

(a) Results of the circular and square absorber for the dominant waveguide mode

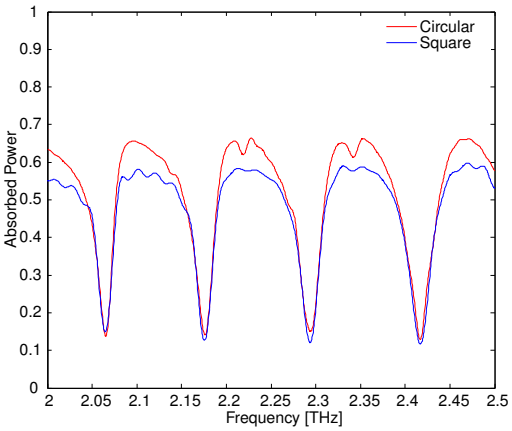

(b) Results of the circular and square absorber for the 3rd waveguide mode

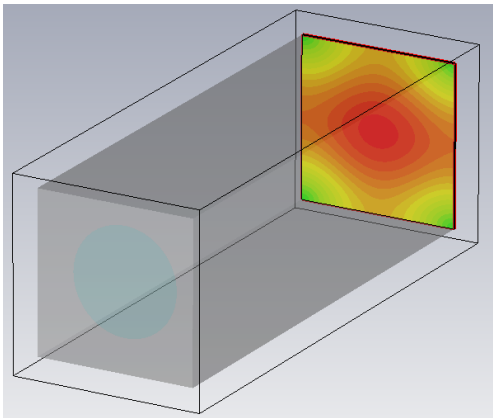

(c) Form of the dominant waveguide mode in the case of the circular absorber

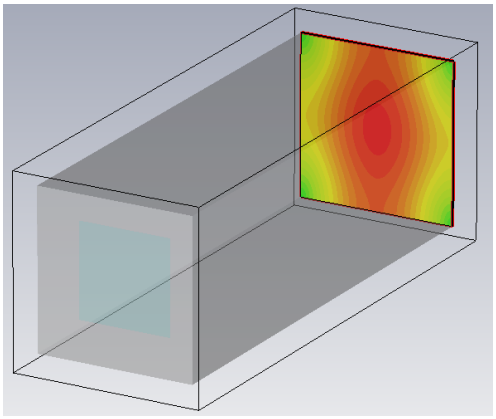

(d) Form of the dominant waveguide mode in the case of the square absorber

Figure 4.22.: The absorbed power, and the excited mode forms, for different absorber geometries of equal surface area and placed $\Delta d = 33.33\,\mu\text{m}$ from the guide backend. The circular absorber dimensions were $\text{r} = 100\,\mu\text{m}$, and the rectangular; $\text{d}_x = \text{d}_y = 177.25\,\mu\text{m}$, and were both inside a multimoded waveguide, dimensions; $\text{d}_x = \text{d}_y = 300\,\mu\text{m}$ and $\text{l} = 900\,\mu\text{m}$, and considered for individual waveguide mode excitations.

was further tested using a sealed multimoded rectangular waveguide $300\,\mu\text{m} \times 300\,\mu\text{m}$ and $900\,\mu\text{m}$ in length and exciting individual modes for a frequency range of 2 to 2.5 THz for a circular and rectangular absorber of equal surface area (circular radius $\text{r} = 100\,\mu\text{m}$ and rectangular widths $\text{d}_x = \text{d}_y = 177.25\,\mu\text{m}$) and placed $33.33\,\mu\text{m}$ from the sealed waveguide end.

The results of this analysis can be seen in figure 4.22. Significant agreement is seen to exist between the results, however not to the same degree as was observed in the single moded case of figure 4.21. Examining the field distributions of the dominant excited mode formed in the presence of the circular and rectangular absorbers reveals that the presence of the absorber itself influences the form of the mode and thus the otherwise expected TE_{10} mode in this case is no longer dominant, as was observed and examined previously in section 4.3.2. Furthermore, the different absorber geometries exert a slightly different influence on the resultant mode form (see figures 4.22(c) and 4.22(d)). As such, it is no longer entirely valid to expect perfect agreement as both cases are not subject to identical excitations. It is considered that a similar situation occurs in the single moded case, however the single moded guide most likely resulted in fewer degrees of freedom and thus less divergent mode forms.

Referring again to the results of figure 4.20 one also observes that the rectangular cavity geometry out performed its circular counterpart. This is considered a consequence of the rectangular cavity in this analysis being fed by a rectangular waveguide and the circular by a circular waveguide. The mode forms of rectangular and circular waveguides are fundamentally different (see chapter 3) and thus both instances were differently excited. Examining the difference between the rectangular and circular modes, an example of which may be seen in figure 4.7, one observes a larger distribution of power over the cross-section of a rectangular guide compared to a more focused power distribution over the cross-section of a circular guide. This would in turn correspond to a greater distribution of power over the absorber area in the rectangular fed case to that of the circular case and is expected to contribute in part to the higher levels of performance of the rectangular cavity. This assumption was tested by considering a rectangular and circular cavity of equal volume and both identically excited by a single moded rectangular waveguide of dimensions $120\,\mu m \times 60\,\mu m$ and $130\,\mu m$ in length. Both cavities were $250\,\mu m$ in length and had a $25\,\mu m$ opening. The rectangular cavity had dimensions of $d_x = d_y = 443.11\,\mu m$ and the circular cavity a radius of $r = 250\,\mu m$. A circular absorber with an impedance of

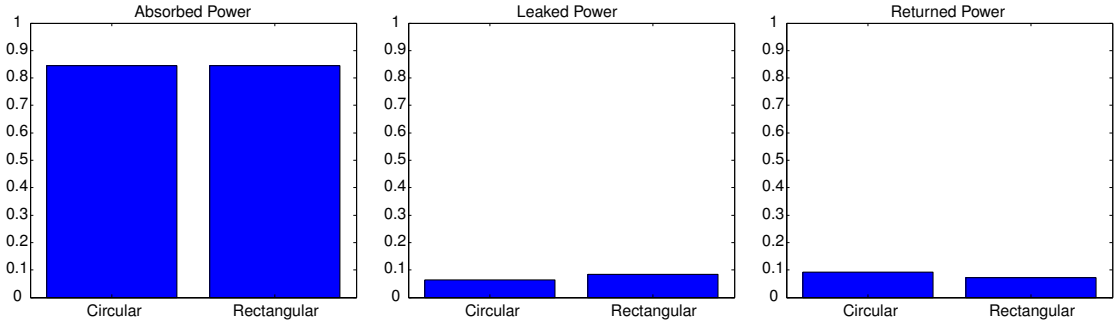

(a) Absorbed power (b) Leaked power (c) Returned power

Figure 4.23.: The results of a circular and rectangular cavity of identical volumes both fed by a single moded rectangular waveguide and containing a circular absorber and a gap.

377 Ω/Sq and radius of 180.54 µm was placed 33.33 µm from the backend of both cavities.

The results of the analysis indeed confirm that for two identically excited hollow cavities the level of absorption is independent of the specific geometry being circular or rectangular. Both the rectangular and circular cavities provide identical results with regard to the amount of power absorbed (see figure 4.23). However, the rectangular cavity is seen to radiate (or leak) more power through the gap than is the case for the circular cavity. It is noteworthy that the difference in leaked power between the circular and rectangular cavities contributes to the returned, and not absorbed, power in the circular case. This difference can again be attributed to the differences in the physical surface areas of the opening as can be seen below.

$$A_{\text{gap(circ)}} = 2\pi r l_{gap} = 39,269.9\,\mu\text{m}^2$$
$$A_{\text{gap(rec)}} = 4 d_x l_{gap} = 44,311\,\mu\text{m}^2$$

4.5.2. Reflector Geometry

For the initial design of an internal cavity geometry a ray tracing approach is considered. Although only an approximation and not entirely reliable for high frequency quasi-optics,

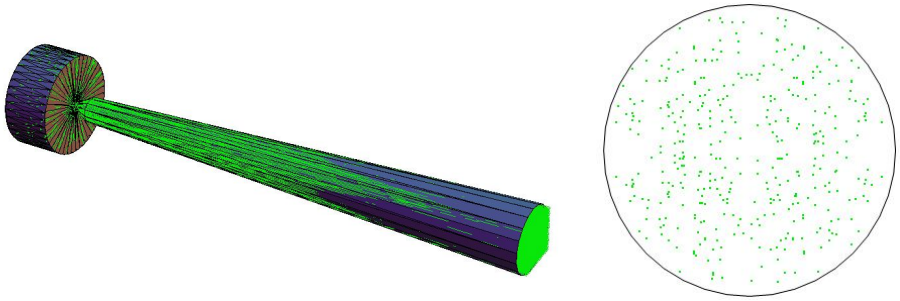

(a) Ray Tracing analysis of a horn fed cavity

(b) Screen acting as the absorber in the ray tracing analysis, where the green points represent ray intersections.

Figure 4.24.: The ray tracing analysis depicting the overall structure and the ray-screen intersections.

this provides a first order approximation, which can then be improved upon using other EM techniques. Since horn antennas are the default antenna type for the frequencies of interest in this chapter, a horn fed cavity is considered in this ray analysis. A screen was used in place of the absorber and set to allow each ray penetrate it a maximum of two times while counting the total number of intersections. This was used to estimate a value for the absorbed power. It should be stressed that the purpose of the ray tracing simulations was to establish a trend between different geometry designs and not to establish absolute values for the absorbed power.

Three different designs were considered. These included first a hemispherical reflector (figure 4.25(c)) with the absorber placed at the center of curvature. From a ray tracing perspective this design would focus parallel rays close to the optical axis at a point corresponding to $\frac{R}{2}$, where R is the radius of curvature. However, rays further removed from the optical axis may result in a catacaustic effect [13] and therefore not be brought to focus in the direction of the absorber.

The next geometry considered was designed for the case of a divergent beam exiting the horn into the cavity. Such a beam pattern would be best served by an oblate spheroidal reflector (figure 4.25(d)), with one focus located at the horn-cavity aperture and the other at the absorber. From a ray tracing perspective any rays passing through the first focal

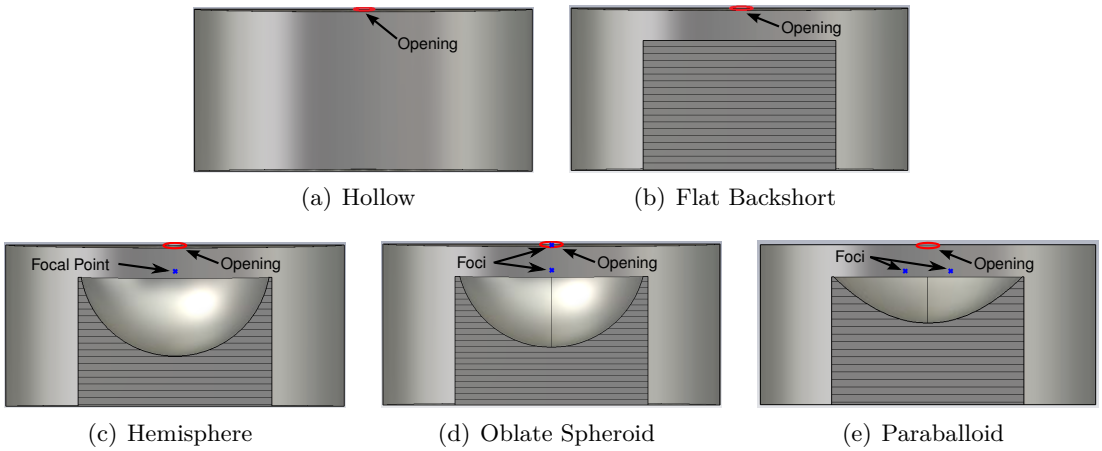

(a) Hollow (b) Flat Backshort

(c) Hemisphere (d) Oblate Spheroid (e) Paraballoid

Figure 4.25.: Graphical representation of the various cavity geometries considered

point (at the horn aperture) would be reflected to the second focal point (at the absorber). However, the exact opposite would also be true for any rays reflected back off the underside of the absorber.

Finally, the case of a collimated beam entering the cavity was considered. In such a case a parabolic reflector geometry (figure 4.25(e)) with the absorber placed at the focus should prove most efficient. Such a reflector would bring any rays travelling parallel to the optical axis to focus. It should be noted that for Scatter simulations these structures were approximated by thin segments of appropriately varying radius, as was done for smooth-walled horn antennas.

The ray tracing results for the three proposed geometries are displayed in figure 4.26(a) and the corresponding Scatter results in figure 4.26(b). Although the exact values of the two simulations aren't equivalent, the trend in performance is consistent; with both ray tracing and mode matching analysis showing the best performance for the oblate spheroid.

A more detailed comparison of these geometries was then conducted using CST Microwave Studio, as this also provides information on power radiated out of such a cavity should an opening in the side walls be present. Furthermore, this analysis included two additional geometries 1) a hollow cavity with no additional internal structure (figure 4.25(a)) and 2)

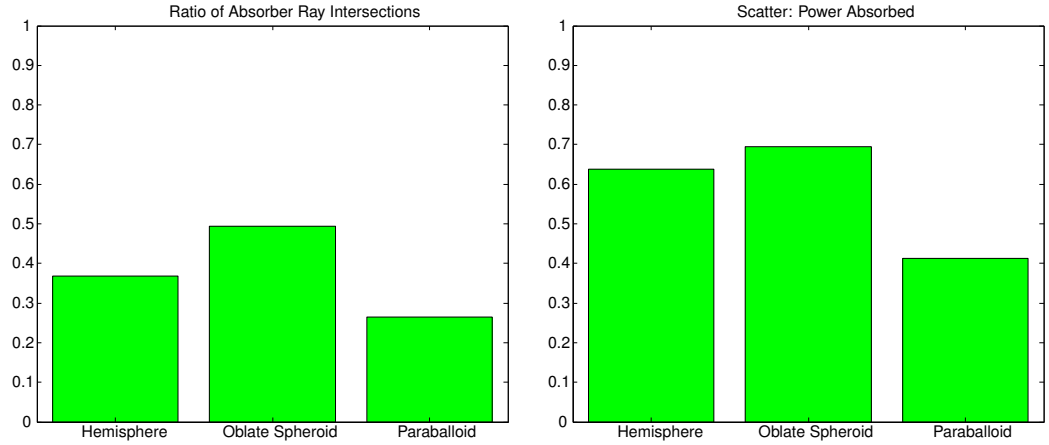

(a) Ray tracing results of three different designs. 900 rays where launched the ratio of the number of launched rays to the number of rays intersecting the absorber is plotted here.

(b) Scatter results for the geometries corresponding to those used in the ray tracing analysis.

Figure 4.26.: Ray Tracing and Mode Matching results for hemispherical, oblate spheroidal and parabolic reflector geometries

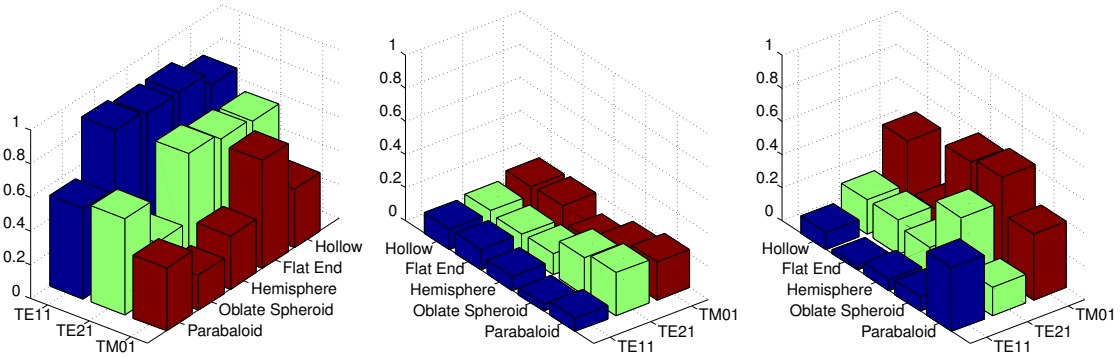

(a) Absorbed power

(b) Radiated power

(c) Returned power

Figure 4.27.: Circular Cavity: Comparison of the various geometrical reflector configurations, considering the absorbed, radiated and returned power

a flat-end reflector (figure 4.25(b)) placed a quarter of a wavelength behind the absorber. Additionally, the input waveguide was expanded to support three modes. This analysis was then repeated for a rectangular cavity, housing the same reflector geometries as used in the circular cavity.

The results of the circular cavity analysis can be seen in figure 4.27. Considering first the fundamental TE_{11} mode the results can be seen to largely agree with those predicted by ray tracing, with the oblate spheroid design performing best in terms of absorbed and

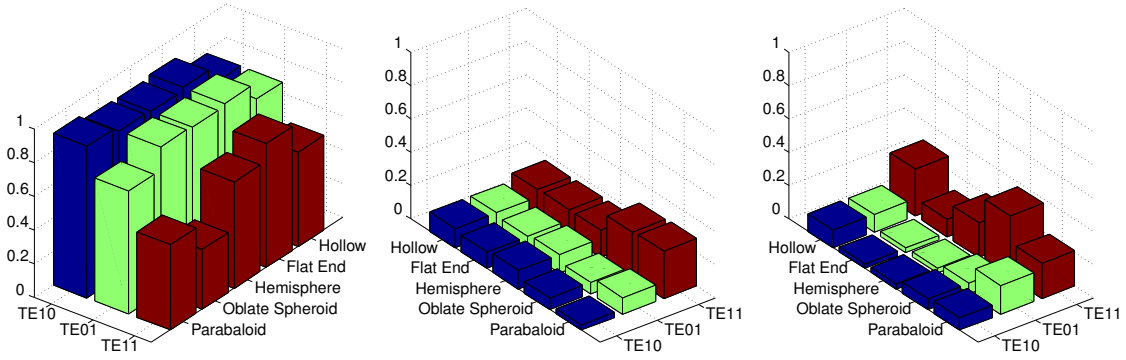

(a) Absorbed power (b) Radiated power (c) Returned power

Figure 4.28.: Rectangular Cavity: Comparison of the various geometrical reflector configurations, considering the absorbed, radiated and returned power

radiated power. The flat end design however performs almost exactly as well as the oblate spheroid in terms of absorbed power, better in terms of the returned power and slightly worse regarding the radiated power. This pattern also holds true for the TM_{11} mode, however the TE_{21} then deviates entirely from this trend showing the worst performance in absorbed power for the oblate spheroid design.

To understand this deviation one must consider the modes themselves, these are depicted in figure 4.29. As can be seen the TE_{11} mode, which best follows the trends expected from ray tracing, is dominant along the axis, or the center of the space. In contrast the TM_{01} and TE_{21} modes are off-axis dominant. It is the conclusion of these results that on-axis dominant modes, generally the fundamental modes, may be reasonably estimated using paraxial ray tracing. Higher order, off-axis dominant, modes however would appear to diverge too greatly from the paraxial assumptions of ray tracing for the technique to be relevant.

The rectangular results (figure 4.28) again confirm the results of the circular cavity, with the oblate spheroid performing best in terms of absorption for the on-axis dominant modes and poorly for the higher order off-axis modes. It may also be noted in the case of the oblate spheroid that when less power is absorbed due to the mode form, the geometry best accommodates for reflections back through the entrance aperture and thus results in high

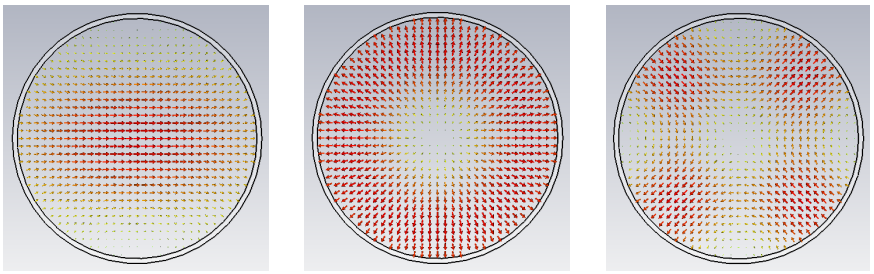

(a) TE11 Mode (b) TM01 Mode (c) TE21 Mode

Figure 4.29.: The first three modes supported in the circular waveguide of the simulations

levels of returned power. Again as was the case in the circular cavity the flat-end design performs best across the range of modes.

In comparing the absolute results of the circular and rectangular cases depicted in figures 4.27 and 4.28 one should appreciate that the mode forms exciting both cases are not equivalent. For example the second (TE_{01}) mode of the rectangular geometry is the orthogonal form of the first (TE_{10}) mode and as such performs equivalently for all circularly symmetric designs, that is all but the paraboloid.

It is the conclusion of this analysis that paraxial ray tracing approximations are only valid for fundamental or on-axis dominant modes. Furthermore, it is concluded that no single reflector geometry performs best for all modal configurations and as such, one must consider the total number of supported modes across the entire bandwidth of the system in question, and the form of those modes, before deciding on a specific reflector design. For broadband systems this will most likely require a trade-off analysis where the optimised design for the fewer moded region of the band may perform worse at higher moded frequencies.

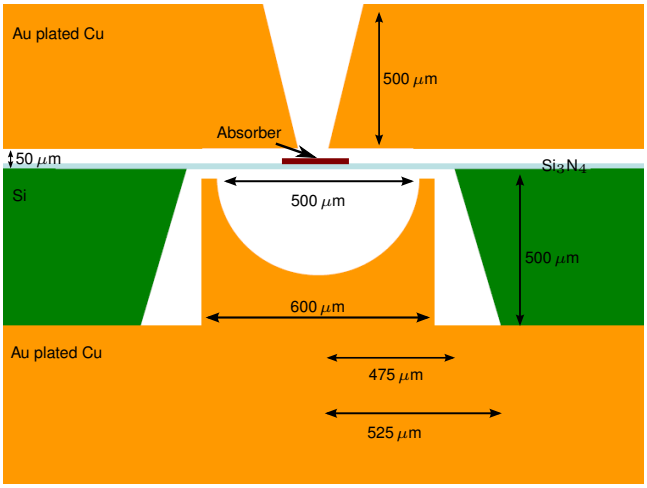

Figure 4.30.: A proposed design of the SAFARI cavity

4.6. SAFARI Detector Cavities

4.6.1. Overview

One of the major motivations behind this work were the detector cavities for the SAFARI instrument of the proposed SPICA mission. Figure 4.30 outlines a proposed design for such a cavity, however, several aspects have still to be analysed in detail before being finally decided upon. This section outlines such an analysis, including the influence of the interior geometry of the structure, the positioning of the absorber, the absorber geometry and, considering the favourable performance of the pyramidal horn designs (see chapter 3), also the difference between a rectangular and circular feed to the cavity. The analysis focuses on the L-band and S-band cases and proposes optimised design configurations.

4.6.2. L-Band

Technique Overview

Where possible initial simulations were conducted using CST Microwave Studio for the individual supported modes of the structure. These simulations provided accurate data on

the absorbed, radiated and returned power levels. To further validate this approach three separate and independently conducted analyses of a single mode of an L-band type cavity were conducted across a frequency range of 1.5 - 3 THz. These included a CST analysis, performed as outlined in this chapter and by the author of this work, a COMSOL analysis completed by Colm Bracken of the NUIM Terahertz group, and the analysis of a group at Cardiff University in Wales using the **H**igh **F**requency **S**tructural **S**imulator (HFSS) of the Ansys Corporation. The cavity considered was hemispherical in geometry, with a diameter of 500 µm, and contained an absorber 50 µm inside of the aperture. A HFSS model of this cavity can be seen in figure 4.31. The radiated and returned power results for an absorber impedance value of 400 Ω/Sq are displayed in figure 4.32 and can be seen to provide a reasonable level of agreement for the three completely independent simulations. The level of variation between the models was considered reasonable considering each the techniques implemented different meshing and domain solver types, as well as different approaches to the calculation of Maxwell's equations. This was considered final validation of the methodology used throughout this section for the SAFARI cavities.

The electrical size of the structures under consideration result in lengthly simulation times and prevent a CST analysis of a complete SAFARI pixel (that is the horn and cavity combined) from being considered. As such, a Scatter analysis of the equivalent closed systems were carried out for the purpose of optimisation runs and for the final complete pixel characterisation. Estimates on the amount of radiated power in this case were taken from the CST analyses.

Cavity Designs

The design originally proposed for the SAFARI cavity was based very much on a ray tracing approximation and contained a hemispherical reflector surface (see figure 4.30). The minimum horn exit aperture (or cavity entrance aperture) considered is 160 µm in width, which at 1.4, 2.0 and 2.7 THz would support 4, 4 and 12 modes respectively. For optimal design purposes the cavity should thus be tailored specifically to the first 4

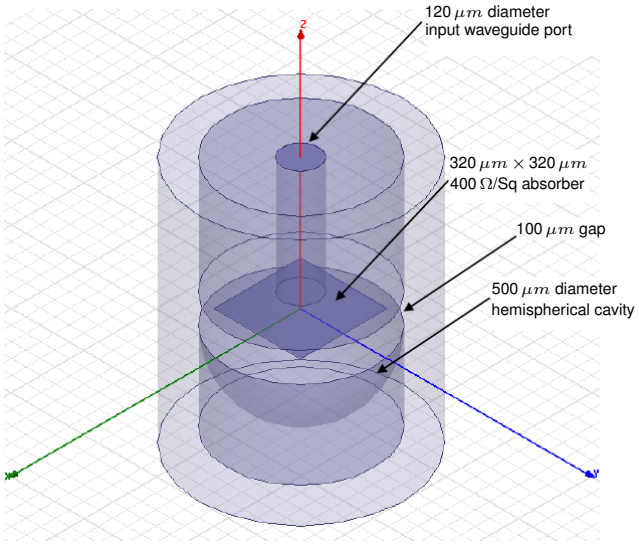

Figure 4.31.: HFSS Model of a test cavity. The cavity is fed by a cylindrical waveguide of diameter 120 µm and contains an resistive sheet 50µm inside the aperture with an impedance value of 400 Ω/Sq. The interior of the cavity have a hemispherical geometry 500 µm in diameter.

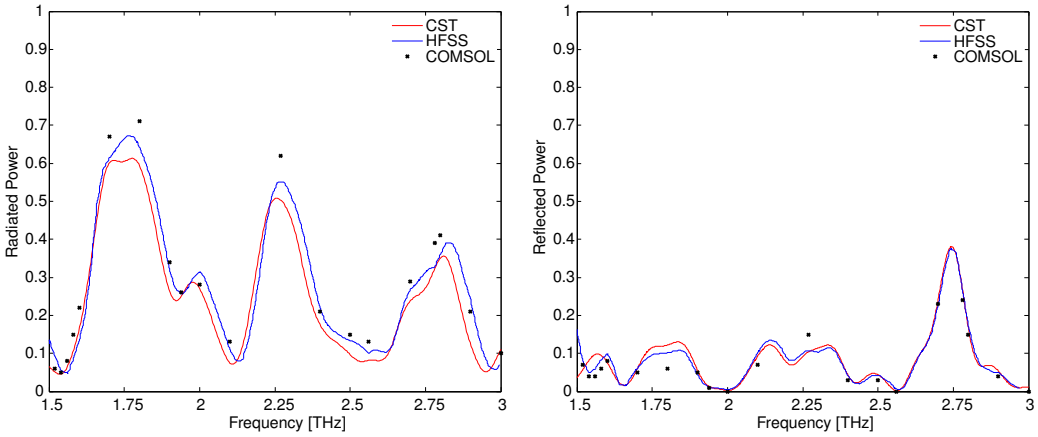

(a) Radiated power (b) Returned power

Figure 4.32.: Sample of results of the CST, HFSS and COMSOL analyses showing the predicted radiated and returned power of the cavity

modes, which alone dominant half of the entire band. These are the TE_{10}, TE_{01}, TE_{11} and TM_{11}. Whilst the TE_{10} and TE_{01} modes are merely orthogonal to one another and on axis dominant, both the TE_{11} and TM_{11} contain significant off-axis power and are thus less well suited to a hemispherical design. Results from section 4.3 suggest that a hollow circular cavity, with a flat backend reflector and an absorber placing one quarter of the averaged effective guide wavelengths would perform best in terms of minimising cross-talk

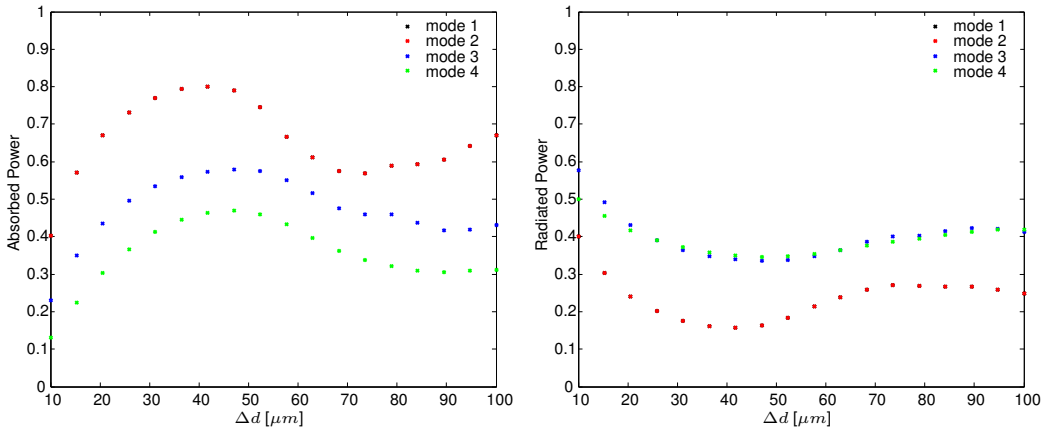

(a) Absorbed power (b) Radiated power

Figure 4.33.: Results (averaged over the entire band from 1.4 - 2.7 THz) of a parameter sweep of Δd carried out in CST Microwave Studio for the four dominant modes of the hollow L-band cavity. The absorbed, radiated and returned power were recorded and the absorbed and radiated results are presented here. Mean of the peak absorption values occur at $\overline{\Delta d} = 44.4118\,\mu\text{m} = 0.33\lambda_f$.

and maximising absorption, respectively. As such, an alternative cavity design, based on these findings, is proposed.

The new L-band cavity design maintains the 100 µm gap, as this results from manufacturing constraints, however removes the hemispherical backend in favour of a simple hollow cavity, 500 µm in depth (including the 100 µm gap) and 250 µm in radius. This is referred to from this point on as the hollow design and was considered using CST Microwave Studio with a 320 µm×320 µm absorber represented by an ohmic sheet with an impedance of $377\,\Omega/Sq$. To optimise the absorber placement the four dominant modes were considered independently for a series of values of Δd ranging from 10 to 100 µm from the sealed end of the cavity. The simulations were conducted for the entire band (1.4 THz - 2.7 THz) and averaged, as such the strong sinusoidal dependance on Δd observed for single modes at discrete frequencies was not to be expected. It may be noted that the modes are referred to not as the conventional waveguide TE and TM modes, but rather simply as modes 1 to 4. This is due to the effect observed of the resistive sheet impacting on the form of the modes.

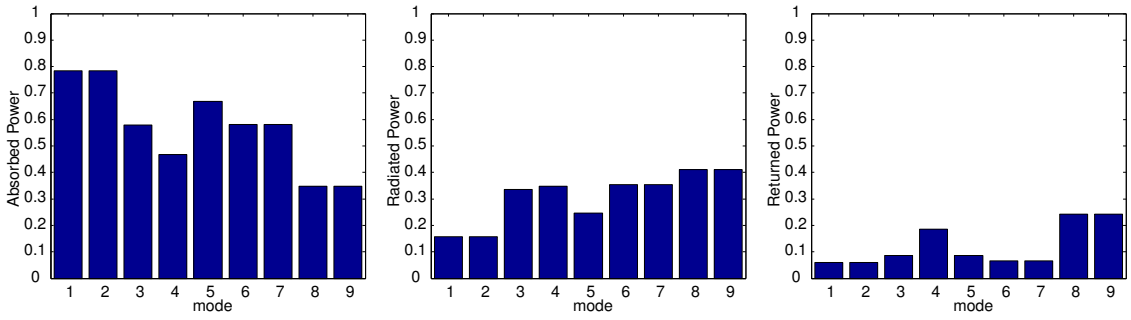

(a) Absorped power (b) Radiated power (c) Returned power

Figure 4.34.: Optimised hollow L-band cavity design total absorbed, radiated and returned power results averaged across the band for the individual modes. Note: The modes are averaged over the region for which they are supported only.

The results of figure 4.33 show both mode 1 and 2 to behave identically, which is as expected considering their orthogonal relationship and the symmetric design of the cavity. Furthermore, the points of peak absorption may be seen to also correspond to minimums in the total radiated power. Averaging the displacement resulting in peak absorption for the four modes results in a value of $\overline{\Delta d} = 44.4118\,\mu\text{m}$, which in terms of the central free space wavelength is $\overline{\Delta d} = 0.33\lambda_f$. This cavity design was then considered again setting Δd to the optimised value. The results of this analysis for the first 9 supported modes are displayed in figure 4.34, the other higher order modes only cut on at the very end of the band were therefore not analysed.

This design as well as the originally proposed hemispherical design were then considered using Scatter. In its present form Scatter requires a consistent geometry, that is one may not yet change between circular and rectangular arrangements. However, it was shown in section 4.5 that both rectangular and circular geometries yield identical results for equivalent surface areas and volumes. As such, both a circular and rectangular approximation to the hollow cavity were considered. In the circular case, the absorber radius was set to ensure an equivalent area to the rectangular $320\,\mu\text{m} \times 320\,\mu\text{m}$ sheet, with $r = 180.54\,\mu\text{m}$. And in the rectangular case the cavity widths were set so as to match the area of the circular cavity with $d_x = d_y = 443.113\,\mu\text{m}$. The proposed hemispherical cavity was also simplified so as it only consisted of the hemispherical region and the step between the

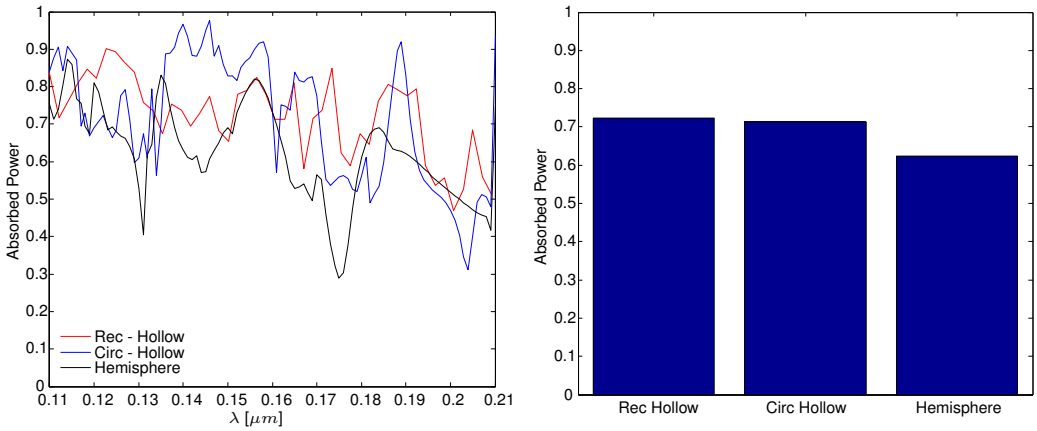

(a) Absorbed power across the band (b) Absorbed power averaged

Figure 4.35.: The absorbed power across the entire bandwidth of the L-band for the hollow and hemispherical cavity designs.

aperture and that region, thus omitting the surrounding trapezoidal cavity between the hemispherical layer and the Si_3N_4 (see figure 4.30 for the actual proposed geometry and figure 4.31 for the simulated model).

The results of this analysis show again good agreement between the rectangular and circular approximations to the hollow design, with the circular cavity predicting an absorption factor of 0.71 and the rectangular arrangement a factor of 0.72 across the band. A more significant difference is observed at discreet frequencies (figure 4.35(a)), however this was to be expected as the rectangular cavity in this instance is fed by a rectangular waveguide and the circular by a circular waveguide and thus the mode excitations are of slightly different forms. Both the circular and rectangular hollow designs are seen to out perform the original hemispherical proposal, which achieves an absorption factor of only 0.62.

Section 3.3 examined how increasing the exit aperture of possible SAFARI horn designs resulted in an improved throughput of the horns. As the exit aperture of the horns will serve as the entrance aperture to the detector cavity the affect of increasing this aperture on the cavity's performance is also of critical importance. To examine this the cylindrical Scatter code was used to consider the affect across the band (95 - 105 GHz) of varying the input guide radius from 0.08 mm to 0.2 mm. Furthermore, it was considered that as

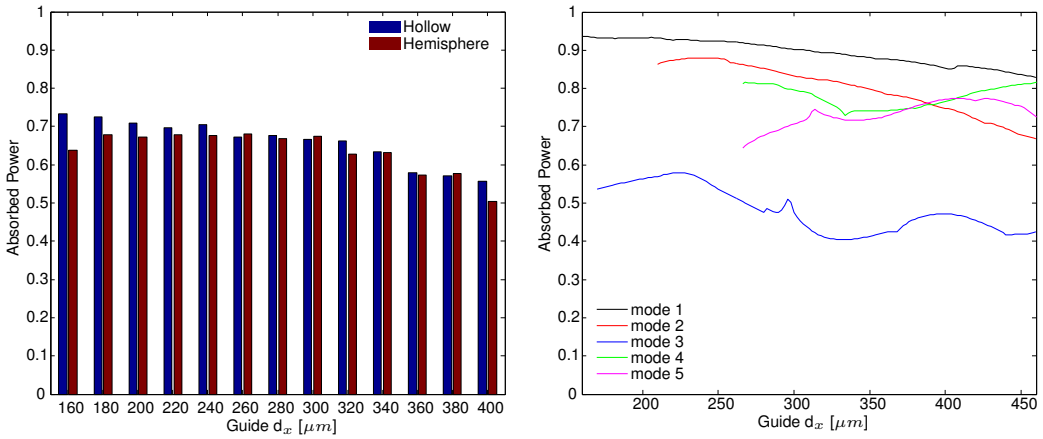

(a) Total absorbed power for the hollow and hemispherical cavity designs for varying input guide dimensions.

(b) Variation in absorbed power of individual modes for varying input guide dimensions of the hollow cavity design.

Figure 4.36.: Affect of increasing the guide dimensions on the absorbed power of the hollow and hemispherical cavity designs

additional modes were supported by the wider guide the optimum value of Δd may also have varied and as such this was again optimised for each separate guide radius. The results of this analysis can be seen for the hemispherical and the hollow cavity designs in figure 4.36(a). Considering first the results of the hemispherical design an initial rise in the absorption efficiency is observed followed by almost constant absorption for values of the guide dimensions less than those of the absorber, that is for $d_x = d_y < 320\,\mu\text{m}$. This suggests that in the case of the hemispherical design it is the proximity of the absorber to the entrance aperture that dominates its behaviour. Conversely, the hollow design displays a more steady and marginal drop off in absorption efficiency as the guide dimensions increase, however continues in general to out perform or match the hemispherical design.

Although the results indicate a gradual drop in performance for wider guide dimensions in the hollow design, the possibility remains that the dominant modes of the narrow guide case continue to perform as well but that the overall efficiency is reduced by poorer performing higher order modes. Should this prove to be the case, the lower overall efficiency would still represent a higher total level of absorption, as the additional modes would represent further contributions to the total absorbed power, albeit with a lower efficiency.

To examine this the modified Scatter code of section 4.3.2 was used to investigate the behaviour of certain individual modes in the hollow design. The results of this analysis can be seen in figure 4.36(b), it may also be noted that each mode was considered only from the guide dimensions at which it was supported across the entire band. Although some of the higher order modes demonstrate a less linear trend, in general the majority of modes appear to directly drop in efficiency with increasing guide dimensions. As such, one may not assume constant performance of individual modes and the overall reduction in absorbed power should be taken as generally indicative of the individual modes trend with increasing guide widths (in the case of the hollow cavity design).

Considering the almost constant trend of the hemispherical design, which is attributed to the absorbers proximity to the aperture, one may conclude that the results observed for the hollow cavity may be the result of the field diverging to beyond the bounds of the absorber for the larger input dimensions. As such, a third design was considered in which the absorber is kept 50 μm from the aperture and no cavity structure is in place, but instead a simple flat backend is positioned at an optimum distance Δd behind the absorber. A CAD model of this design may be seen in figure 4.37(b). The results of this design for various input guide dimensions can be seen in figure 4.37(a) and significantly out performs both the hemispherical and hollow designs as well as maintaining relatively constant absorption levels for varying guide dimensions, provided the dimensions remain smaller than those of the absorber. Furthermore, a comparison of the performance of the individual modes of the flat backend and hollow designs (figures 4.37(c) and 4.37(d)) indicate that as well as improved absorption less power is also radiated for the flat backend design.

Although CST simulations do allow for coupling of power between modes, each mode is nonetheless considered independently. As such, one must consider the specifics of each mode in the analysis of the data. The results of figure 4.37(e) show the absorption efficiency of each individual mode across the frequency range for which that mode is supported. Therefore, the spectral power distribution of the modes is not equal and thus cannot

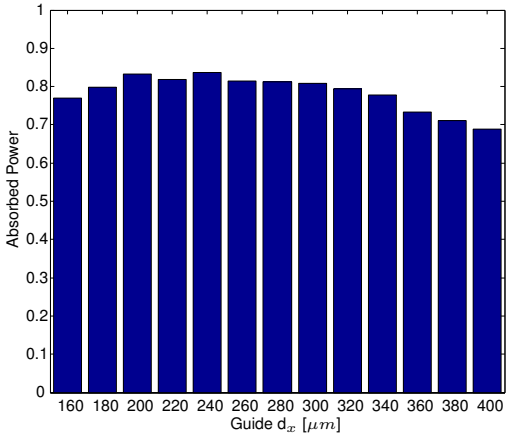

(a) Absorption efficiency of the flat backend design for varying input guide dimensions

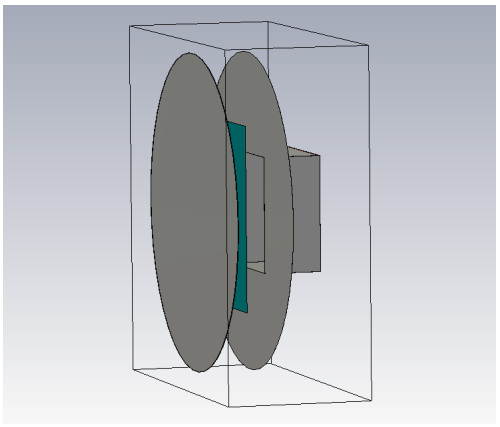

(b) CAD model of the flat backened design

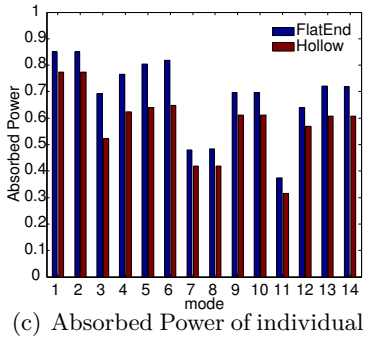

(c) Absorbed Power of individual modes, $d_x = 200\mu$m

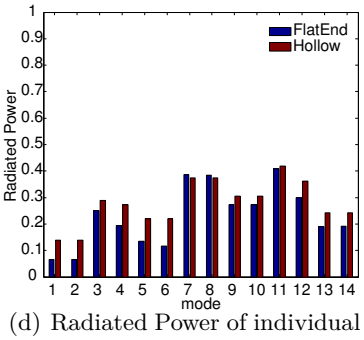

(d) Radiated Power of individual modes, $d_x = 200\mu$m

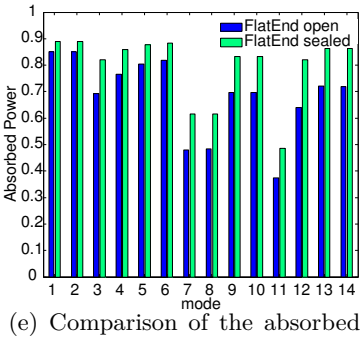

(e) Comparison of the absorbed power of individual modes with the opening to free space sealed.

Figure 4.37.: The flat backend cavity design, including its analysis for varying input guide dimensions, the performance of the individual supported modes and the improvement to be gained in sealing the cavity. The average absorbed power ratio for the open and sealed variations (CST simulations) of the design are; $P_{\text{open}} = 0.747$ and $P_{\text{sealed}} = 0.835$, respectively with the Scatter absorption efficiency for the $d_x = 200\,\mu$m case equating to $P_{\text{scatter}} = 0.832$

simply be averaged to establish the total absorption efficiency. Instead the efficiency of the system is determined by considering the mean of all modes supported at a specific frequency and averaged with the respective mean of all modes supported at all subsequent cut-off frequencies. This is outlined in table 4.3.

Originally the hollow cavity design was intended to optimise the absorption and minimise returned and radiated power, however due to the manufacturing constraints of the SAFARI system a 50 µm opening has to be maintained. The results of figure 4.37 indicate that, given the presence of such an opening, one may not trap additional power by ex-

Table 4.3.: Establishing the total absorption efficiency of the CST simulations of the open and sealed flat backend designs and comparison with the equivalent Scatter simulation. The results of figure 4.37(e) represent the absorption efficiencies of each mode from the point at which that mode is supported. As such, the average absorption ratio must be calculated for all modes supported at each subsequent cut-off frequency and these again averaged to better account for the spectral power distribution.

Mode	$\nu_{\text{cut-off}}$ [THz]	$\overline{P_{\text{open}}}$	$\overline{P_{\text{sealed}}}$	P_{Scatter}
1	<1.4	0.79	0.864	
2	<1.4			
3	<1.4			
4	<1.4			
5	1.5	0.797	0.87	
6	1.5			
7	1.68	0.714	0.811	
8	1.68			
9	1.68			
10	1.68			
11	2.12	0.686	0.796	
12	2.12			
13	2.12			
14	2.12			
Total		0.747	0.835	0.832

tending the cavity depth as was attempted in the hollow cavity design. As opposed to trapping the power the deeper cavity instead allows for a more divergent field distribution to ultimately avoid absorption. Thus, the best solution involves maintaining a close proximity to the entrance aperture and placing the flat backend at the optimised distance behind the absorber, regardless of the resulting side wall opening. If the manufacturing constraints could be overcome so as to seal the walls in this arrangement then the CST simulations predict an absorption factor of $P_{\text{sealed}} = 0.835$, which compares favourably with the Scatter predictions of $P_{\text{scatter}} = 0.832$ that also do not consider the opening. As was seen in section 4.4.1 figure 4.16, introducing an opening to the cavity walls alters the electromagnetics of the structure and consequently prevents one from establishing exact values for the absorbed and radiated power through comparison of the sealed and open cases. This effect is again observed here, where the average radiated power (accounting for the spectral power distribution) of the flat backend design in figure 4.37(d) equates to

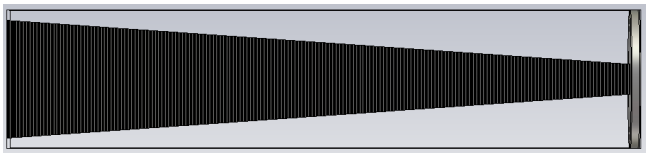

(a) SAFARI Pixel

Figure 4.38.: A SAFARI type horn and cavity for a Scatter analysis

$P_{\text{radiated}} = 0.208$. One may note that the total absorbed power of the open case however, $P_{\text{open}} = 0.747$, is not equivalent to the absorbed power of the sealed case less the radiated power of the open case, which would result in $P_{\text{sealed}} - P_{\text{radiated}} = 0.627$. It was further observed (figure 4.23) that when the surface area of the cavity wall opening is reduced additional power is reflected at the transition to the cavity, or returned from the cavity. This additional increase in returned power would be accounted for in determining the absorbed power of the sealed case and as such, the observed results are as expected, with the absorbed power of the open case P_{open} lying between P_{sealed} and $P_{\text{sealed}} - P_{\text{radiated}}$. One may also note from this approximation that the center point of P_{sealed} to $P_{\text{sealed}} - P_{\text{radiated}}$ equates to 0.731, which agrees reasonable with the actual value of $P_{\text{open}} = 0.747$.

Including the Horn

The cavity analysis thus far has focused on a simple waveguide feed and furthermore also assumed all supported modes of that guide to be equally excited. This is not truly representative of the SAFARI system, where the detector cavities will be fed by a horn antenna. Considering the variation in absorption efficiency for the different supported modes of the previously considered waveguides, one may appreciate that it is the effective field distribution entering the cavity that is of key importance. In the case of a horn antenna the effective field distribution results from significant coupling of power between modes as they propagate through the antenna and may differ to the field formed in a waveguide in which all modes are equally excited. Consequently, one may also expect the optimum positioning of the backend Δd to differ to that of the waveguide fed case.

The electrical size of the SAFARI horn antenna preclude them from being considered in CST Microwave Studio and as such this analysis relies completely on the mode matching Scatter approach. To consider both the horn antenna and the detector cavity in a Scatter simulation one must excite the horn from its actual entrance aperture and attach the cavity to the exit aperture, as can be seen in figure 4.38(a). As previously outlined, the Scatter approach determines the absorbed power from the returned power as P_{in} - $|S_{11}|^2$. In the case of a single waveguide entering into a larger cavity this may be directly applied, however, a horn antenna supports successively fewer modes along its length, when excited at the wider aperture. Therefore, the S_{11} of such a system will contain significant reflected contributions from modes not present in the detector cavity region and thus will not directly relate to the amount of absorbed power. To account for this the primary Scatter loop must be split into two sections, one considering the horn antenna and the other the cavity. At the junction between these sections the Scatter loop is essentially re-initialised while taking the throughput of the horn as the cavity excitation. This is accomplished by setting $S_{11a} = S_{22a} = 0$, $S_{21a} = S_{21\text{horn}}$ and $S_{12a} = S_{12\text{horn}}$. As previously mentioned (see chapter 3), an extended initial section is often required in Scatter to suppress otherwise excited evanescent modes. This is also the case here and the initial waveguide segment should be extended by approximately one wavelength. Alternatively, one may also account for an entire pixel through eigendecomposition. Considering the eigenvalues of $\mathbf{S_{11}^{\dagger}}.\mathbf{S_{11}}$ allows one to ascertain which fields are completely reflected at, or before, the throat aperture (as they contain eigenvalues of one). Furthermore, evanescent modes do not propagate and result in eigenvalues of zero. Thus, by considering the eigenvectors of the system one may identify the modes of interest as those with fractional eigenvalues. As such, the reception pattern can be synthesised by adding in quadrature the far field patterns of those eigenfields which suffer some absorption and ignore the eigenvalues of value 0 or 1.

In an effort to approximate the leakage and resulting absorbed power for the open full pixel case, the mean of the radiated power of all modes, again accounting for the spectral power distribution, of the waveguide fed case is considered. For comparison with horn designs 1

and 2 a waveguide of width $d_x = 160\,\mu\text{m}$ is considered and results in $\overline{Rad_{160\mu\text{m}}} = 0.194$ and for horn designs 3 and 4 a width of $300\,\mu\text{m}$ results in $\overline{Rad_{300\mu\text{m}}} = 0.163$. These waveguide dimensions correspond to the respective horn exit apertures. The median of the distribution between the sealed results ($P_{scatter}$) and the sealed results less the radiated power of the waveguide fed cases ($P_{scatter} - Rad$) was taken as an estimated value for the actual absorption factor with the width of that distribution representing the uncertainty.

Table 4.4.: Absorption ratio of a L-band SAFARI pixel using the flat backend cavity design and the proposed horn designs. The average radiated power of the waveguide fed cases corresponding to the dimensions of the respective horn exit apertures are considered in approximating the actual absorbed power of the open case P_{approx}.

Horn	Δd	$P_{scatter}$	P_{approx}
Design 1	$68\,\mu\text{m}$	0.679	0.582 ± 0.097
Design 2	$68\,\mu\text{m}$	0.694	0.597 ± 0.097
Design 3	$51\,\mu\text{m}$	0.859	0.777 ± 0.082
Design 4	$52\,\mu\text{m}$	0.859	0.777 ± 0.082

Table 4.5.: Absorption ratio of a L-band SAFARI pixel with the cylindrical horn variants and using the flat backend cavity design. The average radiated power of the waveguide fed cases corresponding to the dimensions of the respective horn exit apertures are considered in approximating the actual absorbed power of the open case P_{approx}.

	$d_{absorber} = 320\,\mu\text{m}$			$d_{absorber} = 640\,\mu\text{m}$		
Horn	Δd	$P_{scatter}$	P_{approx}	Δd	$P_{scatter}$	P_{approx}
Design 1	$22\,\mu\text{m}$	0.770	0.673 ± 0.097			
Design 2	$22\,\mu\text{m}$	0.768	0.671 ± 0.097			
Design 3	$30\,\mu\text{m}$	0.589	0.507 ± 0.082	$30\,\mu\text{m}$	0.819	0.722 ± 0.097
Design 4	$30\,\mu\text{m}$	0.587	0.505 ± 0.082	$30\,\mu\text{m}$	0.815	0.718 ± 0.097

This analysis was conducted for the pyramidal horn designs of table 3.9 and the cylindrical variations of these designs. The results of both these analyses are outlined in tables 4.4 and 4.5. In the pyramidal case a clear improvement in the level of absorption is observed for designs 3 and 4, which support a higher total number of modes. In the circular case this is seen first not to hold, however, considering that the diameter of the cylindrical horn

designs equates to twice the width of the pyramidal designs (in order to sustain equivalent numbers of modes, see section 1.2.2), one observes that the entrance aperture of diameter 600 μm significantly exceeds the absorber dimensions of diameter 320 μm. As such, the analysis of the cylindrical variations of design 3 and 4 were repeated for an absorber width of 640 μm and the results can be seen to be in broad agreement with those of the pyramidal case. It should be noted that should this design be implemented in SAFARI the larger absorber surface area required would also increase it's susceptibility to cosmic rays.

4.6.3. S-band

The results of the L-band analysis predict optimum performance for the flat backend design. Ideally, one could merely scale this design in terms of wavelength and obtain identical results for the S-band. Considering the mid wavelength of the L-band to be 160 μm then the 100 μm gap equates to 0.625 λ_0. In the case of the S-band with $\lambda_0 = 52.5$ μm the gap would have to be reduced to a length of only 32.8 μm. This is unfortunately not possible for manufacturing reasons, and should these obstacles be overcome then the reduced opening would also improve the L-band performance. As opposed to scaling the design, the L-band cavity is instead directly taken for application to the S-band. Although this results in a significantly larger gap in terms of wavelength, the electrical size of the absorber is also equivalently larger and should therefore result in higher levels of absorption. The results of a CST Microwave Studio analysis of the waveguide fed case of this design confirms this assumption and yields higher absorption levels per individual mode than were observed in the L-band (see figure 4.39(a)). The levels of radiated power also compare favourable with those of the L-band.

The analysis was expanded to include the entire SAFARI pixel using the Scatter technique in conjunction with the levels of radiated power determined using CST Microwave Studio for the equivalent waveguide fed cases. The results of this analysis are outlined in table 4.6 and 4.7 for the pyramidal and cylindrical horn variations, respectively. Again reasonable agreement is observed between both the pyramidal and cylindrical designs.

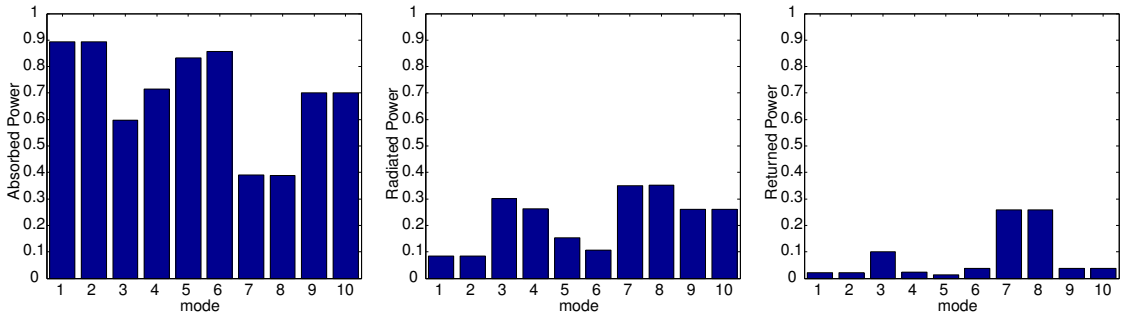

(a) Absorbed Power (b) Radiated Power (c) Returned Power

Figure 4.39.: CST Microwave Studio simulation results for the S-band flat backend design fed by a waveguide 50 µm × 50 µm with $\Delta d = 14.1$ µm. The average absorption factor equates to 0.757 and the average factor of radiated power to 0.19.

Table 4.6.: Absorption ratio of a S-band SAFARI pixel using the flat backend cavity design and the proposed horn designs. The average radiated power of the waveguide fed cases corresponding to the dimensions of the respective horn exit apertures are considered in approximating the actual absorbed power of the open case P_{approx}.

Horn	Δd	$P_{scatter}$	P_{approx}
Design 1	31 µm	0.515	0.420 ± 0.095
Design 2	31 µm	0.529	0.434 ± 0.095
Design 3	56 µm	0.733	0.641 ± 0.092

Table 4.7.: Absorption ratio of a S-band SAFARI pixel with the cylindrical horn variants and using the flat backend cavity design. The average radiated power of the waveguide fed cases corresponding to the dimensions of the respective horn exit apertures are considered in approximating the actual absorbed power of the open case P_{approx}.

Horn	Δd	$P_{scatter}$	P_{approx}
Design 1	25 µm	0.551	0.456 ± 0.095
Design 2	25 µm	0.547	0.452 ± 0.095
Design 3	45 µm	0.790	0.698 ± 0.092

4.6.4. Conclusions

The results of this analysis suggest the flat backend cavity design to yield optimum results for the SAFARI system. However, this analysis has also made certain assumptions of which one should remain aware. Firstly, in considering a full SAFARI pixel all modes were equally excited at the horn antenna's entrance aperture. This may not accurately

represent the reality of the SAFARI system and could most importantly impact on the optimum value of Δd, which for example was seen to shift when the horn antenna replaced the waveguide feed. As such, it is suggested that the above analysis be repeated once the front end optics have been finalised to better account for the coupling of the field into the horn antennas.

Secondly, approximating the level of radiated power for the full pixel case was achieved using results from the waveguide fed cavity. In the case of the waveguide feed each of the supported modes is equally excited, whereas in the case of the horn antenna power couples between modes before entering the cavity and hence results in a different field distribution. As such, the level of radiated power may be expected to differ to that of the waveguide fed system. In the case of an improvement in the levels of absorption for the sealed horn fed cavity compared to those of the sealed waveguide fed system one may assume that the effective field distribution of the horn antenna more closely resembles that of the highly absorbed modes and that consequently the levels of radiated power may be expected to be less than the averaged waveguide case, where all higher order modes where equally excited. This assumption however only holds for the case of the horn antenna feed out performing the equivalent sealed waveguide fed system. Should this not be the case then the opposite may be assumed to hold true.

Future work may therefore examine including the gap in the Scatter code. This may be achieved using the approach of the annular trap model outlined in this chapter, however, instead of expanding to waveguide modes, considering the coupling to free space modes upon entering the cavity and then stepping back to waveguide modes. Additionally, one may consider exporting the field at the horn exit aperture provided by Scatter in one of the supported field file formats of CST Microwave Studio (these include .fsm, .rsd, .nfd or .esf). Presumably, it would then be possible to consider the horn antenna in Scatter and conduct a complete cavity analysis using CST. Finally, once the SAFARI front end optics are finalised a subsequent analysis should be conducted to include coupling from the optics to the pixels.

5. SEARCH

5.1. Introduction

This chapter outlines some additional work made to an ESA mission proposal, which evolved out of the initial participation of the author of this work in a ESA - FFG (Research Organisation of Austria "**F**orschungs**f**örderungs**g**esellschaft") workshop and summer school hosted in Alpbach, Austria. This was a two week workshop with a total of 60 participants, the goal of which was the development of a possible Exoplanet mission proposal. The structure of the program broke the participants into four groups of 15, each tasked with the development of a unique proposal, and was also accompanied by a series of lectures relevant to the area. This was then complemented by a second one week follow on ESA-FFG workshop and hosted by the FFG in Graz, Austria. This involved a workgroup of 15 of the previous 60 participants and aimed at expanding on one of the initial proposals. The workshop allowed for the fundamentals of the proposal to be finalised in a group setting, however specific details were subsequently analysed by the workgroup in the following months.

The author of this work remained heavily involved in maturing and finalising the mission proposal in the months following both workshops and the final resulting mission plan was selected by ESA for consideration as a future roadmap project. The work was also submitted to the peer reviewed journal Experimental Astronomy as a co authored paper of the workgroup members, which included, along with the author of this work, M. Mohler,

J. Bühl, S. Eggl, V.T. Eybl, F. Farago, A. Jacimovic, L. Hunger, N.L.B. Lauritsen, D. Ludena, M. Meisnar, A. Reissner, N. Sarda, B. Toullec, and M. Viñas Tió.

The author's contribution to the work of this journal paper, which may be seen in appendix B, was in the optical design of the payload and involved, along with S. Eggl, J. Bühl (also on the optical design team) and input from the group at large, in moving from the concept of using spectropolarimetry to the design of an actual optical system. Subsequent to the publication of this journal paper the author of this work further advanced some of the optical designs proposed. Specifically, additional work was completed on assessing the exact mirror configuration of the telescope design and the range calculations, originally completed by S. Eggl in the journal paper of the proposed system were recalculated. These two additions are outlined below:

5.2. Telescope Configuration

As outlined in the previous sections the telescope configuration proposed is that of a Ritchey-Chrétien with a focus positioned between the primary and secondary, where the light would enter a tapered baffle through a stop for stray light reduction. A basic ray tracing analysis (as this work is only meant as a proof of concept) of such a telescope design was carried out using ZEMAX.

Spot diagrams of the ray tracing analysis can be seen in figure 5.1(b) and show that although a small amount of coma and some minor spherical aberrations are present, the system is nearly diffraction limited. The outlined design is a more than sufficient starting point for a future complete optical design should the project ever be built upon by ESA. The mirrors are separated by 12 m and their parameters, arrived at through a ZEMAX analysis, are given in table 5.1.

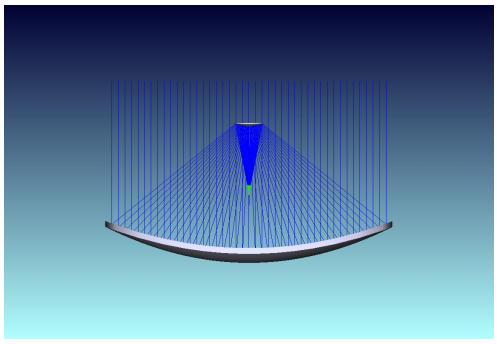

(a) 3D Zeemax ray trace of the proposed Telescope design

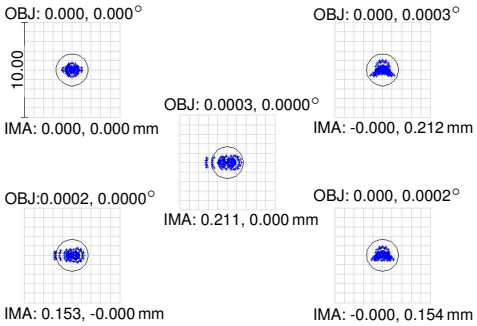

(b) Spot diagrams of a Zeemax ray tracing analysis

Figure 5.1.: Zeemax Analysis of one possible telescope configuration

Table 5.1.: Telescope mirror parameters

Mirror	**Radius**	**Semi-Diameter**	**Conic**
Primary Mirror	-18 m	9 m	-1.013
Secondary Mirror	-2.083 m	0.89 m	-2.52

5.3. Range of the Proposed System

Considering the telescope and instrument design outlined and making reasonable assumptions for other factors in the system the following estimate of the proposed system's range was conducted. An estimation of the amount of photons arriving at the system's CCD from an exoplanet was calculated by assuming a star to be a perfect black body radiator. As such, the number of photons emitted per second from a star, for a single polarisation, could be determined by considering the energy density in the spectrum using Planck's law, as shown in equation 5.1.

$$N_{Star} = 2\pi r_s^2 \int_{\lambda}^{\lambda+\Delta\lambda} \left(\frac{\frac{8\pi hc}{\lambda^5} \frac{1}{\exp \frac{hc}{\lambda kT} - 1}}{E_{Photon}(\lambda)} \right) d\lambda \tag{5.1}$$

Where h, c and k have their standard values, r_s represents the radius of the host star and $E_{Photon}(\lambda)$ the energy of a photon at the relevant frequency. An estimate of the number of photons reaching the CCD of the proposed setup from the star itself for an exposure time of τ can thus be determined by accounting for the inverse square dispersion $\frac{1}{4\pi d_s^2}$, where

d_s is the distance to the host star, and also accounting for the total collecting area of the telescope, A, the throughput of the optical system, Θ and the quantum efficiency of the detector, Q. This results in equation 5.2, where *reduction* refers to the reduction factor imposed on the host star through use of the phase mask and the integral spectrograph.

$$N_{Star-CCD} = \left(\frac{r_s}{d_s}\right)^2 \tau A \Theta Q \int_{\lambda}^{\lambda+\Delta\lambda} \left(\frac{4\pi}{\lambda^4} \frac{1}{\exp\frac{hc}{\lambda kT} - 1}\right) d\lambda \times reduction \tag{5.2}$$

The number of photons detected by the CCD from the exoplanet is determined by considering the distance of the planet to its host star, $\frac{1}{4\pi d_p^2}$, where d_p is the distance between the planet and host star, and also factoring in the effective area of the planet upon which light may be incident, πr_p^2, the phase angle, ϕ, the planetary albedo, a_{geo} and the hemispherical expansion of the reflected radiation, $\frac{1}{2\pi d_p^2}$. This results in equation 5.3.

$$N_{Planet-CCD} = \left(\frac{r_s}{d_s}\right)^2 \tau A \Theta Q \int_{\lambda}^{\lambda+\Delta\lambda} \left(\frac{4\pi}{\lambda^4} \frac{1}{\exp\frac{hc}{\lambda kT} - 1}\right) d\lambda \tag{5.3}$$

$$DL = \frac{Full\,Well\,Capacity}{RMS_{noise}} \tag{5.4}$$

In establishing the range of the proposed system the detection limit of the CCD is considered ($N_{Planet-CCD}$), and a very simple approach for determining a lower bound on this value is outlined in equation 5.4. Two criteria were then set for the system: firstly, the number of photons reaching the CCD from the exoplanet must be greater than 10 times this limit; $N_{Panet-CCD} \geq 10 \times DL$, and secondly, the contrast ratio between the detected photons of the host star and those of the exoplanet must also be greater than 10 times the limit; $\frac{N_{Panet-CCD}}{N_{Star-CCD}} \geq 10 \times DL$. Setting these limits and solving equations 5.1 to 5.4 for the smallest detectable exoplanet radius r_p results in equations 5.5 and 5.6.

$$R_{Planet-CCD} \geq \frac{d_s d_p}{r_s} \sqrt{\frac{2 \times 10 \times DL}{\tau \phi a_{geo} A \Theta Q \int_{\lambda}^{\lambda+\Delta\lambda} \left(\frac{8\pi}{\lambda^4} \frac{1}{\exp\frac{hc}{\lambda kT} - 1}\right) d\lambda}} \tag{5.5}$$

$$R_{Planet-Contrast} \geq d_p \sqrt{\frac{2 \times 10 \times DL}{\phi a_{geo}}} \times \sqrt{reduction} \tag{5.6}$$

The only completely unknown factor in equation 5.5 is that of the host star's radius. This can be interpolated from the Hertzsprung-Russel (HR) diagram for a given temperature if the target sample is restricted to main sequence stars. The HR diagram relates the temperature of a star to its luminosity and there is a constant relationship between a star's luminosity, radius and temperature, as outlined in equation 5.7.

$$\frac{L}{L_\odot} = \left(\frac{R}{R_\odot}\right)^2 \left(\frac{T}{T_\odot}\right)^{-4} \tag{5.7}$$

Using the formulas derived in this section an analysis was carried out on the proposed system to establish a lower bound on its range. In carrying out this analysis, stellar and planetary absorption losses were neglected. The planetary phase angle ϕ, which ranges from 0 to 1, was set at 0.5 and a planetary albedo equivalent to that of the Earth's (0.36) was assumed. The total collecting area of the telescope, A, was taken as the surface area of the primary mirror and the total throughput, $\Theta = 0.3$. Regarding this estimate, the phase mask coronagraph will reduce the planet's light close to the optical axis by approximately 50%, as can be seen in [31]. The photonic spectrograph has been considered as having a throughput of 60%. All other components are considered as providing lossless performance, except for the CCD's quantum efficiency. A quantum efficiency, Q, of 0.9 was assumed and a CCD detection limit DL of 10^{-5}. With the initial values outlined the range of the system was calculated for exposure times of 1 and 45 days, resolutions of 70 and 700 and for targets 10 and 30 pc distant. The results of these calculations can be seen in figure 5.2.

Figures 5.2(a) and 5.2(c) represent the detection limits for the highest frequencies in low resolution mode. Restricted to an exposure time of 1 day, these plots suggest that the proposed system would be most effective for F and G type stars and would be capable of a full characterisation of a Super-Earth type planet up to 30 pc distant - dependent on its

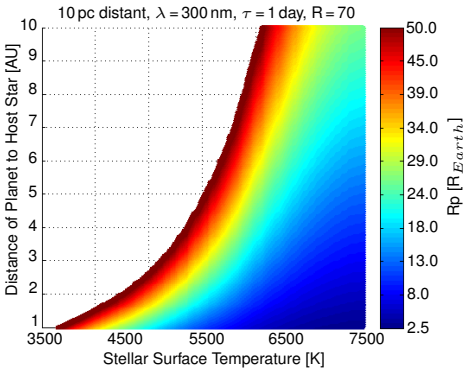

(a) Minimum detectable exoplanet radius 10 pc distant in low resolution mode for 1 day exposure time

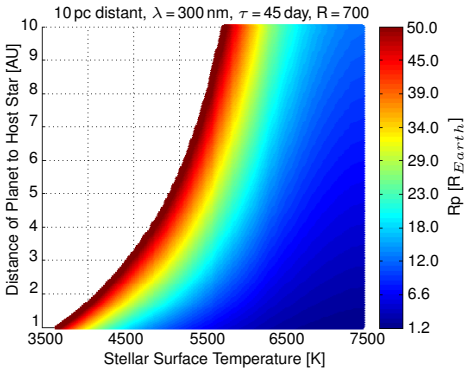

(b) Minimum detectable exoplanet radius 10 pc distant in high resolution mode for 45 day exposure time

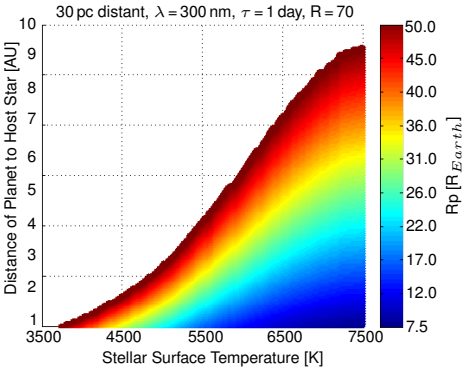

(c) Minimum detectable exoplanet radius 30 pc distant in low resolution mode for 1 day exposure time

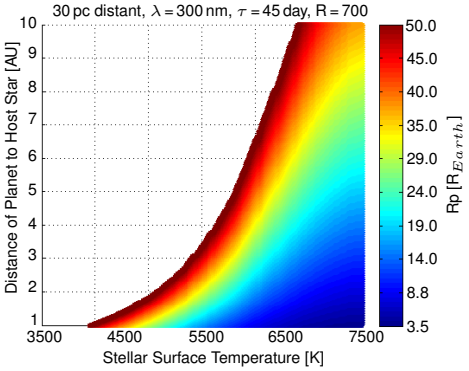

(d) Minimum detectable exoplanet radius 30 pc distant in high resolution mode for 45 day exposure time

Figure 5.2.: The detection limits of the system calculated at the highest frequencies of interest and at the extremities of the target sample, i.e. 10 pc and 30 pc. Each calculation was carried out for the proposed 1 day low resolution scan and the more in depth high resolution 45 day scan.

distance from the host star. Figures 5.2(b) and 5.2(d) consider the high resolution mode with an exposure time of 45 days. As can be seen these plots present a larger range of targets for the high resolution scans than was predicted for the low resolution mode. This is the result of the higher exposure time, which more than compensates for the increase in resolution. It should be noted that the specific CCD chosen will ultimately restrict the value of the maximum exposure time. From this basic analysis the outlined system may be considered promising and theoretically capable of characterising terrestrial planets at distances of $\approx 10\,pc$ and Super-Earth and Sub-Jovian planets at further distances.

6. Conclusion

The subject area of this thesis considered Terahertz systems and the development of quasi-optical modelling techniques for the analysis of such systems. This work was primarily driven by an ESA Technology Research Programme (TRP) to develop a Transition Edge Sensor (TES) array technology for future mm-wave to Far- Infrared (FIR) space applications. One particular future instrument requiring such technology, and which was taken as the reference case, is the Far-Infrared Instrument (SAFARI), which will constitute the European contribution to the proposed **SP**ace **I**nfrared-Telescope for **C**osmology and **A**strophysics (SPICA). The **A**tacama **L**arge **M**illimeter **A**rray (ALMA) also drove the work of this thesis in the development and application of quasi-optical analysis techniques. Furthermore, this work included the development of a novel optical design capable of characterising Exoplanets on a proposed future mission **S**pectropolarimetric **E**xoplanet **A**tmosphe**R**e **CH**aracerisation (SEARCH), the preliminary aspects of which were also considered in detail.

Chapter 1 of this thesis provides a general overview of these sources of motivation for the work. This includes a breakdown and description of the science cases of both SPICA and ALMA building on the experiences of past Infrared Space Observatories and others. The scientific benefits of moving to the Terahertz region of the spectrum are elaborated upon and examples given of areas not available at other bandwidths. This chapter also outlines some of the technical challenges associated with moving to the Terahertz band. Specifically, manufacturing difficulties encountered by Rutherford Appleton Laboratories - Space (RAL-Space), a partner institution of the TES-TRP, are outlined. The assembly

of the cavity structure with a horn antenna array leads to the inclusion of a gap between detector cavities, and the manufacturing techniques used in the construction of the horn arrays necessitates a two step horn design. It is important to consider these limitations in interpreting the design analysis carried out through the subsequent thesis chapters. The final section of this chapter highlights some of the design criteria of the ALMA Band 5 system, which was considered in more detail in chapter 3.

The work reported on in this thesis made extensive use of commercial software packages, particularly CST Microwave Studio, and ray tracing packages, such as Optica. These served the purpose of both validating in-house developed modelling techniques, as well as allowing for the simulation of systems beyond the scope of the in-house mode matching software. Chapter 2 provides an overview of these commercial packages. The principle of the Finite Integration Technique employed by CST Microwave Studio is outlined and a description provided of the various solver types supported by the software. As well as outlining how to establish simulations of the type conducted throughout this work, specific features made use of are considered in more detail, so as the constraints and limitations are well understood. The principle of Gaussian Beam Mode analysis is also made use of in the work of the thesis and as such this chapter outlines the basis of the technique. Furthermore, a description of the operation of a Vector Network Analyser (VNA) is provided with a basic overview of the methodology and calibration of such a system.

Chapter 3 focuses on the application of in-house mode matching models to the analysis of horn antenna. This includes the use of the previously developed cylindrical Scatter code, as well as the newly developed pyramidal version of the code. Further enhancements made to both the cylindrical and pyramidal versions included the addition of a Singular Value Decomposition (SVD) analysis for the purpose of establishing the aperture efficiency, and ultimately the total horn efficiency, when coupling to incident fields. The work performed successfully implemented the mode matching approach for a structure with a rectangular cross-section and verified the model against both theoretical predictions and CST Microwave Studio simulations. A study on the input parameters of both the pyramidal and

cylindrical Scatter codes suggested that between 10 - 20 segments per wavelength be considered when constructing a geometry file and that the total number of modes considered, in the pyramidal case, should exceed that supported by the largest single element. In the cylindrical case, as no power couples between azimuthal orders, it was found that a maximum azimuthal order equivalent to that supported at the entrance aperture is sufficient. The coupling of a single moded pyramidal horn to a plane wave at normal incidence was found to agree with with the theoretical maximum, thus verifying the SVD technique employed. These new simulation tools were then applied to the analysis of SAFARI type horn antenna and the ALMA band 5 system.

The analysis of the SAFARI horn antenna considered both the long wavelength, or L-band, and the short wavelength, S-band, designs. Initially a traditional single moded pyramidal horn was designed and considered in the L-band followed by horns supporting 8 and 23 modes at the center of the band. This analysis concluded that additional modes contribute to the coupling to the incident field and thus improve the overall efficiency. However, the higher number of modes also broaden the beam pattern, which could result in cross-talk between neighbouring pixels in an array configuration. For manufacturing purposes, two step horn designs were also considered. The analysis concluded that the discontinuity results in the excitation of higher order eigenmodes, which, although increase the overall mode number, also often alter the form of the dominant mode to one that couples less well to a normally incident plane wave and thus adversely affects the resultant aperture efficiency. For comparative purposes this analysis was extended to cylindrical horn designs. It was found that in order for a cylindrical horn antenna to support approximately the same number of modes as its pyramidal counterpart its diameter must be almost double the width of the pyramidal variation. This significantly restricts the applicability of a cylindrical design to a SAFARI type array, in which the physical dimensions are limited by the pixel design. It is worth noting here, that this analysis is with no regard to the polarisation of the horns as the SAFARI system will not be sensitive to polarisation. Furthermore, for coupling to a plane wave at normal incidence only modes with on-axis power were found to contribute to the coupling. Only cylindrical modes of azimuthal order

1 contain on-axis power and as no coupling of power exists between various azimuthal orders this significantly reduces the effectiveness of the cylindrical designs. The results of the S-band horn designs confirmed the findings of the L-band analysis. Additionally, when examining the effectiveness of pyramidal and cylindrical designs in an array configuration, one must consider the packing density factors achieved by both designs. Accounting for this demonstrated that a cylindrical horn would have to out perform its pyramidal counterpart by a factor of 0.093 in order to provide the equivalent efficiency values.

The ALMA band 5 system was also considered. This included a Scatter analysis of the proposed horn design and the effectiveness of a hexagonal circular to rectangular transition step. These simulations found the horn design to perform as required in terms of cross-polar power and beam form and the hexagonal stage to also improve the transition across the geometrical discontinuity. The setup and alignment of a VNA measurement system was also outlined and measurement results found to be in agreement with the simulated data. A Scatter and Gaussian Beam Mode Analysis technique was implemented to analyse standing waves in the optical system. High frequency standing waves were found between the secondary mirror and the horn antenna and oscillated about the S_{11} pattern of the horn antenna itself, however at the level of -35 dB these were well within the operating parameters of the system. Incorporating an IR filter to the standing wave analysis yielded a significant increase in the level of reflected power, however considering the refractive index considered this was to be expected. Regular standing waves almost 5 dB in amplitude were also observed, however it is suggested that introducing a tilt to the IR filter setup could reduce this effect.

Chapter 4 examined the behaviour of sealed cavity regions. This included the construction, measurement and simulation of a simple aluminium structure, the comparison of the results of which allowed for the various resonant, ohmic and geometric discontinuity losses to be individually identified. This also provided excellent confirmation of the technique employed by CST Microwave Studio, which in turn was used to validate the in-house developed mode matching software, Scatter. Following consideration of a simple

hollow cavity, a novel approach to including a thin resistive sheet absorbing element to the Scatter code was developed and implemented. This technique was validated against CST Microwave Studio and found to provide excellent agreement for the case of the field distribution lying primarily within the boundaries of the resistive sheet. In the instances of significant power existing beyond these bounds it was concluded that to accurately account for the coupling of power around the sheet a coaxial mode set should be considered. Initially it was assumed that maximum absorption would occur when the absorbing sheet material was placed at a displacement of one quarter of the guide wavelength from the sealed end of a waveguide. Both Scatter and CST were used to examine this scenario and it was observed that the point of maximum absorption did not correspond to a quarter of the guide wavelength, as had been expected. Further examination revealed that the resistive sheet itself influences the field distribution and thus alters the intrinsic wavelength of the guide. An effort to experimentally verify these results was attempted using a newly designed cavity kit, composed of multiple annular rings between which a sheet material could be clamped in place. Unfortunately, repeatable results could not be obtained, due to the creases formed in the $75\,\mu m$ thick sheet. Furthermore, differences in the returned power for identical cavity geometries but constructed of different ring arrangements were observed. It was therefore concluded that the contact between ring elements significantly impacted on the results, suggesting closed resonant structures to be sensitive to sub-wavelength surface features.

The situation was also investigated of a gap existing in the side wall of a cavity. Initially, for empty PEC cavities, the amount of leaked power through such an opening was determined as one less the return power, using CST Microwave Studio. Given the difficulties associated with simulating electrically large structures, using Finite Integration Techniques, efforts were made to extrapolate the behaviour of larger cavities by examining smaller scaled variations. It was found however that, due to the significant difference in the number of higher order modes supported by successively larger cavities, no such trend exists. The situation was then considered of an open cavity housing an absorber. In such an instance it was found that a sealed cavity sustains a fundamentally different mode set to that of an

open cavity and as such monitoring only the returned power does not allow for both the leaked and absorbed power to be established. Using the farfield monitors of CST provided another means of calculating the leaked power, which could be combined with an absorber. This technique was confirmed against published results of simulations conducted for the SPIRE instrument. Efforts to develop a model in Scatter to account for the leaked power were made by introducing a trap region, that is a waveguide section with a radius larger to that of the cavity. The ratio of the field distribution of the supported modes that existed beyond the bounds of the cavity and in the larger trap region were recorded and the power coupled into these modes determined from the scattering parameters. Although, this did produce results which converged to an upper bound, the width of the trap region proved a free variable requiring an extensive number of modes and thus necessitating large simulation times. Future work may examine the technique in conjunction with a transformation to free space modes.

Having developed the necessary tools various cavity geometries were examined. Rectangular and circular cavities housing both circular and square absorbers were first considered. The absorber's surface area and not its geometry was found to influence its performance, with square and circular absorbers of equivalent surface area performing identically. However, the geometry of the waveguide proved critical, as circular and rectangular waveguide modes sustain significantly different field distributions. The geometry of the cavity region itself was of less significance for the sealed case. If an opening in the wall of the cavity was however introduced then a rectangular cavity results in a gap of larger surface area, compared to that of a circular cavity, and thus more power is lost for the rectangular case. Following this, various cavity back-short geometries were investigated. This included those designed by considering ray tracing principles, such as a hemispherical, oblate spheroidal and parabolic designs, and those resulting from microwave principles, including a flat back-short. From the analysis of these designs it was concluded that ray tracing designs only hold for field distributions with significant on-axis power, such as is found in the fundamental modes. For higher order modes and particularly multi-moded structures however, the flat back-short design performs best. This analysis was then extended to the specific

SAFARI cavity designs. Here it was again found that a flat back-end yielded optimum results. Furthermore, the various SAFARI horn designs of chapter 3 were considered in conjunction with the cavities. Here one observed that, provided the exit aperture dimensions do not exceed those of the absorber, a larger exit aperture, supporting a higher number of modes, improves the total levels of absorbed power.

Chapter 5 presents work which evolved out of an initial two week ESA workshop hosted in Alpbach, Austria. The chapter outlines some additional results obtained since the publication of a journal paper. This included an on-axis cassegrainian configuration telescope with a primary mirror 9 m in diameter. A novel form of choronagraphy was considered along with a light weight integral spectrograph, which, in conjunction with polarimetry, were shown to be capable of detecting an exoplanet up to 30 pc distant and as close as 1 AU to its host star. The chapter journal paper of appendix B should be considered to provide further context to these results.

Bibliography

[1] B. Swinyard and T. Nakagawa. The space infrared telescope for cosmology and astrophysics: SPICA A joint mission between JAXA and ESA. 2008.

[2] A. Burrows, M. Marley, W.B. Hubbard, J.I. Lunine, T. Guillot, et al. A Nongray Theory of Extrasolar Giant Planets and Brown Dwarfs. *Astrophys.J.*, 1997.

[3] H. Dole, G. Lagache, J.L. Puget, et al. The Cosmic Infrared Background Resolved by Spitzer. Contributions of Mid-Infrared Galaxies to the Far-Infrared Background. *A&A (Astronomy and Astrophysics)*, 2006.

[4] C. M. Baugh, C. G. Lacey, C. S. Frenk, et al. Can the faint submillimetre galaxies be explained in the Λ cold dark matter model? *Monthly notices of the Royal Astronomical Society.*, 356(3):1191–1200, January 2005.

[5] A. Pope, D. Scott, M. Dickinson, et al. The Hubble Deep Field North SCUBA Supermap IV - Characterizing submillimetre galaxies using deep Spitzer imaging. *Monthly Notices of the Royal Astronomical Society*, 370(3):1185–1207, 2006.

[6] SPICA Study Team Collaboration. SPICA Assesment Study Report - ESA/SRE(2009)6, 2009.

[7] D. Benford et al. Superconducting transition edge sensor bolometer arrays for submillimeter astronomy, 2007.

[8] P. de Bernardis, M. Bucher, C. Burigana, and L. Piccirillo. B-Pol: Detecting Primordial Gravitational Waves Generated During Inflation. *Experimental Astronomy*, 23:5–16, 2009.

[9] D. Leisawitz, C. Baker, A. Barger, et al. The Space Infrared Interferometric Telescope (SPIRIT): High-resolution imaging and spectroscopy in the far-infrared. *Advances in Space Research*, 40(5), 2007.

[10] A.B. Peck and A.J. Beasley. High resolution sub-millimeter imaging with ALMA. *Journal of Physics: Conference Series*, 131(1):012049, 2008.

[11] R. Bachiller and J.C. Quintanilla. *Science with the Atacama Large Millimeter Array: A New Era for Astrophysics*. Astrophysics and space science proceedings. Springer, 2008.

[12] B.E.A. Saleh and M.C. Teich. *Grundlagen Der Photonik*. Lehrbuch Physik. Wiley-VCH, 2008.

[13] F. Matossi, L. Bergmann, C. Schaefer, et al. *Lehrbuch der Experimentalphysik. 3. Optik*. Lehrbuch der Experimentalphysik: zum Gebrauch bei akademischen Vorlesungen und zum Selbststudium / von L. Bergmann und Cl. Schaefer. “de” Gruyter, 1972.

[14] P.F. Goldsmith. *Quasioptical Systems: Gaussian Beam Quasioptical Propogation and Applications*. IEEE Press/Chapman & Hall Publishers Series on Microwave Technology and Rf. John Wiley & Sons, 1998.

[15] E. McLoughlan. *Optimisation of a Near Field Scanning System*. Master Thesis, NUI Maynooth, 2012.

[16] B. Schincke and J. Lunn. *Basics of Vector Network Analysis*. 2005.

[17] E. Gleeson. *Single and Multi-moded Corrugated Horn Design for Cosmic Microwave Background Experiments*. Ph.D. Thesis, NUI Maynooth, 2004.

[18] K.A. Milton and J. Schwinger. *Electromagnetic Radiation: Variational Methods, Waveguides and Accelerators: Including Seminal Papers of Julian Schwinger*. Particle Acceleration and Detection. Springer, 2010.

[19] A.D. Olver, P.J.B. Clarricoats, A.A. Kishk, and L. Shafi. Microwave horns and feeds, 1994.

[20] Emil Wolf. New theory of partial coherence in the space-frequency domain. Part I: spectra and cross spectra of steady-state sources. *J. Opt. Soc. Am.*, 72(3):343–351, 1982.

[21] H.H. Hopkins. The concept of partial coherence in optics. *Proceedins of the Royal Society of London. Series A. Mathematical and Physical Sciences*, 208(1093):263–277, 1951.

[22] H. H. Hopkins. The Concept of Partial Coherence in Optics. *Proceedings of the Royal Society of London. Series A. Mathematical and Physical Sciences*, 208(1093):263–277, 1951.

[23] J.C. Dainty and R. Shaw. *Image science: principles, analysis and evaluation of photographic-type imaging processes*. Academic Press, 1974.

[24] C.A. Balanis. *Antenna Theory: Analysis and Design*. Knovel library. John Wiley & Sons, 2005.

[25] Q par Angus Ltd. Standard gain horns. `http://www.q-par.com/products/horn-antennas/standard-gain-horns`.

[26] H. Steinhaus. *Mathematical Snapshots*. Dover science book. Dover Publications, 1999.

[27] S. Asayama. Circular to Square Waveguide Transition for ALMA Band 5 OMT. Technical report, National Astronomical Observatory of Japan (NAOJ), 2007.

[28] M. Carter, A. Baryshev, M. Harman, B. Lazareff, et al. dALMA Front-end Optics. Technical report, 2004.

[29] N. Trappe. *Quasi-optical Analysis of the HIFI Instrument for the Herschel Space Observatory.* Ph.D. Thesis, NUI Maynooth, 2002.

[30] G. Chattopadhyay, J. Glenn, J.J. Bock, et al. Feed horn coupled bolometer arrays for SPIRE - design, simulations, and measurements. *Microwave Theory and Techniques, IEEE Transactions on*, 51(10):2139 – 2146, oct. 2003.

[31] N. Murakami, R. Uemura, N. Baba, et al. An Eight-Octant Phase-Mask Coronagraph. *Publications of the Astronomical Society of the Pacific*, 120:1112–1118, 2008.

Appendices

A. CST - Macros

A.1. Conical Horn Construction

```
'\#Language "WWB-COM"

Option Explicit
' Horn
Sub Main ()

'@ use template: Antenna (Horn, Waveguide)
' Template for Antenna in Free Space
' ================================
' (CSTxMWSxONLY)
' draw the bounding box
Plot.DrawBox True
' set units to mm, ghz
With Units
     .Geometry "mm"
     .Frequency "ghz"
     .Time "ns"
End With
' set background material to vacuum
With Background
     .Type "Normal"
     .Epsilon "1.0"
```

```
     .Mue "1.0"
     .XminSpace "0.0"
     .XmaxSpace "0.0"
     .YminSpace "0.0"
     .YmaxSpace "0.0"
     .ZminSpace "0.0"
     .ZmaxSpace "0.0"
End With

' set boundary conditions to open
With Boundary
     .Xmin "expanded open"
     .Xmax "expanded open"
     .Ymin "expanded open"
     .Ymax "expanded open"
     .Zmin "expanded open"
     .Zmax "expanded open"
     .Xsymmetry "none"
     .Ysymmetry "none"
     .Zsymmetry "none"
End With

' switch on FD-TET setting for accurate farfields
FDSolver.ExtrudeOpenBC "True"
Mesh.FPBAAvoidNonRegUnite "True"
Mesh.ConsiderSpaceForLowerMeshLimit "False"
Mesh.MinimumStepNumber "5"

'================================================================================

' Read in data from the geometry files
Dim sNextLength As Variant, sNextRadii As Variant, i As Integer, n As Integer
```

```
n = 382
Dim Lengths(10000) As Variant
Dim Radii(10000) As Variant, OuterR(10000) As Variant

Open "C:\...\Geometry_lengths.txt" For Input As #1
For i = 0 To n
        Line Input #1, sNextLength
        Lengths(i) = sNextLength
Next
Close #1
Open "C:\...\Geometry_radii.txt" For Input As #2
For i = 0 To n
        Line Input #2, sNextRadii
        Radii(i) = sNextRadii
        OuterR(i) = sNextRadii + 0.05
Next

Close #2
'================================================================================
'@ new component: component

Component.New "component"
With Cylinder
     .Reset
     .Name "Neck"
     .Component "component"
     .Material "PEC"
     .OuterRadius OuterR(1)
     .InnerRadius Radii(0)
     .Axis "z"
     .Zrange "0", Lengths(0)
     .Xcenter "0"
     .Ycenter "0"
```

```
     .Segments "0"
     .Create
End With
For i = 1 To n

' activate global coordinates
WCS.ActivateWCS "global"

' activate local coordinates
WCS.ActivateWCS "local"

' move WCS
WCS.MoveWCS "local", "0.0", "0.0", Lengths(i-1)

' Define cylinder
Dim r As String
If (i < n) Then
                If (OuterR(i) < OuterR(i+1)) Then
                r = OuterR(i+1)
                Else
                r = Radii(i) + 0.05
                End If
Else
        r = Radii(i) + 0.05
End If

If (i = n) Then
        If (OuterR(i)< OuterR(i-1)) Then
                r = OuterR(i-1)
        End If
End If

With Cylinder
```

```
     .Reset
     .Name i
     .Component "component"
     .Material "PEC"
     .OuterRadius r
     .InnerRadius Radii(i)
     .Axis "z"
     .Zrange "0", Lengths(i)
     .Xcenter "0"
     .Ycenter "0"
     .Segments "0"
     .Create
End With
Next
End Sub
```

A.2. Rectangular Horn Construction

```
'#Language "WWB-COM"

Option Explicit
' Rectangular Horn

Sub Main ()
'@ use template: Antenna (Horn, Waveguide)
' Template for Antenna in Free Space
' ================================
' (CSTxMWSxONLY)
' draw the bounding box
Plot.DrawBox True
' set units to mm, ghz
With Units
```

```
     .Geometry "mm"
     .Frequency "ghz"
     .Time "ns"
End With
' set background material to vacuum
With Background
     .Type "Normal"
     .Epsilon "1.0"
     .Mue "1.0"
     .XminSpace "0.0"
     .XmaxSpace "0.0"
     .YminSpace "0.0"
     .YmaxSpace "0.0"
     .ZminSpace "0.0"
     .ZmaxSpace "0.0"
End With
' set boundary conditions to open
With Boundary
     .Xmin "expanded open"
     .Xmax "expanded open"
     .Ymin "expanded open"
     .Ymax "expanded open"
     .Zmin "expanded open"
     .Zmax "expanded open"
     .Xsymmetry "none"
     .Ysymmetry "none"
     .Zsymmetry "none"
End With
' switch on FD-TET setting for accurate farfields
FDSolver.ExtrudeOpenBC "True"
Mesh.FPBAAvoidNonRegUnite "True"
Mesh.ConsiderSpaceForLowerMeshLimit "False"
Mesh.MinimumStepNumber "5"
```

```
'================================================================================

' Read in data from the geometry files
Dim sNextA As Variant, sNextB As Variant, sNextDelta As Variant, i As Integer,
n As Integer

n = 100
Dim a(10000) As Variant
Dim b(10000) As Variant
Dim OuterA(10000) As Variant
Dim OuterB(10000) As Variant
Dim delta(10000) As Variant

Open "C:\...\Geometry_a.txt" For Input As #1
For i = 0 To n
        Line Input #1, sNextA
        a(i) = sNextA
        OuterA(i) = sNextA + 0.05
Next
Close #1

Open "C:\...\Geometry_b.txt" For Input As #2
For i = 0 To n
        Line Input #2, sNextB
        b(i) = sNextB
        OuterB(i) = sNextB + 0.05
Next
Close #2

Open "C:\...\Geometry_delta.txt" For Input As #3
For i = 0 To n
        Line Input #3, sNextDelta
```

```
        delta(i) = sNextDelta
Next
Close #3

'================================================================================
'@ new component: component
Component.New "component"
With Brick
     .Reset
     .Name "Neck"
     .Component "component"
     .Material "PEC"
     .Xrange -0.5*OuterA(0), 0.5*OuterA(0)
     .Yrange -0.5*OuterB(0), 0.5*OuterB(0)
     .Zrange "0", delta(0)
     .Create
End With

With Brick
     .Reset
     .Name "solid2"
     .Component "component"
     .Material "Vacuum"
     .Xrange -0.5*a(0), 0.5*a(0)
     .Yrange -0.5*b(0), 0.5*b(0)
     .Zrange "0", delta(0)
     .Create
End With

'@ boolean subtract shapes: component1:solid1, component1:solid2
With Solid
     .Version 9
     .Subtract "component:Neck", "component:solid2"
```

```
End With


For i = 1 To n
' activate global coordinates
WCS.ActivateWCS "global"
' activate local coordinates
WCS.ActivateWCS "local"
' move WCS
WCS.MoveWCS "local", "0.0", "0.0", delta(i-1)

' Define Block
With Brick
     .Reset
     .Name i
     .Component "component1"
     .Material "PEC"
     .Xrange -0.5*OuterA(i), 0.5*OuterA(i)
     .Yrange -0.5*OuterB(i), 0.5*OuterB(i)
     .Zrange "0", delta(i)
     .Create
End With

With Brick
     .Reset
     .Name i
     .Component "component2"
     .Material "Vacuum"
     .Xrange -0.5*a(i), 0.5*a(i)
     .Yrange -0.5*b(i), 0.5*b(i)
     .Zrange "0", delta(i)
     .Create
End With
```

```
'@ boolean subtract shapes: component1:i, component1:i

With Solid
     .Version 9
     .Subtract "component1:" & i, "component2:" & i
End With


Next
End Sub
```

B. SEARCH

Exp Astron (2010) 28:101–135
DOI 10.1007/s10686-010-9193-2

ORIGINAL ARTICLE

Opening a new window to other worlds with spectropolarimetry

Maren Mohler · Johannes Bühl · Stephen Doherty · Siegfried Eggl · Vera Theresa Eybl · François Farago · Aleksandar Jaćimović · Lars Hunger · Nynne L. B. Lauritsen · David Ludena · Martina Meisnar · Alexander Reissner · Nicolas Sarda · Benjamin Toullec · Meritxell Viñas Tió

Received: 3 June 2010 / Accepted: 20 July 2010 / Published online: 9 September 2010

Abstract A high level of diversity has already been observed among the planets of our own Solar System. As such, one expects extrasolar planets to present a wide range of distinctive features, therefore the characterisation of Earth- and super Earth-like planets is becoming of key importance in

M. Mohler (✉)
Institute for Astrophysics, University of Göttingen, Göttingen, Germany
e-mail: marenmohler@gmx.de

J. Bühl
Institute of Applied Optics, Friedrich-Schiller-University Jena, Jena, Germany

S. Doherty
Dept. of Experimental Physics, National University of Ireland (NUI)—Maynooth, Maynooth Co., Kildare, Ireland

S. Eggl · V. T. Eybl
Institute for Astronomy, University of Vienna, Vienna, Austria

F. Farago
ASD, IMCCE-CNRS UMR8028, Observatoire de Paris, Paris, France

A. Jaćimović
Utrecht University, Utrecht, The Netherlands

L. Hunger
Institut für Astro- und Teilchenphysik, Universität Innsbruck, Innsbruck, Austria

N. L. B. Lauritsen
Niels Bohr Institute, University of Copenhagen, Copenhagen, Denmark

D. Ludena
Deutsches Zentrum für Luft- und Raumfahrt (DLR), Institut für Planetenforschung, Berlin, Germany

scientific research. The SEARCH (**S**pectropolarimetric **E**xoplanet **A**tmosphe**R**e **CH**aracerisation) mission proposal of this paper represents one possible approach to realising these objectives. The mission goals of SEARCH include the detailed characterisation of a wide variety of exoplanets, ranging from terrestrial planets to gas giants. More specifically, SEARCH will determine atmospheric properties such as cloud coverage, surface pressure and atmospheric composition, and may also be capable of identifying basic surface features. To resolve a planet with a semi major axis of down to 1.4 AU and 30 pc distant SEARCH will have a mirror system consisting of two segments, with elliptical rim, cut out of a parabolic mirror. This will yield an effective diameter of 9 m along one axis. A phase mask coronagraph along with an integral spectrograph will be used to overcome the contrast ratio of star to planet light. Such a mission would provide invaluable data on the diversity present in extrasolar planetary systems and much more could be learned from the similarities and differences compared to our own Solar System. This would allow our theories of planetary formation, atmospheric accretion and evolution to be tested, and our understanding of regions such as the outer limit of the Habitable Zone to be further improved.

Keywords Spectrography · Polarimetry · Coronography · Characterisation of atmospheres · Extrasolar planets

1 Introduction

In recent years, efforts to find extrasolar planets steadily increased and continue to do so. Advanced telescope technologies, such as those in Chile, allowed us to find a variety of exoplanets. The HARPS spectrograph at the 3.6-m telescope at La Silla is one of the leading ground-based data sources of exoplanet radial velocity curves and has already detected and confirmed a significant number of exoplanet targets [57, 59]. The launch of the CoRoT satellite in 2006 offered new possibilities for detecting exoplanets using high resolution photometry to measure transit curves. Together with ground-based

M. Meisnar
Institute for Solid State Physics, Vienna University of Technology, Vienna, Austria

A. Reissner
AIT—Austrian Institute of Technology, Wien, Austria

N. Sarda
Astrium Ltd, Hertfordshire, UK

B. Toullec
Supaero—Institut Supérieur de l'Aéronautique et de l'Espace, Toulouse, France

M. Viñas Tió
Escola Politécnica Superior de Castelldefels (EPSC), Barcelona, Spain

follow-up observations with HARPS the detection of the rocky Super-Earth planet CoRoT-7b was recently confirmed [46, 61]. High expectations have been raised by NASAs Kepler spacecraft, launched in March 2009, which will observe over 100,000 stars in the Cygnus constellation [12] with the aim of identifying specifically Earth and Super-Earth-sized planets.

Several more projects are in the pipeline. One example being ESPRESSO (Echelle Spectrograph for PREcision Super Stable Observations), a new generation instrument for the European Southern Observatory's VLT. It will combine the high stability of HARPS and the efficiency of UVES at the VLT and is planned to be the precursor of CODEX, a high resolution spectrograph for the European ELT [48]. A space mission with the primary objective of finding Earth-sized planets outside our solar system is NASAs SIM (Space Interferometry Mission) [78]. A ground-based version of this instrument, PRIMA (Phase Referenced Imaging and Microarcsecond Astrometry), is installed at the VLTI (the Very Large Telescope Interferometer) [15]. These two missions are expected to identify several more Earth-sized exoplanets via interferometry. Furthermore, ESA's GAIA mission scheduled for 2011 will provide a huge catalogue of approximately 1 billion stars up to magnitude 20 and will include astrometric, spectroscopic and radial velocity data. As such, one may assume that many new targets for further exoplanetary research will be available in a few years [44, 51]. Another two concepts being considered in Europe and Japan are the PLATO and SPICA projects.

The next logical step following detection is the characterisation and analysis of the catalogued exoplanets. A detailed analysis of the connection between planet features and host star characteristics will also be made possible by future detections in conjunction with the GAIA data. The characterisation of a large number of varied targets would be invaluable for the further development of present models. This characterisation of exoplanets in terms of their atmospheric properties is the purpose of the mission study SEARCH presented in this paper. The mission concept was developed during the Summer School held in Alpbach during July 21–30, 2009 with the title: Exoplanets: Discovering and Characterising Earth Type Planets and further studied during a Post Alpbach week at the Space Research Institute of the Austrian Academy of Sciences during November 24–27, 2009, in Graz, Austria.

Spectropolarimetry is still a relatively new technique, however the potential of the technique is being realised. This is reflected in similar approaches being suggested for both ground- and space-based projects [5, 67], which are currently on the exoplanetary communities' drawing-boards.

2 Science case

2.1 The method: spectropolarimetry

Polarimetry is a powerful technique for enhancing the contrast between a star and an exoplanet. Indeed, the light from an inactive star integrated over its

whole disk is usually unpolarised. However, when scattered by a planetary atmosphere and/or surface, the light becomes polarised, and thus the reflected light which reaches us presents a significant degree of polarisation. Therefore, measuring the polarisation degree of the incoming light very precisely, is equivalent to gaining five orders of magnitude in contrast [37]. Additionally, the dependence of the degree of polarisation on the wavelength presents characteristic features which can be used to infer the structure of the scattering atmosphere/surface. Significant work has been carried out to produce characteristic spectra of a wide range of planetary atmospheres and surfaces [27, 64, 69, 72–75].

One of the characteristics of planetary atmospheres which could be easily obtained through spectropolarimetry is the surface pressure. The Rayleigh scattering cross-section is $\propto \lambda^{-4}$. For low surface pressures, the atmospheric density allows only for single scattering events at short wavelengths, and the wavelength dependence of the Rayleigh cross-section suppresses the scattering of longer wavelengths. The degree of polarisation thus decreases with wavelength. For higher surface pressures, the atmospheric density will allow multiple scattering events at short wavelengths, which destroy the polarisation in this domain, while longer wavelengths will undergo only single scattering events and are significantly polarised.

Numerical simulations of different kinds of planetary atmospheres and surfaces, together with the observation of the planets of the Solar System, have shown that many planetary features have clear signatures in the polarisation spectrum: cloud coverage, cloud particle size and shape, ocean coverage, and other surface coverage properties such as the existence of potential vegetation. By comparing such simulations with measurements one is able to characterise these properties and acquire a quite detailed picture of the observed atmosphere.

The polarisation spectrum has broad features which do not require a high spectroscopic resolution: $R \approx$70–80 is sufficient to resolve them [32]. As such, a rough characterisation of an observed atmosphere is possible after only a short amount of time. The integration times needed to achieve a sufficient signal-to-noise ratio at this low resolution would allow for the rapid exploration of about 50 targets with different phase angles for each target, as will be described below. The variation of the polarisation signal with respect to phase angle provides information on the orbital inclination of the target exoplanet, which is a missing parameter in radial-velocity data. In turn, the orbital inclination allows for a more precise determination of the planetary masses (see Fig. 1, right). After a first orbital sampling phase at low spectral resolution ($R \approx 70$) high-interest exoplanets can be identified, on which further analysis could be carried out with longer exposure times and a higher spectral resolution. This would yield data on the the absorption lines in the full flux spectrum and on the chemical composition of the atmosphere.

The power of spectropolarimetry comes from its utilisation of both the spectral information and also polarised nature of the signal, which is usually lost when only a flux spectrum is taken. Limiting measurements to the

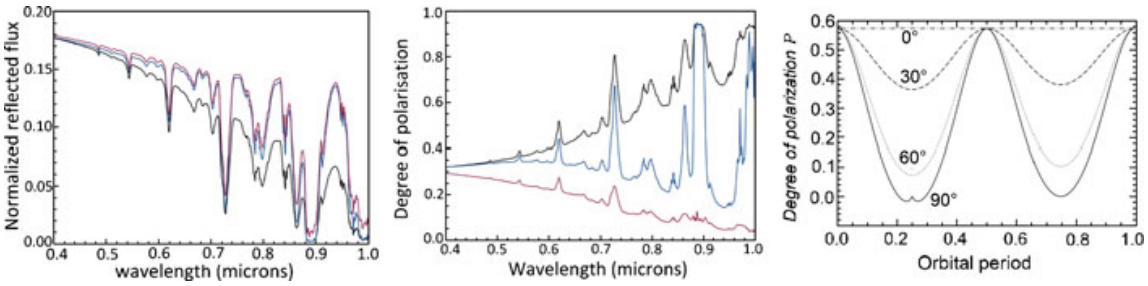

Fig. 1 The flux (*left*) and degree of polarisation (*middle*) of starlight reflected by three Jupiter-like exoplanets for the phase angle alpha 90. Planetary model atmosphere 1 (*black line*) contains only molecules, model 2 (*blue line*) is similar to model 1 except for a tropospheric cloud layer and model 3 (*red line*) is similar to model 2 except for a stratospheric haze layer. The flux spectra exhibit very similar features which are hard to interpret, while the polarisation spectra have distinctive slopes, giving easy access to atmospheric structure. Found in Stam et al. [75]. *Right* Variation of the polarisation degree with respect to planetary phase angle depending on orbital inclination for a Jovian planet [75]

flux spectrum would provide data only on the chemical composition of the atmosphere. It would be difficult to infer many important characteristics of the observed atmosphere, for example cloud properties and the surface pressure. That means it would be hard to distinguish between a thick Venus-like atmosphere and a thin Mars-like atmosphere. Basic surface features would also be inaccessible. Since this project aims at characterising planetary atmospheres, the aforementioned parameters are also of interest. For this reason spectropolarimetry was chosen as the preferred method.

2.2 Understanding the diversity of Exoplanets

Spectropolarimetry makes it possible to observe the distinct characteristics of planets around stars other than the Sun for the first time. Investigating the atmospheric and surface properties of a sample of extrasolar planets around different types of stars allows one to test current models of atmospheric evolution and habitability concepts. The proposed mission would be able to resolve a planet as close to its host star as 0.5 AU in a distance of 10 pc, and as close as 1.4 AU in a distance of 30 pc. That provides a wide range of planets from terrestrial Earth-like planets to gas giants, which would be sufficient for statistical analysis.

2.2.1 Exploring the diversity of rocky and icy worlds

For planets in the Earth to super-Earth mass range a huge variety of possible compositions can be expected. Planets unknown in the Solar System have been discovered, providing a possibility to check our understanding of planetary formation and evolution. The suggested types of low-mass planets range from Earths and super-Earths to ocean worlds, icy planets and even rocky cores of Neptune-type bodies. Models predict an upper radius limit

for terrestrial-type planets with a given mass [3, 79], separating dry rocky compositions from planets containing 10% and more water and other volatiles.

At the moment there is little knowledge of the early stages of planetary evolution. Numerical simulations have been performed, showing that planets may form with a much higher water content than is observed in the Solar System [3, 62]. Furthermore, it has been suggested that a super-Earth with the same bulk composition as Earth should be completely covered in water, since the surface of the planet scales with the square of the radius, while the volume follows a cubic law [49]. This could make ocean planets very common.

Above the terrestrial-type mass-radius limit, water worlds cannot be distinguished from planets with a significant atmospheric layer of H/He based on planetary radius and mass measurements alone [1]. Planets within this regime could be either super-Earths or mini-Neptunes [4]. It's possible to draw conclusions about the bulk composition from the mass/radius relationship (Fig. 2), but there are uncertainties regarding helium and carbon planets [71]. To make conclusions about the applicability of planetary composition models, one has to gain additional information about the planets atmospheric and surface properties. Williams and Gaidos [82] suggest the direct detection of the oceans glint, which makes a partially water-covered planet appear brighter near crescent phase. A planet that is covered completely with water appears darker than a Lambertian disk. Planets formed beyond the ice line, migrating inwards, as well as planets with a high concentration of volatiles delivered from impacts of planetesimals, end up as icy worlds, like Titan in the Solar System. Carbon planets [39] and rocky Neptune-cores are examples of exoplanets yet unknown. Neptune-like bodies could lose all of their hydrogen atmospheres due to stellar wind and high XUV flux either in the early phases of stellar

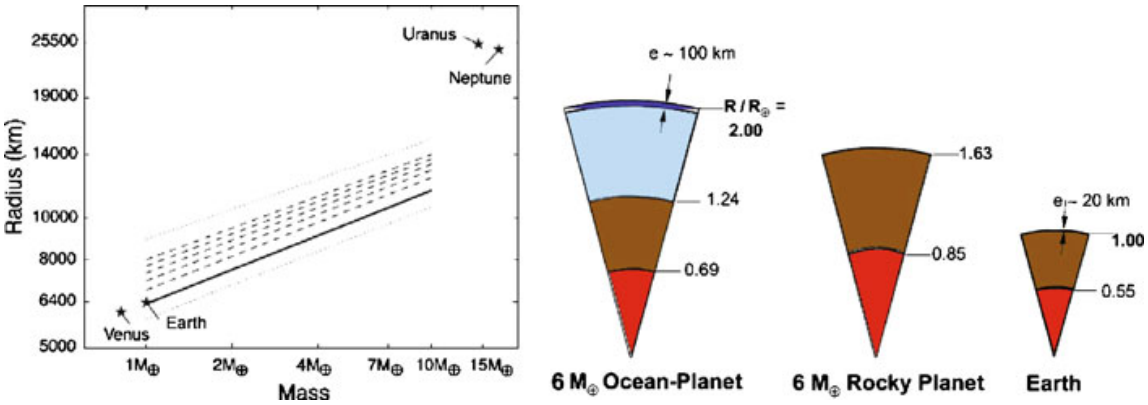

Fig. 2 *Left* Mass-radius relationship for ocean and rocky massive planets. The *solid black line* is the power-law relationship for terrestrial planets with 1–10 $M_\oplus$. The *dashed lines* above progressively represent the relationship for planets with 10, 20, 30, 40, and 50% H_2O. This family of planets has a fixed mantle-to-core proportion of 2:1. The minimum and maximum planetary radius relations with mass are shown as *dotted lines*. Venus, Earth, Uranus, and Neptune are shown for reference [79]. *Right* From *left* to *right*: calculated internal structure of a 6 $M_\oplus$ ocean planet, a 6 $M_\oplus$ rocky planet and the Earth, respectively [45]

evolution or during inward migration. These rocky bodies could evolve to a new species of terrestrial-type planets [38, 43].

While there is no theory to date regarding the suitability of water and ice worlds for hosting life, models exist to quantify the habitability of terrestrial-type, rocky planets. The Habitable Zone [36] (Fig. 5, right) is the concept widely used to describe the region around a star where life could possibly exist. Our concept of habitability is strongly based on the conditions suitable for life as we know it on Earth. Although used in a broader sense recently, the Habitable Zone (HZ) is originally defined as the distance from a star, where liquid water on a planets surface can exist. It is calculated based on the stellar flux received by a planet with an Earth-like atmosphere.

The inner edge of the HZ is determined by evaporation of oceans caused by a runaway greenhouse effect and the subsequent loss of water to space. This is believed to have happened on Venus, making it a dry planet with a dense CO_2 atmosphere [35]. The original paper by Kasting gives a conservative estimate for the inner border of the habitable zone of a G-star of 0.95 AU. The outer edge however is not as clearly defined, as the influence of CO_2 clouds is not yet fully understood. Estimates for the outer border of the HZ for a G-type star range from 1.37 AU [36] to 2.4 AU [20, 54]. Besides liquid water, a second factor for habitability is the presence of an atmosphere dense enough to maintain a stable surface temperature by the greenhouse effect. The greenhouse effect is caused by atmospheric gases like H_2O, CO_2 and CH_4, which are very efficient absorbing in the infrared, but not in the visible range of the spectrum. On Earth, the amount of CO_2 in the atmosphere is controlled by the carbonate-silicate-cycle, acting as a thermostat. Volcanic activity releases CO_2 into the atmosphere, which is washed out by weathering and subsequently gets buried in ocean sediments. At the subduction zones, these are transferred into the mantle. Therefore, plate tectonics is considered to be a major factor in making a planet a potential habitat, since it provides an efficient mechanism enabling a CO_2 cycle [26, 42].

At very early stages of planetary evolution chemical reactions in the freshly formed crust of the planet produce methane and ammonia, creating the planet's atmosphere together with water vapour. Since young stars are most active, photolysis in the upper layers of the atmosphere breaks up the molecules of CH_4, NH_3 and H_2O. As well as outgassed CO_2, hydrogen is lost to space, while carbon and oxygen react to form CO_2. So all terrestrial-type planets should start out with a CO_2-rich atmosphere [40–42]. If plate tectonics is active on a planet in the habitable zone, CO_2 from the atmosphere is recycled into the planets mantle, leaving behind an atmosphere dominated by nitrogen and depleted of carbon dioxide, similar to Earth [36]. Accordingly, the amount of CO_2 and nitrogen, respectively, in a planets atmosphere can be an indicator of the presence of plate tectonics.

There has been an ongoing discussion about whether Super-Earths are to be expected to maintain plate tectonics, and if there is a mass limit on plate tectonics. Some models predict stronger convection on terrestrial planets larger than Earth [80]. Others state that the increased mantle depth reduces

convection thus decreasing the likelihood of plate tectonics [58]. A sufficiently large sample of terrestrial planets should allow more stringent conclusions. Since nitrogen can not be observed in the spectral lines, the observation of non-CO_2 versus CO_2-rich atmospheres in different environments provides insights into the conditions for habitability.

Using spectropolarimetry, it is possible to not only determine the composition of the atmosphere, but also distinguish between dense and thin/no atmospheres. This information can be used to separate Earth-like, Mars-like and Venus-like atmospheres. Weather phenomena like clouds can be observed, which helps in gaining a deeper understanding of the conditions present at a planets surface.

Investigating samples of low-mass planets (1–30 $M_\oplus$) around different types of stars in various stages of evolution, the concept of habitability can be tested and refined, giving us the unique opportunity to set the Solar System in context. Observations of surface features like oceans and continents as well as atmospheric properties will provide the data needed to verify and improve currently adopted models.

Features that can be studied As mentioned before the analysis of atmospheres is based on the analysis of different features in the obtained spectrum. Table 1 shows several atmospheric features in the visible region of the spectrum.

One of the important features mentioned in Table 1 is the so called "red edge". A closer look at the Earth's spectrum reveals a high jump in it around 700 nm, which is the result of the chlorophyll in plants on Earth. The plants green colour is due to the absorbtion of light between ≈450–680 nm by the chlorophyll. As Fig. 3 (right) shows, the plants stop absorbing the light around 700 nm and the relative reflectivity spikes in this wavelength region. The expectation to see this feature in spectra of exoplanets is based on the assumption that plant life on other planets is similar to that on Earth. Unfortunately, the probability of observing this particular feature with the proposed telescope remains low.

2.2.2 Gas giants

The diversity among extrasolar planets is not limited to that of rocky planets. Extrasolar giant planets (EGPs), the most abundant among the currently catalogued exoplanets, offer, like the rocky ones, a considerable degree of

Table 1 Line position of atmospheric features in the visible range

Feature	Wavelength (nm)
H_20	514, 575, 610, 730, 830
O_2	626, 688, 767
O_3	Chappuis bands between 375–650
NH_3	552, 647
CH_4	486, 543, 576, 595, 629, 681, 703, 727, 790, 840, 864, 889
Red edge	≈700

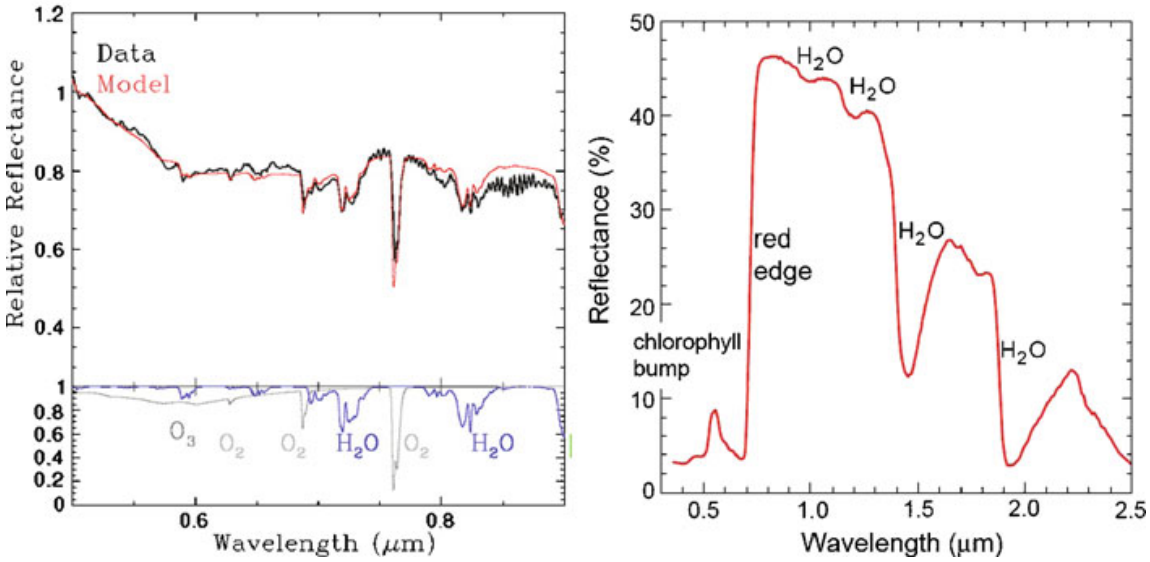

Fig. 3 *Left* Observed reflectivity spectrum in the visible of the Earth, as determined from earthshine. The data is shown in *black* and the model in *red*. The reflectivity scale is arbitrary [32]. *Right* Reflectance of a deciduous leaf with visible red edge [70]

variety due to the differences in their mass, age, radius, distance from host star, the stellar type and luminosity and the properties of the planetary system. The characterisation of the known EGPs combined with the knowledge of the Solar System giants would definitely improve our understanding of how planets and planetary systems form and evolve. The ongoing and scheduled missions for exploring the Solar System's gas giants, Cassini for Saturn and Juno for Jupiter and EJSM for Galilean moons will provide important information on the composition and the properties of the outer atmospheres, which will provide improved models of the gas giants. On the other hand, the characterisation of EGPs would be useful for making valuable comparisons between giant planets, placing in that way the Solar System's giants in a more general context. EGPs are easier to observe than rocky planets, considering that the flux from a Jupiter sized planet is about 100 times larger than the flux from an Earth sized one and that the number of available EGP targets is also much higher than the number of lower mass ones.

The EGPs, unlike their stars, have atmospheric temperatures that are low enough for the chemical composition to be of overriding importance. The atmospheric levels of EGPs that are emitting detectable radiation are the thin outer layers of molecules that control the absorption and emission spectra and the cooling rate. The dominant constituents are hydrogen and helium molecules, but depending on the above listed properties of the planet the presence of other molecules can be inferred or even directly observed using advanced spectroscopy. Spectropolarimetric observations of EGPs, i.e. the observations of the flux and the state of polarisation of planetary radiation from EGPs could allow going further in the planets characterisation than only estimating its size and distance from the star, which sum up the basic steps in making a first estimate of how comparable the system is to the Solar System. Information

about the structure and composition can be inferred from the reflected visual and near infra red spectrum. The reflected and emitted spectra of EGPs are mainly products of the scattering of incident light from clear atmospheric gases above the clouds (Rayleigh scattering), and form the aerosols, cloud particles, and the absorption and emission of gaseous absorbers in the clouds and hazes (Mie scattering) [50]. Reflected starlight from the EGPs will, thus, in general be polarised in comparison to the overall integrated starlight of the stellar disc, and the degree of polarisation is, as in rocky planets, strongly dependent on the composition of the planetary atmosphere. As an example, in their spectropolarimetric studies, Joos et al. find that methane bands enhance polarisation in the red and near IR [28]. The photons that undergo multiple scatterings or penetrate deeply into the atmosphere to the cloud layers lead to strong methane absorptions which further reduce the unpolarised scattered light. Joos et al. also conclude that this enhanced polarisation can be detected in EGPs and they recommend the observation of the strong methane bands for all exoplanet characterisation. However, Stam et al. concluded that the degree of polarisation can as well decrease in the absorption bands for different models of EGPs atmospheres [75]. The degree of polarisation of reflected starlight from an EGP is strongly dependent on the ratio of single scattered to the multiply scattered light. With little or no absorption in the atmosphere, multiply scattered light is observed with lower degree of polarisation. With some absorption by gas or cloud particles, most of the observed light is single scattered and therefore has a high degree of polarisation. With a lot of absorption, single scattered light will originate at different altitudes in the atmosphere and hence is likely to come from different types of particles. The single scattered light can therefore, in some models of the atmosphere, have a lower degree of polarisation then that of the multiply scattered light [73]. Next to the methane, principal absorbers are water and ammonia and hydrogen dipoles, as given in the Fig. 4 for the solar giants. Further on, the degree of polarisation followed in continuum for increasing wavelengths contains the differential information on particles at various altitudes in the atmosphere, as higher wavelengths penetrate deeper in the atmosphere. The degree of polarisation is a relative measure, and therefore free of the conditions of the star-planet-observer system which allows the extraction of the information on EGPs atmospheres even though the other, system characterising variables are not correctly measured [75]. For the discussion on EGPs it is common to split them on the hot and cold Jupiters. Hot Jupiters are the giant plants that inhabit regions very close to their stars, and therefore have intrinsically different features and are beyond the scope of the mission. However there exists a significant step variation between the true representatives of cold and hot Jupiters. They are usually, depending on their T-P profile and distance from the star, divided by the Sudarsky exosolar planet classification into five different classes, three out of which Class I, II and III are still within the scope of this mission [76]. The noted classes comprise the giant planets that are at least 0.5 AU away from the star and have equilibrium temperatures on average below 500 K. These classes also depend on the type of the absorbers present in

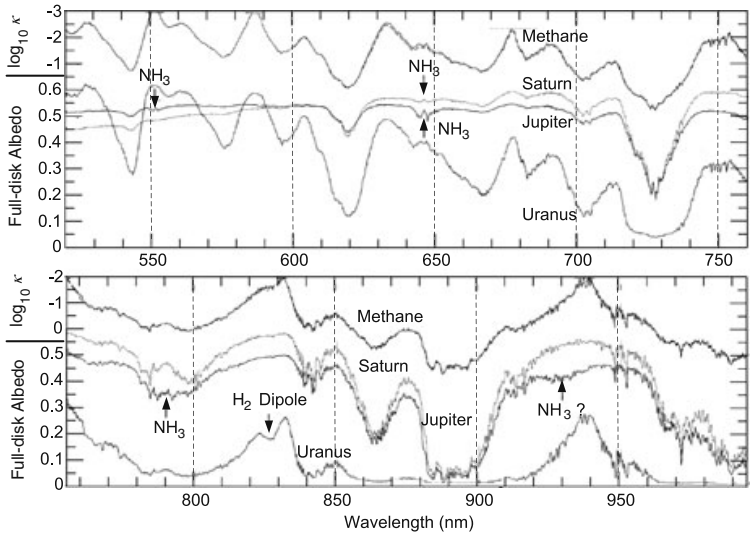

Fig. 4 Full-disk albedo spectra of Jupiter, Saturn, and Uranus at 0.4 nm spectral resolution. For comparison of spectral features, the methane spectrum for the temperatures of the Jovian planets is shown on top with the *solid line* at 0.4 nm spectral resolution. The *dashed line* at 1 nm resolution is from Karkoschka [34]. Methane absorption is shown on a logarithmic scale. *Arrows mark* wavelengths of some ammonia bands and hydrogen dipole absorptions bands [34]

the atmosphere. For the colder Class I it would be methane or ammonia clouds, for a slightly warmer Class II it would be water vapour clouds, with sulphuric acid clouds in the more extreme cases. The Class III planets are expected not to form global cloud cover as they are too warm to form water vapour clouds and too cold for a silicate layer to reach the upper troposphere. Hence, they would appear as featureless blue globes due to Rayleigh scattering, which is why Sudarsky names them clear. The Class III EGPs should, therefore, like Class II EGPs show significant absorptions of water, methane and collision induced molecular hydrogen, but as well some alkali metals like Na and K could appear in the visible. As all these lines are detectable in red and near infrared region, they are well within the scope of this mission. Finally, in accordance with the core accretion theory, planets that are more massive than 10 $M_{\oplus}$ should have a gaseous envelope from their surrounding nebula [50]. During planetary evolution the bombardment of planetesimals can lead to the enrichment of planets in heavier elements, i.e. to higher metallicity. The carbon enrichment in the solar giants has already been detected for Jupiter (three times the solar abundance), Uranus and Neptune (30 times that of solar abundance). Determining whether the majority of the EGPs are similarly enriched in heavy elements is one of the major goals of future observation and would greatly contribute to our understanding of planet formation and evolution.

2.3 Targets

A spectropolarimetric instrument allows for the observation of inactive stars. Indeed, the light of active stars is usually sufficiently polarised to contaminate

any usable signal from a planet. M stars being quite active, the targets must thus be limited to inactive F, G, and K stars. Moreover, the optical design of this proposal and its elliptical mirror would allow for the observation of targets up to 30 pc away while achieving reasonable integration times (see Figs. 8 and 9 for estimates of the integration times). These two properties of the target population (inactive and nearby stars) lead to a target sample which is very close to that of the radial velocity surveys (HARPS and Lick/Keck/AAT in the present, ESPRESSO and CODEX in the future).

Since an eight-octant phase mask (EOPM) is proposed as the coronagraph, the inner working angle of the instrument is equal to the angular resolution of the telescope. It translates into a linear relation between the minimal observable planetary semi-major axis $a_{\min}$ around a target star at distance D_*:$a_{\min} \propto D_*$. The spectropolarimetric technique yields an improvement in the contrast ratio between the planetary and stellar fluxes of five orders of magnitude; the EOPM improves the contrast by another ten orders of magnitudes. This means that planetary light with a flux ratio of up to $\phi_p/\phi_* > 10^{-11}$ can be distinguished. Using a very rough estimation of the stellar flux reflected by the disk of a planet of radius R, albedo 0.4 and semi-major axis a, seen at a phase angle of 90°, one can deduce that $\phi_p = 0.4 \times 0.5 \times (\pi R^2/4\pi a^2) \times \phi_*$. This gives a limiting relation between the observable planetary radii with respect to the semi-major axes:

$$\frac{a}{1\mathrm{AU}} \lessapprox 3 \cdot \frac{R}{R_\oplus}. \tag{1}$$

This relation means that the achievable contrast using the combination of coronagraphic and spectropolarimetric techniques described in this paper allows, theoretically, for the observation of planets of 1 Earth radius up to 3 AU, and 10 Earth radii up to 30 AU. Unfortunately, much harsher restrictions follow from photon flux induced integration time limits (see Section 3.2.6) as well as the telescope's resolution capacities (see Section 3.2.2). Nevertheless, the higher the achievable contrast ratio, the better the conditions of delectability in terms of technical feasibility, e.g. CCD full-well capacity.

2.3.1 Statistics in the solar neighborhood

The SEARCH telescope of this study would observe in a 45° cone always facing away from the sun because of the design of the telescope's sun shield. This constraint is also a part of the Darwin mission design (see [13]). As such, the Darwin star catalog can be used [31, 33], which provides a reasonable number of 280 target stars with spectral types suited to spectropolarimetry, as shown in Fig. 5. The current extrasolar planetary surveys have found planets around $\approx 6\%$ of all observed stars. The growing number of ground and space based instruments as well as their improving sensitivities will increase this number.

Figure 6 (left) shows the planetary companions which have already been detected under 30 pc in a mass–semimajor axis diagram. The red rectangle

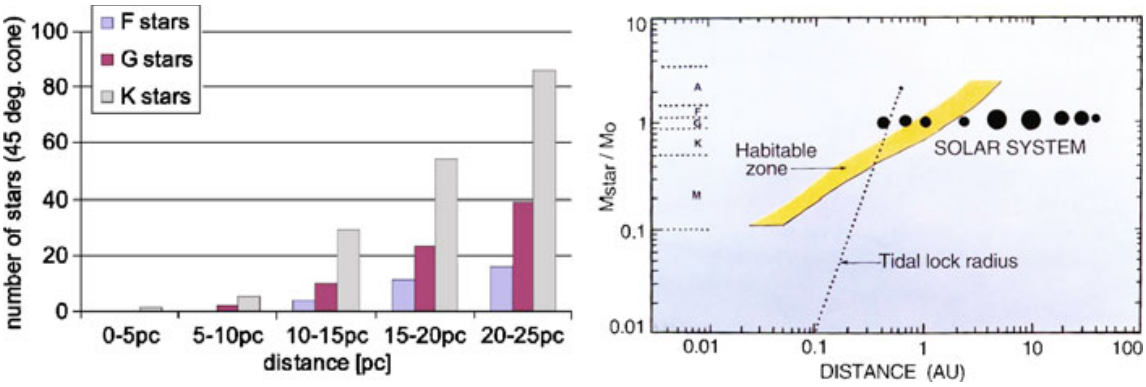

Fig. 5 *Left* Number of F, G, K suitable target stars vs. distance in a 45° cone [31]. *Right* Habitable Zone as a function of stellar type and orbital distance [36]

shows the main interest target population, between 1 and 10 Earth masses and between 1 and 5 AU, while the black rectangle shows all the accessible targets. There are already a good number of accessible targets, and present and future radial velocity surveys are expected to provide a suitable number of planets in the primary interest range. Figure 6 (right) shows the same mass–semimajor axis diagram for all the already detected exoplanets without limitation on stellar distance, and shows that targets in the main interest domain are becoming accessible.

2.3.2 Example mission schedule

The proposed scientific schedule consists of the first third of the mission spent on an exploration of a target list as large as possible. This preliminary phase

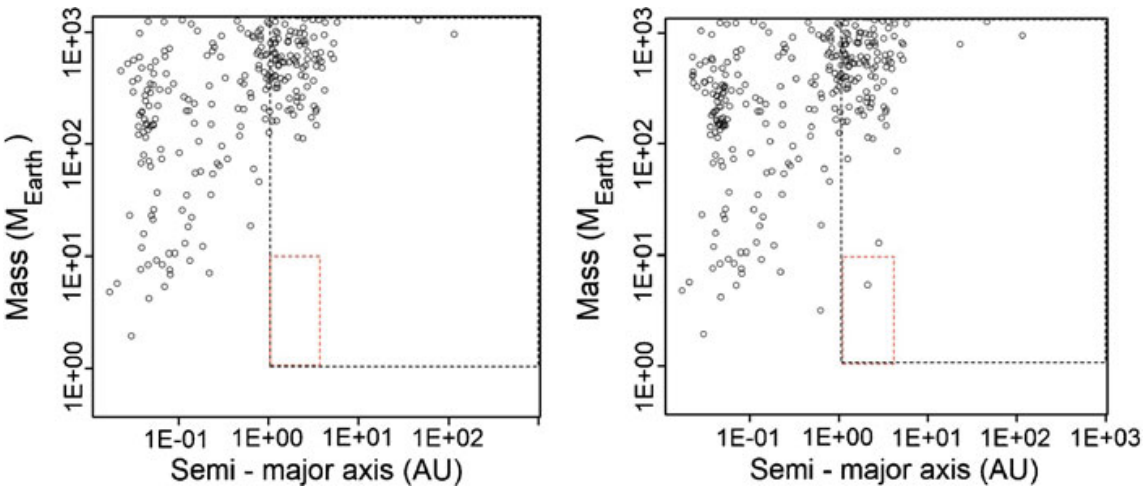

Fig. 6 *Left* Mass vs semi major axis for all detected extrasolar planets around stars under 30 pc. *Right* Mass vs semi major axis for all detected extrasolar planets. Based on data from exoplanet.eu. The detections within the target box are achieved by gravitational microlensing

will be conducted using the low resolution mode observations, in order to obtain the broad features of the signal. Ideally, targets will be observed several times at different orbital and phase angles to derive an orbital inclination for them. After an analysis of the data gathered during this preliminary phase, the rest of the mission will be dedicated to in-depth investigation of the most interesting targets, using the high resolution mode of the spectropolarimeter. Amongst other properties this may allow the detection of the presence or absence of potential biomarkers as pointed out in Table 1. In the final phases of the mission, the instrument could be opened up to a more general scientific community. It could for instance be put to use in the study of protoplanetary disks, multiple stars, highly polarised objects such as AGNs, etc.

3 Payload design

3.1 Polarimetry concept

As outlined in the science case spectropolarimetry has significant potential in the characterisation and indeed the detection of exoplanets. The power of polarisation for characterising planets has been demonstrated numerous times in past studies of Solar System planets, such as Venus, Mars, Jupiter and Earth, see Hansen and Hovenier [25], Braak et al. [11] and Ebisawa and Dollfus [17].

The technique involves measuring the Stokes Q and U parameters, which are essentially determined as the difference between the intensity of orthogonally polarised components of the electric field. The Q parameter is found when one axis lies in the plane of polarisation and U when the system is rotated through 45°. The exact system configuration is outlined in the following sections.

3.2 Optical system

3.2.1 Main optical system

To meet the measurement criteria stated above an optical telescope is proposed in Cassegrain layout with an f/1 elliptical mirror with a size of 9×3.7 m. The secondary mirror is placed on-axis and has roughly 1/10 the size of the primary. Including the obstruction of the secondary the aperture size is $\pi \cdot 9 \cdot 3.7 - \pi \cdot 0.9 \cdot 1.85 \approx 25.5$ m^2. The mirror size is a tradeoff between angular resolution, photon flux and the present launch capabilities of an Ariane 5 ECB launcher. To fit the telescope into the launcher the main mirror will be made of two segments. This will call for high accuracy positioning in the alignment of the two segments. This setup is again a tradeoff between the optical quality and the complexity of the deployment mechanisms needed for the mirror and sun shield.

3.2.2 Angular resolution

To resolve a planet 1 AU distant to its host star up to a distance of 30 pc an angular resolution of 1/30 arcsec = 0.033 arcsec is required. The angular resolution of a telescope is determined by applying the Rayleigh-Criterion

$$\beta_{\min} = 1.22\frac{\lambda}{D} \tag{2}$$

where λ is the wavelength and D is the diameter of telescope aperture.

Thus a mirror with a diameter of 9 m has an angular resolution of $\beta_{\min} = 1.22\frac{900\cdot 10^{-9}}{9} = 0.025$ arcsec at 900 nm. This would be enough to resolve the planet at the longest wavelength considered for this proposal's observations. But the resolving power of the whole optical system depends on several factors. Since the contrast ratio between the star and the planet is too large to directly record the signal the use of a coronagraph is inevitable. As is explained in Section 3.3 these instruments have a certain inner working angle (IWA). The IWA of the coronagraph used in this mission will be between 1.0 and 2.0 λ/D. As such, in the worst case scenario the proposed 9-m telescope would only be capable of separating a true Earth-like planet (1 AU from the host star) in a distance of 30 pc at a wavelength of approximately 600 nm. This would restrict the mission at the outer edge of the 30-pc observation radius. But as explained in Section 2.2 this would only result in a minor drawback to the scientific goals of the mission. The goal is not only to characterise true Earth-like planets but also to shed light on the diversity of extrasolar planets in the low mass range.

3.2.3 Quality of the main optical system

Aside from the requirement for high angular resolution, the high contrast ratio between star and planet proves the main optical challenge. In theory the optical system images all the collected light from a point source in an Airy disc which is the Fourier transform of the aperture geometry. In a real optical system the imperfect optical surfaces always reflect light on the area outside the Airy disc. In this area the light interferes and creates a characteristic speckle pattern (see Section 3.2.4). A main criterion for the quality of an optical system is the Strehl-ratio S. This is the ratio between the intensity collected within the real Airy disc and the theoretical intensity collected in an ideal Airy disc. For highly corrected optics, the Strehl-ratio of a mirror can directly be calculated from the standard deviation of the mirror surface:

$$S = e^{-\sigma^2} \approx 1 - \sigma^2 \tag{3}$$

Here σ is the standard deviation of the mirror surface normalized on the observation wavelength. The approximation is valid for small standard deviations. To make the Strehl-ratio as high as possible the mirror surface has to be very smooth. Considering the large mirror of the SEARCH design, one cannot expect a low standard deviation over the whole mirror surface. For this reason active optics (AO) actuators are introduced, which can correct the

surface variations of the mirror in place. ("Active optics" may be distinguished from the "adaptive optics" systems used to correct atmospheric distortions). That means the mirror has only to be manufactured with high precision over patch sizes corresponding to the displacement between the actuators.

3.2.4 Reduction of speckle noise

Given a telescope with a certain Strehl ratio S a fraction $(1 - S)$ of the light entering the system is not focused into the Airy function, but spread over the image plane in a characteristic speckle pattern. A speckle is a patch of light with the size of an Airy function which—in this case—becomes especially problematic, because it resembles the image of a planet. According to Bloemhof [6] and Roddier [63] two types of speckle patterns are created: an antisymmetric and a symmetric pattern. The antisymmetric speckles are located on the Airy disc and are effectively removed by the coronagraph, the symmetric pattern however is not affected by the coronagraph. The relative intensity of a quadratic speckle behind the coronagraph and the Lyot stop is approximately given by

$$I_{\text{quadratic}} \approx (1 - S)\frac{1}{0.352}\left(\frac{a}{D}\right)^2\left(\frac{D_{\text{Lyot}}}{D}\right)^2. \tag{4}$$

where S is the Strehl-ratio, a is a characteristic coefficient, D is the aperture diameter and D_{Lyot} is the diameter of the Lyot stop projected into the aperture.

The characteristic coefficient is approximately given by the displacement of the Active Optics (AO) actuators. The intensity is normalised on the Strehl ratio S and therefore gives directly the mean contrast between the star and a speckle. In Fig. 7 (right) the relative speckle intensity is calculated using (3) and (4), and plotted for different surface standard deviations (Strehl ratios) and Lyot stops. It is obvious that neither a smaller surface standard deviation nor a larger Lyot stop will decrease the speckle intensity significantly. According to Fig. 7 (right) the speckle intensity can only be significantly lowered with AO actuator displacements of less than 5 cm on the primary mirror or less

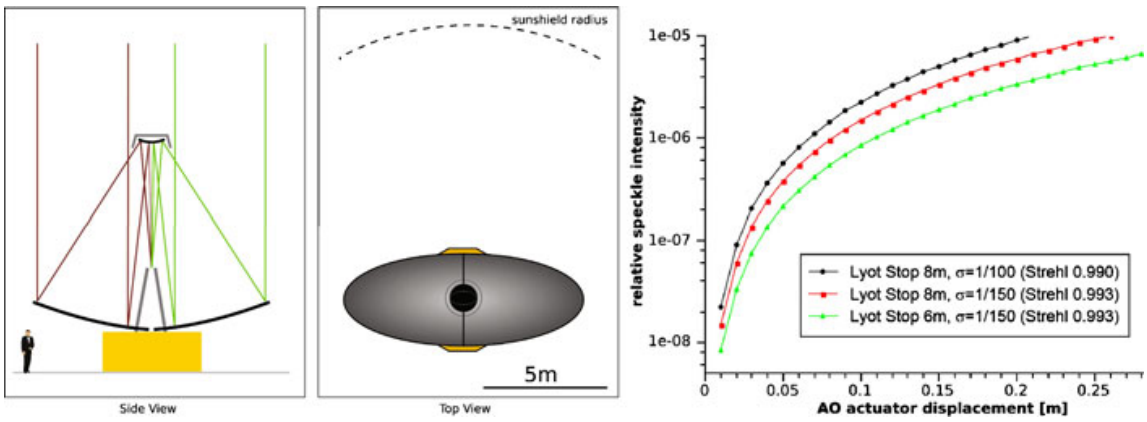

Fig. 7 *Left* Telescopic system. *Right* Calculation of relative speckle intensity for different systems

than 5 mm on the secondary. A high AO actuator density does represent a technical challenge, nonetheless, it would prove more practical to place high-density AO on the secondary mirror due to size and weight considerations. A surface standard deviation of $\sigma = 1/150$ yielding a Strehl ratio of $S = 0.993$, a medium distance of $a = 0.01$ m between the AO actuators, a primary mirror diameter of $D = 9.5$ m and a moderate Lyot stop of 8 m would lead to a speckle intensity of about 10^{-8}. This is one to three orders of magnitude too low to directly image an exoplanet. Therefore, additional measures for speckle reduction are inevitable. One possibility would be to close the Lyot stop even more, but this would directly affect integration times. If the dynamic range of the CCD-chip is large enough, the symmetry of the speckle pattern could be used to effectively suppress it after the recording. In such a case, the image would be copied, flipped by 180° and subtracted from the original. With the speckle pattern being symmetrical the only asymmetric part in the image would be the planet. This method can also be applied to spectroscopy if an integral field spectrograph is used.

A very elegant way to get rid of speckles is interferometric speckle nulling. This technique is discussed in Bordé and Traub [9, 10] and Guyon [22]. Speckle nulling has to be considered carefully. It is a very powerful, which could prove necessary to directly image faint exoplanets. Of course this presents several technical issues to be overcome, including a certain loss of light, which is critical when working with a very limited aperture size. The speckle noise level also leads to very strict requirements to the accuracy of the polarisation measurements. To measure a polarisation signal to an accuracy of 0.5% with speckle noise being three orders of magnitude higher than the signal itself, an on-axis telescope with very small cross-polarisation is required.

3.2.5 Straylight considerations

There are different sources of straylight to be taken into account. Since the intention is to detect the very faint signal of the planet very close to its host star special measures are required to reduce the stray light. Primary sources of straylight include:

1. light emitted from the sun and the Earth–Moon system
2. light scattered from the spacecraft
3. local zodiacal light

Overcoming the **first** point is accomplished using a deployable sunshield and always pointing the spacecraft away from the sun. This allows an observation angle of ±45° above and beneath the ecliptic.

The amount of stray light generated by obstructions in the optical path (**second** point) depends on the spacecraft design, which is discussed later in Section 4. The boom holding the secondary mirror is placed in the middle of the primary mirror as shown in Fig. 13. As such, the struts holding the secondary mirror are obstructing the aperture. In this situation the image of the star would have additional spikes extending outwards from its center. These

spikes point ±45° away from the major axis of the primary mirror. Thus, the line of highest resolution parallel to the major axis will be free of this straylight. The **second** point is taken care of using a tapered baffle and a pinhole near to the first focal plane of primary and secondary mirror. This system can reduce the stray light coming from other light sources outside the aperture. For a very powerful baffle design see Plesseria et al. [60].

The **third** point is not a major problem in this design because it only delivers a constant intensity background to the observations which can be subtracted during the image post processing as shown in Section 3.2.4.

3.2.6 Photon flux

The expected count rate (*cnt* [photons/s]) of the observed target has been calculated as follows:

$$cnt = \frac{\pi}{2} \cdot \left(\frac{r_\star r_p}{d_\star d_p}\right)^2 \cdot \int_\lambda^{\lambda+\Delta\lambda} \frac{I(T,\lambda)}{E_{\text{photon}}(\lambda)} d\lambda \cdot \phi \cdot a_{\text{geo}} \cdot A \cdot \Theta \cdot Q \tag{5}$$

Here $r_\star, d_\star$ denote the radius and the distance of the host-star respectively, r_p, d_p the target planet's radius, and the distance to its host star. The black body irradiation intensity function per photon energy $\frac{I(T,\lambda)}{E_{\text{photon}}(\lambda)}$ is integrated over spectral bands,[1] corresponding to the spectrograph's resolution (e.g. $R = 70 \rightarrow \Delta\lambda \simeq 4.3$ nm at $\lambda = 300$ nm), neglecting stellar and planetary absorption losses. ϕ represents the orbital phase factor, ranging from 1 at full phase (phase angle $\alpha = \pi$) to 0 at $\alpha = 0$. The planet's geometric albedo a_{geo}, the primary mirror's surface A, the total instrumental throughput Θ, as well as the detector's quantum efficiency Q range from 0 to 1. The count rate is linked to the required signal to noise ratio (SNR) via

$$cnt = \frac{SNR}{\tau}\left(SNR + \sqrt{4N_{\text{pix}} \cdot (n^2_{\text{readout}} + n_{\text{straylight}} + n_{\text{thermal}}) + SNR^2}\right) \tag{6}$$

Where τ denotes total exposure time, N_{pix} the number of CCD-pixels, n_{readout} the number of photons due to read-out, $n_{\text{straylight}}$ due to stray-light and n_{thermal} due to thermal noise. Combining (5) and (6), one can derive an expression for the systems range in terms of planetary radii.

$$r_p = \frac{d_p d_\star}{r_\star}\sqrt{\frac{2}{\pi}\frac{SNR^2 + SNR\sqrt{4N_{\text{pix}} \cdot (n^2_{\text{readout}} + n_{\text{straylight}} + n_{\text{thermal}}) + SNR^2}}{\tau \cdot \phi \cdot a_{\text{geo}} \cdot A \cdot \theta \cdot Q \cdot \int_\lambda^{\lambda+\Delta\lambda} \frac{I(T,\lambda)}{E_{\text{photon}}(\lambda)} d\lambda}} \tag{7}$$

[1]The numerical integration of Planck's function has been performed following Widger and Woodall [81].

Present assumptions on the setup proposed are $\Theta = 0.3$,[2] $a_{\text{geo}} = a_{\text{Earth}} = 0.36$, and the measurements are considered at $\phi = 0.5$. The two segments of the primary mirror have a total collecting area of $A = 25\ \text{m}^2$. Since no specific assumptions on the detection device have been made, and no reliable stray-light calculations could be performed until further investigations into the main optical design can take place, N_{pix} has been set to zero, driving SNR calculation towards pure photon noise. Nevertheless, a reasonable quantum-efficiency of $Q = 0.9$ over the whole spectral band has been assumed. Stellar radii have been interpolated from Habets and Heinze [23] corresponding to F-K type surface temperatures.

The resulting estimates on the instrumental range can be regarded in Fig. 8. Assuming a total integration time of one day per spectrum, a characterisation of Earth like exoplanets around G-stars and Super Earths around fainter stars is possible providing a spectral resolution of 70. Compared to the restrictions on continuous observation time due to the spacecraft's solar panel configuration—currently approximately 90 days—polarimetry can also be performed. The maximum exposure plots (45 days, Fig. 9) were generated having a very generous amount of time reserved for down-link-, re-calibration and reorientation phases of the spacecraft. It is plainly visible, that high resolution spectra can be achieved for planets within the habitable zone around G-type stars for a slightly narrowed spectral range at a distance of 10 pc. At 30-pc high resolution spectrometry can still be performed for sub-Jovian planets.

3.3 Instrument

The optical layout of the instrument is outlined in Fig. 11. A field stop is positioned at the focal point of the telescope, through which the light enters the instrument. A lens then refocuses the light onto a coronagraph. This serves the purpose of blocking out the host star light of the planet under investigation. The subsequent optics includes a collimator, Lyot stop and the fibre bundle placed at the imaging plane.

3.4 Coronagraph

The specific type of coronagraph selected for this project is the Eight Octant Phase Mask or EOPM [56]. The mask is composed of eight sections, each of which is phase-shifted by π compared to its neighbouring octant (Fig. 10). Thus, any symmetrical image centered on the mask undergoes destructive interference and is cancelled out. The light focused by the first lens of the system produces an Airy disk centered exactly on the crosshair of the phase mask. Due to the design of the mask, destructive interference occurs between

[2]Regarding this estimate, the phase mask coronagraph will reduce the planets light close to the optical axis by approximately 50%, as can be seen in Murakami et al. [55]. The photonic spectrograph has been considered as having a throughput of 60%. All other components are considered as providing lossless performance, except for the CCD's quantum efficiency.

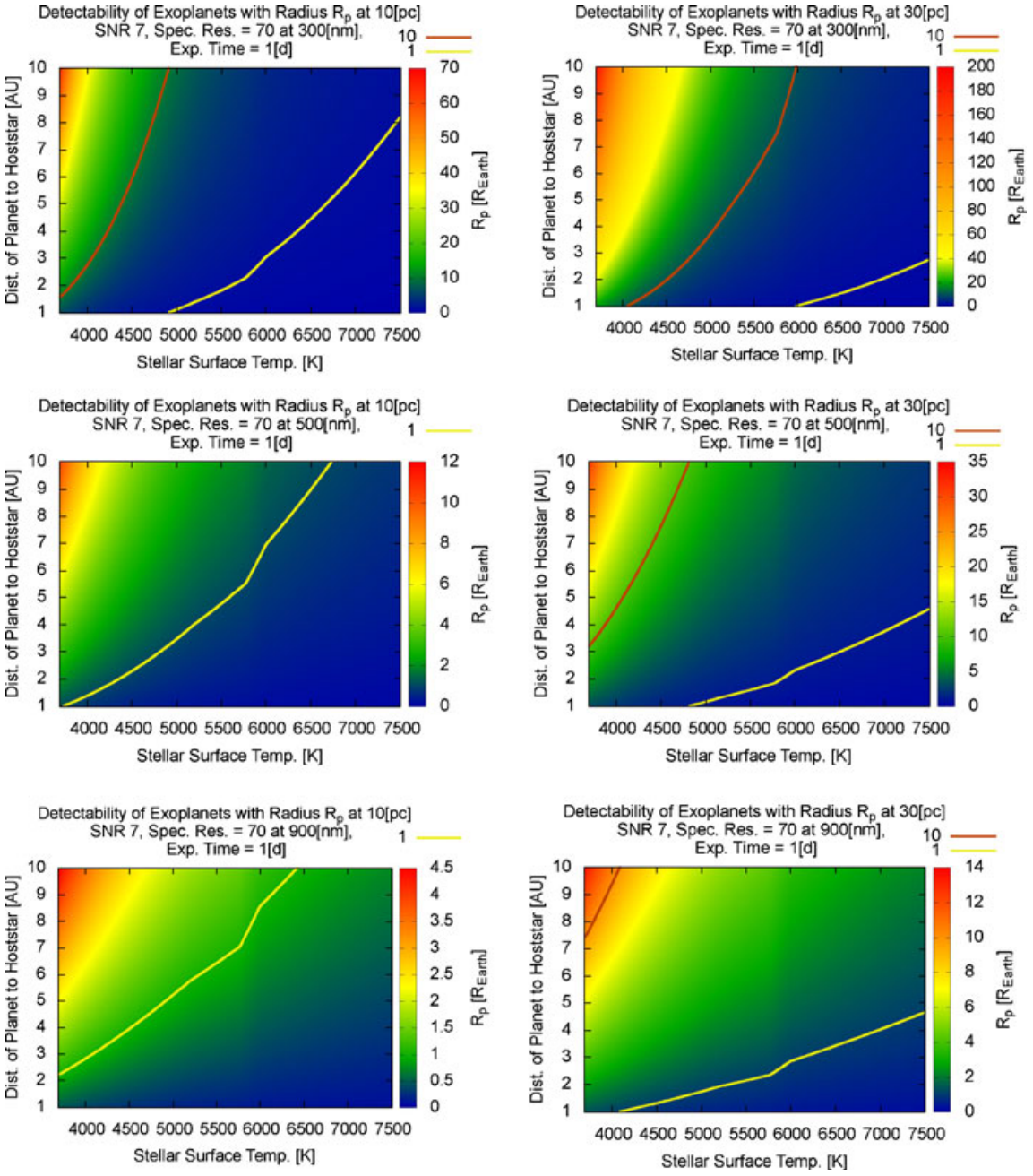

Fig. 8 Instrumental range in low resolution mode. *Left* Spectrometric capacities at a distance of 10 pc. *Right* At a distance of 30 pc. Terrestrial planets around G-stars can be fully characterised almost up to 30 pc

the phase shifted components of the electric field. As such, at the next pupil plane most of the light is in the area surrounding the pupil. A Lyot stop in this pupil plane blocks out the light surrounding the pupil. Thus, when focusing the electric field after the Lyot stop the flux in the center is attenuated significantly. Optimum attenuation occurs only for an object perfectly centered on the mask's crosshair, any off-axis object or structure in the nearby region of a star (such as an orbiting planet) will not suffer this effect and remain visible. A more detailed explanation of the function of phase mask technology in general can be found in Murakami et al. [56]. One clear challenge in the application

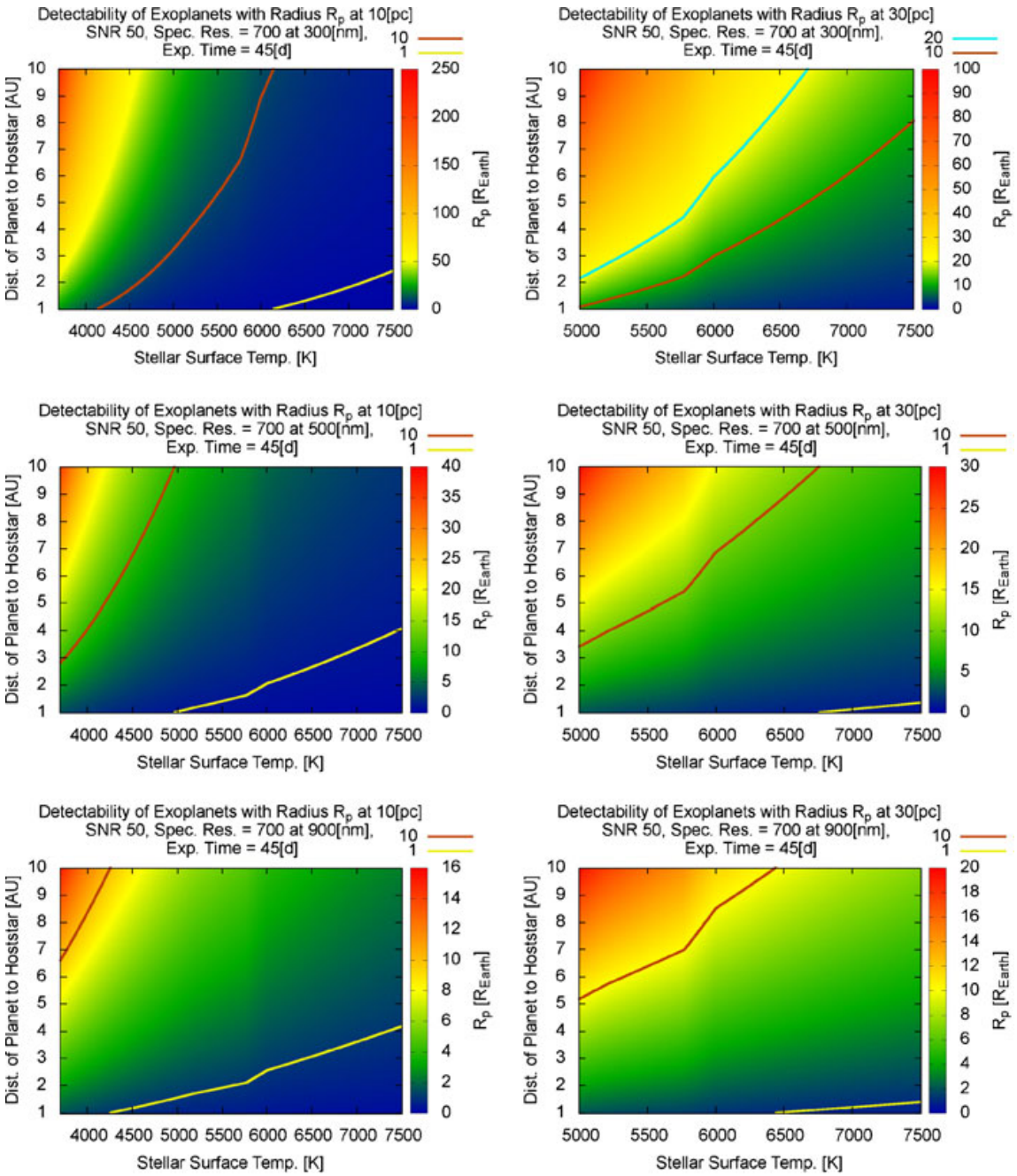

Fig. 9 Instrumental range at maximum exposure time, high resolution mode. *Left* Spectrometric capacities at a distance of 10 pc. *Right* At a distance of 30 pc. Super Earths around G-stars may be characterised with a spectral resolution of 700 up to 30 pc

of the phase mask technology is the large spectral bandwidth of 300–900 nm considered by the mission. Achromatic development in this technology should prove capable of meeting these requirements. Approaches for achieving achromaticity include multi-layer thin film design or an emulation of dielectric phase plates used as achromatic phase shifters in nulling interferometers [7]. More details on the development of achromatic phase masks can be found in Boccaletti et al. [8], which outlines a prototype covering a spectral range of 950–1,800 nm.

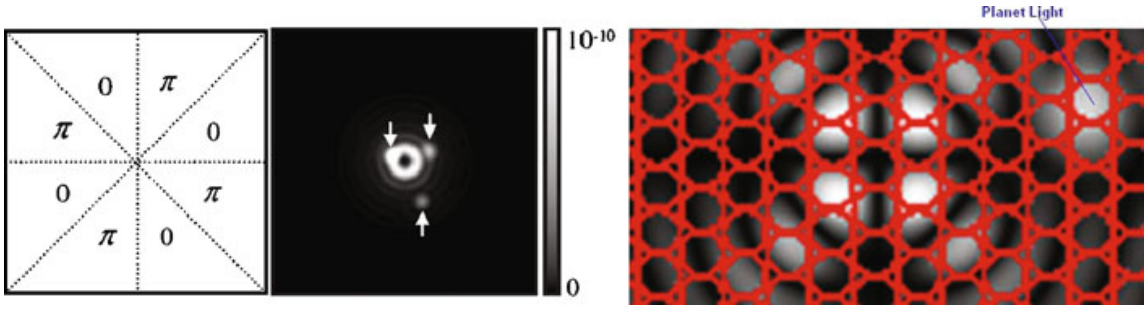

Fig. 10 *Left* Schematic of the EOPM mask [56]. *Right* Graphic representation of a nulled stellar image resulting from a phase mask with an overlay of the fibre arrangement, each one of which feeds back to a single spectrograph

Although the chromaticity of the coronagraph is not expected to pose a significant problem, the possibility exists of mounting two EOPMs with differing central frequencies onto a rotator wheel and shifting between them. Further restrictions in the spectral range may result from the other optical components, such as for example the lens materials. Although this may prevent the lower limit of 300 nm being reached, a lower limit of 400 nm would not prove problematic. The EOPM technology has to date been prototyped using liquid crystals. Should the technology not have advanced beyond the requirement for liquid crystals, which are not yet space proofed, then the Four Quadrant Phase Mask could be employed in its place [56].

3.5 Integral field spectrograph

3.5.1 Imaging outline

The coronagraphic mask reduces the stellar light by a factor of up to 10^{-11}. Despite the significant reduction in star light the planet light will still be much fainter than that of the star. In order to extract the spectrum of the planet, the point spread function (PSF) is sampled over 800 fibres, each of which feeds back to an individual spectrometer. As such, the star light is distributed over

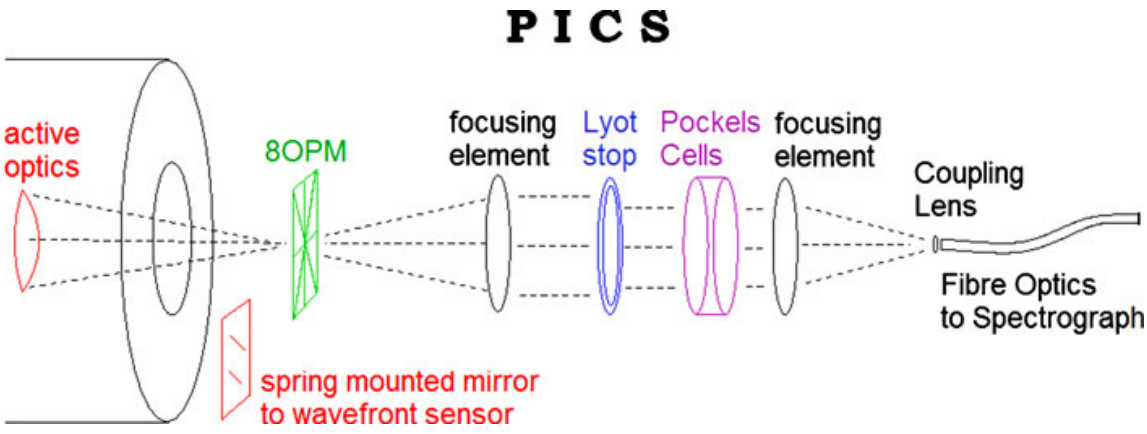

Fig. 11 Outline of the optical path of the instrument

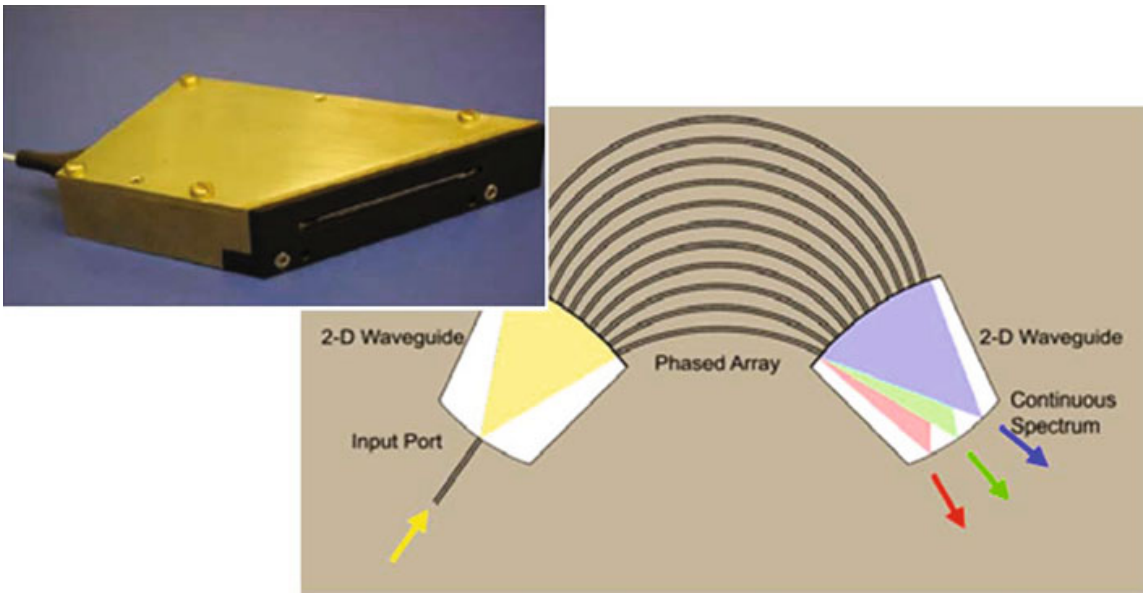

Fig. 12 The Integrated Photonics Spectrograph

the entire array, whereas the planet light is contained across a small bundle of fibres.

3.5.2 Spectrographs

Considering that each of the 800 fibres feeds back to a separate spectrometer, a particularly light weight and affordable unit is required. Meeting both of these requirements is the Integrated Photonics Spectrograph from the Anglo-Australian Observatory. Each of these fibre spectroscopes have dimensions of 100 mm × 75 mm × 2 mm, a mass of 0.8 kg and a transmission profile of 60–65%, see Fig. 12. This results in a total array dimension of 1.2 m × 1.5 m × 0.015 m and mass of 630 kg.

3.6 Polarimetry

As previously stated spectropolarimetry is the technique chosen to accomplish the science goals outlined. Apart from yielding polarimetric data, which is of itself scientifically important, polarimetry also improves the contrast ratio between the star and the planet. The technique involves examining the difference between P and S polarised light to determine the Stokes Q and U vectors. This can be done either temporally or spatially. The spatial approach employs a polarising beam splitter and reads in both the P and S polarised beams simultaneously on two different CCDs. A disadvantage of this approach is the calibration requirement of the CCDs, which must be as identical as possible to ensure that only the difference in radiation intensity is measured. As such, the temporal option is favoured in this study (this approach is adopted in the ZIMPOL device [66]).

The same CCD design as implemented in ZIMPOL is also proposed for use here. This requires that every second row of the CCD be masked so that charge

packages created in the unmasked row during one half of the modulation cycle are shifted for the second half of the cycle to the next masked row, which is used as temporary buffer storage. After several thousand modulation periods the CCD is read out in less than 1 s. The sum of the two images is proportional to the intensity, while the normalised difference is the polarisation degree of one Stokes component [66]. Pockels cells are suggested as polarisers, these would have high transmission of over 98% and avoid the necessity of rotating parts. Two Pockels cells could be placed in the collimated beam after the phase mask. These cells would be oriented orthogonal to one another. As such, when a voltage was applied to one it would polarise at 90° whereas the second cell would polarise at 0° when subjected to the same voltage. The Pockels cells could then be activated and deactivated as required to polarise the signal. Should the use of Pockels cells prove in any way problematic the option of using standard polarisers on a rotator wheel could also be used.

3.7 Measurement procedure

Before the actual image acquisition the optical system is calibrated to ensure maximum suppression of host starlight and speckles. First of all the coronagraph is aligned with the help of a wavefront sensor which monitors the light from the host star. The actuators on the telescope mirrors are iteratively adjusted in such a way that the light from the host star is minimised behind the coronagraph. The effect of the coronagraph can be measured by a CCD-camera or a photometer. Because the host star is usually very bright, only a very small fraction of the incoming light is needed for both wavefront sensing and photometric measurements. That means alignment of the coronagraph can be measured and maintained during image acquisition.

If the telescope moves thermally more than about one quarter of a wavelength the speckle pattern changes. Therefore, either the telescope has to be stable enough to ensure speckle nulling over the time of image acquisition or speckle nulling has to be done in real time during the measurement. The latter would of course result in greater loss of light. In this way a stack of images is recorded. The exposure time for each individual image has to be small enough that the remaining light from the host star does not overflow the CCD-detector. This procedure is valid for both direct imaging and integral-field-spectroscopy. In both cases a symmetric speckle nulling can be applied in post-processing. For polarimetry, different images are recorded with orthogonal states of the polariser.

4 Spacecraft

4.1 Spacecraft general design

The overall spacecraft design is driven by the telescope size and accommodation and the need for a very stable environment to achieve the scientific goals.

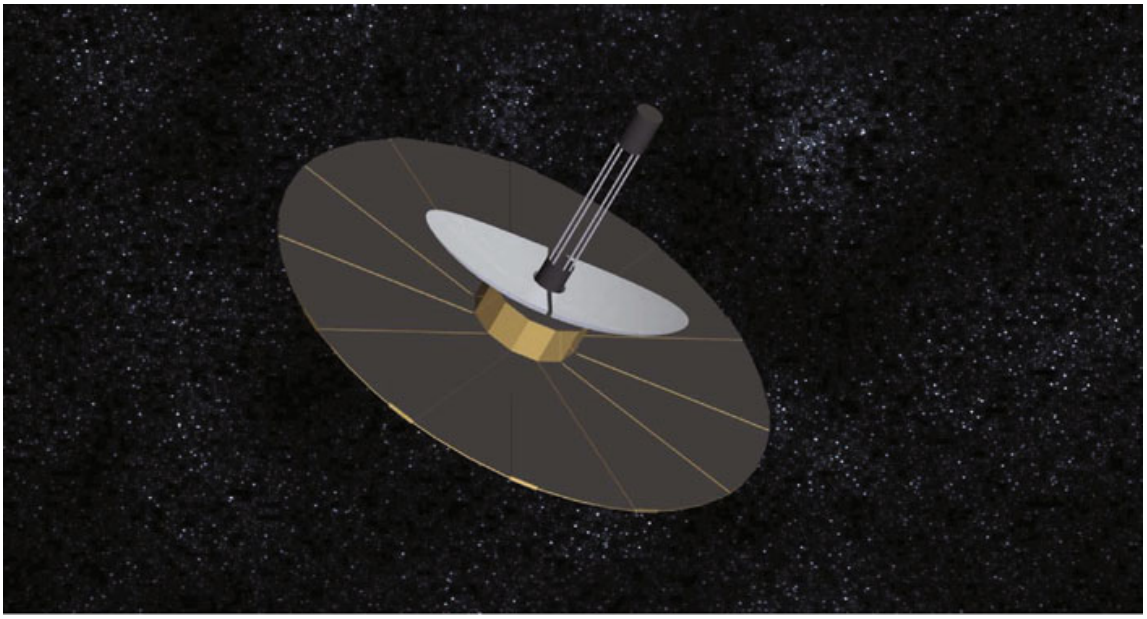

Fig. 13 SEARCH deployed configuration

The proposed spacecraft in its deployed configuration will be 9.5 m in height and 22 m in diameter for a total mass of 5.5 t. The primary mirror form an elliptical shape and surrounds the central boom, this is complemented by a 80-cm secondary mirror (also split in the center), mounted with active optics and located on top of a central boom of 8 m length from the primary mirrors position. They will be protected by a corona sunshield with a corona radius of 9 m, with a hexagonal shape, using the same technology as the GAIA project [21]. The deployed configuration can be seen on Fig. 13.

The critical parts of the spacecraft design include the general configuration, with particular emphasis placed on the sunshield to reduce stray light, and the deployment mechanisms. The sunshield is designed to protect the secondary mirror from direct sun light. As the spacecraft will point to different targets, it must be shielded within a pointing range of $[-45°,\ 45°]$ making 14% of the sky available for observation at a given time. These values assume the sunshield is fixed at a 9-m radius and with a hexagonal configuration. During the launch phase, the mirrors and the sunshield are in a stowed configuration, as seen in Fig. 14 (right).

In space, the circular sunshield is deployed to its full extent in order to shield the two off-axis mirrors. Moreover, due to the vibrations expected during launch, the secondary mirror boom needs to be in a stowed configuration of 7.5 m length. The boom is then extended in space with a telescopic system to the required length of 9.5 m. The mission could be launched by an Ariane 5 ECB from the Guiana Space Center at Kourou. It would then be transferred to an orbit around the Lagrange L2 point of the Sun–Earth system with a cruise duration of 3 months. The mission baseline would be 5 years in orbit once it arrived and had successfully completed its commissioning phase.

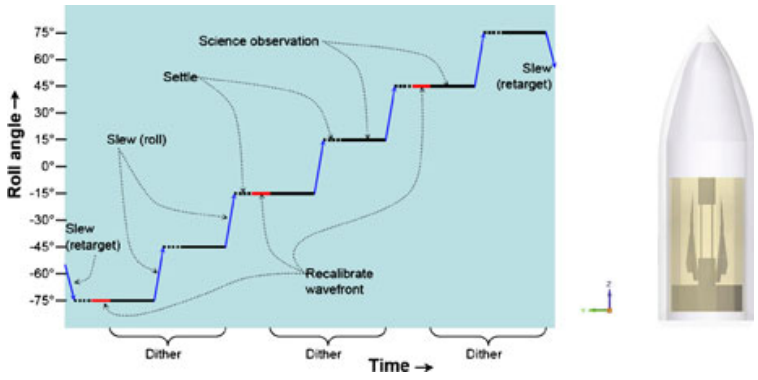

Fig. 14 *Left* SEARCH possible mission operation scenario for the first year: timeline for a planet observation around one star. The observation includes six science integration periods separated by five roll slews. Each slew is followed by settling time. Each pair of science integrations constitutes a dither, and each dither is preceded by recalibration of the wavefront [47]. *Right* SEARCH stowed configuration

The mission observation scenario would be as follows: The maximum time of exposure for the selected targets is approximately 1 day for low-resolution scans. Since the orbital inclination of the target will not generally be available, a period of quick observations of the target at different spacecraft roll angles would first be carried out. These would follow the TPF-C observation strategy at six roll angles, as illustrated in Fig. 14. Assuming a day for manoeuvres and data transmission each month, it would be possible to achieve this general sweep of the selected targets during the first year of the mission, however very little time would remain for other observations. The second phase of the mission would focus on more precise observations of interesting targets. Assuming an exposure time of 45 days for high-resolution spectroscopy (including manoeuvres and data transmission), it would be possible to have a precise observation for two out of five targets, and still have 50% of the observation time available for general astronomical observations. Alternatively, a dedicated mission could achieve detailed observations of up to four out of five targets.

4.2 Spacecraft subsystems

The Attitude and Orbit Control System (AOCS) is one of the most critical parts of the spacecraft's subsystems, because of high pointing and stability requirements of the optics. The main requirements are 0.01 arcsec of pointing accuracy and a maximum of 3 ma of deviation during the typical integration time of 1 day for low-resolution images, and more for high-resolution scans, with a total integration time of up to 45 days. To achieve this, both star trackers and gyrometers will be used to make a first measure of position. CCD data from the telescope itself will then be made directly available to the AOCS loop, and 16 FEEP thrusters in order to counter the very small perturbations of the L2 environment. 12 classical thrusters each of 10 N will be used for orbit correction manoeuvres.

The spacecraft is protected from solar irradiation by the deployable sunshield covered with multi layer insulation sheets. Where required, heaters and multi layer insulation are used at other parts of the spacecraft, resulting in a mostly passive thermal control. In order to guarantee thermal stability at the sensors, the CCD will be passively cooled by means of a heat pipe and a radiator.

The scientific data will be transmitted in X-band through a set of phased array antennae located at the bottom of the spacecraft. This high gain antenna concept is based on the GAIA communication architecture. Two low-gain omni-directional antennas are used for telemetry and telecommand, available also during eclipses or other survival situations. In order to meet the power requirements the spacecraft will have 13 m^2 of solar panels, with a Li-ion battery system providing power during critical phases. The solar arrays geometry is similar to the GAIA configuration, with six separate solar panels in a hexagonal arrangement.

4.3 Possible mission schedule

Figure 15 depicts a possible schedule of the mission. Accounting for necessary technology development phases A and B have been extended. Launch would then be foreseen by 2027. The scientific duration of the mission would be 5 years; extendable by 2 years depending on the fuel reserves.

4.4 TRL and risk analysis

The Technology Readiness Level (TRL) is a measure used by space agencies to assess the feasibility of a given technology. It has a scale ranging from 1 to 9, 1 being "Basic principles observed and reported" and 9 "Actual system Flight proven through successful mission operations" according to ESA's definition of TRL [18].

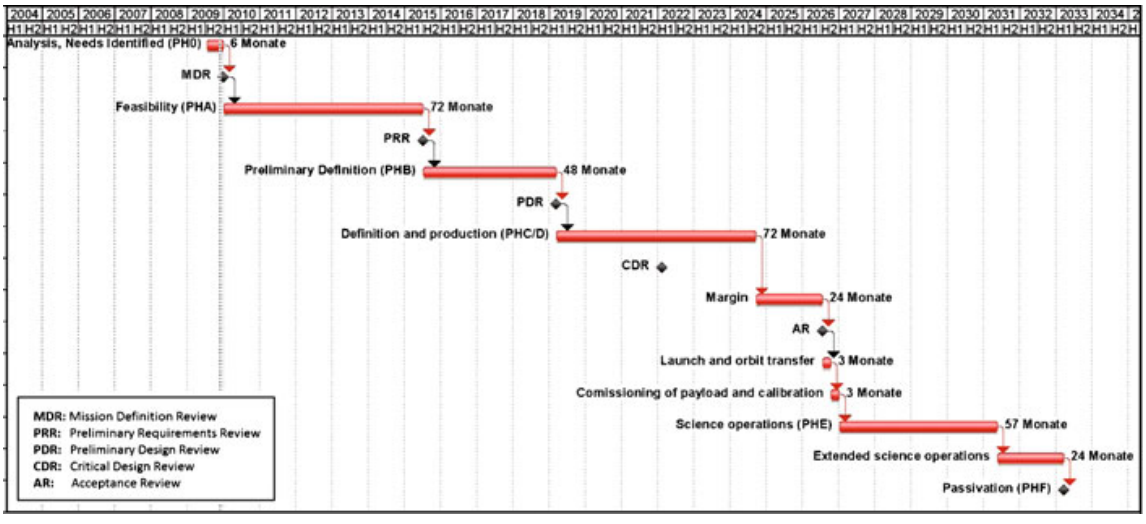

Fig. 15 SEARCH—Possible mission schedule

No detailed analysis of the readiness of the various subsystems has yet been carried out. Further work is needed to define a clear roadmap of technology development and a risk assessment. However, some critical technologies required in order to satisfy the scientific requirements can be highlighted. The grinding of the mirror will prove a major challenge, as well as the development of a set of new deployment mechanisms for the main mirror and deployable boom. Other subsystems, such as the sunshield and AOCS thrusters, have already been developed for missions such as LISA Pathfinder and GAIA but will require some modifications. The main driver, as is often the case in the design of a satellite system, will be the mass of the spacecraft, which needs to satisfy the capability of a launch on Ariane 5 ME with an injection into an orbit around the Sun–Earth Langrange point L2.

4.5 Descoping and upscoping options

The presented configuration may be considered the baseline design. The mirror size is one of the main issues: the Ariane fairing size is not a limitation, so it is possible to increase the mirror size if more ambitious scientific goals are considered, or decrease it if the mission proves itself too expensive. It is also possible to descope the mission to only one mirror and to abandon the deployment challenges, however this would greatly decrease the mission performance.

4.5.1 Scientific consequences

As discussed above, the primary mirror of the proposed system is the main driver in the cost of the mission. On the other hand, the ambitious scientific goals of characterising Earth-like planets require such a large effective diameter—as described in Section 3.2. The proposed system with a mirror divided in to two 4-m segments is considered a reasonable trade-off between meeting the scientific goals and the expense and technology development. Descoping the total mirror size from 9 to 4 m (Fig. 16) would significantly limit the possible targets. The limitation is a result of the decreased resolution, and would mean that SEARCH could only observe planets within a minimum distance of 3 AU to the host star at 30 pc.

Consequently Earth size planets could not remain in the target list, and SEARCH would have to focus on characterising the diversities of gaseous planets (Section 2.2.2). Receiving this kind of information would still be of great interest in understanding the atmospheric composition and evolution of the outer regions of planetary systems. However, the even more interesting inner regions would not be accessible. It is also possible to lower the cost of the

Fig. 16 SEARCH upscoping and descoping options. The upscoping option has a 20-m mirror size and the descoping a 4-m size

mission by simply using one half of the proposed system (only one primary mirror) as an off axes telescope as proposed for the Japanese Terrestrial Planet Finder(JTPF), with the same targets limitations.

The most significant technical challenge is seen to be in the production of such large mirrors. As shown, the major axes of the mirror could be decreased in size or increased up to 20 m, whereas the minor axes will be the same for all designs, so the manufacturing of such a mirror will prove a major issue. It is also possible to envisage segmenting either of the two 10-m mirrors. The proposed launch and deployment strategies should be possible with an Ariane 5. Due to the symmetric deployment, problems with the center of gravity being off axes in the launch configuration can be overcome (see Fig. 16).

5 Summary and discussion

The dedicated space mission SEARCH (**S**pectropolarimetric **E**xtrasolar **A**tmosphe**R**e **CH**aracerisation), proposed in this paper, will study the diversity of terrestrial extra solar planets using spectropolarimetry. Since the host star's light scattered from an exoplanet will be polarised to a certain degree, depending on surface and atmospheric features, polarimetric measurements contain valuable information about these characteristics not accessible by other methods. Examples are cloud coverage, cloud particle size and shape, ocean coverage, atmospheric pressure among others. Also the change in the degree of polarisation over one orbital period contains valuable information on the orbital inclination, which is not accessible via radial velocity measurements. By combining this method with a spectral measurement, it is possible to obtain information about the atmospheric composition and to detect molecules such as H_2O, O_2, O_3, NH_3 and CH_4. In order to achieve these ambitious goals two main obstacles have to be overcome: these are high contrast ratio between the planet and its host star and the need to spatially resolve those two with the spacecraft's telescope. To meet these two challenges, new design concepts have been developed and presented in this paper.

The proposed mirror is an f/1 parabolic mirror with elliptical rim of size of 9 m $\times$ 3.7 m in a Cassegrain layout. It is cut in half and folded towards the secondary mirror to fit into the Ariane 5 fairing. Thus, problems regarding the symmetric distribution of weight at launch can be overcome. Also an on axis-configuration significantly decreases the polarisation losses introduced by the system. This design allows for an angular resolution high enough to resolve planets as close to their host stars as 0.5 AU in a distance of 10 pc and as close as 1.4 AU in a distance of 30 pc, for the first time being able to characterise real Earth type planets in a significant target sample. It is also important to mention, that the proposed mirror design is a way to launch a mirror into space with Ariane 5 more or less regardless of its size in one dimension. If the technical problems in the manufacturing of such large mirrors can be overcome, launching a 20-m $\times$ 3.7-m mirror within Ariane 5 can be envisaged. The mirror's surface smoothness is critical to the quality of the optical system.

Since it is not possible to meet the required smoothness over the whole area of the mirrors, the concept of active optics has been proposed to correct the wavefront from deviations on the mirror surface.

Regarding contrast ratio, it has been shown that polarimetry itself can reduce the contrast ratio between host star and planet by five orders of magnitude during the post observational reduction phase, because the host star's light is on average unpolarised. For the proposed mission, a Half-Wave-Achromatic Eight Octant Phase Mask has been chosen as the coronograph and Pockel Cells suggested as polarisors. In addition, the use of an integral field spectrograph is proposed for separation of light from the star and the planet as well as the reduction of speckle noise.

Of course there are technological developments to be undertaken before a concept like the proposed SEARCH mission can be realised. Nevertheless, since nearly all of those are key developments for other planned or already scheduled space missions, future projects like SEARCH will be able to use these developments to achieve the ambitious goal of characterising Earth-like planets.

Acknowledgements The authors want to thank Andre Balogh, Antonio Castro, Malcolm Fridlund, Eike Günther, Günter Kargl, Helmut Lammer, and Jörg Weingrill for their valuable comments and useful discussions and Michaela Gitsch (FFG) for her organisatorial skills. This work originated at the Alpbach Summer School 2009; we thank the lecturers and tutors, as well as our fellow students for the unique learning experience there. The mission proposal presented in this paper was continued during the Post Alpbach Workshop hosted by the Space Research Institute (IWF) of the Austrian Academy of Sciences (ÖAW) in Graz; we would like to thank the Institute's Director, Wolfgang Baumjohann for hosting it. We acknowledge the financial support of ESA's Education Office that made the event possible, and the support from FFG, ISSI and Austrospace. Siegfried Eggl and Nicola Sarda acknowledge the support from the European Science Foundation (ESF) for presenting the SEARCH mission concept during the ESF Exploratory Workshop on "Observation, Characterization and Evolution of Habitable Exoplanets and their Host Stars" in Bairisch Kölldorf, Austria, Nov. 2009. Finally Siegfried Eggl would like to acknowledge the support of the Austrian FWF project P20216 and Veresa Eybl wants to acknowledge the support of the Austrian FWF project P18930-N16. Nicolas Sarda would like to acknowledge financial support from Astrium Ltd.

References

1. Adams, E.R., Seager, S., Elkins-Tanton, L.: Ocean planet or thick atmosphere: on the mass-radius relationship for solid exoplanets with massive atmospheres. ApJ **673**, 1160–1164 (2008). doi:10.1086/524925, 0710.4941
2. Adamson, A., Aspin, C., Davis, C., Fujiyoshi, T. (eds.): Astronomical Polarimetry: Current Status and Future Directions. Astronomical Society of the Pacific Conference Series, vol. 343 (2005)
3. Alibert, Y., Broeg, W., Bens, G., Wuchterl, O., Grasset, C., Sotin, Eiroa, C., Henning, T., Herbst, T., Kaltenegger, L., Le, A., Liseau, L., Lammer, H., Beichman, C., Danchi, W.,

Fridlund, M., Lunine, J., Paresce, F., Penny, A., Quirrenbach, A., Roettgering, H., Selsis, F., J. S., Stam, D., Tinetti, G., White, G.: Origin and formation of planetary systems. Astrobiology **10**, 19–32 (2010)
4. Barnes, R., Jackson, B., Raymond, S.N., West, A.A., Greenberg, R.: The HD 40307 planetary system: super-Earths or mini-Neptunes? ApJ **695**, 1006–1011 (2009). doi:10.1088/0004-637X/695/2/1006, 0901.1698
5. Beuzit, J., Feldt, M., Dohlen, K., Mouillet, D., Puget, P., Antichi, J., Baruffolo, A., Baudoz, P., Berton, A., Boccaletti, A., Carbillet, M., Charton, J., Claudi, R., Downing, M., Feautrier, P., Fedrigo, E., Fusco, T., Gratton, R., Hubin, N., Kasper, M., Langlois, M., Moutou, C., Mugnier, L., Pragt, J., Rabou, P., Saisse, M., Schmid, H.M., Stadler, E., Turrato, M., Udry, S., Waters, R., Wildi, F.: SPHERE: a 'Planet Finder' instrument for the VLT. Messenger **125**, 29 (2006)
6. Bloemhof, E.E.: Speckle noise in highly corrected coronagraphs. In: Gonglewski, J.D., Gruneisen, M.T., Giles, M.K. (eds.) Society of Photo-Optical Instrumentation Engineers (SPIE) Conference Series. Presented at the Society of Photo-Optical Instrumentation Engineers (SPIE) Conference, vol. 5553, pp. 281–289 (2004). doi:10.1117/12.560370
7. Bloemhof, E.E.: Achromatic four-quadrant phase mask (FQPM) coronagraphy using natural beam splitter phase shifts. Opt. Express **13**, 10055–10060 (2005). doi:10.1364/OPEX.13.010055
8. Boccaletti, A., Abe, L., Baudrand, J., Daban, J., Douet, R., Guerri, G., Robbe-Dubois, S., Bendjoya, P., Dohlen, K., Mawet, D.: Prototyping coronagraphs for exoplanet characterization with SPHERE. In: Society of Photo-Optical Instrumentation Engineers (SPIE) Conference Series. Presented at the Society of Photo-Optical Instrumentation Engineers (SPIE) Conference, vol. 7015 (2008). doi:10.1117/12.789341
9. Bordé, P., Traub, W.: Speckle noise reduction techniques for high-dynamic range imaging. C. R. Acad. Sci., Phys. **8**(3–4), 349–354 (2007). doi:10.1016/j.crhy.2007.04.004. Optical techniques for direct imaging of exoplanets. http://www.sciencedirect.com/science/article/B6X19-4NXGSG8-2/2/4e7c525c56f714b72742c1a960135bdf
10. Bordé, P.J., Traub, W.A.: High-contrast imaging from space: speckle nulling in a low-aberration regime. ApJ **638**, 488–498 (2006). doi:10.1086/498669, arXiv:astro-ph/0510597
11. Braak, C., Haan, J., Hovenier, J., Travis, L.: Galileo photopolarimetry of jupiter at 678.5 nm. Icarus **157**, 401–418 (2002)
12. Christensen-Dalsgaard, J., Arentoft, T., Brown, T.M., Gilliland, R.L., Kjeldsen, H., Borucki, W.J., Koch, D.: The Kepler mission. Commun. Asteroseismol. **158**, 328 (2009)
13. Cockell, C.S., Herbst, T., Léger, A., Absil, O., Beichman, C., Benz, W., Brack, A., Chazelas, B., Chelli, A., Cottin, H., Coudé Du Foresto, V., Danchi, W., Defrère, D., den Herder, J., Eiroa, C., Fridlund, M., Henning, T., Johnston, K., Kaltenegger, L., Labadie, L., Lammer, H., Launhardt, R., Lawson, P., Lay, O.P., Liseau, R., Martin, S.R., Mawet, D., Mourard, D., Moutou, C., Mugnier, L., Paresce, F., Quirrenbach, A., Rabbia, Y., Rottgering, H.J.A., Rouan, D., Santos, N., Selsis, F., Serabyn, E., Westall, F., White, G., Ollivier, M., Bordé, P.: Darwin—an experimental astronomy mission to search for extrasolar planets. Exp. Astron. **23**, 435–461 (2009). doi:10.1007/s10686-008-9121-x
14. Codona, J.L.: Exoplanet imaging with the Giant Magellan Telescope. In: Bonaccini Calia, D., Ellerbroek, B.L., Ragazzoni, R. (eds.) Society of Photo-Optical Instrumentation Engineers (SPIE) Conference Series. Presented at the Society of Photo-Optical Instrumentation Engineers (SPIE) Conference, vol. 5490, pp. 379–388 (2004). doi:10.1117/12.552450
15. Delplancke, F.: The PRIMA facility phase-referenced imaging and micro-arcsecond astrometry. New Astron. Rev. **52**, 199–207 (2008). doi:10.1016/j.newar.2008.04.016
16. D'Odorico, V., the CODEX/ESPRESSO team: CODEX/ESPRESSO: the era of precision spectroscopy. Mem. Soc. Astron. Ital. **78**, 712 (2007). 0708.1258
17. Ebisawa, S., Dollfus, A.: Dust in the martian atmosphere: polarimetric sensing. Astron. Astrophys. **272**, 671–686 (1992)
18. European Space Agency: Esa Science and Technology—Strategic Readiness Level. http://sci.esa.int/science-e/www/object/index.cfm?fobjectid=37710 (2006)
19. Feldt, M., Gratton, R., Hippler, S., Schmid, H.M., Turatto, M., Waters, R., Henning, T.: The CHEOPS Project: Characterizing Exoplanets by Opto-infrared Polarimetry and Spectroscopy, pp. 261–264. Springer (2007)
20. Forget, F., Pierrehumbert, R.T.: Warming early Mars with carbon dioxide clouds that scatter infrared radiation. Science **278**, 1273–1276 (1997)

21. GAIA Science advisory group: Gaia, Composition, Formation and Evolution of the Galaxy. Tech. Rep., European Space Agency (2000)
22. Guyon, O.: Imaging faint sources within a speckle halo with synchronous interferometric speckle subtraction. Astrophys. J. **615**(1), 562–572 (2004). http://stacks.iop.org/0004-637X/615/562
23. Habets, G.M.H.J., Heinze, J.R.W.: Tables vii, viii, empirical bolometric corrections for the main-sequence. Astron. Astrophys., Suppl. Ser. **46**, 193–237 (1981)
24. Haguenauer, P., Serabyn, E., Bloemhof, E.E., Wallace, J.K., Gappinger, R.O., Mennesson, B.P., Troy, M., Koresko, C.D., Moore, J.D.: An off-axis four-quadrant phase-mask coronagraph for Palomar: high contrast near bright stars imager. In: Coulter, D.R. (ed.) Society of Photo-Optical Instrumentation Engineers (SPIE) Conference Series. Presented at the Society of Photo-Optical Instrumentation Engineers (SPIE) Conference, vol. 5905, pp. 261–271 (2005). doi:10.1117/12.615234
25. Hansen, J., Hovenier, J.: Interpretation of the polarization of venus. J. Atmos. Sci. **31**, 1137–1160 (1973)
26. Holland, H.: The Chemistry of the Atmosphere and Oceans (1978)
27. Hough, J.H., Lucas, P.W.: Polarimetry as an Aid to the Detection of Extra-Solar Planets. ESA Special Publication, vol. 539, pp. 11–17 (2003). http://adsabs.harvard.edu/abs/2003ESASP.539...11H
28. Joos, F., Schmid, H.M., Gisler, D., Feldt, M., Brandner, W., Stam, D.M., Quirrenbach, A., Stuik, R.: Spectropolarimetry of CH4 bands of solar system planets. In: Adamson, A., Aspin, C., Davis, C., Fujiyoshi, T. (eds.) Astronomical Polarimetry: Current Status and Future Directions. Astronomical Society of the Pacific Conference Series, vol. 343, p. 189 (2005)
29. Joss, F., Schmid, H.M.: Polarimetry of solar system gaseous planets. Messenger **130**, 27–31 (2007)
30. Kaltenegger, L., Selsis, F.: Biomarkers set in context. In: Dvorak, R. (ed.) Extrasolar Planets: Formation, Detection and Dynamics, pp. 79–98 (2007)
31. Kaltenegger, L., Eiroa, C., Friedlund, M.: Target star catalogue for DARWIN: nearby habitable star systems. In: Protostars and Planets V, Proceedings of the Conference held 24–28 October 2005, Hilton, Waikola Village, Hawaii. LPI Contribution no. 1286, p. 8206 (2005)
32. Kaltenegger, L., Traub, W.A., Jucks, K.W.: Spectral evolution of an Earth-like planet. ApJ **658**, 598–616 (2007). doi:10.1086/510996 arXiv:astro-ph/0609398
33. Kaltenegger, L., Eiroa, C., Fridlund, C.V.M.: Target Star Catalog for Darwin: Nearby Stellar Sample for a Search for Terrestrial Planets (2008). ArXiv e-prints 0810.5138
34. Karkoschka, E.: Methane, ammonia, and temperature measurements of the Jovian planets and Titan from CCD-spectrophotometry. Icarus **133**, 134–146 (1998). doi:10.1006/icar.1998.5913
35. Kasting, J.: Runaway and moist greenhouse atmospheres and the evolution of Earth and Venus. Icarus **74**, 472–494 (1988). doi:10.1016/0019-1035(88)90116-9
36. Kasting, J., Whitmire, D., Reynolds, R.: Habitable zones around main sequence stars. Icarus **101**, 108–128 (1993). doi:10.1006/icar.1993.1010
37. Keller, C.U., Stenflo, J.O.: The second solar spectrum. In: Bulletin of the American Astronomical Society, vol. 28, p. 912. American Astronomical Society (1996)
38. Khodachenko, M.L., Lammer, H., Lichtenegger, H.I.M., Langmayr, D., Erkaev, N.V., Grießmeier, J., Leitner, M., Penz, T., Biernat, H.K., Motschmann, U., Rucker, H.O.: Mass loss of "Hot Jupiters"—implications for CoRoT discoveries. Part I: the importance of magnetospheric protection of a planet against ion loss caused by coronal mass ejections. P&SS **55**, 631–642 (2007). doi:10.1016/j.pss.2006.07.010
39. Kuchner, M.J., Seager, S.: Extrasolar Carbon Planets (2005). ArXiv Astrophysics e-prints: arXiv:astro-ph/0504214
40. Kulikov, Y.N., Lammer, H., Lichtenegger, H.I.M., Penz, T., Breuer, D., Spohn, T., Lundin, R., Biernat, H.K.: A comparative study of the influence of the active young sun on the early atmospheres of Earth, Venus, and Mars. Space Sci. Rev. **129**, 207–243 (2007). doi:10.1007/s11214-007-9192-4
41. Lammer, H., Kasting, J.F., Chassefière, E., Johnson, R.E., Kulikov, Y.N., Tian, F.: Atmospheric escape and evolution of terrestrial planets and satellites. Space Sci. Rev. **139**, 399–436 (2008). doi:10.1007/s11214-008-9413-5

42. Lammer, H., Bredehöft, J.H., Coustenis, A., Khodachenko, M.L., Kaltenegger, L., Grasset, O., Prieur, D., Raulin, F., Ehrenfreund, P., Yamauchi, M., Wahlund, J., Grießmeier, J., Stangl, G., Cockell, C.S., Kulikov, Y.N., Grenfell, J.L., Rauer, H.: What makes a planet habitable? Astron. Astrophys. Rev. **17**, 181–249 (2009). doi:10.1007/s00159-009-0019-z
43. Lammer, H., Odert, P., Leitzinger, M., Khodachenko, M.L., Panchenko, M., Kulikov, Y.N., Zhang, T.L., Lichtenegger, H.I.M., Erkaev, N.V., Wuchterl, G., Micela, G., Penz, T., Biernat, H.K., Weingrill, J., Steller, M., Ottacher, H., Hasiba, J., Hanslmeier, A.: Determining the mass loss limit for close-in exoplanets: what can we learn from transit observations? Astron. Astrophys. **506**, 399–410 (2009). doi:10.1051/0004-6361/200911922
44. Lattanzi, M.G., Casertano, S., Jancart, S, Morbidelli, R., Pourbaix, D., Pannunzio, R., Sozzetti, A., Spagna, A.: Detection and characterization of extra-solar planets with Gaia. In: Turon, C., O'Flaherty, K.S., Perryman, M.A.C. (eds.) The Three-Dimensional Universe with Gaia. ESA Special Publication, vol. 576, p. 251 (2005)
45. Léger, A., Selsis, F., Sotin, C., Guillot, T., Despois, D., Mawet, D., Ollivier, M., Labèque, A., Valette, C., Brachet, F., Chazelas, B., Lammer, H.: A new family of planets? "Ocean-Planets". Icarus **169**, 499–504 (2004). doi:10.1016/j.icarus.2004.01.001, arXiv:astro-ph/0308324
46. Léger, A., Rouan, D., Schneider, J., et al.: Transiting exoplanets from the CoRoT space mission. VIII. CoRoT-7b: the first super-Earth with measured radius. Astron. Astrophys. **506**, 287–302 (2009). doi:10.1051/0004-6361/200911933, 0908.0241
47. Levine, M., Lisman, D., Shaklan, S.: Terrestrial Planet Finder—Coronagraph (tpf-c) Flight Baseline Mission Concept. Tech. Rep., National Aeronautical and Space Administration/Jet Propulsion Laboratory (2009)
48. Liske, J., Pasquini, L., Bonifacio, P., Bouchy, F., Carswell, R.F., Cristiani, S., Dessauges, M., D'Odorico, S., D'Odorico, V., Grazian, A., Garcia-Lopez, R., Haehnelt, M., Israelian, G., Lovis, C., Martin, E., Mayor, M., Molaro, P., Murphy, M.T., Pepe, F., Queloz, D., Rebolo, R., Udry, S., Vanzella, E., Viel, M., Wiklind, T., Zapatero, M., Zucker, S.: From espresso to codex. In: Moorwood, A. (ed.) Science with the VLT in the ELT Era, pp. 243–247 (2009). doi:10.1007/978-1-4020-9190-2_41
49. Lissauer, J.J.: How common are habitable planets? Nature **402**, C11–C24 (1999)
50. Marley, M.S., Fortney, J., Seager, S., Barman, T.: Atmospheres of extrasolar giant planets. In: Protostars and Planets V, pp. 733–747 (2007). arXiv:astro-ph/0602468
51. Mignard, F.: Overall science goals of the Gaia mission. In: Turon, C., O'Flaherty, K.S., Perryman, M.A.C. (eds.) The Three-Dimensional Universe with Gaia, vol. 576, p. 5. ESA Special Publication (2005)
52. Miller-Ricci, E., Seager, S., Sasselov, D.: The atmospheres of extrasolar super-Earths. In: IAU Symposium, vol. 253, pp. 263–271 (2009). doi:10.1017/S1743921308026483
53. Miller-Ricci, E., Seager, S., Sasselov, D.: The atmospheric signatures of super-Earths: how to distinguish between hydrogen-rich and hydrogen-poor atmospheres. ApJ **690**, 1056–1067 (2009). doi:10.1088/0004-637X/690/2/1056, 0808.1902
54. Mischna, M.A., Kasting, J.F., Pavlov, A., Freedman, R.: Influence of carbon dioxide clouds on early martian climate. Icarus **145**, 546–554 (2000). doi:10.1006/icar.2000.6380
55. Murakami, N., Uemura, R., Baba, N., Nishikawa, J., Tamura, M., Hashimoto, N., Abe, L.: An Eight-Octant Phase-Mask Coronagraph. Publications of the Astronomical Society of the Pacific (2008)
56. Murakami, N., Uemura, R., Baba, N., Sato, Y., Nishikawa, J., Tamura, M. (2008) Four quadrant phase mask coronagraph with Jacquinot-Lyot stop. Astrophys. J. **677**, 1425–1432
57. O'Donovan, F.T., Charbonneau, D., Hillenbrand, L: Detection and exploration of planets from the trans-atlantic exoplanet survey. In: Bulletin of the American Astronomical Society, vol. 38, p. 1212. American Astronomical Society (2006)
58. O'Neill, C., Lenardic, A.: Geological consequences of super-sized Earths. GeoRL **34**, 19204–19207 (2007). doi:10.1029/2007GL030598
59. Pepe, F., Lovis, C.: High resolution and high precision-spectroscopy with HARPS. In: Kaufer, A., Kerber, F. (eds.) The 2007 ESO Instrument Calibration Workshop. Proceedings of the ESO Workshop held in Garching, Germany, 23–26 January 2007,, pp. 375–384, (2008). ISBN: 978-3-540-76962-0, doi:10.1007/978-3-540-76963-7_50

60. Plesseria, J.Y., Mazy, E., Defise, J.M., Rochus, P., Magnan, A., Costes, V.: Straylight analysis of the external baffle of COROT. In: Warmbein, B. (ed.) 5th International Conference on Space Optics. ESA Special Publication, vol. 554, pp. 543–550 (2004)
61. Queloz, D., Bouchy, F., Moutou, C., Hatzes, A., Hébrard, G., Alonso, R., Auvergne, M., Baglin, A., Barbieri, M., Barge, P., Benz, W., Bordé, P., Deeg, H.J., Deleuil, M., Dvorak, R., Erikson, A., Ferraz Mello, S., Fridlund, M., Gandolfi, D., Gillon, M., Guenther, E., Guillot, T., Jorda, L., Hartmann, M., Lammer, H., Léger, A., Llebaria, A., Lovis, C., Magain, P., Mayor, M., Mazeh, T., Ollivier, M., Pätzold, M., Pepe, F., Rauer, H., Rouan, D., Schneider, J., Segransan, D., Udry, S., Wuchterl, G.: The CoRoT-7 planetary system: two orbiting super-Earths. Astron. Astrophys. **506**, 303–319 (2009). doi:10.1051/0004-6361/200913096
62. Raymond, S.N., Quinn, T., Lunine, J.I.: Making other earths: dynamical simulations of terrestrial planet formation and water delivery. Icarus **168**, 1–17 (2004). doi:10.1016/j.icarus.2003.11.019, arXiv:astro-ph/0308159
63. Roddier, F.: The effects of atmospheric turbulence in optical astronomy. In: Wolf, E. (ed.) Progress in Optics, vol. 19, pp. 281–376. North-Holland, Amsterdam (1981)
64. Saar, S.H., Seager, S.: Uses of Linear Polarization as a Probe of Extrasolar Planet Atmospheres, vol. 294, pp. 529–534 (2003). http://adsabs.harvard.edu/abs/2003ASPC..294..529S
65. Sasselov, D.D., Valencia, D., O'Connell, R.J.: Massive terrestrial planets (super-Earths): detailed physics of their interiors. Phys. Scr., T **130**(1), 14,035 (2008). doi:10.1088/0031-8949/2008/T130/014035
66. Schmid, H.M., Quirrenbach, A., Wolstencroft, R.D.: Polarization of terrestrial planets and the ZIMPOL technique. In: Proceedings Second TPF/Darwin Conference (2004)
67. Schneider, J., Riaud, P., Tinetti, G., Schmid, H.M., Stam, D., Udry, S., Baudoz, P., Boccaletti, A., Grasset, O., Mawet, D., Surdej, J., The See-Coast Team: SEE-COAST: the super-Earth explorer. In: Barret, D., Casoli, F., Lagache, G., Lecavelier, A., Pagani, L. (eds.) SF2A-2006: Semaine de l'Astrophysique Francaise, p. 429 (2006)
68. Schneider, J., Boccaletti, A., Mawet, D., Baudoz, P., Beuzit, J., Doyon, R., Marley, M., Stam, D., Tinetti, G., Traub, W., Trauger, J., Aylward, A., Cho, J., Keller, C., Udry, S.: Super Earth explorer: a coronagraphic off-axis space telescope. Exp. Astron. **23**, 357–377 (2009). doi:10.1007/s10686-008-9129-2, 0811.3908
69. Seager, S., Whitney, B.A., Sasselov, D.D.: Photometric light curves and polarization of close-in extrasolar giant planets. Astrophys. J. **540**, 504–520 (2000). http://adsabs.harvard.edu/abs/2000ApJ...540..504S
70. Seager, S., Turner, E.L., Schafer, J., Ford, E.B.: Vegetation's red edge: a possible spectroscopic biosignature of extraterrestrial plants. Astrobiology **5**, 372–390 (2005). doi:10.1089/ast.2005.5.372, arXiv:astro-ph/0503302
71. Seager, S., Kuchner, M., Hier-Majumder, C.A., Militzer, B.: Mass-radius relationships for solid exoplanets. ApJ **669**, 1279–1297 (2007). doi:10.1086/521346, 0707.2895
72. Stam, D.M.: Polarization Spectra of Extrasolar Planets, vol. 539, pp. 615–619 (2003). http://adsabs.harvard.edu/abs/2003ESASP.539..615S
73. Stam, D.M.: Spectropolarimetric signatures of Earth-like extrasolar planets. Astron. Astrophys. **482**, 989–1007 (2008). doi:10.1051/0004-6361:20078358, 0707.3905
74. Stam, D.M., Hovenier, J., Waters, R.: Polarization of Extrasolar Planets: Sample Simulations, vol. 294, pp. 535–538 (2003). http://adsabs.harvard.edu/abs/2003ASPC..294..535S
75. Stam, D.M., Hovenier, J.W., Waters, L.B.F.M.: Using polarimetry to detect and characterize jupiter-like extrasolar planets. Astron. Astrophys. **428**, 663–672 (2004). doi:10.1051/0004-6361:20041578
76. Sudarsky, D., Burrows, A., Hubeny, I.: Theoretical spectra and atmospheres of extrasolar giant planets. ApJ **588**, 1121–1148 (2003). doi:10.1086/374331, arXiv:astro-ph/0210216
77. Tanner, A.M., Catanzarite, J., Shao, M.: Detection and mass characterization of terrestrial planets in the habitable zone with SIM PlanetQuest. In: Protostars and Planets V, p. 8304 (2005)
78. Unwin, S.C., Shao, M., Tanner, A.M., Allen, R.J., Beichman, C.A., Boboltz, D., Catanzarite, J.H., Chaboyer, B.C., Ciardi, D.R., Edberg, S.J., Fey, A.L., Fischer, D.A., Gelino, C.R., Gould, A.P., Grillmair, C., Henry, T.J., Johnston, K.V., Johnston, K.J., Jones, D.L., Kulkarni, S.R., Law, N.M., Majewski, S.R., Makarov, V.V., Marcy, G.W., Meier, D.L., Olling, R.P., Pan, X., Patterson, R.J., Pitesky, J.E., Quirrenbach, A., Shaklan, S.B., Shaya, E.J., Strigari, L.E.,

Tomsick, J.A., Wehrle, A.E., Worthey, G.: Taking the measure of the universe: precision astrometry with SIM PlanetQuest. PASP **120**, 38–88 (2008) doi:10.1086/525059, 0708.3953
79. Valencia, D., O'Connell, R.J., Sasselov, D.D.: Inevitability of plate tectonics on super-Earths. ApJ **670**, L45–L48 (2007). doi:10.1086/524012, 0710.0699
80. Valencia, D., Sasselov, D.D., O'Connell, R.J.: Detailed models of super-Earths: how well can we infer bulk properties? ApJ **665**, 1413–1420 (2007). doi:10.1086/519554, 0704.3454
81. Widger, W.K.J., Woodall, M.: Integration of the planck blackbody radiation function. Bull. Am. Meteorol. Soc. **57**, 1217–1219 (1976)
82. Williams, D.M., Gaidos, E.: Detecting the glint of starlight on the oceans of distant planets. Icarus **195**, 927–937 (2008). doi:10.1016/j.icarus.2008.01.002, 0801.1852